MCGILL UNIVERSITY

Parametric driving as a route to topological states and quantum devices

Martin Houde

Department of Physics

July 2018

McGill University, Montreal, Quebec

A thesis submitted to McGill University in partial fulfillment of the requirements of the degree of Doctor of Philosophy

Abstract

In this thesis, we theoretically study novel ways to use parametric driving in bosonic systems as a resource to generate interesting properties and states.

We parametrically drive a topologically trivial bosonic system and show that properly tuning the phases and strengths of the drive induces a topological phase transition. We study the phase diagram and show that parametrically-driven topological bosonic systems are distinct from their fermionic analogues as well as topological systems without parametric driving. For a finite-sized system, we use standard input-output formalism to study the transport of classical signals. We show that parametrically-driven topological bosonic systems mediate protected chiral inelastic transport in conjunction with the usual chiral elastic transport.

When weakly coupled to a zero-temperature environment, we show that parametrically driving a bosonic system can lead to interesting steady-states. Under certain circumstances, we show that it is possible to obtain a steady-state for non-conserved bosons, such as photons, that is thermally occupied at a finite temperature and chemical potential.

In a different scheme, we study how vacuum fluctuations propagate in parametrically-driven topological bosonic systems. We show how to obtain parametrically-unstable edge states, while maintaining stable bulk modes, by choosing the frequency and phases of the drive accordingly. Furthermore, we show how to exploit this property to realize a topologically-protected, travelling-wave amplifier. Such a device is experimentally cost-heavy to produce: requires parametrically driving many lattice sites. We thus numerically study if it is possible to achieve a resource-efficient device with similar amplifying properties. We show that we can greatly reduce the number of parametrically driven sites, increasing the resource-efficiency.

Finally, we study the effects of having different loss rates for the bosonic modes in travelling-wave parametric amplifiers. We study two different loss models and show that having loss asymmetry can greatly deteriorate the squeezing of collective output quadratures while leaving your state strongly entangled. As several protocols require the use of squeezed collective quadratures, we propose a correction scheme which allows one to regain some level of squeezing for the collective quadratures. Furthermore, we show that asymmetry increases the amount of noise added by the amplifier.

Résumé

Dans cette thèse, nous étudions d'un point de vue théorique de nouvelles façons d'utiliser la modulation paramétrique dans des systèmes bosonique comme une ressource pour générer des propriétés et des états intéressants.

Nous modulons de manière paramétrique un système de bosons topologiquement trivial et nous montrons que le réglage correct des phases et des amplitudes de la modulation induit une transition de phase topologique. Nous établissons le diagramme de phase et nous montrons que les systèmes de bosons topologiques à modulation paramétrique sont distincts de leurs analogues fermioniques ainsi que des systèmes topologiques sans modulation paramétrique. Pour un système de taille finie, nous utilisons le formalisme d'entrée-sortie standard pour étudier le transport des signaux classiques. Nous montrons que les systèmes de bosons topologiques à modulation paramétriques peuvent servir de médiateur pour le transport inélastique et chiral en conjonction avec le transport élastique et chiral habituel.

Lorsque faiblement couplé à un environnement à température nulle, nous montrons que la modulation paramétrique d'un système bosonique peut conduire à des états d'équilibre intéressants. Nous montrons qu'il est possible d'observer sous certaines conditions un état d'équilibre pour des bosons non conservés, comme par exemple des photons, qui est thermiquement occupés à une température finie et à un potentiel chimique non-nulle.

Dans un second temps, nous étudions comment les fluctuations du vide se propagent dans des systèmes de bosons topologiques à modulation paramétrique. Nous montrons comment obtenir des états de bord paramétriquement instables, tout en maintenant les modes de volume stables, en choisissant la fréquence et les phases de la modulation en conséquence. Nous exploitons ensuite ces proprietés pour réaliser un amplificateur à ondes de déplacement topologiquement protégé. Un tel dispositif est expérimentalement coûteux à produire puisqu'il nécessite la modulation paramétrique de nombreux sites. Nous étudions donc numériquement la possibilité de réaliser un dispositif économe en ressources sans compromettre l'amplification. Nous montrons que nous pouvons réduire considérablement le nombre de sites modulé paramétriquement, augmentant ainsi l'efficacité des ressources du dispositif.

Enfin, nous étudions les effets d'avoir des taux de relaxation non-uniform pour les

modes bosoniques présent dans les amplificateurs paramétrique à ondes de déplacement. Nous étudions deux modèles de perte différents et montrons que l'asymétrie de perte peut grandement détériorer la compression de la quadrature collective de sortie tout en laissant l'état fortement intriqué. Comme plusieurs protocoles nécessitent l'utilisation de quadrature collective compressée, nous proposons un protocol de correction d'erreur qui permet de retrouver un certain niveau de compression pour les quadratures collectifs. De plus, nous montrons que l'asymétrie augmente la quantité de bruit produite par l'amplificateur.

Contributions of authors

This thesis is written in a manuscript based format. The main chapters of this dissertation (2, 3, 4, 5, 6) are self-contained and each contains its own introduction, conclusion, and appendices. All of these papers have been written during my candidature. Chapters 2 and 4 have been published, whereas chapters 3, 5, and 6 are to be submitted for publication. The contributions of each author to the manuscripts contained in this dissertation are listed below.

Topological phase transitions and chiral inelastic transport induced by the squeezing of light

Vittorio Peano, Martin Houde, Christian Brendel, Florian Marquardt, and Aashish A. Clerk

Nat. Commun. 7, 10779 (2016)

Calculations and simulations were done by myself, VP and CB. VP, AAC and FM contributed to the conceptual development of the project and interpretation of results.

Steady-states of parametrically driven systems

Martin Houde and Aashish A. Clerk

To be submitted for publication

I performed all calculations and wrote the manuscript under the guidance of AAC who assisted in the interpretation of results and revised the manuscript.

Topological quantum fluctuations and travelling wave amplifiers

Vittorio Peano, Martin Houde, Florian Marquardt, and Aashish A. Clerk

Phys. Rev. X 6, 041026 (2016)

Calculations, simulations, and writing of the manuscript were done by myself and VP. AAC and FM contributed to the conceptual development of the project, interpretation of results, and revision of the manuscript.

Resource efficient topological travelling wave amplifier

Martin Houde and Aashish A. Clerk
To be submitted for publication

I performed all calculations, simulations, and wrote the manuscript. AAC supervised the work, assisted in the interpretation of the results, and revised the manuscript.

Loss asymmetries in quantum travelling wave parametric amplifiers

Martin Houde, L. C. G. Govia, and Aashish A. Clerk
To be submitted for publication

Calculations, simulations, and writing of the manuscript were done by myself with assistance from LCGG. AAC initially suggested the problem and helped with the interpretation of results and revision of the manuscript.

Acknowledgments

My first words of acknowledgement go without question to my supervisor Prof. Aashish A. Clerk. Aash has an incredible knowledge of physics and phenomenal physical intuition that is always enlightening. I thank him for the time he took in guiding me throughout this thesis. None of this would have been possible without his guidance. I would also like to thank the members of my Ph.D. supervisory committee Jack C. Sankey and Tamar Pereg-Barnea. Thank you Tami for graciously accepting to become my official supervisor.

The research presented in this thesis has also benefited from greatly appreciated collaborators. I would like to thank Vittorio Peano, Florian Marquardt, and Christian Brendel for their incredible work and intuition which was extremely valuable for the completion of this thesis. I would also like to thank Luke C. G. Govia for the great collaborative work.

My life as a Ph.D. student involved a lot of work, but it also involved a lot of good company. First and foremost, I would like to thank everyone from Urban Groove dance project. There are no words to describe how good you have all been to me throughout this degree. A warm thank you to Tommy *Wolfgang* and David King-Hope for being there when I needed someone to talk to and distract myself. Thank you as well to Aidan Oliver Howenstine and the DnD crew. I really had a blast with you guys. I would then like to thank all the incredible people I have befriended at McGill during my degree. Thank you to Jean-René Souquet, Alexandre Baksic, Luke C. G. Govia, Nicolas Dider, and Felix Beaudoin. Your company during lunch and Friday evenings always brightened up my days. It hasn't been the same without you guys.

I would like to thank my parents Guy Houde and Christine Arbour as well as my brothers Christian Houde and Jeff houde. Your love and support mean the world to me. There is no doubt that I would not be where I am today without all that you have given and done for me.

A special thank you to my friends Kevin Droun-Léger, Léa Messier, and Thomas F. Lemaire. Your support and company means the world to me and it has helped me in more ways than you can think. You have helped make this journey and my life more enjoyable.

Finally, an incredible and heartfelt thank you to Brittany Barbeau.

Contents

List of Figures

List of Tables

1

Introduction

Parametric driving in bosonic systems refers to processes where pairs of bosons are coherently created and annihilated. These processes occur in a variety of systems such as photonic crystal nanocavities made from non-linear $\chi^{(2)}$ materials [1–4], superconducting resonators with Josephson non-linearities[5], and optomechanical systems [6, 7] to name a few. Such processes can be used as a resource for: the amplification of quantum signals where the noise injected by the amplifying process is at the lowest limit allowed by quantum mechanics (quantum-limited), the squeezing of vacuum fluctuations and light, and generating entanglement [8]. This thesis explores new fundamental uses and physical applications of parametric driving. We study how parametric driving can be used as a resource to induce topology and interesting steady-states. Furthermore, we study how topological systems, subject to parametric driving, can be engineered to create a quantum-limited, travelling-wave parametric amplifier that is robust to disorder due to topology (topologically protected). For more general travelling-wave amplifiers, which are not robust to disorder, we study how different loss rates for the bosonic modes of the system affects the amplifying, squeezing, and entanglement properties in travelling-wave amplifiers. This chapter provides a brief introduction to parametric driving by studying

the properties of a single-cavity model (Sec. 1.1) as well as briefly introducing the notion of topology in systems where time-reversal symmetry is broken, also known as Chern insulators [22], and the consequences of topology in finite systems (Sec. 1.2)

1.1 Parametric driving

Before exploring parametric driving and amplification in the quantum regime, we begin by studying a simple classical analog of a linear amplifier: a mechanical oscillator whose spring constant is modulated in time. In this setup, we consider the signal we want to amplify as being the position, $x(t)$, of the harmonic oscillator. For a time-independent spring constant, the position is given by

$$x(t) = x(0)\cos(\omega_S t) + \frac{p(0)}{m\omega_S}\sin(\omega_S t) \tag{1.1.1}$$

which is separated into two quadratures: the amplitudes of the sine and cosine components. We parametrically drive the oscillator by modulating the spring constant periodically in time such that $k(t) = k_S + 2\sqrt{k_S}\sqrt{\delta k}\sin(\omega_P t)$ and assume a weak modulation ($\delta k \ll k_S$). Note that the form for the amplitude of the modulation is written out this way for simplicity. Properly setting the modulation frequency to be twice the natural frequency, $\omega_P = 2\omega_S$, will result in amplification. To see this, we start from the equation of motion for the position

$$\ddot{x}(t) + \omega_S^2 x(t) = -2\omega_S \delta\omega \sin(2\omega_S t)x(t), \tag{1.1.2}$$

where $\delta\omega = \sqrt{\delta k/m}$ and we have expressed everything in terms of the natural frequency ω_S. We can solve for the dynamics by assuming a solution of the form

$$x(t) = A(t)\cos(\omega_S t) + B(t)\sin(\omega_S t) \tag{1.1.3}$$

where we assume $A(t)$ and $B(t)$ are slowly varying envelope functions. Under this assumption, we have that $\ddot{A}(t) \approx 0$ and $\ddot{B}(t) \approx 0$. Using this ansatz, we can re-write the left-hand side of Eq.(1.1.2) as

$$-\omega_S\delta\omega\left[A(t)\left(\sin(\omega_S t) + \sin(3\omega_S t)\right) + B(t)\left(\cos(3\omega_S t) - \cos(\omega_S t)\right)\right]. \tag{1.1.4}$$

The left-hand side now has driving terms at frequencies ω_S and $3\omega_S$. The terms oscillating at $3\omega_S$ are highly off-resonant and are neglected under the rotating wave approximation. Combining both the rotating wave approximation and neglecting the second-order time derivatives of the slowly vary envelope functions leads to the equations of motion

$$\dot{A}(t) = \frac{\delta\omega}{2}A(t) \tag{1.1.5}$$

$$\dot{B}(t) = -\frac{\delta\omega}{2}B(t) \tag{1.1.6}$$

for the envelope functions. The resulting dynamics are

$$x(t) = x(0)e^{\delta\omega t/2}\cos(\omega_S t) + \frac{p(0)}{m\omega_S}e^{-\delta\omega t/2}\sin(\omega_S t). \tag{1.1.7}$$

We see that one quadrature grows exponentially and is amplified while the other is suppressed. The basic processes responsible for amplification involved here are akin to those of bosonic systems. Having shown how parametric driving leads to amplification in a classical system, we now turn our attention to a quantum-mechanical system.

To begin our discussion of parametric driving in a quantum system, we consider the simplest model in which it arises. We consider a single cavity with a non-linear element. The cavity has three internal resonances which are coupled together through the non-linear element [9]. We focus on the case where the non-linearity generates three-wave mixing interactions. We label the three modes as pump, signal, and idler and for energy conservation demand that their frequencies obey $\omega_P = \omega_I + \omega_S$. This way, a pump photon will be converted into a signal and idler photon. Setting $\hbar = 1$, the Hamiltonian of the system is given by

$$\hat{H} = \omega_P \hat{a}_P^\dagger \hat{a}_P + \omega_S \hat{a}_S^\dagger \hat{a}_S + \omega_I \hat{a}_I^\dagger \hat{a}_I + i\lambda(\hat{a}_S^\dagger \hat{a}_I^\dagger \hat{a}_P - \hat{a}_S \hat{a}_I \hat{a}_P^\dagger) \tag{1.1.8}$$

where $\hat{a}_n$ is a bosonic operator which annihilates a photon at frequency ω_n for $n = S, I, P$, and λ is the three-wave interaction strength which is taken to be real without loss of generality. We note that any other three-wave mixing terms are energy non-conserving and omitted in the rotating wave approximation.

We can solve the nonlinear equations of motion by first assuming a strong classical pump. That is to say, we are assuming that the pump mode is coherently driven, say by a laser, such that it has a large amplitude. Under this assumption, we can express the pump mode as

$$\hat{a}_P = (\psi_P + \hat{d}_P)e^{-i\omega_P t} \tag{1.1.9}$$

where ψ_P is the large average pump amplitude, taken to be real without loss of generality, and $\hat{d}_P$ describes quantum fluctuations. By assuming a very large pump amplitude and a weak interaction, we can linearize the system by dropping interaction terms which are independent of ψ_P. This will result in a quadratic mean-field Hamiltonian where

we can disregard the dynamics of the pump. When these assumptions no longer hold, the dynamics of the pump become important and can no longer be described by a time-independent average. The conversion of pump photons to signal and idler photons will cause the pump amplitude to decrease which will in turn affect the amplifying properties of our system. This effect is known as pump depletion. However, for the systems of interest in this thesis, these assumptions will always hold and we ignore the effects of pump depletion. Taking everything into account, we are left with the reduced Hamiltonian

$$\hat{H} = \omega_S \hat{a}_S^\dagger \hat{a}_S + \omega_I \hat{a}_I^\dagger \hat{a}_I + i\nu(\hat{a}_S^\dagger \hat{a}_I^\dagger e^{-i\omega_P t} - \hat{a}_S \hat{a}_I e^{i\omega_P t}) \tag{1.1.10}$$

where $\nu = \lambda\psi_P$ is the parametric drive strength. We move into a rotating frame by applying the unitary transformation

$$\hat{U} = e^{i(\omega_S \hat{a}_S^\dagger \hat{a}_S + \omega_I \hat{a}_I^\dagger \hat{a}_I)t} \tag{1.1.11}$$

which in turn modifies the Hamiltonian such that $\hat{H} = \hat{U}\hat{H}_{\text{old}}\hat{U}^\dagger + i\left(\partial\hat{U}/\partial t\right)\hat{U}^\dagger$. Doing so, and keeping in mind that $\omega_P = \omega_I + \omega_S$ we obtain the Hamiltonian

$$\hat{H} = i\nu(\hat{a}_S^\dagger \hat{a}_I^\dagger - \hat{a}_S \hat{a}_I) \tag{1.1.12}$$

which is time-independent and quadratic. Without additional damping or connection to external waveguides, we obtain the Heisenberg equations of motion

$$\dot{\hat{a}}_S = \nu \hat{a}_I^\dagger, \;\; \dot{\hat{a}}_I^\dagger = \nu \hat{a}_S \tag{1.1.13}$$

for the signal and idler modes. We can readily solve the set of equations 1.1.13 and

obtain the solutions

$$\hat{a}_S(t) = \cosh(\nu t)\hat{a}_S(0) + \sinh(\nu t)\hat{a}_I^\dagger(0), \tag{1.1.14}$$

$$\hat{a}_I^\dagger(t) = \sinh(\nu t)\hat{a}_S(0) + \cosh(\nu t)\hat{a}_I^\dagger(0). \tag{1.1.15}$$

We see that the modes grow exponentially in time while preserving commutation relations. Although these solutions exist, looking at the Hamiltonian in Eq. (1.1.12) we see that we cannot diagonalize it via a Bogoliubov transformation. Doing so leads to purely complex energies which are consistent with the exponential growth in Eqs. (1.1.14, 1.1.15). If one could diagonalize the Hamiltonian, one would expect simple oscillatory dynamics. In fact, because we are not considering any form of damping, this system is dynamically unstable. We can create a pair of signal and idler photons at no energy cost. Hence, our pump keeps creating these pairs until the number of photons diverges. This is an adverse effect. We want a system that is dynamically stable. In other words, we want a system that eventually relaxes to a time-independent state (steady-state) with a finite number of photons. Later in the introduction, we consider the effects of damping via standard input-output theory [8, 10] to dynamically stabilize the system. Stabilizing the system will allow the system to evolve to a steady-state which exhibits amplification, as we will show.

1.1.1 Degenerate versus nondegenerate driving

Before studying the properties of the quadratic Hamiltonian in Eq. (1.1.12) with additional damping, we give a brief definition of two different parametric processes. We define processes where a pump photon is converted into a pair of distinct signal and idler photons as nondegenerate or phase-preserving parametric driving. The special case where the signal and idler modes are the same (i.e the labels $S = I$) is referred

to as degenerate or phase-sensitive parametric driving. This case is described by the Hamiltonian (setting $\hbar = 1$)

$$\hat{H} = \omega_P \hat{a}_P^\dagger \hat{a}_P + \omega_S \hat{a}_S^\dagger \hat{a}_S + i\lambda \left((\hat{a}_S^\dagger)^2 \hat{a}_P - (\hat{a}_S)^2 \hat{a}_P^\dagger \right). \tag{1.1.16}$$

In this case, only signals injected with the proper phase are amplified. For the rest of the introduction we focus on the case where the signal and idler modes are distinct.

1.1.2 Amplification

We stabilize the system by connecting the cavity to an external waveguide. This waveguide serves as a port for both signals and noise to enter and leave the cavity. Using input-output theory [8, 10], we treat the waveguide as a Markovian bath: it does not keep memory of the interactions with the cavity. This treatment results in the damping of the cavity modes. This damping will inhibit the exponential growth and lead to a finite amplitude gain. The resulting Heisenberg-Langevin equations of motion are given by

$$\dot{\hat{a}}_S(t) = -\frac{\kappa_S}{2} \hat{a}_S(t) + \nu \hat{a}_I^\dagger(t) - \sqrt{\kappa_S} \left(\bar{\xi}_{S,in}(t) + \hat{\xi}_{S,in}(t) \right), \tag{1.1.17}$$

$$\dot{\hat{a}}_I^\dagger(t) = -\frac{\kappa_I}{2} \hat{a}_I^\dagger(t) + \nu \hat{a}_S(t) - \sqrt{\kappa_I} \left(\bar{\xi}^\star_{I,in}(t) + \hat{\xi}^\dagger_{I,in}(t) \right), \tag{1.1.18}$$

where κ_S and κ_I are the decay rates of the signal and idler modes respectively. The additional terms $\bar{\xi}_{S,in}(t)$ and $\bar{\xi}_{I,in}(t)$ describe coherent classical signals which could be injected into the cavity via the external waveguide. The operators $\hat{\xi}_{S,in}(t)$ and $\hat{\xi}_{I,in}(t)$ describe additional quantum noise entering the cavity via the waveguide. The quantum noise operators are Gaussian and describe vacuum fluctuations: they have zero average

value and their only non-zero two-point correlation functions are

$$\langle \hat{\xi}_{S,in}(t)\hat{\xi}^{\dagger}_{S,in}(t')\rangle = \langle \hat{\xi}_{I,in}(t)\hat{\xi}^{\dagger}_{I,in}(t')\rangle = \delta(t-t'). \tag{1.1.19}$$

As we are interested in a setting where an injected signal is amplified, we have that $\bar{\xi}_{S,in}(t) \neq 0$ and $\bar{\xi}^{\star}_{I,in}(t) = 0$.

To study the amplification properties, we solve the Heisenberg-Langevin equations of motion in frequency space and for simplicity focus on the zero frequency results. Note that we Fourier transform into frequency space using the convention

$$\hat{a}[\omega] = \int_{-\infty}^{\infty} dt\ \hat{a}(t)e^{i\omega t} \tag{1.1.20}$$

$$\hat{a}^{\dagger}[\omega] = \int_{-\infty}^{\infty} dt\ \hat{a}^{\dagger}(t)e^{i\omega t} \tag{1.1.21}$$

for generic operator $\hat{a}^{\dagger}(t)$, such that $\hat{a}^{\dagger}[\omega] = (\hat{a}[-\omega])^{\dagger}$. The zero frequency solutions to the Heisenberg-Langevin equations are

$$\hat{a}_S[0] = \frac{2\nu}{\kappa_S}\hat{a}^{\dagger}_I[0] - \frac{2}{\sqrt{\kappa_S}}\left(\bar{\xi}_{S,in}[0] + \hat{\xi}_{S,in}[0]\right), \tag{1.1.22}$$

$$\hat{a}^{\dagger}_I[0] = \frac{2\nu}{\kappa_I}\hat{a}_S[0] - \frac{2}{\sqrt{\kappa_I}}\hat{\xi}^{\dagger}_{I,in}[0], \tag{1.1.23}$$

which we can conveniently re-express in matrix form as

$$\begin{pmatrix} \hat{a}_S[0] \\ \hat{a}^{\dagger}_I[0] \end{pmatrix} = \frac{2}{\frac{4\nu^2}{\kappa_S\kappa_I} - 1}\begin{pmatrix} 1 & \frac{2\nu}{\kappa_S} \\ \frac{2\nu}{\kappa_I} & 1 \end{pmatrix}\begin{pmatrix} \frac{1}{\sqrt{\kappa_S}}\left(\bar{\xi}_{S,in}[0] + \hat{\xi}_{S,in}[0]\right) \\ \frac{1}{\sqrt{\kappa_I}}\hat{\xi}^{\dagger}_{I,in}[0] \end{pmatrix} \tag{1.1.24}$$

where the matrix on the right-hand side is known as the dynamical matrix. For our system to be stable, we require the eigenvalues of the dynamical matrix be real and finite. Imaginary eigenvalues lead to exponentially growing modes and hence dynamical

instability. From this requirement, we find that for our system to be dynamically stable we must have that $2\nu < \sqrt{\kappa_S \kappa_I}$. With this in mind, we look at the signal mode which leaves the cavity and enters the external waveguide. We describe this mode by the operator $\hat{\xi}_{S,out}$. Via standard input-output theory [8, 10], we can relate this outgoing signal to the reflected incoming signal and radiation coming from the cavity:

$$\hat{\xi}_{S,out}[0] = \bar{\xi}_{S,in}[0] + \hat{\xi}_{S,in}[0] + \sqrt{\kappa_S}\hat{a}_S[0]. \tag{1.1.25}$$

From this relation, we find that the outgoing signal is

$$\hat{\xi}_{S,out}[0] = \frac{Q^2+1}{Q^2-1}\left(\bar{\xi}_{S,in}[0] + \hat{\xi}_{S,in}[0]\right) + \frac{2Q}{Q^2-1}\hat{\xi}^{\dagger}_{I,in}[0] \tag{1.1.26}$$

where we have defined

$$Q \equiv \frac{2\nu}{\sqrt{\kappa_S \kappa_I}}. \tag{1.1.27}$$

Similarly, for the outgoing idler, we find

$$\hat{\xi}^{\dagger}_{I,out}[0] = \frac{Q^2+1}{Q^2-1}\hat{\xi}^{\dagger}_{I,in}[0] + \frac{2Q}{Q^2-1}\hat{\xi}_{S,in}[0] \tag{1.1.28}$$

From our stability condition, we require that $Q^2 < 1$. If this condition is not met, pairs of signal and idler photons will be created at a rate faster than they can decay out of the cavity: there is again no steady-state in this case. When the condition is met, the interplay between cavity loss and parametric driving relax to a steady-state where the number of photons leaving the cavity is finite and larger than the number of photons

injected. We define a photon-number gain G_0

$$-\sqrt{G_0} = \frac{Q^2+1}{Q^2-1} \tag{1.1.29}$$

such that

$$\hat{\xi}_{S,out}[0] = -\sqrt{G_0}\left(\bar{\xi}_{S,in}[0] + \hat{\xi}_{S,in}[0]\right) - \sqrt{G_0-1}\hat{\xi}^{\dagger}_{I,in}[0]. \tag{1.1.30}$$

An incoming coherent classical signal $\bar{\xi}_{S,in}[0]$ comes out with a multiplicative factor $\sqrt{G_0} > 1$ and is hence amplified. With the assumption that the input noise is vacuum, this input-ouput relation describes an ideal quantum-limited amplifier [11, 12]. That is to say, the noise added by the amplifier reaches the limit allowed by quantum mechanics. We characterize the added noise by looking at the noise spectral density of the output mode. Written in terms of the noise spectral density of the input signal, and taking the idler to be vacuum we find

$$(\Delta\hat{\xi}_{S,out}[0])^2 = G_0(\Delta\hat{\xi}_{S,in}[0])^2 + \frac{|G_0-1|}{2}. \tag{1.1.31}$$

where we have that $(\Delta\hat{b})^2 = \frac{1}{2}\langle\{\hat{b},\hat{b}^{\dagger}\}\rangle - |\langle\hat{b}\rangle|^2$ for generic operator $\hat{b}$. The first term in Eq. (1.1.31) describes the amplified noise of the input and the second term describes the noise added by the amplifier due to the presence of the idler mode. Note that we have omitted the frequency space delta function coming from the idler mode vacuum correlations in the second term. The added noise by the amplifier becomes important when considering the large photon number gain limit ($G_0 \gg 1$). We divide by the photon

number gain to express the output noise as an equivalent noise at the input

$$(\Delta\bar{\xi}_{S,out}[0])^2/G_0 = (\Delta\bar{\xi}_{S,in}[0])^2 + \frac{|G_0 - 1|}{2G_0}. \tag{1.1.32}$$

From the second term, we see that a quantum limited nondegenerate parametric amplifier in the large gain limit ($G_0 \gg 1$) adds a half quanta of noise to the input signal. For a degenerate quantum limited amplifier on the other hand, where there is no idler mode, the added noise can be arbitrarily small. However, only a specific quadrature gets amplified in a degenerate amplifier. That is to say, only signals with the proper phase get amplified.

1.1.3 Squeezing

Parametric driving can also be used to generate squeezing of vacuum fluctuations. When a state is squeezed, the variance of an operator or combination of operators will be lower than that of a coherent vacuum state. To characterize the squeezing, we begin by introducing hermitian operators via $\hat{\xi}_{S/I,out}(t) = \left(\hat{X}_{S/I,out}(t) + i\hat{P}_{S/I,out}(t)\right)/\sqrt{2}$. We then define symmetric collective quadratures

$$\hat{X}_{\pm,out}(t) = \frac{\hat{X}_{S,out}(t) \pm \hat{X}_{I,out}(t)}{\sqrt{2}} \tag{1.1.33}$$

with a similar definition for $\hat{P}_{\pm,out}(t)$. We then study the output squeezing of our cavity by looking at the noise spectral density (defined here for a generic hermitian quadrature $\hat{X}(t)$)[13]

$$S_{\hat{X}}[\omega] = \int_{-\infty}^{\infty} \frac{dt}{2} e^{i\omega t} \left\langle \left\{ \hat{X}(t), \hat{X}(0) \right\} \right\rangle \tag{1.1.34}$$

As we have taken ν to be real and positive (without loss of generality), the squeezed quadrature is the $\hat{X}_{-,out}$ quadrature. To show that we obtain squeezing below zero-point, the value of the noise spectral density for purely vacuum operators (i.e. $S_{\hat{X}}[\omega] = 1/2$), we again focus for simplicity on the $\omega = 0$ case. At this frequency, the solutions to the output signal and idler modes are given by Eq. (1.1.26) and Eq. (1.1.28) respectively.

For the single cavity case, and the fact that we have chosen ν to be real and positive, we find that the squeezed quadrature is the $\hat{X}_{-,out}$ quadrature. Assuming that every input field is vacuum noise (setting both $\bar{\xi}_{S,in}[0] = \bar{\xi}_{I,in}[0] = 0$), we can easily obtain the numerous correlators in Eq. 1.1.34. We find that the zero frequency noise spectral density is given by

$$S_{\hat{X}_{-,out}}[0] = \frac{1}{2}\left[1 + 2(G_0 - 1) - 2\sqrt{G_0}\sqrt{G_0 - 1}\right] \tag{1.1.35}$$

which at first glance might not seem to be squeezed below vacuum ($S_{\hat{X}_{-,out}}[0]$=1/2). As $G_0 \geq 1$ we define $G_0 = \cosh^2 r$ where $r \geq 0$ is the squeezing parameter. The squeezing parameter is an increasing function with respect to the parametric drive strength and goes to zero when the parametric interaction strength goes to 0. Written out in this form, we find that the noise spectral density is

$$S_{\hat{X}_{-,out}}[0] = \frac{e^{-2r}}{2} \tag{1.1.36}$$

which is always below zero point squeezing for non-zero squeezing parameter.

1.1.4 Entanglement

Parametric driving also generates entanglement between the outgoing signal and idler modes. By entanglement we mean that we cannot describe the outgoing signal mode

independently of the idler mode [14]. To see this, we go back to the solutions of the mean-field quadratic Hamiltonian without additional damping (see Eq. (1.1.14) and Eq. (1.1.15)). Assuming that the input state is vacuum, we can find the output state of the system denoted by $|\Omega(t)\rangle$. This state is known as the "two-mode squeezed vacuum state" and in the Fock space representation is given by [15, 16]

$$|\Omega(t)\rangle = \frac{1}{\cosh(\nu t)} \sum_{n=0}^{\infty} \tanh^n(\nu t) \, |n, n\rangle \tag{1.1.37}$$

where $|n, n\rangle$ is the Fock state with n signal and n idler photons. Already from this form, we see that the state is highly entangled. To further show that it is entangled, we consider the density matrix of the output state. As this state is obtained from unitarily evolving the vacuum input state it is a pure state with no entropy. The density matrix is given by

$$\rho(t) = |\Omega(t)\rangle \langle\Omega(t)| = \frac{1}{\cosh^2(\nu t)} \sum_{n,m=0}^{\infty} \tanh^n(\nu t) \tanh^m(\nu t) \, |m, m\rangle \langle n, n| \, . \tag{1.1.38}$$

We now consider the density matrix of a subsystem by tracing out the idler mode. The result is the reduced density matrix for the signal mode

$$\rho_S(t) = \mathrm{Tr}_{\mathrm{Idler}}(\rho(t)) = \frac{1}{\cosh^2(\nu t)} \sum_{n_S=0}^{\infty} \tanh^{2n_S}(\nu t) \, |n_S\rangle \langle n_S| \, . \tag{1.1.39}$$

Similarly, we get the same result for the reduced density of the idler mode with the substitution $S \to I$ when tracing out the signal mode. Using second quantization notation, we can re-express the reduced density matrix as

$$\rho_S(t) = \frac{1}{Z(t)} \sum_{n=0}^{\infty} \frac{\left[\tanh^2(\nu t)\right]^n}{n!} (\hat{a}_S^\dagger(0))^n \, (\hat{a}_S(0))^n = \frac{1}{Z(t)} e^{-\beta E(t) \hat{a}_S^\dagger(0) \hat{a}_S(0)} \tag{1.1.40}$$

where we have substituted $Z(t) = \cosh^2(\nu t)$ and $e^{-\beta E(t)} = \tanh^2(\nu t)$. As we can see, the reduced density matrix is a thermal equilibrium distribution, which has non-zero entropy. This is a signature of entanglement. If two subsystems are in a pure entangled state, then we cannot assign a pure wavefunction to either of the subsystems alone [14]. This tells us, in other words, that the reduced density matrix cannot describe a pure state and so it cannot be factored into the outer product of a single wavefunction. A thermal equilibrium distribution describes a mixed state as it cannot be factored in such a way, hence, the output state is entangled.

When we consider additional damping, the output state is no longer pure. However, we still maintain entanglement. In this case, there are different ways of characterizing the entanglement of the output state such as using the logarithmic negativity. More information on this measure of entanglement and how to calculate it is given in chapter 6 of the thesis.

We have shown, using a simple cavity model, that parametric driving leads to amplification, squeezing, and entanglement. In this thesis, we explore more complicated systems of arrays of coupled cavities subjected to parametric driving. Assuming periodicity of the arrays, we can describe these systems using band theory and Bloch wavefunctions [17]. For more complicated systems, one might expect certain phase transitions to occur as a function of the system's parameters. We can make use of the wavefunctions to characterize the different bands of the system at hand and verify if the system undergoes a topological phase transition.

1.2 Topological Insulator

As Chapters 2, 4, and 5 deal with parametric interactions and topology, we give a brief and heuristic introduction to Chern insulators in the context of condensed matter systems.

For simplicity, we focus on particle number-conserving Hamiltonians (i.e. without parametric driving) which break time-reversal symmetry. Anomalous Quantum Hall insulators [18] are well known examples of such systems. In these systems, time-reversal symmetry is broken with the use of a staggered magnetic fields, implying that the total integrated flux across the system is zero. The extension of the same principles to the case of particle number non-conserving Hamiltonians is discussed in chapter 2 of this thesis.

Generally speaking, when discussing topology, we are interested in the geometric properties of closed surfaces. Physical two-dimensional surfaces, such as spheres or tori for example, can be topologically classified by their genus g. The genus of a surface is an integer quantity robust to smooth deformations of the surface. Physically, the genus represents the number of holes in the surface. For example, a sphere has a genus $g = 0$ whereas a torus has $g = 1$. To change the genus of a surface, one must drastically alter the surface by either "punching" a hole in the surface or "stitching" one closed. These alterations are not smooth. It is also important to note that the genus is obtained by integrating the Gaussian curvature of the surface over the entire surface. The Gauss-Bonet theorem tells us that this integral is proportional to the genus of the surface and is quantized.

Similarly, we can use topology to describe different energy bands in two-dimensional, periodic, band insulators [19]. In this case, the closed surface is the Brillouin zone and the curvature is the Berry curvature given by [20]

$$\mathcal{F}_m = \nabla_{\mathbf{k}} \times \left(i \left\langle u_m(\mathbf{k}) \right| \nabla_{\mathbf{k}} \left| u_m(\mathbf{k}) \right\rangle \right) \tag{1.2.1}$$

where $|u_m(\mathbf{k})\rangle$ is the momentum space wavefunction of the m^{th} band and $\mathbf{k} = (k_x, k_y)$. We construct a topological invariant, called the Chern number, by integrating the Berry

curvature over the Brillouin zone. The Chern number, for a band m, is given by [21]

$$n_m = \frac{1}{2\pi} \int d\mathbf{k}\, \mathcal{F}_m \tag{1.2.2}$$

and for similar arguments as in the case of the genus, this quantity is quantized. Physically, the Chern number tells us how many times the phase of the wavefunction "winds" when it is adiabatically transported around a closed loop in the Brillouin zone. It tells us if the wavefunction at the end of the loop is related to the initial wavefunction but with an additional phase factor $e^{2\pi i \cdot n_m}$, where n_m is the Chern number. As the Chern number is an integer, it is also robust to smooth deformations of the Hamiltonian (which in turn modify the wavefunctions). In fact, the only drastic deformation one can do to change the Chern number is by closing a gap in the Hamiltonian [19].

An interesting and important consequence of topology in band insulators is the existence of uni-directionally propagating modes at the interface where the topological invariant changes. These modes are often referred to as edge-modes as they live on the edges of finite samples. If we consider the interface between a band insulator with non-zero Chern number and vacuum (which has a Chern number of zero), we know that something drastic has to occur at the interface to change the Chern number: there must be a closure of the gap. This tells us that there will be low-energy modes bound to the interface where the energy gap passes through zero. This is what is known as the Bulk-Edge correspondence [19, 22].

These edge-modes are robust to disorder in the band insulator. Such disorder could be random on-site potentials, irregularities in the lattice, and removal of lattice sites to name a few. Because the modes propagate uni-directionally, there are no other edge-modes to backscatter to due to disorder. Furthermore, the energy of these edge-modes is drastically different than those of the bulk states (i.e. band energies), hence a process where an

edge-mode scatters to a bulk mode is highly suppressed due to energy conservation.

1.3 Thesis outline

The remainder of this thesis is organized as follows. Chapter 2 begins by exploring how to use parametric driving as a resource to induce topology by modifying the band structure of an array of coupled cavities which form a regular lattice. Once we show that such interactions can prompt a topological phase transition, we study the transport properties in a finite system. Chapter 3 moves away from the band structure of a parametrically driven system and instead focuses on how the energy eigenstates of parametrically driven arrays of coupled cavities are occupied, in the realistic case where we are weakly coupled to a zero-temperature environment. Chapter 4 combines the notion of topology and the amplification properties of parametric driving to construct a topologically protected travelling wave amplifier. Chapter 5 builds on the results of Chapter 4, but we consider more efficient ways of obtaining similar results, such that it is experimentally more feasible. Finally, Chapter 6 focuses on a more generic travelling wave amplifier. We consider two different ways to model how the modes, which are coherently created by parametric driving, experience loss. By allowing for the two modes to decay at different rates, we study the amplification and squeezing properties of the travelling wave amplifier.

This thesis is written as a manuscript-based thesis. Chapters 2 through 6 can be read independently and they each include their own introduction, conclusion, and appendices. To make this thesis a cohesive work, there is a preface at the beginning of each chapter which also states the contribution to knowledge.

References

[1]M. Notomi, E. Kuramochi, and T. Tanabe, Nature Photon. **2**, 741–747 (2008).

[2]S. Mookherjea, and A. Yariv, Ieee J Quantum Elect **8**, 448 (2002).

[3]B. J. Eggleton, B. Luther-Davies, and K. Richardson, Nat Photonics **5**, 141 (2011).

[4]J. Dahdah, M. Pilar-Bernal, N. Courjal, G. Ulliac, and F. Baida, J. Appl. Phys. **110**, 074318 (2011).

[5]D. L. Underwood, W. E. Shanks, J. Koch, and A. A. Houck, Phys. Rev. A **86**, 023837 (2012).

[6]A. H. Safavi-Naeini, S. Gröblacher, J. T. Hill, J. Chan, M. Aspelmeyer, and O. Painter, Nature **500**, 185–189 (2013).

[7]T. P. Purdy, P. L. Yu, R. W. Peterson, N. S. Kampel, and C. A. Regal, Phys. Rev. X **3**, 031012 (2013).

[8]A. A. Clerk, M. H. Devoret, S. M. Girvin, F. Marquardt, and R. J. Schoelkopf, Reviews of Modern Physics **82**, 1155–1208 (2010).

[9]B. Yurke, L. R. Corruccini, P. G. Kaminsky, L. W. Rupp, A. D. Smith, A. H. Silver, R. W. Simon, and E. A. Whittaker, Phys. Rev. A **39**, 2519–2533 (1989).

[10]D. F. Walls, and G. J. Milburn, (Springer,Berlin, 1994).

[11]H. A. Haus, and J. A. Mullen, Phys. Rev. **128**, 2407–2413 (1962).

[12]C. M. Caves, Phys. Rev. D **26**, 1817–1839 (1982).

[13]C. C. Gerry, and P. L. Knight, in *Introductory quantum optics* (Cambridge University Press, 2005).

[14]I. Chuang, and M. Nielsen, in *Quantum computation and quantum information* (Cambridge University Press, 2000).

[15]C. M. Caves, and B. L. Schumaker, Phys. Rev. A **31**, 3068–3092 (1985).

[16]C. C. Gerry, Phys. Rev. A **31**, 2721–2723 (1985).

[17]F. Bloch, Zeitschrift für Physik **52**, 555–600 (1929).

[18]C.-X. Liu, S.-C. Zhang, and X.-L. Qi, Annual Review of Condensed Matter Physics **7**, 301–321 (2016).

[19]M. Z. Hasan, and C. L. Kane, Rev. Mod. Phys. **82**, 3045–3067 (2010).

[20]Proceedings of the Royal Society of London A: Mathematical, Physical and Engineering Sciences **392**, 45–57 (1984).

[21]D. J. Thouless, M. Kohmoto, M. P. Nightingale, and M. den Nijs, Phys. Rev. Lett. **49**, 405–408 (1982).

[22]B. A. Bernevig, and T. L. Hughes, in *Topological insulators and topological superconductors* (Princeton University Press, 2013).

Preface to Chapter 2

In this first article, we study topological phases that are induced by parametric driving. We consider a model of photons hopping on an array of coupled cavities forming a Kagome lattice which allows for on-site and nearest neighbour parametric driving. We take the photon hopping to be purely real which conserves time-reversal symmetry and does not induce topologic phases. We break time-reversal symmetry and induce a topological phase by varying the phases of the pump modes used for parametric driving. To characterize the different possible phases, we calculate the band Chern numbers as a function of the driving strengths. We find a very rich phase diagram which allows for multiple different phases. Furthermore, these topological states are distinct from their fermionic analogues (topological superconductors). As we cannot map these topological states by a local transformation onto topological states found in models without parametric driving, these states represent a new type of topological system. We also study the transport properties of the protected edge states in a finite system using input-output theory. We find that parametric driving leads to both chiral elastic and inelastic photon transport. Inelastic photon transport is not exhibited in

particle-conserving topological systems (i.e. without parametric driving). The results presented in this chapter show that parametric driving can lead to novel topological states with interesting transport properties.

2

Topological phase transitions and chiral inelastic transport induced by the squeezing of light

Vittorio Peano[1], Martin Houde[2], Christian Brendel[1], Florian Marquardt[1,3], and Aashish A. Clerk[2]

[1]Institute for Theoretical Physics, University of Erlangen-Nürnberg, Staudtstraße 7, 91058 Erlangen, Germany

[2]Department of Physics and the Centre for Physics of Materials, McGill University, Montreal, Quebec, Canada H3A 2T8

[3]Max Planck Institute for the Science of Light, Günther-Scharowsky-Straße 1/Bau 24, 91058 Erlangen, Germany

This chapter has been published in Nature Communications.
Journal Reference: Nat. Commun. 7, 10779 (2016)

Abstract

There is enormous interest in engineering topological photonic systems. Despite intense activity, most works on topological photonic states (and more generally bosonic states) amount in the end to replicating a well-known fermionic single-particle Hamiltonian. Here, we show how the squeezing of light can lead to the formation of qualitatively new kinds of topological states. Such states are characterized by non-trivial Chern numbers, and exhibit protected edge modes which give rise to chiral elastic and inelastic photon transport. These topological bosonic states are not equivalent to their fermionic (topological superconductor) counterparts and, in addition, cannot be mapped by a local transformation onto topological states found in particle-conserving models. They thus represent a new type of topological system. We study this physics in detail in the case of a kagome lattice model, and discuss possible realizations using nonlinear photonic crystals or superconducting circuits.

Waves are not only ubiquitous in physics, but the behaviour of linear waves is also known to be very generic, with many features that are independent of the specific physical realization. This has traditionally allowed us to transfer insights gained in one system (e.g. sound waves) to other systems (e.g. matter waves). That strategy has even been successful for more advanced concepts in the field of wave transport. One important recent example of this kind is the physics of topological wave transport, where waves can propagate along the boundaries of a sample, in a one-way chiral manner that is robust against disorder scattering. While first discovered for electron waves, this phenomenon has by now also been explored for a variety of other waves in a diverse set of systems, including cold atoms [1], photonic systems [2] and more recently phononic systems [3–9].

In the case of topological wave transport, the connection between waves in different physical implementations can actually be so close that the calculations turn out to be the same. In particular, if we are dealing with matter waves moving in a periodic potential, the results do not depend on whether they are bosons or fermions, as long as interactions do not matter. The single-particle wave equation to be solved happens to be exactly the same. This has allowed to envision and realize photonic analogues of quantum-Hall effect [10–18], the spin Hall effect [19–22], Floquet topological insulators [23, 24] and even Majorana-like modes [25]. More generally, the well-known classification of electronic band structures based on the dimensionality and certain generalized symmetries [26] directly applies to photonic systems provided that the particle number is conserved. As we now discuss, this simple correspondence will fail in the presence of squeezing.

Consider the most general quadratic Hamiltonian describing photons in a periodic

potential in the presence of parametric driving:

$$\hat{H} = \sum_{\mathbf{k},n} \varepsilon_n[\mathbf{k}]\hat{b}^\dagger_{\mathbf{k},n}\hat{b}_{\mathbf{k},n} + \sum_{\mathbf{k},n,n'} \left(\lambda_{nn'}[\mathbf{k}]\hat{b}^\dagger_{\mathbf{k},n}\hat{b}^\dagger_{-\mathbf{k},n'} + \text{h.c.}\right) \tag{2.0.1}$$

The first term describes a non-interacting photonic band-structure, where $\hat{b}_{\mathbf{k},n}$ annihilates a photon with quasimomentum $\mathbf{k}$ in the n-th band. The remaining two-mode squeezing terms are induced by parametric driving and do not conserve the excitation number. As we discuss below, they can be controllably realized in a number of different photonic settings. While superficially similar to pairing terms in a superconductor, these two-mode squeezing terms have a profoundly different effect in a bosonic system, as there is no limit to the occupancy of a particular single-particle state. They can give rise to highly entangled ground states, and even to instabilities.

Given these differences, it is natural to ask how anomalous pairing terms can directly lead to topological phases of light. In this work, we study the topological properties of 2D photonic systems described by equation (2.0.1), in the case where the underlying particle-conserving band structure has no topological structure, and where the parametric driving terms do not make the system unstable. We show that the introduction of particle non-conserving terms can break time-reversal symmetry (TRS) in a manner that is distinct from having introduced a synthetic gauge field, and can lead to the formation of bands having a non-trivial pattern of (suitably defined) quantized Chern numbers. This in turn leads to the formation of protected chiral edge modes: unlike the particle conserving case, these modes can mediate a protected inelastic (but still coherent) scattering mechanism along the edge (i.e. a probe field injected into the edge of the sample will travel along the edge, but emerge at a different frequency). In general, the topological phases we find here are distinct both from those obtained in the particle-conserving case, and from those found in topological superconductors. We also discuss possible realizations of this

model using a nonlinear photonic crystal or superconducting microwave circuits. Finally, we discuss the formal analogies and crucial differences between the topological phases of light investigated here and those recently proposed for other kinds of Bogoliubov quasiparicles [27–31] (see Discussion section).

2.1 Results

2.1.1 Kagome lattice model

For concreteness, we start with a system of bosons on a kagome lattice (see Fig.2.1),

$$\hat{H}_0 = \sum_{\mathbf{j}} \omega_0 \hat{a}^\dagger_{\mathbf{j}} \hat{a}_{\mathbf{j}} - J \sum_{\langle \mathbf{j},\mathbf{j}' \rangle} \hat{a}^\dagger_{\mathbf{j}} \hat{a}_{\mathbf{j}'} \tag{2.1.1}$$

(we set $\hbar = 1$). Here, we denote by $\hat{a}_{\mathbf{j}}$ the photon annihilation operator associated with lattice site $\mathbf{j}$, where the vector site index has the form $\mathbf{j} = (j_1, j_2, s)$. $j_1, j_2 \in Z$ labels a particular unit cell of the lattice, while the index $s = A, B, C$ labels the element of the sublattice. $\langle \mathbf{j}, \mathbf{j}' \rangle$ indicates the sum over nearest neighbors, and J is the (real valued) nearest neighbor hopping rate; ω_0 plays the role of an on-site energy. As there are no phases associated with the hopping terms, this Hamiltonian is time-reversal symmetric and topologically trivial. We chose the kagome lattice because it is directly realizable both in quantum optomechanics [5] and in arrays of superconducting cavity arrays [13, 16]; it is also the simplest model where purely local parametric driving can result in a topological phase.

We next introduce quadratic squeezing terms to this Hamiltonian that preserve the translational symmetry of the lattice and that are no more non-local than our original,

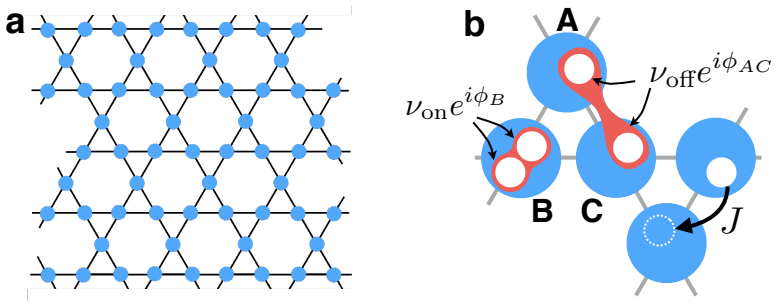

Figure 2.1: Setup figure: (a) An array of nonlinear cavities forming a kagome lattice. (b) Photons hop between nearest-neighbor sites with rate J. Each cavity is driven parametrically leading to the creation of photon pairs on the same lattice site (rate $\nu_{\rm on}$) and on nearest-neighbor sites (rate $\nu_{\rm off}$). A spatial pattern of the driving phase is imprinted on the parametric interactions, breaking the time-reversal symmetry (but preserving the $\mathcal{C}3$ rotational symmetry).

nearest-neighbor hopping Hamiltonian:

$$\hat{H}_{\rm L} = -\frac{1}{2}\left[\nu_{\rm on}\sum_{\mathbf{j}} e^{i\phi_s}\hat{a}^\dagger_{\mathbf{j}}\hat{a}^\dagger_{\mathbf{j}} + \nu_{\rm off}\sum_{\langle \mathbf{j},\mathbf{j}'\rangle} e^{i\phi_{ss'}}\hat{a}^\dagger_{\mathbf{j}}\hat{a}^\dagger_{\mathbf{j}'}\right] + \text{h.c.} \tag{2.1.2}$$

Such terms generically arise from having a nonlinear interaction with a driven auxiliary pump mode (which can be treated classically) on each site, see e.g. [32]. As we discuss below, the variation in phases in $\hat{H}_L$ from site to site could be achieved by a corresponding variation of the driving phase of the pump. Note that we are working in a rotating frame where this interaction is time-independent, and thus ω_0 should be interpreted as the detuning between the parametric driving and the true on-site (cavity) frequency $\omega_{\rm cav}$ (i.e. $\omega_0 = \omega_{\rm cav} - \omega_{\rm L}/2$, where the parametric driving is at a frequency $\omega_{\rm L}$). The parametric driving can cause the system to become unstable; we will thus require that the on-site energy (i.e. parametric drive detuning) ω_0 to be sufficiently large that each parametric driving term non-resonant enough to ensure stability. If one keeps ω_0 fixed, this means that the parametric driving amplitudes $\nu_{\rm on}$, $\nu_{\rm off}$ will be limited to some fraction of ω_0 (the particular value of which depends on J, see Supplementary Note 1).

For a generic choice of phases in the parametric driving Hamiltonian of equation (2.1.2), it is no longer possible to find a gauge where $\hat{H} = \hat{H}_0 + \hat{H}_{\rm L}$ is purely real when expressed in terms of real-space annihilation operators: hence, even though the hopping Hamiltonian $\hat{H}_0$ corresponds to strictly zero flux, the parametric driving can itself break TRS. In what follows, we will focus for simplicity on situations where time-reversal and particle-conservation are the only symmetries broken by the parametric driving: they will maintain the inversion and $\mathcal{C}3$ rotational symmetry of the kagome lattice. We will also make a global gauge transformation so that $\nu_{\rm off}$ is purely real, while $\nu_{\rm on} = |\nu_{\rm on}|e^{i\varphi_\nu}$. In this case, the only possible choices for the ϕ phases have the form $(\phi_A, \phi_B, \phi_C) = (\phi_{AB}, \phi_{BC}, \phi_{CA}) = \pm(0, \delta, 2\delta)$ with $\delta = 2\pi m_\nu/3$, m_ν is an integer and is the vorticity of the parametric driving phases. We stress that these phases (and hence the sign of the TRS breaking) are determined by the phases of the pump modes used to generate the parametric interaction.

2.1.2 Gap opening and non-trivial topology

$\hat{H}_0$ is the standard tight-binding kagome Hamiltonian for zero magnetic field, and does not have band gaps: the upper and middle bands touch at the symmetry point $\Gamma \equiv (0, 0)$, whereas the middle and lower bands touch at the symmetry points $K = (2\pi/3, 0)$ and $K' = (\pi/3, \pi/\sqrt{3})$ where they form Dirac cones [see Fig. 2.2(a)].

Turning on the pairing terms, the Hamiltonian $\hat{H} = \hat{H}_0 + \hat{H}_{\rm L}$ can be diagonalized in the standard manner as $\hat{H} = \sum_{n,\mathbf{k}} E_n[\mathbf{k}]\hat{\beta}^\dagger_{n,\mathbf{k}}\hat{\beta}_{n,\mathbf{k}}$, where the $\hat{\beta}_{n,\mathbf{k}}$ are canonical bosonic annihilation operators determined by a Bogoliubov transformation of the form (see Method section):

$$\hat{\beta}^\dagger_{n,\mathbf{k}} = \sum_{s=A,B,C} u_{n,\mathbf{k}}[s]\hat{a}^\dagger_{\mathbf{k},s} - v_{n,\mathbf{k}}[s]\hat{a}_{-\mathbf{k},s}. \tag{2.1.3}$$

Here, $\hat{a}_{\mathbf{k},s}$ are the annihilation operators in quasi-momentum space, and $n = 1, 2, 3$ is a

band index; we count the bands by increasing energy. The photonic single-particle spectral function now shows resonances at both positive and negative frequencies, $\pm E_n[k]$, corresponding to particle- and hole-type bands, see Fig. 2.2(d). Because of the TRS breaking induced by the squeezing terms, the band structure described by $E_n[\mathbf{k}]$ now exhibits gaps, see Fig. 2.2(b); further, for a finite sized system, one also finds edge modes in the gap, see Fig. 2.2(d).

The above behaviour suggests that the parametric terms have induced a non-trivial topological structure in the wavefunctions of the band eigenstates. To quantify this, we first need to properly identify the Berry phase associated with a bosonic band eigenstate in the presence of particle non-conserving terms. For each $\mathbf{k}$, the Bloch Hamiltonian $\hat{H}_{\mathbf{k}}$ corresponds to the Hamiltonian of a multi-mode parametric amplifier. Unlike the particle-conserving case, the ground state of such a Hamiltonian is a multi-mode squeezed state with non-zero photon number; it can thus have a non-trivial Berry's phase associated with it when $\mathbf{k}$ is varied, see Supplementary Note 2. The Berry phase of interest for us will be the difference of this ground state Berry phase and that associated with a single quasiparticle excitation. One finds that the resulting Berry connection takes the form

$$\mathcal{A}_n = i\langle \mathbf{k}, n|\hat{\sigma}_z \boldsymbol{\nabla}_{\boldsymbol{k}}|\mathbf{k}, n\rangle, \tag{2.1.4}$$

Here, the 6-vector of Bogoliubov coefficients

$$|\mathbf{k}, n\rangle \equiv (u_{n,\mathbf{k}}[A], u_{n,\mathbf{k}}[B], u_{n,\mathbf{k}}[C], v_{n,\mathbf{k}}[A], v_{n,\mathbf{k}}[B], v_{n,\mathbf{k}}[C]) \tag{2.1.5}$$

plays the role of a singe-particle wavefunction, and $\hat{\sigma}_z$ acts in the particle-hole-space, associating $+1$ to the u-components and -1 to the v-components, see Method section.

These effective wavefunctions obey the symplectic normalization condition

$$\langle \mathbf{k}, n|\hat{\sigma}_z|\mathbf{k}, n'\rangle = \sum_s u^*_{n,\mathbf{k}}[s]u_{n',\mathbf{k}}[s] - v^*_{n,\mathbf{k}}[s]v_{n',\mathbf{k}}[s] = \delta_{n,n'} \tag{2.1.6}$$

Having identified the appropriate Berry connection for a band eigenstate, the Chern number for a band n is then defined in the usual manner:

$$C_n = \frac{1}{2\pi}\int_{BZ} (\boldsymbol{\nabla} \times \mathcal{A}_n) \cdot \hat{z} \tag{2.1.7}$$

This definition agrees with that presented in Ref. [27] and (in 1D) Ref. [29]; standard arguments [27] show that the C_n are integers with the usual properties. We note that, as for superconductors, breaking the $U(1)$ (particle-conservation) symmetry remains compatible with a first-quantized picture after doubling the number of bands. The additional hole bands are connected to the standard particle bands by a particle-hole symmetry; see Method section. In bosonic systems, the requirement of stability implies that particle and hole bands can not touch. Thus, the sum of the Chern numbers over the particle bands (with $E > 0$) must be zero, and there cannot be any edge states with energies below the lowest particle bulk band (or in particular, at zero energy); see Supplemetary Note 1.

In the special case where we only have onsite parametric driving (i.e. $\nu_{\text{off}} = 0, \nu_{\text{on}} \neq 0$), the Chern numbers can be calculated analytically (see Supplemetary Note 3). They are uniquely fixed by the pump vorticity. If $m_\nu = 0$, we have TRS and the band structure is gapless, while for $m_\nu = \pm 1$, $\mathbf{C} = (\mp 1, 0, \pm 1)$. This set of topological phases also occurs in a particle-number conserving model on the kagome lattice with a staggered magnetic field, i.e. the Oghushi-Murakami-Nagaosa (OMN) model of the anomalous quantum Hall effect [33, 34].

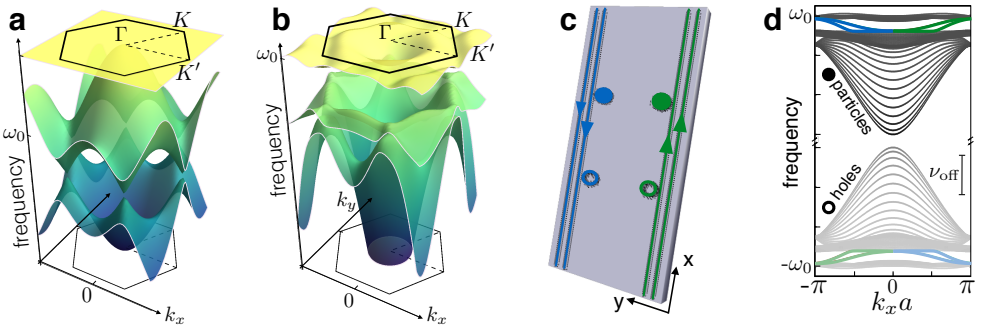

Figure 2.2: Topological Band structure: (a-b) 3D plots of the bulk band structure. The hexagonal Brillouin zone is also shown. (a) In the absence of parametric driving, neighboring bands touch at the rotational symmetry points K and K' and Γ. (b) The parametric driving opens a gap between subsequent bands. For the parameters of choice, there is a global band gap between the second and third band. (d) Hole and particle bands, $\pm E_m[k_x]$, in a strip geometry [sketched in (c)]. The line intensity is proportional to the weight of the corresponding resonance in the photon spectral function, see Supplementary Note 1. The edge states localized on the right (left) edge, plotted in green (blue), have positive (negative) velocity. Parameters: Hopping rate $J = 0.02\omega_0$ (ω_0 is the onsite frequency); in (b) and (d), the parametric couplings are $\nu_{\rm on} = -0.085\omega_0$ and $\nu_{\rm off} = 0.22\omega_0$.

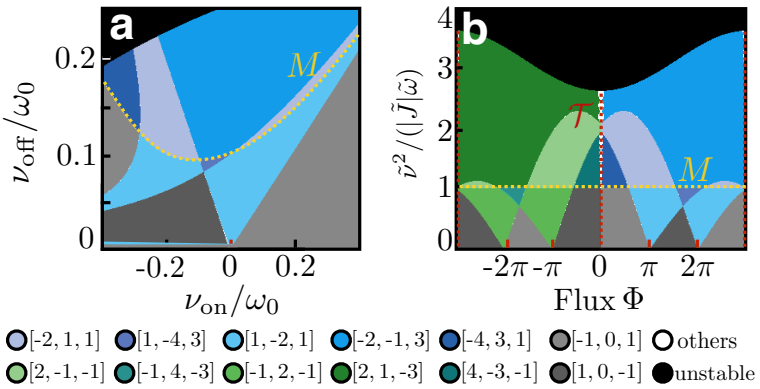

Figure 2.3: Symplectic Topological phase diagrams. (a)Topological phase diagram for the parametrically driven kagome lattice model. The y (x) axis corresponds to the strength of the onsite parametric drive $\nu_{\rm on}$ (off-site parametric drive $\nu_{\rm off}$), and different colours correspond to different triplets $\mathbf{C} = (C_1, C_2, C_3)$ of Chern numbers for the three bands of the model. Note that only the gray and dark-gray phases are found in the particle-conserving version of our model with a staggered field. We have fixed the hopping rate $J/\omega_0 = 0.02$, and the vorticity of the pump $m_\nu = 1$. (b) Same phase diagram, but now plotted in terms of the effective flux $\tilde{\Phi}$ and effective parametric drive $\tilde{\nu}$ experienced by α quasiparticles.

In the general case, including offsite parametric driving, entirely new phases appear. We have computed the Chern numbers for that case numerically, using the approach of Ref. [35]. In Fig. 2.3(a), we show the topological phase diagram of our system, where J/ω_0 and m_ν are held fixed, while the parametric drive strengths $\nu_{\rm on}, \nu_{\rm off}$ are varied. Different colors correspond to different triplets $\mathbf{C} \equiv (C_1, C_2, C_3)$ of the band Chern numbers, with gray and dark-gray corresponding to the two phases already present in the OMN model. Strikingly, a finite off-diagonal coupling $\nu_{\rm off}$ generates a large variety of phases which are not present in the OMN model. The border between different topological phases represent topological phase transitions, and correspond to parameter values where a pair of bands touch at a particular symmetry point; we discuss this further below. Via a standard bulk-boundary correspondence (see Supplementary Note 4), the band Chern numbers for a particular phase determine the number of protected edge states that will be present in a system with a boundary; as usual, the number of edge states in a particular bandgap is obtained by summing the Chern numbers of lower-lying bands. We discuss these edge states in greater detail in a following subsection. Finally, the black regions in the phase diagram indicate regimes of instability which occur when the parametric driving strength becomes too strong.

2.1.3 Dressed-state picture

To gain further insight into the structure of the topological phases found above, it is useful to work in a dressed-state basis that eliminates the local parametric driving terms from our Hamiltonian. We thus first diagonalize the purely local terms in the Hamiltonian; for each lattice site $\mathbf{j}$ we have

$$\hat{H}_{\mathbf{j}} \;=\; \omega_0 \hat{a}_{\mathbf{j}}^\dagger \hat{a}_{\mathbf{j}} - \frac{1}{2}\left[\nu_{\rm on} e^{i\phi_{\mathbf{j}}} \hat{a}_{\mathbf{j}}^\dagger \hat{a}_{\mathbf{j}}^\dagger + h.c.\right] = \tilde{\omega} \hat{\alpha}_{\mathbf{j}}^\dagger \hat{\alpha}_{\mathbf{j}}. \tag{2.1.8}$$

Here $\tilde{\omega} = \sqrt{\omega_0^2 - \nu_{\rm on}^2}$, and the annihilation operators $\hat{\alpha}_{\mathbf{j}}$ are given by a local Bogoliubov (squeezing) transformation $\hat{\alpha}_{\mathbf{j}} = e^{i\phi_{\mathbf{j}}} e^{-i\varphi_\nu/2} \left(\cosh r a_{\mathbf{j}} - e^{i\phi_{\mathbf{j}}} e^{i\varphi_\nu} \sinh r \hat{a}_{\mathbf{j}}^\dagger \right)$, where the squeezing factor r is

$$r = \frac{1}{4} \ln \left[\frac{\omega_0 + \nu_{\rm on}}{\omega_0 - \nu_{\rm on}} \right]. \tag{2.1.9}$$

On a physical level, the local parametric driving terms attempt to drive each site into a squeezed vacuum state with squeeze parameter r; the $\hat{\alpha}_{\mathbf{j}}$ quasiparticles correspond to excitations above this reference state. Note that we have included an overall phase factor in the definition of the $\hat{\alpha}_{\mathbf{j}}$ which will simplify the final form of the full Hamiltonian.

In this new basis of local quasiparticles, our full Hamiltonian takes the form

$$\hat{H} = \sum_{\mathbf{j}} \tilde{\omega} \hat{\alpha}_{\mathbf{j}}^\dagger \hat{\alpha}_{\mathbf{j}} - \sum_{\langle \mathbf{j},\mathbf{l} \rangle} \tilde{J}_{\mathbf{jl}} \hat{\alpha}_{\mathbf{j}}^\dagger \hat{\alpha}_{\mathbf{l}} - \left(\frac{\tilde{\nu}}{2} \sum_{\langle \mathbf{j},\mathbf{l} \rangle} \hat{\alpha}_{\mathbf{j}}^\dagger \hat{\alpha}_{\mathbf{l}}^\dagger + h.c. \right). \tag{2.1.10}$$

The transformation has mixed the hopping terms with the non-local parametric terms: The effective counter-clockwise hopping matrix element is

$$\begin{aligned} \tilde{J}_{\mathbf{jl}} &= J e^{i\delta} + \\ & e^{3i\delta/2} \left[2J \cos\left(\frac{\delta}{2}\right) \sinh^2 r + \nu_{\rm off} \sinh 2r \cos\left(\frac{\delta}{2} + \varphi_\nu\right) \right], \end{aligned} \tag{2.1.11}$$

and the magnitude of the effective non-local parametric driving is

$$\begin{aligned} |\tilde{\nu}| = \Big| & \nu_{\rm off} e^{-i(\delta/2 + \varphi_\nu)} + 2\nu_{\rm off} \cos(\delta/2 + \varphi_\nu) \sinh^2 r \\ & + J \sinh 2r \cos(\delta/2) \Big|. \end{aligned} \tag{2.1.12}$$

Note that the phase of $\tilde{\nu}$ can be eliminated by a global gauge transformation, and hence

it plays no role; we thus take $\tilde{\nu}$ to be real in what follows.

Our model takes on a much simpler form in the new basis: the onsite parametric driving is gone, and the non-local parametric driving is real. Most crucially, the effective hoppings now can have spatially-varying phases, which depend both on the vorticity of the parametric driving in $\hat{H}_{\mathrm{L}}$ (through δ), and the magnitude of the on-site squeezing (through r). In this transformed basis, the effective hopping phases are the only route to breaking TRS. Our model has thus been mapped onto the standard OMN model for the anomalous quantum Hall effect, with an additional (purely real) nearest-neighbour two-mode squeezing interaction. In the regime where the parametric interactions between the $\hat{\alpha}$-quasiparticles are negligible (see Supplementary Note 3), the complex phases correspond in the usual manner to a synthetic gauge field (i.e. the effective flux Φ piercing a triangular plaquette would be $\Phi = 3\arg\tilde{J}$). In other words, the squeezing creates a synthetic gauge field for Bogoliubov quasiparticles. However, in the presence of substantial parametric interaction between $\hat{\alpha}$-quasiparticles, the parameter Φ can not be interpreted anymore as a flux : a flux of 2π can not be eliminated by a gauge transformation because the complex phases reappear in the parametric terms. In that case, only a periodicity of 6π in Φ is retained, since that corresponds to having trivial hopping phases of 2π.

Understanding the topological structure of this transformed Hamiltonian is completely sufficient for our purposes: one can easily show that the Chern number of a band is invariant under any local Bogoliubov transformation, hence the Chern numbers obtained from the transformed Hamiltonian in equation (2.1.8) will coincide exactly with those obtained from the original Hamiltonian in equation (2.1.2). We thus see that the topological structure of our system is controlled completely through only three dimensionless parameters: the flux Φ associated with the hopping phase, the ratio $|\tilde{\nu}/\tilde{J}|$ and the ratio $\tilde{\omega}/|\tilde{J}|$.

The topological phase diagram for the effective model is shown in Fig. 2.3(b). Again, one sees that as soon as the effective non-local parametric drive $\tilde{\nu}$ is non-zero, topological phases distinct from the standard (particle-conserving) OMN model are possible. The sign of the parametric pump vorticity m_ν determines the sign of the effective flux Φ, c.f. equation (2.1.11). As such, the right half of Fig. 2.3(b) (corresponding to $\Phi > 0$) is a deformed version of the phase diagram of the original model for pump vorticity $m_\nu = 1$, as plotted in Fig. 2.3(a). Changing the sign of m_ν (and hence Φ) simply flips the sign of all Chern numbers, see Supplemetary Note 3.

Our effective model provides a more direct means for understanding the boundaries between different topological phases. Most of these are associated with the crossing of bands at one or more high-symmetry points in the Brillouin zone; this allows an analytic calculation of the phase boundary (see Supplemetary Note 3). Perhaps most striking in Fig. 2.3(b) is the horizontal boundary (labelled $\mathcal{M}$), occurring at a finite value of the effective offsite parametric drive, $\tilde{\nu} \approx \sqrt{\tilde{J}\tilde{\omega}}$. This boundary is set by the closing of a band gap at the M points; as these points are associated with the decoupling of one sublattice from the other two, this boundary is insensitive to the flux Φ. Similarly, the vertical line labeled $\mathcal{T}$ denotes a line where the system has TRS, and all bands cross at the symmetry points K, K' and Γ. The case of zero pump vorticity $m_\nu = 0$ (not shown) is also interesting. Here, the effective flux Φ depends on the strength of the parametric drivings, but is always constrained to be 0 or 3π. This implies that the effective Hamiltonian has TRS, even though the original Hamiltonian may not (i.e. if Im $\nu_{\text{off}} \neq 0$, the original Hamiltonian does not have TRS). For $m_\nu = 0$, the parametric drivings do not open any band gap and the Chern numbers are not well defined.

2.1.4 Edge states and transport

Despite their modified definition, the Chern numbers associated with our Bogoliubov bands still guarantee the existence of protected chiral edge modes in a system with boundaries via a standard bulk-boundary correspondence, see Supplemetary Note 4. These states can be used to transport photons, by exciting them with an auxiliary probe laser beam which is focused on an edge site and at the correct frequency. The lack of particle-number conservation manifests itself directly in the properties of the edge states: along with the standard elastic transmission they can also mediate inelastic scattering processes. In terms of the original lab frame, light injected at a frequency ω_p can emerge on the edge at frequency $\omega_{\mathrm{L}} - \omega_p$ where ω_{L} is the frequency of the laser parametrically driving the system. This is analogous to the idler output of a parametric amplifier. Here, both signal and idler have a topologically protected chirality.

Shown in Fig. 2.4 are the results of a linear response calculation describing such an experiment, applied to a finite system with corners. We incorporate a finite photon decay rate κ in the standard input-output formalism, see Methods section. Narrow-band probe light inside a topological band gap is applied to a site on the edge, and the resulting inelastic transmission probabilities to each site on the lattice are plotted, see Fig. 2.4(a). One clearly sees that the probe light is transmitted in a uni-directional way along the edge of the sample, and is even able to turn the corner without significant backscatter. The corresponding elastic transmission [not shown] is also chiral and shows the same spatial dependence. In Fig. 2.4(b) we show the elastic and inelastic transmittions to the sites indicated in red (rescaled by the overall transmission, $1 - R$ where R is the reflection probability at the injection site) as a function of the probe frequency ω_{p}. By scanning the laser probe frequency one can separately address particle and hole band gaps. The relative intensity of the inelastic scattering component is highly enhanced when the

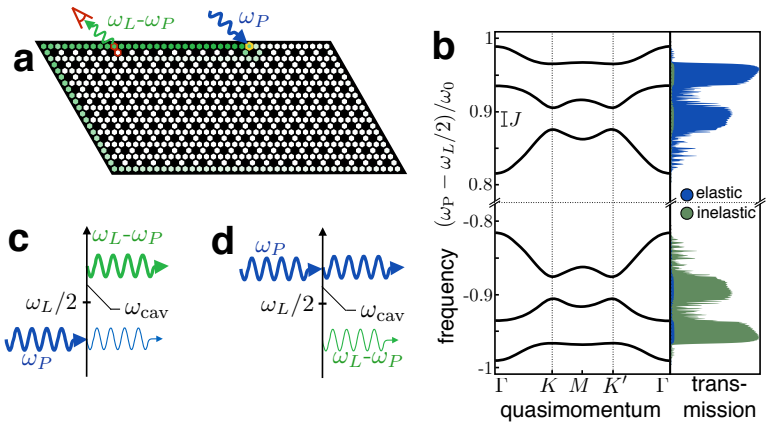

Figure 2.4: Topologically protected transport in a finite system. (a) A probe beam at frequency $\omega_{\rm p}$ inside the bulk band gap is focused on a site (marked in yellow) at the edge of a finite sample. The probability map of the light transmitted inelastically at frequency $\omega_{\rm L} - \omega_{\rm p}$ (where $\omega_{\rm L}$ is the frequency of the parametric pump driving) clearly shows that the transport is chiral. (b) The elastic and inelastic transmission probability to a pair of sites along the edges [indicated in red in (a)] is plotted in blue and green, respectively. A cut through the bulk bands is shown to the left. (c,d) Sketch of the relevant scattering processes and energy scales. The inelastic (elastic) transmission has a larger rate when the light is injected in the hole (particle) band gap. Parameters: Hopping rate $J = 0.02\omega_0$ (ω_0 is the onsite frequency), parametric couplings $\nu_{\rm on} = 0.4\omega_0$ and $\nu_{\rm off} = 0.02\omega_0$, optical decay rate $\kappa = 0.001\omega_0$. In panel (a) $\omega_{\rm p} - \omega_{\rm L}/2 = 0.95\omega_0$.

probe beam is inside a hole band gap, see also the sketches in Fig. 2.4(c-d). When the parametric interaction between the $\hat{\alpha}$ quasiparticles is negligible, the ratio of elastic and inelastic transmissions depends only on the squeezing factor r, [c. f. equation (2.1.9)], see Methods section.

2.1.5 Physical realization

Systems of this type could be implemented in photonic crystal coupled cavity arrays [36] fabricated from nonlinear optical $\chi^{(2)}$ materials [37–39]. The array of optical modes participating in the transport would be supplemented by pump modes (resonant with the pump laser at twice the frequency). One type of pump mode could be engineered to be spatially co-localized with the transport modes (ν_{on} processes), while others could be located in-between (ν_{off}). The required periodic phase pattern of the pump laser can be implemented using spatial light modulators or a suitable superposition of several laser beams impinging on the plane of the crystal. One method for realizing the required kagome lattice of defect cavities was discussed in [5]. Optomechanical systems offer another route towards generating optical squeezing terms [40, 41], via the mechanically induced Kerr interaction, and this could be exploited to create an optomechanical array with a photon Hamiltonian of the type discussed here. Alternatively, these systems can be driven by two laser beams to create phononic squeezing terms [42]. A fourth alternative consists in superconducting microwave circuits of coupled resonators, where Josephson junctions can be embedded to introduce $\chi^{(2)}$ and higher-order nonlinearities, as demonstrated in [43, 44]. kagome lattices of superconducting resonators have recently been implemented [45].

2.2 Discussion

Before concluding, it is worthwhile to discuss the connections between our work and other recent studies. A Hamiltonian of the general form of Eq. (2.0.1) arises naturally in the mean-field description of a Bose-condensed phase. In this setting, the anomalous pairing terms describe the interactions with the condensate treated at the mean-field level. A few recent studies have proposed to take advantage of these interactions to selectively populate topological edge states [28, 30] or, closer to our settings, induce novel topological phases. These include a study of a magnonic crystal [27], as well as general Bose-Einstein condensates in 1D [29] and in 2D [31].

There are some crucial differences between the above studies and our work. In our case, Eq. (1) describes the real particles of our system, not quasiparticles defined above some background. This difference is not just a question of semantics: in our case, topological effects can directly seen by detecting photons, whereas in Refs. [29, 31], one would need to isolate the contribution of a small number of Bogoliubov quasiparticles sitting upon a much larger background of condensed particles. In addition, in our work the pairing terms in Eq. (1) are achieved by driving the system, implying that negative and positive frequencies are clearly physically distinguished (i.e. they are defined relative to a non-zero pump frequency). This is at the heart of the topologically-protected inelastic scattering mechanism we describe, and is something that is not present in previous studies.

Our work opens the door to a number of interesting new directions. On the more practical side, one could attempt to exploit the unique edge states in our system to facilitate directional, quantum-limited amplification. On the more fundamental level, one could use insights from the corresponding disorder problem [46] and attempt to develop a full characterization of particle non-conserving bosonic topological states

that are described by quadratic Hamiltonians. This would then be a counterpart to the classification already developed for fermionic systems [26].

2.3 Methods

2.3.1 Bogoliubov transformation and first-quantized picture

We find the normal mode decompositions leading to the band structures in Fig. (2.2) and the topological phase diagrams in Fig. (2.3) by introducing a first-quantized picture. Since the relevant Hamiltonians do not conserve the excitation number, this is only possible after doubling the degrees of freedom. This is achieved by grouping all annihilation operators with quasimomentum $\mathbf{k}$ and the creation operators with quasimomentum $-\mathbf{k}$ in the $2N$-vector of operators $\hat{\Psi}_{\mathbf{k}} = (\hat{a}_{\mathbf{k}1}, \ldots, \hat{a}_{\mathbf{k}N}, \hat{a}^{\dagger}_{-\mathbf{k}1}, \ldots, \hat{a}^{\dagger}_{-\mathbf{k}N})$ (where N is the unit cell dimension), and by casting the second quantized Hamiltonian $\hat{H}$ in the form

$$\hat{H} = \frac{1}{2} \sum_{\mathbf{k}} \hat{\Psi}^{\dagger}_{\mathbf{k}} \hat{h}(\mathbf{k}) \hat{\Psi}_{\mathbf{k}}. \tag{2.3.1}$$

The $2N \times 2N$ hermitian matrix $\hat{h}(\mathbf{k})$ plays the role of a single-particle Hamiltonian and is referred to as the Bogoliubov de Gennes Hamiltonian. By definition of the normal modes $\hat{H} = \sum_{\mathbf{k},n} E_n[\mathbf{k}] \hat{\beta}^{\dagger}_{n,\mathbf{k}} \hat{\beta}_{n,\mathbf{k}}$, we have $[\hat{H}, \hat{\beta}^{\dagger}_{n,\mathbf{k}}] = E_n[\mathbf{k}] \hat{\beta}^{\dagger}_{n,\mathbf{k}}$. By plugging into the above equation the Bogoliubov ansatz Equation (2.1.3) one immediately finds

$$\hat{h}(\mathbf{k}) |\mathbf{k}_n\rangle = E_n[\mathbf{k}] \hat{\sigma}_z |\mathbf{k}_n\rangle. \tag{2.3.2}$$

Likewise, from $[\hat{H}, \beta_{n,-\mathbf{k}}] = -E_n[-\mathbf{k}] \hat{\beta}_{n,-\mathbf{k}}$ one finds

$$\hat{h}(\mathbf{k})(\mathcal{K}\hat{\sigma}_x |-\mathbf{k}_n\rangle) = -E_n[-\mathbf{k}] \hat{\sigma}_z (\mathcal{K}\hat{\sigma}_x |-\mathbf{k}_n\rangle). \tag{2.3.3}$$

Here, $\mathcal{K}$ denotes the complex conjugation and the matrix $\hat{\sigma}_x$ exchanges the u's and the v's Bogoliubov coefficients,

$$\hat{\sigma}_x = \begin{pmatrix} 0 & \mathbb{1}_N \\ \mathbb{1}_N & 0 \end{pmatrix}.$$

Thus, the spectrum of the $2N$ matrix $\hat{\sigma}_z\hat{h}(\mathbf{k})$ is formed by the set of $2N$ eigenenergies $E_n[\mathbf{k}]$ (belonging to the particle bands) and $-E_n[-\mathbf{k}]$ (belonging to the hole bands). Vice versa, to calculate the eigenenergies $E_n[\mathbf{k}]$ and $E_n[-\mathbf{k}]$ and the vector of Bogoliubov coefficients in Equation (2.1.3), we have to solve the eigenvalue problem

$$\hat{\sigma}_z\hat{h}(\mathbf{k})|m\rangle = \lambda_m|m\rangle, \tag{2.3.4}$$

The solutions we are interested in should also display the symplectic orthonormality relations Equation (2.1.6).

We note in passing that so far we have implicitly assumed that the normal mode decomposition is possible. However, this is not always the case. When the matrix $\hat{\sigma}_z\hat{h}(\mathbf{k})$ has any complex eigenvalue, the Hamiltonian is unstable. Moreover, at the border of the stable and unstable parameter regions, the matrix $\hat{\sigma}_z\hat{h}(\mathbf{k})$ is not diagonalizable. The Supplementary Note 1 contains a stability analysis of our specific model.

In the stable regime of interest here, the matrix $\hat{\sigma}_z\hat{h}(\mathbf{k})$ is diagonalizable and all its eigenvalues are real. In this case, its eigenvectors $|m\rangle$ can be chosen to be mutually $\hat{\sigma}_z$-orthogonal. In addition, there are exactly N positive (negative) norm eigenvectors. Thus, it is always possible to enforce the symplectic orthonormality relations Eq. (2.1.6) by identifying the (appropriately normalized) positive and negative norm solutions with $|\mathbf{k}_n\rangle$ and $\mathcal{K}\hat{\sigma}_x|-\mathbf{k}_n\rangle$, respectively. The corresponding eigenvalues are then to be identified with $E_n[\mathbf{k}]$ (particle band structure) and $-E_n[-\mathbf{k}]$ (hole band structure), respectively

Particle-hole symmetry. The Bogoliubov de Gennes Hamiltonian has the generalized

symmetry $\mathcal{C}^\dagger \hat{h}(\mathbf{k})\mathcal{C} = -\hat{h}(-\mathbf{k})$ where the charge conjugation operator $\mathcal{C}$ is anti-unitary and $\mathcal{C}^2 = \mathbb{1}_{2N}$. Thus, our system represents the Bosonic analogue of a superconductor in the Class D of the standard topological classification. This is a simple consequence of the doubling of the degrees of freedom in the single-particle picture. It simply reflects that the set of ladder operators $\hat{\beta}^\dagger_{n,\mathbf{k}}$ and $\hat{\beta}_{n,-\mathbf{k}}$ calculated from $\hat{h}(\mathbf{k})$ are the adjoint of the set of operators $\hat{\beta}_{n,\mathbf{k}}$ and $\hat{\beta}^\dagger_{n,-\mathbf{k}}$ calculated from $\hat{h}(-\mathbf{k})$.

2.3.2 Details of the transport calculations

In our transport calculations we have included photon decay. We adopt the standard description of the dissipative dynamics of photonic systems in terms of the Langevin equation and the input-output theory [47], for each site:

$$\dot{\hat{a}}_j = i[\hat{H}, \hat{a}_j] - \kappa \hat{a}_j/2 + \sqrt{\kappa}\hat{a}^{(\mathrm{in})}_j. \tag{2.3.5}$$

In practice, we consider an array of detuned parametric amplifiers with intensity decay rate κ and add to the standard description of each parametric amplifier the inter-cell coherent coupling described in the main text. The last term describe the influence of the input field $\hat{a}^{(\mathrm{in})}_j$ injected by an additional probe drive including also the environment vacuum fluctuations. The field $\hat{a}^{(\mathrm{out})}_j$ leaking out of each cavity at site j is given by the input-output relations

$$\hat{a}^{(out)}_j = \hat{a}^{(in)}_j - \sqrt{\kappa}\hat{a}_j. \tag{2.3.6}$$

The above formulas give an accurate description of a photonic system where the intrinsic losses during injection and inside the system are negligible. Intrinsic photon absorption can be incorporated by adding another decay channel to the equation for the light field. It reduces the propagation length but does not change qualitatively the dynamics.

In Fig. (3), we show the probabilities $T_E(\omega, l, j)$ and $T_I(\omega, l, j)$ that a photon injected on site j with frequency $\omega_{\rm in} = \omega + \omega_L/2$ is transmitted elastically (at frequency $\omega + \omega_L/2$) or inelastically (at frequency $\omega_L/2 - \omega$) to site l where it is detected. From the Kubo formula and the input-output relations we find

$$T_E(\omega, l, j) = |\delta_{lj} - i\kappa \tilde{G}_E(\omega, l, j)|^2 \tag{2.3.7}$$

$$T_I(\omega, l, j) = \kappa^2 |\tilde{G}_I(\omega, l, j)|^2. \tag{2.3.8}$$

Here, $\tilde{G}_{E/I}(\omega, l, j)$ are the elastic and inelastic components of the Green's function in frequency space,

$$\tilde{G}_E(\omega, l, j) = -i \int_{-\infty}^{\infty} dt \Theta(t) \langle [\hat{a}_l(t), \hat{a}_j^\dagger(0)] \rangle, \tag{2.3.9}$$

$$\tilde{G}_I(\omega, l, j) = -i \int_{-\infty}^{\infty} dt \Theta(t) \langle [\hat{a}_l^\dagger(t), \hat{a}_j^\dagger(0)] \rangle. \tag{2.3.10}$$

In a N site array with single-particle eigenstates $|n\rangle = (u_n[1], \ldots, u_n[N], v_n[1], \ldots, v_n[N])^T$, the Green's functions read

$$G_E(\omega, l, j) = \sum_n \frac{u_n[l] u_n^*[j]}{\omega - E[n] + i\kappa/2} - \frac{v_n^*[l] v_n[j]}{\omega + E[n] + i\kappa/2}, \tag{2.3.11}$$

$$G_I(\omega, l, j) = \sum_n \frac{v_n[l] u_n^*[j]}{\omega - E[n] + i\kappa/2} - \frac{u_n^*[l] v_n[j]}{\omega + E[n] + i\kappa/2}. \tag{2.3.12}$$

We note that for a probe field inside the bandwidth of the particle (hole) sector but far detuned from the hole (particle) sector, only the first (second) term of the summand in equation (2.3.11) and (2.3.12) is resonant. Thus, as expected, the inelastic scattering is comparatively larger when the probe field is in the hole band gap.

It is easy to estimate quantitatively the relative intensities of elastically and inelastically transmitted light when the parametric interaction of the $\hat{\alpha}$ Bogoliubov quasiparticles is small [the regime where Φ can be interpreted as a synthetic gauge field experienced by the Bogoliubov quasiparticles]. In this case, it is straightforward to show that $|v_n[j]/u_n[j]| \approx \tanh r$ independent of the eigenstate n and the site j. By putting together Eqs. (2.3.8,2.3.11,2.3.12) and neglecting the off-resonant terms we find that for $\omega, \tilde{\omega} \gg |\tilde{J}|, \kappa, |\omega - \tilde{\omega}|$,

$$\begin{aligned} T_I(\omega, l, j) &\approx (\tanh r)^2 T_E(\omega, l, j) \approx T_I(-\omega, l, j) \\ &\approx (\coth r)^2 T_E(-\omega, l, j). \end{aligned}$$

These analytical formulas agree quantitatively with the numerical results shown in Fig. 4(b) [note that in Fig. 4(b) the transmission at the output sites is rescaled by the overall transmission, $\sum_{l \neq j} T_I(\omega, l, j) + T_E(\omega, l, j)$].

2.4 Acknowledgements

VP, CB, and FM acknowledge support by an ERC Starting Grant OPTOMECH, by the DARPA project ORCHID, and by the European Marie-Curie ITN network cQOM. MH and AC acknowledge support from NSERC.

2.5 Author contributions

VP, AAC and FM contributed to the conceptual development of the project and interpretation of results. Calculations and simulations were done by VP, MH and CB. The authors declare no competing financial interests.

2.6 Supplementary Note 1: Details of the calculation of the band structure

2.6.1 Numerical calculation of the band structure

From Eqs. (2,3,13) of the main text, one can immediately derive the explicit expression of the Bogoliubov de Gennes Hamiltonian

$$\hat{h}(\mathbf{k}) = \begin{pmatrix} \omega_0 - J\hat{\tau}(\mathbf{k}) & h_L(\mathbf{k}) \\ h_L^\dagger(\mathbf{k}) & \omega_0 - J\hat{\tau}(\mathbf{k}) \end{pmatrix} \tag{2.6.1}$$

where $\hat{h}_L = -\nu_{\text{on}}\hat{\Lambda}^{m_\nu} - \nu'_{\text{off}}(\hat{\Lambda}^{m_\nu}\hat{\tau} + \hat{\tau}\hat{\Lambda}^{m_\nu})$ (m_ν is the pump vorticity). The matrices $\hat{\tau}(\mathbf{k})$ and $\hat{\Lambda}$ are single-particle operators acting on the sub-lattice degrees of freedom. They have matrix elements: $\Lambda_{AA} = 1$, $\Lambda_{BB} = e^{i2\pi/3}$, $\Lambda_{CC} = e^{-2i\pi/3}$, $\tau_{BA} = \tau^*_{AB} = 1 + e^{i\mathbf{k}\cdot\boldsymbol{a}_1}$, $\tau_{CB} = \tau^*_{BC} = 1 + e^{i\mathbf{k}\cdot\boldsymbol{a}_2}$, $\tau_{AC} = \tau^*_{CA} = 1 + e^{i\mathbf{k}\cdot\boldsymbol{a}_3}$ where $\boldsymbol{a}_1 = (-1, -\sqrt{3})$, $\boldsymbol{a}_2 = (2, 0)$, and $\boldsymbol{a}_3 = (-1, \sqrt{3})$ are lattice vectors. All other matrix elements are zero. Notice that $\hat{\Lambda}$ raises the quasi-angular momentum by one unit: $\hat{\Lambda}|p, m\rangle = |p, m+1\rangle$ where $|p, m\rangle = (1, \exp[i2m\pi/3], \exp[-i2m\pi/3], 0, 0, 0)$ and likewise for the holes. Here, $m = 0$ is the vortex free eigenstate, $m = 1$ has a vortex, and $m = -1$ an anti-vortex (m is defined modulo 2). Thus, a hole with quasimomentum m is converted into a particle with quasi-angular momentum $m+m_\nu$. In other words, a pair of down-converted photons have quasi-angular momenta $-m$ and $m_\nu + m$, respectively. The additional quasimomentum m_ν is provided by the pump photons. In order to write the off-diagonal parametric interaction compactly in terms of the quasi-angular momentum raising operator $\hat{\Lambda}$ we have introduced the rescaled off-diagonal parametric coupling $\nu'_{\text{off}} = e^{-i\delta/2}\nu_{\text{off}}$ for pump vorticity $m_\nu = \pm 1$ and $\nu'_{\text{off}} = \nu_{\text{off}}/2$ for pump vorticity $m_\nu = 0$.

For the effective model Equation (8) of the main text the Bogoliubov de Gennes

Hamiltonian reads

$$\hat{\tilde{h}}(\mathbf{k}) = \begin{pmatrix} \tilde{\omega} - \tilde{J}\hat{\tilde{\tau}}(\mathbf{k},\Phi) & -\tilde{\nu}\hat{\tau}(\mathbf{k}) \\ -\tilde{\nu}\hat{\tau}(\mathbf{k}) & \tilde{\omega} - \tilde{J}\hat{\tilde{\tau}}(\mathbf{k},-\Phi) \end{pmatrix}. \tag{2.6.2}$$

Here, we have introduced the hopping matrix $\hat{\tau}(\mathbf{k},\Phi)$ in the presence of the synthetic magnetic field flux Φ. It has the following non zero matrix elements: $\tilde{\tau}_{BA} = \tilde{\tau}^*_{AB} = e^{i\Phi/3}(1+e^{i\mathbf{k}\cdot\boldsymbol{a}_1})$, $\tilde{\tau}_{CB} = \tilde{\tau}^*_{BC} = e^{i\Phi/3}(1+e^{i\mathbf{k}\cdot\boldsymbol{a}_2})$, $\tilde{\tau}_{AC} = \tilde{\tau}^*_{CA} = e^{i\Phi/3}(1+e^{i\mathbf{k}\cdot\boldsymbol{a}_3})$. In the most general case, we calculate the band structure and the single-particle wavefunctions by diagonalizing the 6×6 matrix $\hat{\sigma}_z\hat{h}(\mathbf{k})$ numerically.

2.6.2 Analytical calculation of the band structure close to the symmetry points

One can gain much insight on the array dynamics, including the stability requirements and the array topology, by calculating analytically the band strucure at the symmetry points. This is a particularly easy task at the rotational symmetry points Γ, K, and K'. There, the hopping matrix $\hat{\tau}$ is diagonal in the basis of the quasi-angular momentum eigenstates. Thus, in this basis the Hamiltonian becomes block diagonal with 2-dimensional blocks. Each block is described by a two-mode squeezing Hamiltonian, except for the quasi-momentum $\mathbf{k}=\Gamma$ and $m=-m_\nu$, when it is a single mode squeezing Hamiltonian

$$\begin{aligned}
\hat{H}_{\rm L}(\mathbf{k}) &= -\sum_m [\nu_{\rm on} + \nu'_{\rm off}(\tau_m + \tau_{m-m_\nu})]\hat{\tilde{a}}^\dagger_{\mathbf{k},m}\hat{\tilde{a}}^\dagger_{-\mathbf{k},m_\nu-m} + \text{H. c.}\,, \quad \text{for} \quad \mathbf{k}=K,K', \\
\hat{H}_{\rm L}(\Gamma) &= -\Big\{ \sum_{m\neq m_\nu} [\nu_{\rm on} + \nu'_{\rm off}(\tau_m + \tau_{m-m_\nu})]\hat{\tilde{a}}^\dagger_{\mathbf{\Gamma},m}\hat{\tilde{a}}^\dagger_{\mathbf{\Gamma},m_\nu-m} - (\nu_{\rm on}/2 + \nu'_{\rm off}\tau_{m_\nu})\hat{\tilde{a}}^{\dagger 2}_{\mathbf{\Gamma},-m_\nu}\Big\} \\
&\quad +\text{H. c.}\,.
\end{aligned}$$

where $\hat{\tilde{a}}_{\mathbf{k},m}$ is the creation operator of an excitation with quasimomentum $\mathbf{k}$ ($\mathbf{k} = \Gamma, K, K'$) and quasi-angular momentum m. Moreover, τ_m indicates the corresponding eigenvalue of the hopping matrix $\hat{\tau}$: $\tau_0(\Gamma) = 4$, $\tau_1(\Gamma) = \tau_{-1}(\Gamma) = \tau_1(K) = \tau_{-1}(K') = -2$, $\tau_0(K) = \tau_1(K') = \tau_0(K') = \tau_{-1}(K) = 1$. By diagonalizing the squeezing Hamiltonian we find the general expression for the eigenvalues

$$E_m = -J\frac{\tau_m - \tau_{m-m_\nu}}{2} + \left[\left(\omega_0 - J\frac{\tau_m + \tau_{m-m_\nu}}{2}\right)^2 - |\nu_{\text{on}} + \nu'_{\text{off}}(\tau_m + \tau_{m-m_\nu})|^2\right]^{1/2} \quad (2.6.3)$$

From an analogous calculation we obtain the spectrum of the effective model at the rotation symmetry points

$$\tilde{E}_m = \left[\left(\tilde{\omega} - \tilde{J}\tilde{\tau}_m(\Phi)\right)^2 - \tau_m^2\tilde{\nu}^2\right]^{1/2} \quad (2.6.4)$$

where $\tilde{\tau}_m(\mathbf{k}, \Phi)$ are the eigenvalues of $\hat{\tilde{\tau}}$: $\tilde{\tau}_0(\Gamma) = 4\cos[\Phi/3]$, $\tau_{\pm1}(\Gamma) = 4\cos[2\pi/3 \mp \Phi/3]$, $\tau_1(K) = \tau_{-1}(K') = -2\cos[\Phi/3]$, $\tau_1(K') = \tau_0(K) = 2\cos[\pi/3 - \Phi/3]$, $\tau_{-1}(K) = \tau_0(K') = 2\cos[\pi/3 + \Phi/3]$.

2.6.3 Stability analysis

The system is stable when all eigenvalues of $\hat{\sigma}_z\hat{h}(\mathbf{k})$ are real. If all eigenenergies of the unperturbed Hamiltonian $\hat{H}_0$ have the same sign the parametric interaction is off-resonant and the system is stable if the parametric couplings are below a finite threshold. On the contrary, if the unperturbed band touches the zero-energy axis, the parametric interaction is resonant for the zero energy modes leading to an instability for any arbitrarily small value of the coupling. Thus, the parametric instability sets an upper limit to the hopping J. For concreteness, we consider a positive onsite energy ω_0 (corresponding to a red detuned drive). In this case, all eigenenergies of $\hat{H}_0$ are positive if $J < \omega_0/4$. In this

case, the system is stable for sufficiently small values of the parametric couplings $\nu_{\rm on}$ and $\nu_{\rm off}$. Nevertheless, the threshold of an instability is reached as soon as the lowest eigenenergy of a particle-type band becomes zero for a finite value of the parametric couplings $\nu_{\rm on}$ and $\nu_{\rm off}$. For the parameters of the topological phase diagram shown in Fig. 3 of the main text the lowest band touches the zero energy axis at the Γ point. Thus, we can find an analytical expression for the instability threshold using the solutions at the rotational symmetry points Eqs. (2.6.3,2.6.4). In Fig. 3(a) the state with zero energy at the border of the unstable region has zero quasimomentum and an anti-vortex. Thus, the instability threshold is given by setting $E_{-1}(\Gamma) = 0$. In Fig. 3(b) the state with zero energy has zero quasi-momentum and quasi-angular momentum. By setting $\tilde{E}_0(\Gamma) = 0$, we find a simple expression for the instability threshold, $\tilde{\nu} = \tilde{\omega}/4 - \tilde{J}\cos[\Phi/3]$.

2.7 Supplementary Note 2: Details of the definition and properties of the symplectic Chern number

2.7.1 Berry phase of a Bogoliubov quasi-particle

For an excitation conserving Hamiltonian, the Chern number of the m-th band can be viewed as a sum of Berry phases accumulated on a set of closed loops covering the whole Brillouin zone. In this case, the state which accumulates the relevant Berry phase is the m-th eigenstate of the single-particle Hamiltonian $\hat{h}_{\mathbf{k}}$ (a block with quasimomentum $\mathbf{k}$ of the single-particle Hamiltonian $\hat{h}$). Below, we show that one can naturally extend this definition of the Chern number to any bosonic Hamiltonian including anomalous terms by identifying the relevant Berry phase in a second-quantized setting.

For each quasi-momentum $\mathbf{k}$, the second-quantized block $\hat{H}_{\mathbf{k}} = \hat{\Psi}^{\dagger}_{\mathbf{k}}\hat{h}(\mathbf{k})\hat{\Psi}_{\mathbf{k}}$ of the full bosonic Hamiltonian $\hat{H}$ is a six-mode squeezing Hamiltonian. If we regard the

quasi-momentum $\mathbf{k}$ as an external parameter, we can ask ourself what is the additional Berry phase accumulated by a single Bogoliubov quasi-particle in a specific band n while the quasi-momentum is varied adiabatically over a closed loop. In other words, we calculate the Berry phase accumulated by the many-body state $\hat{\beta}^\dagger_{\mathbf{k},n}|S_\mathbf{k}\rangle$ where $|S_\mathbf{k}\rangle$ is the Bogoliubov vacuum. We find

$$\begin{aligned}
\varphi_n &= i\oint \langle S_\mathbf{k}|\hat{\beta}_{\mathbf{k},n}\nabla_\mathbf{k}\hat{\beta}^\dagger_{\mathbf{k},n}|S_\mathbf{k}\rangle\cdot d\mathbf{k} \\
&= i\oint \langle S_\mathbf{k}|[\hat{\beta}_{\mathbf{k},n},\nabla_\mathbf{k}\hat{\beta}^\dagger_{\mathbf{k},n}]|S_\mathbf{k}\rangle\cdot d\mathbf{k} + i\oint \langle S_\mathbf{k}|\nabla_\mathbf{k}|S_\mathbf{k}\rangle\cdot d\mathbf{k} \\
&= i\oint \left(u^*_{\mathbf{k},n}[s]\nabla_\mathbf{k}u_{\mathbf{k},n}[s] - v^*_{\mathbf{k},n}[s]\nabla_\mathbf{k}v_{\mathbf{k},n}[s]\right)\cdot d\mathbf{k} + i\oint \langle S_\mathbf{k}|\nabla_\mathbf{k}|S_\mathbf{k}\rangle\cdot d\mathbf{k} \\
&= \oint \mathcal{A}_n\cdot d\mathbf{k} + i\oint \langle S_\mathbf{k}|\nabla_\mathbf{k}|S_\mathbf{k}\rangle\cdot d\mathbf{k}.
\end{aligned}$$

In the second line we have used that $\hat{\beta}_{\mathbf{k},n}|S_\mathbf{k}\rangle = 0$ (by definition of the vacuum). We note that the Bogoliubov vacuum $|S_\mathbf{k}\rangle$ is quasi-momentum dependent and could possibly accumulate a Berry phase by its own, $i\oint\langle S_\mathbf{k}|\nabla_\mathbf{k}|S_\mathbf{k}\rangle\cdot d\mathbf{k} \neq 0$. However, the Berry phase of interest is the additional Berry phase accumulated by the quasi-particle added over the Bogoliubov vacuum.

2.7.2 Properties of the symplectic Chern numbers

Taking into account the orthonormality condition Equation (6) of the main text, one can immediately prove that the Chern numbers have the usual properties: (i) They are integer numbers; (ii) After a phase transition where two or more bands touch the individual Chern number of the band involved in the crossings may change but their sum does not change. Since the crossing of a particle and hole band lead to an instability rather than a phase transition, the sum of the Chern numbers over the particle bands is zero.

2.8 Supplementary Note 3: Details of the calculation of the topological phase diagrams

2.8.1 Symmetry of the topological phase diagram under synthetic magnetic field inversion

In the topological phase diagram shown in Fig. 3(b) all Chern numbers change sign if the direction of the synthetic gauge field is inverted, $\Phi \to -\Phi$. This has a simple explanation: To change the sign of the flux Φ and of the quasimomentum $\mathbf{k}$ corresponds to taking the complex conjugate of the BdG Hamiltonian in momentum space, $\hat{\tilde{h}}(-\mathbf{k}, -\Phi) = \hat{\tilde{h}}^*(\mathbf{k}, \Phi)$, c.f. Supplementary Equation (2.6.2). It follows that the single-particle eigenfunctions for opposite values of the flux and of the quasi-momentum are also related by complex conjugation, $|\mathbf{k}_n(\Phi)\rangle = (|-\mathbf{k}_n(-\Phi)\rangle)^*$. From the definition of the Chern numbers, c. f. Equation (7) of the main text, it immediately follows that the Chern numbers change sign under inversion of the synthetic gauge field Φ.

2.8.2 Border of the different topological phases

At a border of a topological phase transition a pair of Chern numbers can change their values because the corresponding bands touch. Generally speaking bands tend to repel each other rather than crossing. However, at a lattice symmetry point this phenomenon does not necessarily occur because the interaction of a pair of bands can be prevented by a selection rule. In particular, at the rotational symmetry points K, K', and Γ, a hole with quasi-angular momentum m can only be converted into a particle with quasi-angular momentum $m + m_\nu$. We note that due to inversion symmetry the bands must touch simultaneously at the symmetry points K and K'. We refer to the set of parameters

where the bands touch at the symmetry points K and K' (Γ) as K-lines (Γ-lines). When also time-reversal symmetry is present there is band crossing at all rotational symmetry points. We refer to the set of parameters where time-reversal symmetry occurs as $\mathcal{T}$-lines. In addition, a pair of bands can touch at one of the three M points where one sublattice is decoupled from the remaining two sublattices (a particle or hole on that sublattice can not hop on the remaining sublattices). We note that due to rotational symmetry a pair of bands should touch simultaneously at all three M points. We refer to the set of parameters where a pair of bands touch at the M points as M-lines.

In our highly symmetric system, we expect most of the crossings to occur at a symmetry point. However, we note that accidental crossings away from any symmetry point are not forbidden. Indeed most (but not all) borders of the different topological phases in Fig. 2 can be identified with $\mathcal{T}$-lines, K-lines, Γ-lines, or M-lines as explained below.

We first focus on the effective model. The vertical lines $\Phi = 0, \pm 3\pi$ are $\mathcal{T}$-lines (there is time-reversal symmetry because the hopping amplitude $\tilde{J}$ is real). One can also easily recognize the M-lines because they are horizontal. This must be the case because the spectrum at a M-point where a sublattice decouples from the remaining sublattices does not depend on the flux Φ. Indeed, there is such a horizontal line in the phase diagram of Fig. 3(b). We note that it appears for $\tilde{\nu}^2 \approx |\tilde{J}_{ij}|\tilde{\omega}$. Below, we show that this analytical expression holds when the $\hat{\alpha}$ quasi-particles are described by an effective particle-conserving Hamiltonian. We can also find an analytical expression for the K-line and the Γ-lines as explained below.

We initially focus on the Γ-lines. We regard the band crossing condition of a pair of levels with quasi-angular momentum m and m', $\tilde{E}_m(\Gamma) = \tilde{E}_{m'}(\Gamma)$ as an implicit equation for the parametric coupling $\tilde{\nu}$ as a function of the flux Φ. We take advantage of the analytical expression for the spectrum at the rotational symmetry points Supplementary

Equation (2.6.4) to solve this equation. For $m = 0$ and $m' = -1$, we find exactly one real positive solution

$$\tilde{\nu} \;=\; \frac{1}{2\sqrt{3}}\left[\left(\omega_0 - 4\tilde{J}\cos\frac{\Phi}{3}\right)^2 - \left(\omega_0 - 4\tilde{J}\cos\frac{2\pi+\Phi}{3}\right)^2\right]^{1/2}$$

in the intervals $-3\pi \leq \Phi \leq -\pi$ and $2\pi \leq \Phi \leq 3\pi$. Keeping in mind that the phase diagram is periodic with period 6π, this solution can be thought of as a single Γ-line which goes (for increasing flux) from $\tilde{\nu} = 0$ at $\Phi = 2\pi$ back to $\tilde{\nu} = 0$ at $\Phi = 5\pi$ ($\Phi = -\pi$). Indeed, such a line is visible in the phase diagram of Fig. 3(b). From the implicit equations $\tilde{E}_m(\mathbf{k}) = \tilde{E}_{m'}(\mathbf{k})$, $\mathbf{k} = \Gamma, K$ one can find similar formulas for the remaining Γ-line and the K-lines. In particular, the other Γ-line corresponds to the crossings of the levels with angular-momentum $m = 1$ and $m = 0$ and goes from $\tilde{\nu} = 0$ at $\Phi = \pi$ back to $\tilde{\nu} = 0$ at $\Phi = 4\pi$ ($\Phi = -2\pi$), see also Fig. 3(b). There is not a third Γ-line because the levels with quasi-angular momentum $m = 1$ and $m = -1$ are degenerate only on the $\mathcal{T}$-lines. Likewise, one can show that the K-lines go from $\tilde{\nu} = 0$ at $\Phi = -\pi$ back to $\tilde{\nu} = 0$ at $\Phi = \pi$ and from $\tilde{\nu} = 0$ at $\Phi = -2\pi$ back to $\tilde{\nu} = 0$ at $\Phi = 2\pi$, respectively. We note that the formulas for the band crossings are exact and valid for an arbitrary ratio of $\tilde{J}/\tilde{\omega}$. However, if $\tilde{J}/\tilde{\omega}$ is above a finite threshold the unstable region may overlap with the band crossings and not all topological phases will be present in the phase diagram.

Above we have identified all lines forming the border of the different topological phases in Fig. 3(b) except for the lines which appear above the M-lines very close to the $\mathcal{T}$-lines and surrounds the white areas of the topological phase diagram Fig. 3(b). These lines correspond to accidental crossings which occur away from any symmetry point. They enclose four different topological phases (which are not listed in our legend for brevity).

Next, we discuss the topological phase diagram of the original model. For a pump circulation $m_\nu = 1$ ($m_\nu = -1$), the resulting effective flux Φ is positive (negative), see Equation (11) of the main text. Thus, topological phase diagram of the original model is a deformed version of the right (left) half of the effective model phase diagram, see panel (a) of Fig. 2 for the case $m_\nu = 1$ ($m_\nu = -1$). The case $m_\nu = 0$ on the other hand is mapped onto the $\mathcal{T}$-lines of the effective diagram.

A remarkable feature of our model is that there is only a single topological phase for any fixed value m_ν of the pump circulation if the off-diagonal parametric terms are not present ($\nu_{\text{off}} = 0$): $\mathbf{C} = (\mp 1, 0, \pm 1)$ for $m_\nu = \pm 1$ and $\mathbf{C} = (0, 0, 0)$ for $m_\nu = 0$. This is reminiscent of the anomalous Quantum Hall effect on a Kagome lattice with nearest neighbor hoppings (OMN model) where the topological phase is uniquely determined by the sign of the magnetic flux piercing a triangular plaquette, $\mathbf{C} = (\mp 1, 0, \pm 1)$ if the flux is positive or negative, respectively. Indeed, for small squeezing $\nu_{\text{on}}, J \ll \omega_0$, the parametric interaction effectively induces a small synthetic gauge field with a positive flux for $m_\nu = 1$. This can be easily seen by switching to the effective description and neglecting the residual parametric terms. For concreteness we consider the case $m_\nu = 1$. For small squeezing and $\nu_{\text{off}} = 0$ we are somewhere close to $\tilde{\nu} = 0$, $\Phi = 2\pi$ inside the topological phase $\mathbf{C} = (-1, 0, 1)$ at the bottom right corner of the effective diagram. From the above analysis of the effective diagram we know that a topological phase transition can occur only if we cross a Γ or $\mathcal{T}$-line. However, from the analytical solution of the spectrum at the rotational symmetry points of the original model Supplementary Equation (2.6.3) we see that such crossings never occur on the $\nu_{\text{off}} = 0$ axis. Thus, there in no topological phase transition even for large squeezing if $\nu_{\text{off}} = 0$.

2.8.3 Effective excitation-conserving Hamiltonian

When $\tilde{\omega}$ is much larger than $|\tilde{J}|$ and $\tilde{\nu}$ one can derive an effective excitation conserving Hamiltonian. In the regime where $\tilde{\nu} \gg |\tilde{J}|$ it is not enough to keep the excitation conserving terms in Equation (8) of the main text but one should also include the leading order correction in $\tilde{\nu}/\tilde{\omega}$. We arrive at the excitation conserving Hamiltonian with next-nearest-neighbor hoppings,

$$\hat{H}_{\mathrm{RW}} = \sum_{\mathbf{j}} \bar{\omega} \hat{\alpha}_{\mathbf{j}}^{\dagger} \hat{\alpha}_{\mathbf{j}} - \sum_{\langle \mathbf{j},\mathbf{l} \rangle} \bar{J}_{\mathbf{jl}}^{(1)} \hat{\alpha}_{\mathbf{j}}^{\dagger} \hat{\alpha}_{\mathbf{l}} - \sum_{\langle\langle \mathbf{j},\mathbf{l} \rangle\rangle} \bar{J}_{\mathbf{jl}}^{(2)} \hat{\alpha}_{\mathbf{j}}^{\dagger} \hat{\alpha}_{\mathbf{l}}. \tag{2.8.1}$$

Here, $\langle\langle \mathbf{j}, \mathbf{l} \rangle\rangle$ indicates the sum over next-nearest-neighbor sites and

$$\begin{aligned} \bar{\omega} &= \tilde{\omega} - \frac{2\tilde{\nu}^2}{\tilde{\omega}}, \qquad \bar{J}_{\mathbf{jl}}^{(2)} = \frac{\tilde{\nu}^2}{2\tilde{\omega}} \\ \bar{J}_{\mathbf{jl}}^{(1)} &= \tilde{J}_{\mathbf{jl}} + \frac{\tilde{\nu}^2}{2\tilde{\omega}}. \end{aligned}$$

In this simplified picture it is straightforward to calculate the band structure at the M points and finding the bad degeneracy condition $\tilde{\nu}^2 = |\tilde{J}_{\mathbf{jl}}|\tilde{\omega}$ which leads to the horizontal line in the topological phase diagram of the effective model.

2.9 Supplementary Note 4: Bulk-boundary correspondence

It is well known that in a system with a boundary, the net number of edge states (the number of right-movers minus the number of left-movers) in a bulk band gap is a topological invariant [1]. This statement is based on the sole assumption that the band structure and the corresponding eigenvectors change smoothly in the presence of a local perturbation

that does not close a gap. Thus, it clearly applies to any quadratic Hamiltonian. For the special case of an excitation-conserving insulator or a superconductor the bulk boundary correspondence expresses such topological invariant in terms of the Chern numbers: the net number of edge states in a band gap coincides with the sum of the Chern numbers of all bands below that band gap. Here, we explicitly show that the bulk-boundary correspondence is still valid for our model where anomalous terms are present.

We start noticing that the wavefunctions of the RWA Hamiltonian Supplementary Equation (2.8.1) depend only on two parameters: the phase $\Phi/3$ of $\tilde{J}$ and the dimensionless next-nearest-neighbor coupling $\tilde{\nu}^2/(|\tilde{J}|\tilde{\omega})$. By calculating the phase diagram as a function of these parameters [not shown] we see that it supports all topological phases present in the topological phase diagram of the effective Hamiltonian for the $\hat{\alpha}$-quasiparticles [our full model without approximations]. Thus, we can continously interpolate between the two Hamiltonians without crossing any topological phase transition [by sending $\tilde{\omega} \to \infty$ while also tuning Φ and $\tilde{\nu}^2/(\tilde{\omega}|\tilde{J}|)$ to stay in the same topological phase]. Keeping in mind that the bulk-boundary correspondence holds for the excitation-conserving Hamiltonian Supplementary Equation (2.8.1) and that the net number of edge states does not change during the interpolation [unless a gap is closed], we can conclude that such correspondence is valid for our model even for small $\tilde{\omega}$ where the RWA leading to Supplementary Equation (2.8.1) is not a good approximation.

We note that the above reasoning combined with the assumption that a continuous interpolation between any quadratic bosonic Hamiltonian and an excitation conserving Hamiltonian is always possible without closing any band gap, leads to the general validity of the bulk-edge correspondence.

Supplementary References

[1] Hasan M. Z. & Kane C. L., Colloquium: Topological insulators. *Rev. Mod. Phys.* **82**, 3045 (2010).

References

[1]N. Goldman, G. Juzeliūnas, P. Öhberg, and I. B. Spielman, Rep. Prog. Phys **77**, 126401 (2014).

[2]L. Lu, J. D. Joannopoulos, and M. Soljacic, Nat. Photon **8**, 821–829 (2014).

[3]E. Prodan, and C. Prodan, Phys. Rev. Lett **103**, 248101 (2009).

[4]C. L. Kane, and T. C. Lubensky, Nat. Phys **10**, 39–45 (2013).

[5]V. Peano, B. V., S. M. C., and F. Marquardt, Phys. Rev. X **5**, 031011 (2015).

[6]Z. Yang, F. Gao, X. Shi, X. Lin, Z. Gao, Y. Chong, and B. Zhang, Phys. Rev. Lett. **114**, 114301 (2015).

[7]R. Süsstrunk, and S. D. Huber, Science **349**, 47–50 (2015).

[8]J. Paulose, B. G. Chen, and V. Vitelli, Nat. Phys **11**, 153–156 (2015).

[9]L. M. Nash, D. Kleckner, A. Read, V. Vitelli, A. M. Turner, and W. T. M. Irvine, Proceedings of the National Academy of Sciences **112**, 14495–14500 (2015).

[10]F. D. M. Haldane, and S. Raghu, Phys. Rev. Lett **100**, 013904 (2008).

[11]S. Raghu, and F. D. M. Haldane, Phys. Rev. A **78**, 033834 (2008).

[12]Z. Wang, Y. Chong, J. D. Joannopoulos, and M. Soljacic, Nature **461**, 772–775 (2009).

[13]J. Koch, A. A. Houck, K. Le Hur, and S. M. Girvin, Phys. Rev. A **82**, 043811 (2010).

[14]R. O. Umucalılar, and I. Carusotto, Phys. Rev. A **84**, 043804 (2011).

[15]K. Fang, Z. Yu, and S. Fan, Nat. Photon **6**, 782–787 (2012).

[16]A. Petrescu, A. A. Houck, and K. Le Hur, Phys. Rev. A **86**, 053804 (2012).

[17]L. D. Tzuang, K. Fang, P. Nussenzveig, S. Fan, and M. Lipson, Nat. Photon **8**, 701–705 (2014).

[18]M. Schmidt, S. Kessler, V. Peano, O. Painter, and F. Marquardt, Optica **2**, 635–641 (2015).

[19]M. Hafezi, E. A. Demler, M. D. Lukin, and J. M. Taylor, Nature Phys **7**, 907–912 (2011).

[20]A. B. Khanikaev, S. H. Mousavi, W.-k. Tse, M. Kargarian, A. H. MacDonald, and G. Shvets, Nat. Mat. **12**, 233–239 (2012).

[21]M. Hafezi, S. Mittal, J. Fan, A. Migdall, and J. M. Taylor, Nature Photonics **7**, 1001–1005 (2013).

[22]S. Mittal, J. Fan, S. Faez, A. Migdall, J. M. Taylor, and M. Hafezi, Phys. Rev. Lett **113**, 087403 (2014).

[23]T. Kitagawa, M. A. Broome, A. Fedrizzi, M. S. Rudner, E. Berg, I. Kassal, A. Aspuru-Guzik, E. Demler, and A. G. White, Nature Communications **3**, Article, 882 (2012).

[24]M. C. Rechtsman, Y. Plotnik, J. M. Zeuner, D. Song, Z. Chen, A. Szameit, and M. Segev, Phys. Rev. Lett. **111**, 103901 (2013).

[25]C.-E. Bardyn, and A. İmamoğlu, Phys. Rev. Lett. **109**, 253606 (2012).

[26]S. Ryu, A. P. Schnyder, A. Furusaki, and A. W. W. Ludwig, New J. Phys **12**, 065010 (2010).

[27]R. Shindou, R. Matsumoto, M. S., and J. Ohe, Phys. Rev. B **87**, 174427 (2013).

[28]R. Barnett, Phys. Rev. A **88**, 063631 (2013).

[29]G. Engelhardt, and T. Brandes, Phys. Rev. A **91**, 053621 (2015).

[30]B. Galilo, D. K. K. Lee, and R. Barnett, Phys. Rev. Lett **115**, 245302 (2015).

[31]C.-E. Bardyn, T. Karzig, G. Refael, and T. C. H. Liew, Phys. Rev. B **93**, 020502 (2016).

[32]C. C. Gerry, and P. L. Knight, in *Introductory quantum optics.* (Cambridge University Press, 2005).

[33]K. Ohgushi, S. Murakami, and N. Nagaosa, Phys. Rev. B **62**, R6065–R6068 (2000).

[34]D. Green, L. Santos, and C. Chamon, Phys. Rev. B **82**, 075104 (2010).

[35]T. Fukui, Y. Hatsugai, and H. Suzuki, J. Phys. Soc. Jpn **74**, 1674–1677 (2005).

[36]M. Notomi, E. Kuramochi, and T. Tanabe, Nat. Photon. **2**, 741–747 (2008).

[37]S. Mookherjea, and A. Yariv, Ieee J. Quantum Elect **8**, 448 (2002).

[38]B. J. Eggleton, B. Luther-Davies, and K. Richardson, Nat. Photonics **5**, 141–148 (2011).

[39]J. Dahdah, M. Pilar-Bernal, N. Courjal, G. Ulliac, and F. Baida, J. Appl. Phys **110**, 074318 (2011).

[40]A. H. Safavi-Naeini, S. Gröblacher, J. T. Hill, J. Chan, M. Aspelmeyer, and O. Painter, Nature **500**, 185–189 (2013).

[41]T. P. Purdy, P. L. Yu, R. W. Peterson, N. S. Kampel, and C. A. Regal, Phys. Rev. X **3**, 031012 (2013).

[42]A. Kronwald, F. Marquardt, and A. A. Clerk, Phys. Rev. A **88**, 063833 (2013).

[43]N. Bergeal, R. Vijay, V. E. Manucharyan, I. Siddiqi, R. J. Schoelkopf, S. M. Girvin, and M. H. Devoret, Nature Physics **6**, Article, 296 (2010).

[44]B. Abdo, A. Kamal, and M. Devoret, Phys. Rev. B **87**, 014508 (2013).

[45]D. L. Underwood, W. E. Shanks, J. Koch, and A. A. Houck, Phys. Rev. A **86**, 023837 (2012).

[46]V. Gurarie, and J. T. Chalker, Phys. Rev. B **68**, 134207 (2003).

[47] A. A. Clerk, M. H. Devoret, S. M. Girvin, F. Marquardt, and R. J. Schoelkopf, Reviews of Modern Physics **82**, 1155–1208 (2010).

Preface to Chapter 3

In the previous chapter, we studied how parametric driving can lead to interesting band structures and topological phases. In this chapter, we focus on the steady-state of a parametrically driven system. We study how the bands of a driven-dissipative system are occupied when weakly coupled to a zero-temperature environment. We characterize the system by looking at the occupancies and anomalous correlators of the eigenmodes of the system. We focus on a concrete model of photons hopping on a one-dimensional chain with on-site parametric driving. As there has been great interest in obtaining chemical potentials for light and bosonic modes, we determine if there are any parameter regimes for which the eigenmodes are thermally occupied (i.e. are described by a Bose-Einstein distribution for a range of energy, with chemical potential μ and temperature T). Although the modes are never fully thermal, there are regimes where the fidelity between our modes and a thermal mode is very high. We also numerically investigate if there is a long-range, non-local parametric drive which would give rise to a thermal eigenmode. We find that for relatively simple long-range parametric drives, we are able to obtain thermally distributed eigenmodes.

3

Steady-states of parametrically driven systems

Martin Houde[1], **Aashish. A. Clerk**[2]

[1]Department of Physics and the Centre for Physics of Materials, McGill University, Montreal, Quebec, Canada H3A 2T8

[2]Institute for Molecular Engineering, University of Chicago, 5640 S. Ellis Ave., Chicago, IL 60637

This chapter will be submitted for publication.

Abstract

We study how a 1D parametrically-driven array of coupled cavities becomes occupied in the steady-state, when each site is weakly coupled to a zero temperature bath. We determine under what circumstances it is possible to obtain a steady-state which is thermally occupied for the entire band (i.e. the occupancies are described by a Bose-Einstein distribution for a constant temperature T and chemical potential μ for the entire energy band). For the simple case of on-site parametric driving and nearest-neighbour hopping, no such description occurs, however, in certain regimes the occupancies are approximately thermal. By allowing for long-range, non-local parametric driving, we are able to obtain a steady-state which is thermal with non-zero chemical potential and finite temperature for the entire band.

3.1 Introduction

Recently, there have been numerous studies on how parametric driving, the process where pairs of bosons are coherently created or annihilated, can lead to interesting topological band structures in bosonic systems. In systems where the parametric driving is weak and the system remains stable, the bosonic nature of the particles leads to interesting properties which not are observed in fermionic analogues [1–5]. Furthermore, if the drive is strong enough and chosen properly, the system can become dynamically unstable in such a way that only the topological edge states become unstable [3, 6, 7]. These instabilities are similar to the parametric instability which occurs in an oscillator whose spring constant is modulated in time. Although there has been great study on the band structures and their interesting properties, there is little exploration as to how are these bands become occupied in the steady-state when considered as a realistic model that includes weak loss. The fact that these systems are parametrically-driven could lead to interesting steady-states. An interesting outcome would be if the steady-state were thermally occupied.

There has been great interest on how to obtain a driven-dissipative non-equilibrium steady-state of a non-conserved boson, such as photons, to mimic a thermal equilibrium state with a non-zero chemical potential. The notion of a chemical potential for non-conserved bosons is important in understanding a wide variety of single- and many-body effects where the number of particles become effectively conserved. It was shown that when photons are coupled to excitons and confined to a cavity, polaritons form which can themselves thermalize in the steady-state [8–10]. Moreover, when interacting with a nonlinear medium, it was shown that photons can thermalize with a nonzero chemical potential and form a Bose-Einstein condensate [11–14]. More recently, it was shown that by parametrically modulating the coupling of a photonic system with a thermal bath

leads to the thermalization of the system with a tuneable chemical potential [15].

Motivated by the interesting band properties induced by parametric driving and the search for driven-dissipative non-equilibrium steady-states which behave thermally, we study how the bands of parametrically-driven systems become occupied in the steady-state.

In this paper, we study how a one-dimensional parametrically-driven array of coupled cavities becomes occupied in the steady-state, when each site is weakly coupled to a zero temperature bath. We begin with the simplest coupled array and parametric drive where each cavity is parametrically-driven and photons hop to nearest neighbours only. We find that the steady-state of such a system can never fully be described by a Bose-Einstein distribution with high fidelity. However, there are certain parameter regimes where the steady-state behaves approximately thermally with a high fidelity.

By considering more complicated parametric drives, where pairs of photons can also be created on different sites (i.e. the driving is non-local and long-range), we find that it is possible to obtain a steady-state which is thermally occupied. Moreover, these non-local drives can be approximated by experimentally feasible parametric drives.

3.2 Model

We consider a very general model of photons hopping on a one-dimensional lattice of cavities while being subject to parametric two-photon driving. The Hamiltonian of such a system is (taking $\hbar = 1$)

$$\hat{H} = \sum_i \omega_0 \hat{a}_i^\dagger \hat{a}_i - \sum_{i,j} J_{i,j} \hat{a}_i^\dagger \hat{a}_j - \frac{1}{2} \sum_{i,j} \left(\nu_{i,j} \hat{a}_i^\dagger \hat{a}_j^\dagger + h.c. \right) \tag{3.2.1}$$

where $\hat{a}_j$ annihilates a photon on site j, ω_0 is the on-site energy, $J_{i,j}$ is the hopping matrix, and $\nu_{i,j}$ is the parametric drive strength matrix. Note that we are working in a rotating frame where ω_0 represents the detuning of the pump frequency (ω_P) from the cavity frequency (ω_{cav}) (i.e. $\omega_0 = \omega_{\text{cav}} - \omega_P$). For the parametric driving, we assume that the injected photons have no net quasimomentum. In other words, there is no spatial variation in the phase of the parametric driving and we take the matrix elements to be purely real. We assume that both the hopping and the parametric driving are translationally invariant. To simplify the study of the properties of the steady state of our system, we consider periodic systems and begin by fourier transforming into momentum space. In momentum space, the Hamiltonian becomes

$$\hat{H} = \sum_k \epsilon_k \hat{a}_k^\dagger \hat{a}_k - \frac{1}{2}(\nu_k \hat{a}_{-k}^\dagger \hat{a}_k^\dagger + h.c.). \tag{3.2.2}$$

where ϵ_k is a general energy dispersion dependent on the hopping configuration and by assumption ν_k conserves quasimomentum. By inversion symmetry, we have that $\epsilon_k = \epsilon_{-k}$ and $\nu_k = \nu_{-k}$. Without dissipation, the Hamiltonian becomes dynamically unstable when the drive strength exceeds the cost of creating pairs of photons for any quasimomentum k, i.e. when $|\epsilon_k| < |\nu_k|$. When this occurs, our modes will experience exponential growth and never relax to a steady-state. We wish to study steady-states of driven-dissipative systems which are stable even without dissipation. In that case, an extremely weak coupling to dissipation can determine the population of the steady-states, without strongly modifying the dynamics. We therefore assume that the energy dispersion $\epsilon_k > 0$ and $|\epsilon_k| > |\nu_k|$ for all values of quasimomentum. This will ensure that we are always dynamically stable and relax to a steady-state, even with infinitesimal dissipation.

We can diagonalize the Hamiltonian of Eq.(3.2.2) via a Bogoliubov transformation

$$\hat{\alpha}_k = \cosh(r_k)\hat{a}_k - \sinh(r_k)\hat{a}^\dagger_{-k} \tag{3.2.3}$$

where

$$r_k = \frac{1}{4}\ln\left[\frac{\epsilon_k + \nu_k}{\epsilon_k - \nu_k}\right] \tag{3.2.4}$$

is a quasimomentum dependent squeezing factor. The resulting Hamiltonian is

$$\hat{H} = \sum_k E_k \hat{\alpha}^\dagger_k \hat{\alpha}_k \tag{3.2.5}$$

where the energy of the Bogoliubov mode is

$$E_k = \sqrt{\epsilon_k^2 - \nu_k^2} \tag{3.2.6}$$

and by assumption $E_k > 0$ for all values of quasimomentum.

We now consider the effects of dissipation. We assume that each cavity is subject to simple, Markovian loss. We model this loss as arising from a coupling to a zero-temperature, Markovian and Gaussian reservoir (as in standard input-output theory[16]). Assuming that the coupling to the environment is the same on every site ($\kappa_j = \kappa$), the resulting Heisenberg-Langevin equations of motion for the photonic modes are

$$\dot{\hat{a}}_k(t) = -(i\epsilon_k + \frac{\kappa}{2})\hat{a}_k(t) - i\nu_k\hat{a}^\dagger_{-k}(t) + \sqrt{\kappa}\hat{a}^{in}_k(t) \tag{3.2.7}$$

where κ is the coupling rate to the external environment. $\hat{a}^{in}_k$ describes vacuum fluctuations entering the system: the only non-zero correlation function for the input fields is

$\langle \hat{a}_k^{in}(t)\hat{a}_{k'}^{\dagger,in}(t')\rangle = \delta(t-t')\delta_{k,k'}$. We re-express the Heisenberg-Langevin equations of motion in the eigenmode basis of the dissipationless Hamiltonian in Eq. (3.2.2) (i.e. the $\hat{\alpha}_k$ modes)

$$\dot{\hat{\alpha}}_k(t) = -(iE_k + \frac{\kappa}{2})\hat{\alpha}_k(t) + \sqrt{\kappa}\hat{\alpha}_k^{in}(t). \tag{3.2.8}$$

We see that the eigenmodes are subject to input fluctuations of the form

$$\hat{\alpha}_k^{in}(t) = \cosh(r_k)\hat{a}_k^{in}(t) - \sinh(r_k)\hat{a}_{-k}^{in}(t) \tag{3.2.9}$$

which no longer describes vacuum noise. In fact, the non-zero correlation functions for these input operators are

$$\langle \hat{\alpha}_k^{\dagger,in}(t)\hat{\alpha}_{k'}^{in}(t')\rangle = \sinh^2(r_k)\delta(t-t')\delta_{k,k'}, \tag{3.2.10}$$

$$\langle \hat{\alpha}_k^{in}(t)\hat{\alpha}_{k'}^{in}(t')\rangle = \cosh(r_k)\sinh(r_k)\delta(t-t')\delta_{k,k'}. \tag{3.2.11}$$

This leads to squeezing of the input vacuum noise and could potentially lead to interesting non-equilibrium steady-states. To study the steady-state of the system, we will be considering the limit where $\kappa \to 0^+$. This is the standard limit where the coupling to the bath determines how the eigenmodes become occupied, all the while being so weak that it does not affect the dynamics. In this limit, the coupling is much smaller than the minimum energy spacing in the system ($\kappa \ll \min|E_k - E_{k'}|$ for all quasimomentum k and k').

3.3 Steady-state analysis

To study the steady-state of our system, we want to understand how the eigenmodes of our system are occupied. To do so, we evaluate all the equal-time correlation functions of the eigenmodes. Since our Hamiltonian is quadratic and we are taking the input noise to be Gaussian, we need only consider the occupation of the eigenmodes and its anomalous correlator

$$\langle \hat{\alpha}_k^\dagger(t)\hat{\alpha}_{k'}(t)\rangle \equiv \bar{n}_k\delta_{k,k'} \;;\; \langle \hat{\alpha}_k(t)\hat{\alpha}_{k'}(t)\rangle \equiv M_k\delta_{k,k'}, \tag{3.3.1}$$

which are diagonal in quasimomentum due to translational invariance.

To obtain analytical expressions for the correlators, we Fourier transform into frequency space. Note that we are using the convention where $\hat{a}_k^\dagger[\omega] = (\hat{a}_k[-\omega])^\dagger$. In frequency space, the solution to the equations of motion Eq. (3.2.9) are

$$\hat{\alpha}_k[\omega] = \frac{\sqrt{\kappa}}{-i(\omega - E_k) + \frac{\kappa}{2}}\hat{\alpha}_k^{in}[\omega]. \tag{3.3.2}$$

With this solution in hand, we can readily solve for the correlators. For the occupation, we find

$$\begin{aligned}\langle \hat{\alpha}_k^\dagger(t)\hat{\alpha}_{k'}(t)\rangle &= \frac{1}{(2\pi)^2}\int d\omega_1 d\omega_2 \langle \hat{\alpha}_k^\dagger[\omega_1]\hat{\alpha}_{k'}[\omega_2]\rangle \\ &= \frac{1}{2\pi}\int d\omega_1 \frac{\kappa \sinh^2(r_k)}{(-i(\omega_1 - E_k) + \frac{\kappa}{2})(i(\omega_1 - E_k) + \frac{\kappa}{2})}\delta_{k,k'} \\ &= \sinh^2(r_k)\delta_{k,k'},\end{aligned} \tag{3.3.3}$$

where we have used $\delta_{k,k'}$ to express everything in terms of k and the fact that in frequency space the vacuum correlation functions are proportional to $\delta(\omega + \omega')$. Note that the

occupation is independent of κ and can possibly remain non-zero in the limit that $\kappa \to 0^+$. Similarly, we find that the anomalous correlator is

$$\langle \hat{\alpha}_k(t)\hat{\alpha}_{k'}(t)\rangle = \frac{\kappa \cosh(r_k)\sinh(r_k)}{2iE_k + \kappa}\delta_{k,k'}. \tag{3.3.4}$$

Since we have have assumed $E_k > 0$ for stability, taking the limit $\kappa \to 0^+$ gives us $\langle \hat{\alpha}_k(t)\hat{\alpha}_{k'}(t)\rangle = 0$. Hence, our steady-state is fully described by the average occupation of the eigenmodes

$$\bar{n}_k = \sinh^2(r_k) = \frac{\sqrt{E_k^2 + \nu_k^2} - E_k}{2E_k} \tag{3.3.5}$$

where in the last equality, we have expressed everything in terms of the energy E_k (see Eq. 3.2.6).

If we were to be in thermal equilibrium with the Hamiltonian of Eq. (3.2.5), the occupancy of the eigenmode would be that of a Bose-Einsein distribution

$$\bar{n}^{\mathrm{Th}}[E_k, T, \mu] = \frac{1}{e^{\beta(E_k - \mu)} - 1} \tag{3.3.6}$$

for a given inverse temperature $\beta = 1/T$ and chemical potential μ. From the form of Eq. (3.3.5), there is no reason to believe that the eigenmodes are thermally occupied for a constant temperature and chemical potentiol over the entire band. For a specific quasimomenta, we can always equate Eq. (3.3.5) to a thermal occupation, however, different quasimomenta will have different temperatures and chemical potentials. We are interested in the case where the temperature and chemical potential are constant and the equality holds for the whole energy dispersion. Suppose that we could fine-tune the parameters of our Hamiltonian such that $\bar{n}_k = \bar{n}^{\mathrm{Th}}[E_k, T, \mu]$ for constant T, μ over the entire band. In this case, our system is equivalent to having some Heisenberg-Langevin

equation where each eigenmode (which we label by $\hat{\beta}_k$ here) is driven by its own, independent noise source:

$$\hat{\beta}_k[\omega] = \frac{\sqrt{\kappa}}{-i(\omega - E_k) + \frac{\kappa}{2}} \hat{\beta}_k^{in}[\omega]. \tag{3.3.7}$$

where $\langle \hat{\beta}_k^{\dagger in}[\omega] \hat{\beta}_k^{in}[\omega'] \rangle = \bar{n}^{\mathrm{Th}}[w, T, \mu]$ is thermally occupied. We cannot distinguish our fine-tuned Hamiltonian model from this description.

Note, however, that our fine-tuning only gets the noise properties correct "on-shell". That is to say, our noise operators $\hat{\alpha}_k^{in}[\omega]$ are only guaranteed to be thermally occupied when $\omega = E_k$. For different values of ω this is not the case. This property of our fine-tuned model could be useful in the study of quench dynamics [17, 18]. With the fine-tuning, we could initially prepare a thermal state and then turn on additional interactions. These additional interactions would then mix noise terms at different frequencies which are not guaranteed to behave thermally.

3.4 Thermal distribution

Before looking at more specific models (where we specify the hopping and parametric drives), we show how a Bose-Einstein distribution behaves in certain limits. We focus on two important regimes. In the first case, we consider $E_k - \mu \ll T$ for the entire bandwidth of E_k. This is known as the high-occupancy or thermal regime. In this regime, many modes are thermally excited and the approximate behaviour of the Bose-Einstein distribution is approximately

$$\bar{n}^{\mathrm{Th}}[E_k, T, \mu] \approx \frac{1}{\beta(E_k - \mu)}. \tag{3.4.1}$$

We see that the in this regime, the occupancy diverges as the inverse of energy. On the other hand, when $E_k - \mu \gg T$ for the entire bandwidth of E_k, also known as the low-temperature regime, the Bose-Einstein distribution behaves as

$$\bar{n}^{\mathrm{Th}}[E_k, T, \mu] \approx e^{-\beta(E_k-\mu)}. \tag{3.4.2}$$

In this regime, the occupancy is exponentially suppressed. Having looked at the limiting behaviours of the Bose-Einstein distribution, we now turn our attention to specific models of the Hamiltonian in Eq. (3.2.1) and study if the occupancy of the eigenmodes (Eq. (3.3.5)) reproduces these behaviours. We also characterize how close to a thermally occupied state our steady-state is by calculating the fidelity between both our steady-state and a thermal state.

3.5 Fidelity

To characterize how close we are to a Bose-Einstein distribution, we calculate the fidelity between our state and a thermal state. We begin by finding an expression for the density matrix of our steady-state. From section 3.3, we know that there are no correlations between quasimomentum modes and therefore the density matrix of our steady-state, ρ^{ss}, factorizes into a tensor product of all the quasimomentum mode's density matrices, which we label by ρ_k^{ss}. Furthermore, as we have a linear system, each mode is in a Gaussian state. Since $\langle \hat{\alpha}_k(t)\hat{\alpha}_k(t)\rangle = 0$ and $\langle \hat{\alpha}_k(t)\rangle = 0$, by virtue that the input modes are vacuum, ρ_k^{ss} simply describes a thermal state with inverse temperature β_k. Note that each quasimomentum density matrix will have a different temperature. We can express

the density matrix as

$$\rho^{\text{ss}} = \bigotimes_k \rho_k^{\text{ss}} = \bigotimes_k \frac{1}{Z_{\rho^{\text{ss}}_k}} \sum_{n_k=1}^{\infty} (f_k)^{n_k} \, |n_k\rangle\langle n_k|, \tag{3.5.1}$$

where

$$f_k = \frac{\bar{n}_k}{\bar{n}_k + 1} \tag{3.5.2}$$

is just the effective Boltzmann factor $e^{-\beta_k E_k}$ associated with $\bar{n}_k$. Since we have that $f_k < 1$, the normalization factor is $Z_{\rho_k} = \frac{1}{1-f_k}$. Substituting our expression for $\bar{n}_k$ and expressing everything in terms of the eigenmode energy E_k, we obtain

$$f_k = \frac{\sqrt{E_k^2 + \nu^2} - E_k}{\sqrt{E_k^2 + \nu^2} + E_k}. \tag{3.5.3}$$

Having found an analytical expression for the density matrix of our steady-state, we now find an expression for the fidelity. Recall that for a thermal state, at temperature T and chemical potential μ, the density matrix is given by

$$\rho^{\text{Th}} = \bigotimes_k \rho_k^{\text{Th}} \equiv \bigotimes_k \sum_{n_k=1}^{\infty} p_{n_k}^{\text{Th}} |n_k\rangle\langle n_k| = \bigotimes_k \left(1 - e^{-\beta(E_k-\mu)}\right) \sum_{n_k=1}^{\infty} e^{-\beta(E_k-\mu)n_k} |n_k\rangle\langle n_k|. \tag{3.5.4}$$

Since both density matrices are diagonal and commute, we have that the fidelity between these states is

$$F(\rho^{\text{Th}}, \rho^{\text{ss}}) = \prod_k \sum_{n_k=1}^{\infty} \sqrt{p_{n_k}^{\text{Th}} p_{n_k}^{\text{ss}}} = \prod_k \frac{\sqrt{\left(1 - e^{-\beta(E_k-\mu)}\right)\left(1 - f_k\right)}}{1 - e^{-\beta(E_k-\mu)/2}\sqrt{f_k}}. \tag{3.5.5}$$

With an expression for the fidelity at hand, we can determine how close to being thermally

occupied our eigenmodes are when considering specific realizations for the hopping and driving elements.

3.6 Nearest-neighbour hopping and on-site parametric driving

We start by considering the simplest realization of the Hamiltonian of Eq. (3.2.1). We consider only nearest-neighbour hopping and on-site parametric driving. The Hamiltonian thus takes the form ($\hbar = 1$)

$$\hat{H} = \sum_j \omega_0 \hat{a}_j^\dagger \hat{a}_j - J\left(\hat{a}_{j+1}^\dagger \hat{a}_j + \hat{a}_j^\dagger \hat{a}_{j+1}\right) - \frac{\nu}{2}\left((\hat{a}_j^\dagger)^2 + (\hat{a}_j)^2\right). \tag{3.6.1}$$

In momentum space, we find $\epsilon_k = \omega_0 - 2J\cos k$ and $\nu_k = \nu$. For ϵ_k to be greater than zero for all quasimomentum, we require that $\omega_0 > 2J$. Furthermore, for stability, we also require that $\omega_0 - 2J > \nu$. Taking this into account, the eigenmode energies are

$$E_k = \sqrt{(\omega_0 - 2J\cos k)^2 - \nu^2} \tag{3.6.2}$$

and the squeezing parameter takes the form

$$r_k = \frac{1}{4}\ln\left[\frac{\omega_0 - 2J\cos k + \nu}{\omega_0 - 2J\cos k - \nu}\right]. \tag{3.6.3}$$

We wish to find if there are any parameter regimes, within this simple model, where the eigenmodes are thermally occupied with a temperature T and chemical potential μ. Note that the quantity of interest is not the chemical potential itself, but rather how far the bottom of the band is from the chemical potential. We shall therefore be considering the

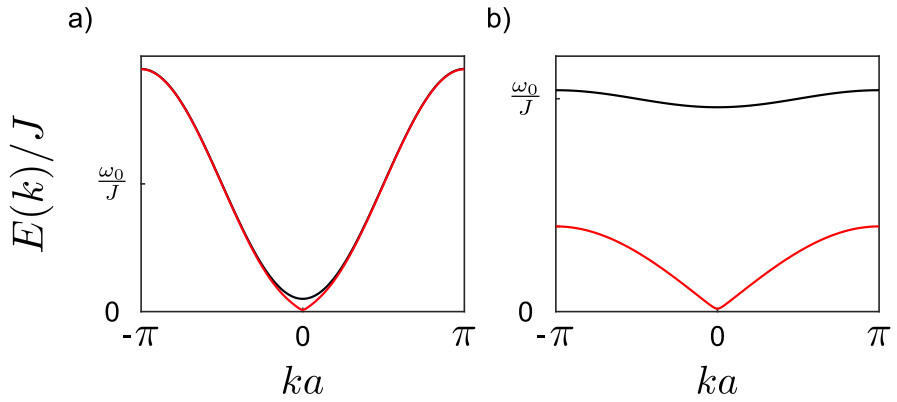

Figure 3.1: Energy bands for the one-dimensional array of cavities with nearest-neighbour hopping and on-site parametric driving (see Eq. (3.6.1)) for two sets of parameter regimes. The black curves are the dispersions when the system is far from instability ($\nu = 0$) whereas the red curves are when the system is on the cusp of instability ($\nu \approx \omega_0 - 2J$).(a) In this regime, the hopping parameter is comparable in size to the on-site energy ($\omega_0 \approx 2J$). In this regime, it does not take a high value of ν to reach instability and only the bottom of the band becomes unstable.(b) The opposite regime, where the hopping parameter is much smaller than the on-site energy ($\omega_0 \gg J$). Here we can have much higher values of ν, which pulls the entire band towards instability.

quantity $\Delta\mu = E_{\min} - \mu$ where $E_{\min}$ is the energy at the bottom of the band E_k.

There are two parameter regimes of interest: when $\omega_0 \gg J$ and $\omega_0 \sim 2J$. We will be considering both regimes as a function of the parametric drive strength (ν). The first regime corresponds to an on-site energy which is much larger than the hopping rate. On the other hand, the second regime corresponds to the case where the on-site energy is on the order of the hopping rate.

3.6.1 On-site energy much larger than hopping rate

We begin by analyzing the regime where $\omega_0 \gg J$. Physically, when $\nu = 0$, this is the regime where the average energy of the band (ω_0) is much, much larger than the dispersion of the band. As a result, when $\nu \neq 0$, the squeezing parameter r_k (c.f. Eq. (3.6.3)) is roughly constant across the entire band. Fig. 3.1 shows the energy dispersion in this

regime when $\nu = 0$ and $\nu \approx \omega_0 - 2J$. For the latter parametric drive strength, our system is at the cusp of instability.

When we are far from instability, the parametric drive strength ν is very small in comparison to the band energy E_k. In fact, when $\nu = 0$, the occupation of the energy modes is zero (c.f. Eq. (3.3.5) with $\nu_k = \nu = 0$). For a small drive strength, the occupation becomes non-zero and is itself very small. We expand the expression for the occupation in terms of the small parameter ν/E_k. Doing so, we find that the occupancy of the eigenmodes behaves as

$$\bar{n}_k \approx \frac{\nu^2}{4E_k^2} \ll 1. \tag{3.6.4}$$

In this regime, the energy E_k is much larger than any other parameter. If the eigenmodes were thermally occupied, we would expect an exponential suppression as a function of energy (c.f. Eq. (3.4.2)). We see that in this regime, the occupation is far from being thermally occupied. However, in this regime E_k is fairly narrow (see Fig. 3.1b)). This leads to an occupation that has a fairly linear dependence and it is possible to fit a Bose-Einstein distribution which leads to high fidelities. When we are close to instability, the behaviour is quite different and here it will be crucial to tune the chemical potential accurately to obtain good fidelities.

As we approach instability, $\nu \approx \omega_0 - 2J$, E_k is small with respect to ν for a considerable range of quasimomenta close to the bottom of the band (see Fig. 3.1b)). In this regime, we expand the occupancy as a function of the small parameter $E_k/\nu \ll 1$ near the bottom of the band. We find that the eigenmode occupancy behaves as

$$\bar{n}_k \approx \frac{\nu}{2E_k} \gg 1. \tag{3.6.5}$$

Comparing to the high-occupancy limit of the thermal distribution, c.f. Eq. (3.4.1), we see that in this limit, our eigenmode occupancy scales similarly to a Bose-Einstein distribution with temperature $T = \nu/2$ and $\mu = 0$. Both occupancies diverge in the same manner. Note that this expansion is only valid at the bottom of the band where $E_k \approx 0$. However, in this regime of parameters, $E_k < \nu$ for all values of quasimomentum. We can therefore keep expanding in powers of E_k/ν to determine how the occupancy scales for higher values of energy. This will tell us how the tail of the occupation dies off. We do the same expansion for a Bose-Einstein distribution with temperature $T = \nu/2$ and $\mu = 0$ to compare how the tails of the occupancy die off. We find

$$\bar{n}_k \approx \frac{\nu}{2E_k} - \frac{1}{2} + \frac{1}{4}\left(\frac{E_k}{\nu}\right) - \frac{1}{16}\left(\frac{E_k}{\nu}\right)^3 + \frac{1}{32}\left(\frac{E_k}{\nu}\right)^5 + \ldots, \quad (3.6.6)$$

$$\bar{n}^{\mathrm{Th}}[E_k, \nu/2, 0] \approx \frac{\nu}{2E_k} - \frac{1}{2} + \frac{1}{6}\left(\frac{E_k}{\nu}\right) - \frac{1}{90}\left(\frac{E_k}{\nu}\right)^3 + \frac{1}{945}\left(\frac{E_k}{\nu}\right)^5 + \ldots. \quad (3.6.7)$$

The powers and signs of our expanded eigenmode occupancy agree with those of the Bose-Einstein distribution, however the coefficients are off. We see that the coefficients of the eigenmode occupancy are bigger than those of the Bose-Einstein distribution. So for larger values of E_k/ν our occupancy will be larger than that of a Bose-Einstein distribution. Our eigenmodes in this regime are not quite thermally occupied. Although the occupancy diverges similarly to a Bose-Einstein distribution for energies close to zero, the higher energy behaviour differs. Table 3.1 gives certain values of the fidelity for different parameters which fall under the regime $\omega_0 \gg J$. We see that even when ν is small, we obtain very high fidelities. The fidelities deteriorate slightly when we are closer to instability. This is due to the fact that the tail of our occupancy is not thermal.

J	ν	T	$\Delta\mu$	$1-F$	photons/site
0.02	0.1	0.499	2.95	$6.40 \cdot 10^{-8}$	0.0025
0.02	0.6	0.499	1.045	$6.40 \cdot 10^{-6}$	0.125
0.02	0.95999	0.480	$4.40 \cdot 10^{-3}$	0.0161	4.12

Table 3.1: Fidelity between the steady-state of our system and a thermal state (c.f. section 3.5 for fidelity and section 3.6 for specific model) for parameters where $\omega_0 \ll J$. We set $\omega_0 = 1$ and choose the hopping rate, J, and the parametric drive strength, ν. The temperatures, T, and chemical potential, μ, are obtained first by fitting to a Bose-Einstein distribution. From the obtained chemical potential, we calculate $\Delta\mu = E_{\min} - \mu$. In this regime, the fidelity is quite good, however, it decreases as we approach instability ($\nu = 0.96$ for chosen J). This is a result of the tail end of the occupancy which differs from a true Bose-Einstein distribution for a longer region as we approach instability. The last column is the average number of photons per lattice site in the large number of site limit. As we increase the drive strength and approach instability, we start obtaining an appreciable number of photons per site. This regime leads to an interesting steady-state: the behaviour is thermal-like and we obtain a sizable number of photons per site.

3.6.2 On-site energy on the order of the hopping rate

Physically, when $\omega_0 \sim 2J$ and $\nu = 0$, this is the regime where the dispersion of the band is very large (on the order of twice the on-site energy) and the bottom of the band approaches zero (see Fig. 3.1a)). To be stable, the parametric drive strength ν must be less than $\omega_0 - 2J \ll \omega_0, J$ which is very small. Thus, in this regime, the squeezing parameter r_k will be heavily suppressed for most of the band and in fact only be appreciable at the bottom of the band.

When we are far from instability, $\nu \approx 0$, and the eigenmode occupancies are roughly zero for the entire band. This regime is uninteresting and the occupancies do not behave thermally.

When we are close to instability, there is a very small range of quasimomenta for which $E_k \approx 0$ and is small compared to ν. For this small range, we expand again with respect to the small parameter E_k/ν and obtain the same result as above: close to instability and $E_k \approx 0$ our occupation diverges as $\nu/2E_k$. Again, this diverges in

the same way as a Bose-Einstein distribution does for $T = \nu/2$ and $\mu = 0$ in the high-occupancy regime. We can also obtain expressions for how the tail of the occupancy behaves (i.e. how it behaves for larger values of energy). There is a large range of quasimomenta for which $E_k \gg \nu$. In this range, we expand the eigenmode occupancies as a function of ν/E_k. We find that the occupancy scales as

$$\bar{n}_k \approx \frac{\nu^2}{4E_k^2} \ll 1. \tag{3.6.8}$$

Once, again, if the modes were thermally occupied, we would expect an exponential suppression for the occupancy (see Eq. (3.4.2)). As we see, our occupancy decays as $1/E_k^2$ for large energies which is very different from a thermal distribution. Table 3.2 shows the fidelity between the steady-state in this regime and a thermal state. We see that when $\omega_0 \sim 2J$ the fidelity is low regardless of the parametric drive strength. Although the fidelity increases as we approach instability, we never achieve high fidelities because of the $1/E_k^2$ decay of the eigenmode occupancies.

We see that for the simplest realization of hopping and parametric driving in a one-dimensional array of cavities, we can never obtain a steady-state where the eigenmodes are purely thermally occupied. However, we can get thermal-like behaviour when we are close to instability across the entire band. This is the case when $\omega_0 \gg 2J$ and $\nu \approx \omega_0 - 2J$. In this case, we get $\bar{n}_k \sim \nu/2E_k \gg 1$, which is very much like a high-temperature thermal distribution with zero chemical potential and temperature $T = \nu/2$.

J	ν	T	$\Delta\mu$	$1-F$	photons/site
0.49	0.001	0.0177	0.116	0.9995	$3.20 \cdot 10^{-5}$
0.49	0.01	0.0166	0.0457	0.9676	0.0036
0.49	0.0199	0.0107	0.0021	0.2604	0.0541

Table 3.2: Fidelity between the steady-state of our system and a thermal state (c.f. section 3.5 for fidelity and section 3.6 for specific model) for parameters where $\omega_0 \sim 2J$. We set $\omega_0 = 1$ and choose the hopping rate, J, and the parametric drive strength, ν. The temperatures, T, and chemical potential, μ, are obtained first by fitting to a Bose-Einstein distribution. From the obtained chemical potential, we calculate $\Delta\mu = E_{\min} - \mu$. In this regime the fidelity error is always large regardless of the drive strength. The last column is the average number of photons per lattice site in the large number of site limit. Even when the bottom of the band is close to instability ($\nu = 0.0199$), the number of photons per site is quite low. This regime does not give an interesting steady-state: we are far from thermal-like behaviour and have a low number of photons per site.

3.7 Nearest-neighbour hopping and fine-tuned parametric driving

We now determine if it is possible to fine-tune the parametric driving ν_k, in quasimomentum space, such that $\bar{n}_k$ is truly equal to a Bose-Einstein distribution for a constant temperature and chemical potential. For simplicity, we only consider the case where the hopping is between nearest-neighbours only. The Hamiltonian describing this system is that of Eq. (3.2.2) where $\epsilon_k = \omega_0 - 2J\cos k$. As previously stated, if such a ν_k exists, then each quasimomentum eigenmode would effectively experience independent, thermal noise.

To see if it possible to obtain such a ν_k, we equate both $\bar{n}_k$ and $\bar{n}^{\mathrm{Th}}[E_k, T, \mu]$ when expressed as a function of ϵ_k (rather than as a function of E_k as in previous sections)

$$\frac{\epsilon_k}{2\sqrt{\epsilon_k^2 - \nu_k^2}} - \frac{1}{2} = \frac{1}{e^{\frac{\sqrt{\epsilon_k^2 - \nu_k^2} - \mu}{T}} - 1}. \tag{3.7.1}$$

To simplify the expression, we define $\tilde{\nu}_k = \nu_k/\epsilon_k$, $\tilde{T}_k = T/\epsilon_k$, and $\tilde{\mu}_k = \mu/\epsilon_k$. We now define $\gamma_k = \sqrt{1-\tilde{\nu}_k^2}$. We keep in mind that this term varies between zero and one, i.e. $\gamma_k \in]0,1[$. $\gamma_k = 1$ represents the uninteresting case where the eigenmode occapancies are zero whereas $\gamma_k = 0$ represents the unphysical case where the occupancies are infinite. For a ν_k to exist such that $\bar{n}_k = \bar{n}^{\mathrm{Th}}[E_k, T, \mu]$, we find that we must satisfy the self-consistent equation

$$\gamma_k = \tanh\left[\frac{\gamma_k - \tilde{\mu}_k}{2\tilde{T}_k}\right]. \tag{3.7.2}$$

We now study two different regimes of $\tilde{\mu}_k$: negative and zero. The case where $\mu > 0$ can result in no solution and so we omit it. Recall that for stability, we have that $\epsilon_k > 0$ for all quasimomentum and so the sign of $\tilde{\mu}_k$ is directly related to the sign of the chemical potential μ. Note that to have the highest occupation, we require γ_k to be as close to zero as possible.

3.7.1 Negative chemical potential

When we allow for a negative value of μ, there will always be a valid solution which has a finite occupation. To obtain numerical solutions, we choose a given μ and a value of ν such that we have a high occupation at the bottom of the band (i.e. we choose ν_0 such that $\bar{n}_0$ is high). We can easily invert the equations above and obtain a value for T. With a chemical potential and temperature at hand, we can now numerically solve Eq. (3.7.1) for ν_k for the remaining values of quasimomentum.

For the highest occupations, we require γ_k as close to zero as possible. Hence, we want the hyperbolic tangent to intercept the y-axis as close to zero as possible. For this to occur, the larger we choose $|\mu|$ the larger T will be. Furthermore, the larger we choose these parameters to be, the more they dominate the whole expression. That is to say, the

variations in ϵ_k will not vary the occupations greatly. By choosing a large occupancy at $k = 0$, solutions for ν_k, when $|\mu|$ is large, generally behave proportionally to ϵ_k. This in turn leads, to small variations in the final dispersion relation E_k, as well as the occupancy. In this regime, $(E[0] - \mu)$ is large and the temperature is much larger than the energy bandwidth.

3.7.2 Zero chemical potential

In the regime where $\tilde{\mu} = 0$, there is always a trivial solution such that $\gamma = 0$, however, this leads to infinite occupation. We focus on the cases where there is another non-trivial solution such that we have a finite occupation. It is interesting to note that in this regime, Eq.(3.7.2) reduces to the self-consistent mean field theory equation for magnetization in the Ising model. To have a non-trivial solution we must meet the same condition for a phase transition in the Ising model:

$$\tilde{T} < \frac{1}{2} \tag{3.7.3}$$

which tells us that

$$T < \frac{\epsilon_k}{2} \tag{3.7.4}$$

for all quasimomentum. The temperature can never exceed the bottom of the band for a valid solution. For the highest occupation, we thus require that $T \to \epsilon_k/2$ which also coincides with half the maximal value of the parametric drive strength before we become unstable. There are now two generic cases depending on the parameters of our non-interacting photon band ϵ_k.

If the on-site energy is much greater than the hopping ($\omega_0 \gg J$), we can initially

choose a high value for ν at the bottom of the band to obtain a high occupation. This in turn gives us a high temperature. Since the hopping term is so small, we also require a high value of the drive strength at the top of the band to obtain a solution. Thus the occupations will be high for the entire band, and the final dispersion relation will have a very small bandwidth. The final thermal distribution will have $(E[0] - \mu) \to 0$ with a temperature which is much greater than the bandwidth. In this regime, the temperature is on the order of ω_0 whereas the bandwidth is on the order of J. Many states will be thermally excited in this regime (see Fig. 3.3).

On the other hand, if the on-site energy is comparable to the hopping ($\omega_0 \approx 2J$) only the bottom of the band will exhibit large populations. In this regime, the temperature will itself be small ($T \ll \omega_0$). When solving for the interaction strength at the top of the band, the only possible solution is a vanishingly small parameter (i.e. $\nu[\pi] \to 0$), thus the energy dispersion will vary from $E_k \in]0, \omega_0 + 2J[$ which is fairly large. The final thermal distribution in this case will also have $(E[0] - \mu) \to 0$, however, the temperature will be much smaller than the bandwidth. This is similar to what happens when we approach a Bose-Einstein condensate phase. The bottom of the band is close to zero energy (corresponding to a small chemical potential when shifting the bands) and the temperature is small compared to the bandwidth. Only low energy modes will be thermally excited in this regime (see Fig. 3.2).

3.7.3 Specific fine-tuning and real-space configuration

Having discussed the different regimes of interest, we now focus on specific parameter values to show how the quasimomentum dependent parametric drive behaves. Figures 3.2b) and 3.3b) show two different solutions. Although these solutions have been obtained numerically, we can approximate their analytical forms quite readily from

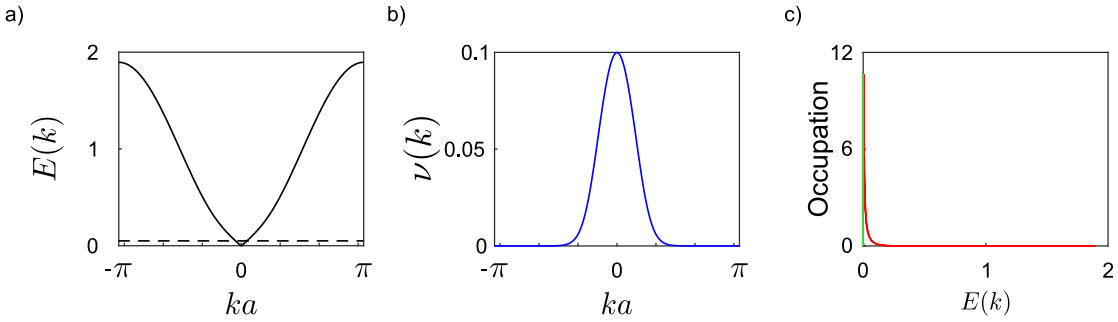

Figure 3.2: Low temperature regime: momentum dependent parametric interaction when $\omega_0 = 1$, $J = 0.45$, $\mu = 0$, $T = 0.05$.(a)Energy dispersion relation which has been shifted such that the bottom of the band is at $E = 0$ and effectively modifying the chemical potential such that $\mu' = \mu - E_{\min}$. The horizontal dashed line represents the value $\mu' + k_{\mathrm{B}}T$: the energy states below this line are thermally excited. (b) Numerical solution for ν_k for the chosen chemical potential and temperature. The form of ν_k can be well approximated by a gaussian function.(b) Bogoliubov occupation for given ν_k which is equivalent to a Bose-Einstein distribution at given chemical potential and temperature. The green line represents the chemical potential when the energies are shifted ($\mu' = -0.0045$)

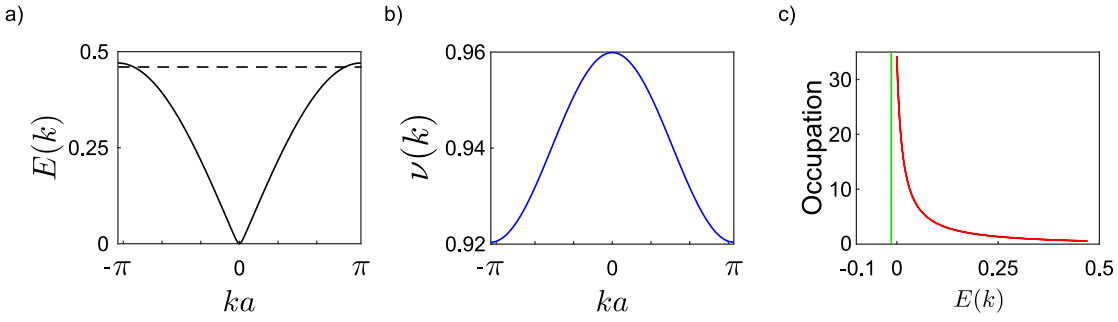

Figure 3.3: Effective thermal regime: momentum dependent parametric interaction when $\omega_0 = 1$, $J = 0.02$, $\mu = 0$, $T = 0.48$.(a) Energy dispersion relation which has been shifted such that the bottom of the band is at $E = 0$ and effectively modifying the chemical potential such that $\mu' = \mu - E_{\min}$. The horizontal dashed line represents the value $\mu' + k_{\mathrm{B}}T$: the energy states below this line are thermally excited. (b) Numerical solution for ν_k for the chosen chemical potential and temperature. The form of ν_k can be well approximated by a sinusoidal function.(b) Bogoliubov occupation for given ν_k which is equivalent to a Bose-Einstein distribution at given chemical potential and temperature. The green line represents the chemical potential when the energies are shifted ($\mu' = -0.0139$)

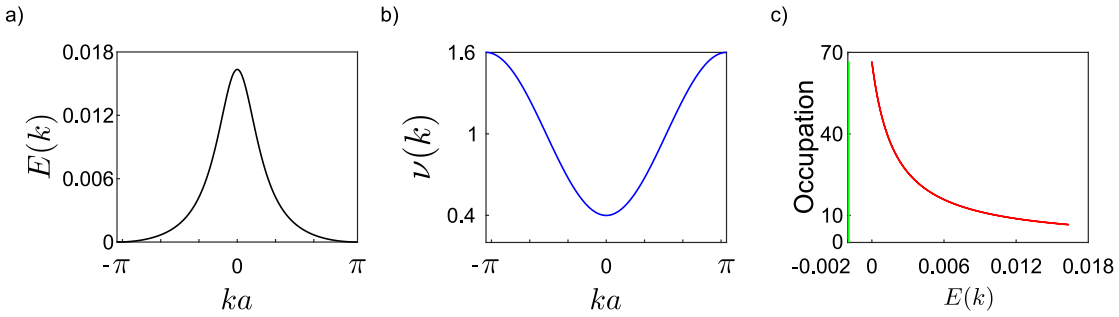

Figure 3.4: Thermal regime: momentum dependent parametric interaction when $\omega_0 = 1$, $J = 0.3$, $\mu = 0.01$, $T = 0.129$.(a) Energy dispersion relation which has been shifted such that the bottom of the band is at $E = 0$ and effectively modifying the chemical potential such that $\mu' = \mu - E_{\min}$. The value $\mu' + k_{\mathrm{B}}T$ is much higher than the maximum energy in this case, and so all states are thermally excited. (b) Numerical solution for ν_k for the chosen chemical potential and temperature. The form of ν_k can be well approximated by a sinusoidal function.(b) Bogoliubov occupation for given ν_k which is equivalent to a Bose-Einstein distribution at given chemical potential and temperature. The green line represents the chemical potential when the energies are shifted ($\mu' = -0.0019$)

the graphs. We now wish to see how feasible it is to recreate these quasimomentum dependent interactions from long-range, non-local parametric interactions.

From Fig. 3.2b), we can approximate ν_k as a gaussian

$$\nu_{\mathrm{approx},k} \approx= a \cdot e^{-bk^2} \tag{3.7.5}$$

where, $a = 0.1$ and $b = 2.62$ are determined from a numerical fit to ν_k. Although this does not completely describe the form of ν_k obtained, it is easily Fourier transformed into real space: it leads to parametric drives which create pairs of photons between all sites with a gaussian weight. The length scale of interest here is b. After roughly three sites, the drive strength become exponentially suppressed. Supposing the best we can do experimentally is to mimic ν_k by $\nu_{\mathrm{approx},k}$, we can once again compute the fidelity between the steady-state of our system with interaction $\nu_{\mathrm{approx},k}$ and its Bose-Einstein counterpart. Doing so, we find that the fidelity is $F = 0.999$ which is

fairly high. Experimentally, we could hope to achieve similar results by having third nearest-neighbour parametric driving with the proper weights

From Fig. 3.2b), we can approximate ν_k as a sinusoidal function

$$\nu_{\text{approx},k} \approx a' + b' \cos k \tag{3.7.6}$$

where again $a = 0.94$ and $b = 0.0197$ are determined from a numerical fit to ν_k. This form of $\nu_{\text{approx},k}$ corresponds to on-site and nearest-neighbour parametric drives where pairs of photons are created on neighbouring sites. Calculating the fidelity as in the previous case, we find $1 - F = 1.7 \cdot 10^{-7}$ which corresponds to a very high fidelity. In fact, by considering the differentials between this $\nu_{\text{approx},k}$ and the numerics, we find that the leading order correction is of the form $c \sin^2 k$ where c is on the order of 10^{-8}.

From these few results, we see that not only is it possible to obtain solutions for ν_k such that our eigenmodes are thermally occupied but we can also find approximate analytical expression which convert to somewhat feasible real-space configurations for parametric drives.

3.8 Conclusion

In this work, we have studied how the steady-state of a one-dimensional array of coupled cavities, subject to parametric driving, is occupied when each site is weakly coupled to a zero-temperature bath. For the simplest case of nearest-neighbour hopping and on-site parametric drive, we have shown that there is no parameter regime in which the steady-state is thermally occupied. We have, however, shown that there are certain regimes where the occupation is thermal-like with high fidelities between the steady-state and a thermal state.

By allowing for the parametric drive to be long-range and non-local, in a translationally invariant way such that photon pairs created have no net quasimomentum in the lattice, while only considering nearest-neighbour hopping we have shown that it is possible to obtain a thermally occupied steady-state. Furthermore, we have shown that these non-local drives can be well approximated by experimentally feasible setups, such as next-nearest-neighbour parametric drives. Using this scheme, it would be possible to initialize a thermal state, in a relatively simple set-up, for photons to potentially study quench dynamics.

References

[1]R. Shindou, R. Matsumoto, S. Murakami, and J.-i. Ohe, Phys. Rev. B **87**, 174427 (2013).

[2]G. Engelhardt, and T. Brandes, Phys. Rev. A **91**, 053621 (2015).

[3]R. Barnett, Phys. Rev. A **88**, 063631 (2013).

[4]C.-E. Bardyn, T. Karzig, G. Refael, and T. C. H. Liew, Phys. Rev. B **93**, 020502 (2016).

[5]V. Peano, M. Houde, C. Brendel, F. Marquardt, and A. A. Clerk, Nat Commun **7**, 10779 (2016).

[6]B. Galilo, D. K. K. Lee, and R. Barnett, Phys. Rev. Lett. **115**, 245302 (2015).

[7]V. Peano, M. Houde, F. Marquardt, and A. A. Clerk, Phys. Rev. X **6**, 041026 (2016).

[8]J. Keeling, F. M. Marchetti, M. H. Szymańska, and P. B. Littlewood, Semiconductor Science and Technology **22**, R1 (2007).

[9]P. R. Eastham, and P. B. Littlewood, Phys. Rev. B **64**, 235101 (2001).

[10]I. Carusotto, and C. Ciuti, Rev. Mod. Phys. **85**, 299–366 (2013).

[11]J. Klaers, J. Schmitt, F. Vewinger, and M. Weitz, Nature **468**, 545 (2010).

[12]J. Klaers, J. Schmitt, T. Damm, F. Vewinger, and M. Weitz, Phys. Rev. Lett. **108**, 160403 (2012).

[13]C. Sun, S. Jia, C. Barsi, S. Rica, A. Picozzi, and J. W. Fleischer, Nature Physics **8**, 470 (2012).

[14]D. W. Snoke, and S. M. Girvin, Journal of Low Temperature Physics **171**, 1–12 (2013).

[15]M. Hafezi, P. Adhikari, and J. M. Taylor, Phys. Rev. B **92**, 174305 (2015).

[16]A. A. Clerk, M. H. Devoret, S. M. Girvin, F. Marquardt, and R. J. Schoelkopf, Reviews of Modern Physics **82**, 1155–1208 (2010).

[17]P. Calabrese, and J. Cardy, Phys. Rev. Lett. **96**, 136801 (2006).

[18]V. Eisler, and I. Peschel, Journal of Statistical Mechanics: Theory and Experiment **2007**, P06005 (2007).

Preface to Chapter 4

In chapter 2, we studied the transport properties of a classical signal in a topological system induced by parametric driving. In this chapter, we study how quantum fluctuations propagate in a similar system. We consider an array of coupled cavities which form a square lattice. By engineering a synthetic gauge field through the hopping phases between the coupled cavities, we generate an effective flux per plaquette of Φ. This is known as the Hofstadter model for photons, which is topological for non-trivial flux. We focus on the case where $\Phi = \pi/2$ and consider additional on-site parametric driving. By tuning the phases of the parametric drive and choosing the frequency of the drive accordingly, we obtain parametrically-unstable chiral edge modes in a finite system, without there being any bulk-mode instabilities. Results show that we can use these properties to achieve a topologically protected, quantum-limited, travelling-wave parametric amplifier. Unlike standard travelling wave parametric amplifiers, our amplifier is protected against internal losses and back-scattering as a consequence of topology.

4

Topological quantum fluctuations and travelling wave amplifiers

Vittorio Peano[1,4], Martin Houde[2], Florian Marquardt[1,3], and Aashish A. Clerk[2]

[1]Institute for Theoretical Physics, University of Erlangen-Nürnberg, Staudtstraße 7, 91058 Erlangen, Germany

[2]Department of Physics and the Centre for Physics of Materials, McGill University, Montreal, Quebec, Canada H3A 2T8

[3]Max Planck Institute for the Science of Light, Günther-Scharowsky-Straße 1/Bau 24, 91058 Erlangen, Germany

[4]Department of Physics, University of Malta, Msida MSD 2080, Malta

This chapter has been published in Physical Review X.

Journal Reference: Physical Review X 6, 041026 (2016)

Abstract

It is now well-established that photonic systems can exhibit topological energy bands; similar to their electronic counterparts, this leads to the formation of chiral edge modes which can be used to transmit light in a manner that is protected against back-scattering. While it is understood how classical signals can propagate under these conditions, it is an outstanding important question how the quantum vacuum fluctuations of the electromagnetic field get modified in the presence of a topological band structure. We address this challenge by exploring a setting where a non-zero topological invariant guarantees the presence of a parametrically-unstable chiral edge mode in a system with boundaries, even though there are no bulk-mode instabilities. We show that one can exploit this to realize a topologically protected, quantum-limited travelling-wave parametric amplifier. The device is naturally protected both against internal losses and back-scattering; the latter feature is in stark contrast to standard travelling wave amplifiers. This adds a new example to the list of potential quantum devices that profit from topological transport.

The quantization of the electromagnetic field introduces a fundamentally new phenomenon into physics: vacuum fluctuations that permeate all of space. These fluctuations were initially seen as a basic unalterable feature of space-time, before it was realized that they could be engineered to great effect. Simply modifying geometric boundary conditions changes the size of the fluctuations as a function of position and frequency, leading to phenomena such as the Purcell enhancement of spontaneous emission. The introduction of nonlinear optical materials gives rise to an even greater level of control, leading to the possibility of squeezed vacuum states [1], with important applications to sensing beyond the limits usually set by quantum mechanics [2–4].

In recent years, new approaches for altering the dynamics of wave fields have gained prominence, based on engineering periodic materials to elicit topological properties. Topologically protected unidirectional wave propagation was originally discovered in the study of 2D electrons in strong magnetic fields, and underlies the robust quantization of the Hall conductance [5]. The engineering of topological photonic materials has been the focus of intense theoretical investigation [6], and various experimental platforms have already been developed [7–10]. Phononic topological states have also attracted recent attention [11–15] and the first experimental steps at the macroscopic scale have been taken [15–17].

Despite this considerable work in topological photonics and phononics, using topology to address the engineering of vacuum fluctuations has not been addressed. Most photonic and phononic topological systems are based on a single particle Hamiltonian which conserves particle number. These topological states mimic well known electronic topological phases such as the Quantum Hall phase [7, 13, 18–25], or the spin Hall phase [10, 16, 26–28] and have a trivial vacuum. In order to modify the properties of the vacuum one has to introduce particle non-conserving terms to the Hamiltonian which can coherently add and remove pairs of particles from the system; these terms have a

formal similarity to pairing terms in the mean-field description of a fermionic superconductor. If the amplitude of these terms is sufficiently weak, the system remains stable; even in this regime, the bosonic nature of the particles makes the topological properties of such Hamiltonians very different from their fermionic (topological superconductor) counterparts [29–32]. An even starker difference occurs when the parametric terms lead to dynamical instabilities [33–35]. These instabilities have no fermionic analogue, and are akin to the parametric instability in an oscillator whose spring constant is modulated in time.

Here, we consider a situation where parametric driving is introduced to a system where photons hop on a lattice in the presence of a synthetic gauge field (see Fig. 1a). We show how to realize an exotic situation where all bulk modes are stable, but where the topologically-protected chiral edge modes that exist in a system with a boundary are unstable. This leads to an unusual spatially-depedent modification of vacuum fluctuations: when the system is stabilized by dissipation, quantum fluctuations in the bulk are only weakly perturbed, whereas those along the system edge are strongly distorted. The result is not just an unusual driven-dissipative quantum state, but also a unique kind of photonic device: as we show in detail, the system serves both as a topologically-protected, non-reciprocal, quantum-limited amplifier, as well as a source of chiral squeezed light. It thus represents a potentially powerful new kind of application of topological materials.

4.1 Identifying unstable modes

Before delving into the details of our proposal, it is useful to discuss the underlying theoretical ideas in a general setting. Our main goal is to exploit topological features of a dynamically unstable Hamiltonian, adding dissipation to realize a non-thermal steady state. In the absence of topological considerations, this is a situation that is

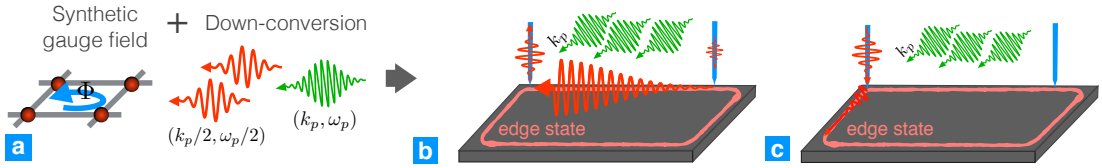

Figure 4.1: Set up figure: (a) Scheme of the basic interactions: (i) Photons hopping anti-clockwise around a plaquette pick up a phase Φ that can be interpreted as a synthetic gauge field flux. (ii) Pump photons with frequency ω_p and quasimomentum k_p are down-converted into a photon pair with frequency $\omega_p/2$ and quasimomentum $k_p/2$. (b-c) Combining the two interactions in a finite geometry allows to engineer a topologically protected quantum-limited amplifier. A signal injected into the device via a tapered fiber propagates unidirectionally along the edge. (b) With the appropriate choice of pump frequency ω_p and quasimomentum k_p, the signal is amplified while it travels along the upper edge. A second tapered fiber detects the amplified signal. (c) When the input and the output fiber are exchanged the signal propagates along a different path where it decays due to the lack of phase matching. This leads to non-reciprocal amplification.

ubiquitous in quantum optics. The simplest bosonic Hamiltonian exhibiting instability is the single-mode squeezing Hamiltonian:

$$\hat{H}_S = \Delta \hat{a}^\dagger \hat{a} + \frac{i}{2}\nu \left(\hat{a}^\dagger \hat{a}^\dagger - \hat{a}\hat{a}\right), \tag{4.1.1}$$

where $\hat{a}$ is a bosonic annihilation operator. Heuristically, $\hat{H}_S$ describes photons in a single cavity mode (effective energy Δ) which are subject to coherent two-particle driving (with amplitude ν). Without dissipation, $\hat{H}_S$ becomes unstable and cannot be diagonalized when the driving amplitude exceeds the energy cost for creating a pair of photons, i.e. when $\nu > |\Delta|$. In this regime, the dynamics corresponds to an ever-growing, exponential accumulation of entangled pairs of bosonic particles: there is no stationary state.

If we now add dissipation, stability can be restored by offsetting the effective two-particle driving described by $\hat{H}_S$ against the decay rate κ of the mode; one requires $\kappa > 2\sqrt{\nu^2 - \Delta^2}$. The result is a non-thermal stationary state having a steady flux of excitations flowing from the driven mode to the dissipative bath (which could be a waveguide serving as an input-output port). This is precisely the situation realized in a

standard parametric amplifier: the linear-response properties of this driven-dissipative steady-state allow for quantum-limited amplification of an additional signal drive. The required two-photon driving in Eq.(4.1.1) is generically realized by using a nonlinearity and parametric down-conversion of a driven pump mode.

Normal mode decomposition of unstable Hamiltonians

With these preliminaries, we now consider a very general quadratic Hamiltonian describing bosons on a lattice subject to parametric driving:

$$\hat{H} = \sum_{\mathbf{k}ss'} \hat{a}^\dagger_{\mathbf{k},s} \mu_{\mathbf{k}ss'} \hat{a}_{\mathbf{k},s'} + \frac{i}{2}\left(\hat{a}^\dagger_{\mathbf{k},s} \nu_{\mathbf{k}ss'} \hat{a}^\dagger_{\mathbf{k_p}-\mathbf{k},s'} - h.c.\right). \tag{4.1.2}$$

Here the ladder operator $\hat{a}_{\mathbf{k},s}$ annihilates a boson with quasimomentum $\mathbf{k}$ in the state s, where $s, s' = 1, \ldots, N$ label polarization and/or sublattice degrees of freedom. The first set of terms describes the hopping of photons on the lattice, and explicitly conserves both particle number and quasimomentum. It could be diagonalized to yield a standard band structure: for each quasimomentum $\mathbf{k}$, we would have N band eigenstates. The second set of parametric driving terms break particle number conservation, and in general also break the conservation of quasimomentum: the two-photon driving injects pairs with a net quasimomentum $\mathbf{k}_\mathrm{p}$, implying that quasimomentum is only conserved modulo $\mathbf{k}_\mathrm{p}$. For a realization based on a driven $\chi^{(2)}$ medium, the two-photon driving terms correspond to the down-conversion of pump photons with quasimomentum $\mathbf{k}_\mathrm{p}$ into a pair of photons with quasimomenta $\mathbf{k}$ and $\mathbf{k}_\mathrm{p} - \mathbf{k}$, respectively. Having a non-zero quasimomentum for injected pairs will be a crucial resource when we attempt to control parametric instabilities.

Analogous to the simple Hamiltonian in Eq.(4.1.1), the lattice Hamiltonian in Eq. (4.1.2) exhibits instabilities when the amplitude for creating a pair of photons exceeds the

energy of the pair. Formally, one can introduce a generalized normal mode decomposition of this generic Hamiltonian which explicitly separates out stable modes and unstable modes. One obtains [see Appendix 4.A]:

$$\hat{H} = \sum_{\mathbf{k}} \sum_{n \in S_{\mathbf{k}}} E_{n,\mathbf{k}} \hat{n}_{n,\mathbf{k}} + \frac{1}{2} \sum_{n \in U_{\mathbf{k}}} \hat{H}_{n,\mathbf{k}}. \tag{4.1.3}$$

For each quasimomentum $\mathbf{k}$ in the first Brillouin zone, we will now have both a set of stable modes (indexed by $n \in S_{\mathbf{k}}$), and a set of unstable modes ($n \in U_{\mathbf{k}}$). The first n-sum in Eq.(4.1.3) describes the stable modes: they are described by canonical bosonic anihiliation operators $\hat{\beta}_{n,\mathbf{k}}$, and enter the Hamiltonian in the standard manner, as a real energy times a number operator $\hat{n}_{n,\mathbf{k}} = \hat{\beta}^{\dagger}_{n,\mathbf{k}} \hat{\beta}_{n,\mathbf{k}}$. The unstable modes can also be described by canonical bosonic anihiliation operators $\hat{\beta}_{n,\mathbf{k}}$. They however enter the Hamiltonian via unstable two-mode squeezing (parametric amplifier) Hamiltonians:

$$\hat{H}_{n,\mathbf{k}} = E_{n,\mathbf{k}}(\hat{n}_{n,\mathbf{k}} - \hat{n}_{n,\mathbf{k_p}-\mathbf{k}}) + i\lambda_{n,\mathbf{k}} \left(\hat{\beta}^{\dagger}_{n,\mathbf{k}} \hat{\beta}^{\dagger}_{n,\mathbf{k_p}-\mathbf{k}} - h.c. \right), \tag{4.1.4}$$

where $E_{n,\mathbf{k}} = -E_{n,\mathbf{k_p}-\mathbf{k}}$ and $\lambda_{n,\mathbf{k}} = \lambda_{n,\mathbf{k_p}-\mathbf{k}}$ are both real. This effective Hamiltonian for the unstable modes has a simple interpretation: pairs of quasiparticles with opposite energies $\pm E_{n,\mathbf{k}}$ are created with an amplitude $\lambda_{n,\mathbf{k}}$. We stress that for any non-zero $\lambda_{n,\mathbf{k}}$, $\hat{H}_{n,\mathbf{k}}$ is unstable (as the total energy for creating the relevant pair of excitations is always zero). The quasiparticle operators $\hat{\beta}^{\dagger}_{n,\mathbf{k}}$ in Eqs.(4.1.3,4.1.4) are a complete set of Bogoliubov ladder operators.

Unstable Hamiltonians for cold atom systems

A few pioneering works have discussed topological unstable Hamiltonians for cold atom systems in 1D [33, 35] and 2D [34]. In this framework, a Hamiltonian of the form of

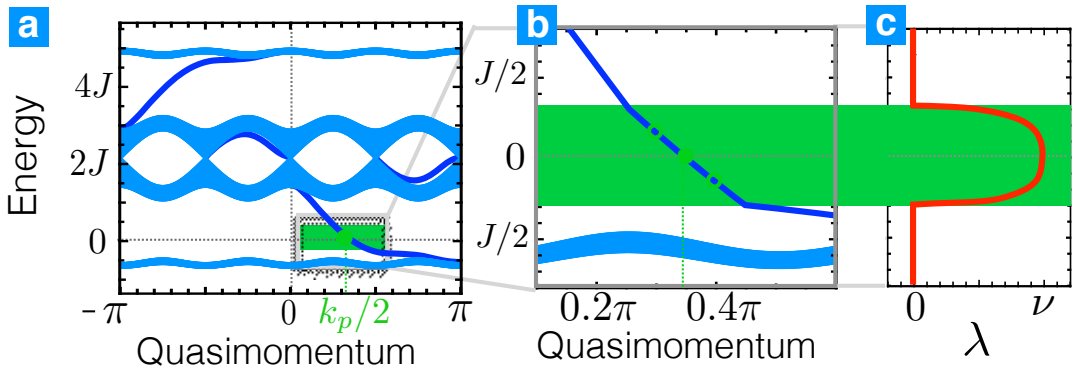

Figure 4.2: Topological Band structure. (a) Band structure of a semi-infinite strip for the Hofstadter model with a flux of $\pi/2$ (when the parametric driving is switched off). The edge states are plotted in dark blue. The energy is counted off from half of the pump photon energy. The solid green circle indicates the tuning of the pump photon quasimomentum k_p required to resonantly excite pairs of down-converted edge state photons with quasimomentum $k_p/2$ (at the quasimomentum $k_p/2$ the edge state should have energy $E = 0$). (b) Zoom of the band structure for a finite laser power. In the unstable energy interval highlighted in green, pairs of Bogoliubov excitations having quasimomenta $k_p/2 \pm \delta k$ are also excited. The corresponding amplification amplitude λ is shown in panel (c) [Parameters: $\omega_0 = 2.15J$, $\Phi = \pi/2$, $k_p = 2.2$. In (b-c) $\nu = 0.08J$]

Eq. (4.1.2) (for $k_p = 0$) emerges when the interactions between atoms in the condensed phase are treated at the mean field level. In particular, Galilo *et. al.* [34] discuss the interesting case of a 2D topological insulator whose only unstable modes are a pair of counter propagating edge states. We emphasize that such unstable Hamiltonians do not describe steady state behaviour, but rather the transient exponential growth of population in the unstable modes after a quench. In contrast, the main focus of our work is on the non-trivial steady state that emerges when similar instabilities are stabilized by controlled dissipation.

4.2 Parametrically driven Hofstadter model

Having established the necessary theoretical framework, we will now show how to engineer a Hamiltonian whose only unstable Bogoliubov modes $\hat{\beta}^{\dagger}_{n,\mathbf{k}}$ are chiral states co-propagating along the physical boundary of a topological system. We consider photons hopping on a 2D square lattice in the presence of a synthetic magnetic field flux, which are also subject to parametric two-photon driving on each site (see Fig. 4.1(c)). Writing the Hamiltonian in the position basis, we have

$$\hat{H} = \sum_{\mathbf{j}} \omega_{\mathbf{j}} \hat{a}^{\dagger}_{\mathbf{j}} \hat{a}_{\mathbf{j}} - \sum_{\langle \mathbf{i},\mathbf{j} \rangle} J_{\mathbf{ij}} \hat{a}^{\dagger}_{\mathbf{i}} \hat{a}_{\mathbf{j}} + \frac{i}{2} \nu \sum_{\mathbf{j}} \left(e^{i\theta_{\mathbf{j}}} \hat{a}^{\dagger}_{\mathbf{j}} \hat{a}^{\dagger}_{\mathbf{j}} - h.c. \right), \tag{4.2.1}$$

where $\hat{a}_{\mathbf{j}}$ is the photon annihilation operator on site $\mathbf{j} = (j_x, j_y)$, and $\omega_{\mathbf{j}}$ are the corresponding onsite energies. As usual, the synthetic gauge field is encoded in the pattern of phases $\phi_{\mathbf{ij}}$ of the nearest-neighbor hopping rates, $J_{\mathbf{ij}} = J \exp(i\phi_{\mathbf{ij}})$. We take the synthetic flux per plaquette to be $\Phi = \pi/2$. Working in the Landau gauge, we then have $\phi_{\mathbf{ij}} = 0$ for vertical hopping and $\phi_{\mathbf{ij}} = -\pi j_y/2$ for rightwards hopping. The parametric driving amplitude on a given site $\mathbf{j}$ is written $\nu e^{i\theta_{\mathbf{j}}}$; we take the phase to vary as $\theta_{\mathbf{j}} = k_p j_x$, implying the injection of pairs with a quasimomentum $\mathbf{k}_{\mathrm{p}} = k_{\mathrm{p}} \mathbf{e}_x$. For a realization based on a driven nonlinear medium, $\nu \propto \sqrt{I_p}$ where I_p is the power of the pump laser, and $k_p \mathbf{e}_x$ would be the quasimomentum of the pump laser photons. Note that a gauge transformation $\hat{a}'_{\mathbf{j}} = \hat{a}_{\mathbf{j}} \exp[i f_{\mathbf{j}}]$ would modify both pattern of phases $\phi_{\mathbf{ij}}$ and $\theta_{\mathbf{j}}$.

When the laser is switched off, $\nu = 0$, and there is no disorder, $\omega_{\mathbf{j}} = \omega_0$, we have the well known Hofstadter model [36]. The band structure of a semi-infinite strip (extending to the lower-half $2D$-plane) is shown in Fig. 4.2a. The continuous bulk band structure consists of four bands (one for each site in the magnetic unit cell). The top and bottom bands are flat Landau levels separated from the two central bands by topological band

gaps. Because of the boundary, one finds inside each topological band gap an edge state (dark line). The net number of these edge states (the number weighted by the sign of their slope) is a topologically protected quantity which does not depend on the shape of the edge and can be calculated from the bulk Hamiltonian [37].

We now turn on the parametric driving such that the resulting Hamiltonian can exhibit instability. Our goal is twofold: we want the system to be unstable *only* if we have a boundary, and in this case, the dominant unstable Bogoliubov modes should be chiral excitations localized at the system's boundary. We do this by choosing the parametric drive parameters so that the only pairs of photons that can be created in an energy and quasimomentum conserving fashion correspond to edge state excitations of the original ($\nu = 0$) model. For concreteness, we will focus on exciting the edge mode in the lower topological band gap (dispersion $\varepsilon_E(k)$). In the lab frame, we will thus tune the pump photon frequency ω_p and quasimomentum k_p so that a single pump photon can be converted into two edge excitations with frequency $\omega_p/2$ and quasimomentum $k_p/2$. In the rotating frame we use to write our Hamiltonians, this requirement reduces to $\varepsilon_E(k_p/2) = 0$. If this resonance condition is met, an arbitrarily weak parametric drive ν will cause instability of the edge mode. The required tuning is shown in Fig. 4.2a.

Because of the approximately linear dispersion relation of the edge mode, the above tuning guarantees that the parametric driving can resonantly create a pair of edge mode photons having momenta $k_p/2 \pm \delta k$, see the hollow circles in Figure 4.2(b). Thus, even for a weak parametric drive amplitude, the edge state will exhibit instability over a range of quasimomenta near $k_p/2$ (corresponding to a finite bandwidth around $\omega_p/2$ in the lab frame), see Figure 4.2(c).

Conversely, the energies of two bulk excitations always add up to a finite value, see Appendix 4.B. In other words, all bulk parametric transitions have a finite detuning. This guarantees the bulk stability (even in the presence of disorder) for a driving amplitude ν

below the minimal value of the bulk detuning.

4.3 Topological non-reciprocal amplifier

Having shown how to realize an unstable topological edge mode, we now want to understand how one can use it. More precisely, we show that a finite size array of nanocavities coupled to simple waveguides can be used as a new kind of topologically-protected, phase-sensitive, quantum-limited amplifier. The role of the waveguides is two-fold: they serve as amplifier input-output ports and they stabilize the dynamics.

We consider a realization of our system using a 30×12 array of nanocavities, and additionally include three coupling waveguides. Each waveguide is coupled to a site at the edge of the sample, as shown in Fig. 4.3a-b. This coupling is described using standard input/output theory, and is entirely characterized by the three rates κ_{in}, κ_{out}, and κ_{sink}, see Appendix 4.C. In addition, we take each cavity to have an internal-loss decay rate κ.

When the small decay rate κ is neglected, and without parametric driving, the array can be operated as an ideal circulator where a signal from any waveguide is entirely transmitted into the next waveguide, see Figure 4.3c. Indeed, it is always possible to match the impedances at each port to cancel the back-reflection by tuning the corresponding coupling rate (κ_{in}, κ_{out}, or κ_{sink}). Once inside the array a wave in a topological band gap has no alternative but to chirally propagate along the edge. In addition, the impedance matching ensures that a wave impinging on a waveguide from the edge channel will be entirely transmitted.

We harness the robust non-reciprocity of this topological circulator to design an amplifier. We use the waveguide on the upper right (left) as input (output) port of the

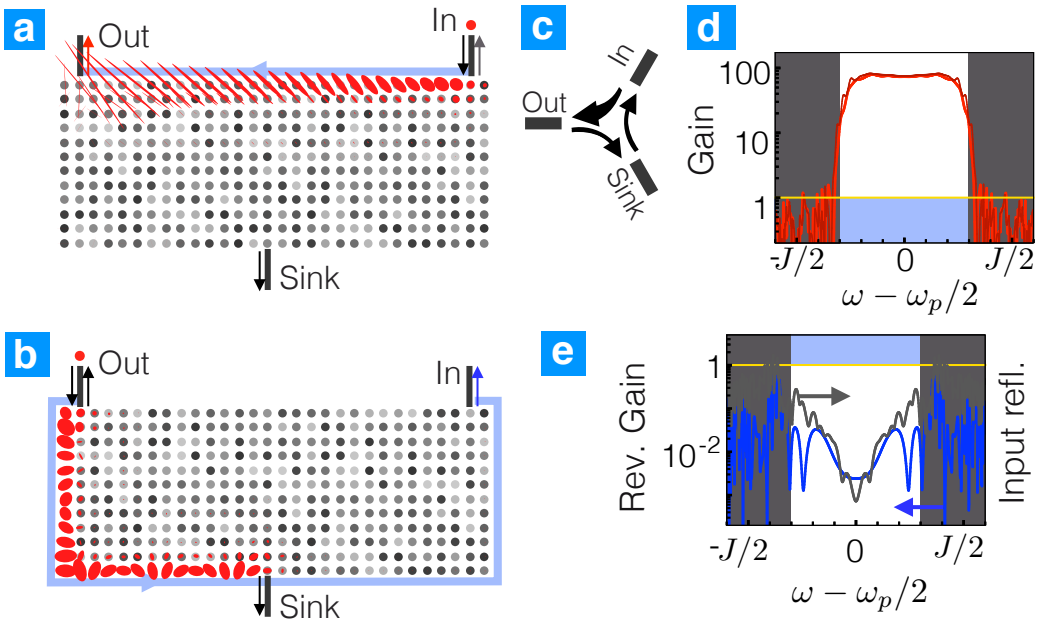

Figure 4.3: Linear response of the topological amplifier. (a-b) The topological amplifier is formed by a 30×12 array of photonic nanocavities. Three of the cavities at the edge of the sample are attached to waveguides, the input and output ports of the amplifier and an additional sink port. (c) The amplifier has the geometry of a circulator. (a-b) The red ellipses represent the linear response of the field inside the photonic array as a function of the incoming signal phase. The signal is injected at the port marked by an inward arrow. (a) A signal injected at the input port propagates unidirectionally toward the output port. The response is strongly phase sensitive, a signal with the right phase is amplified along the way. (d) Transmission power gain for the amplified quadrature as a function of the frequency of the input signal (counted off from half of the pump frequency) for a disordered (light thick line) and a clean sample (dark thin line). The reflection coefficient at the input is shown in panel (e) for the disordered sample. (b) A signal propagating from the output port toward the input port follows a different path and it is not amplified. Moreover, an appropriate matching of the impedances ensures that it leaks out at the sink port. The resulting (small) reverse transmission from the output to the input of the amplifier is the blue curve in panel (e). [Parameters: $\omega_0 = 2.14J$, $\Phi = \pi/2$, $\nu = 0.08J$, $k_p = 2.2$, $\kappa = 0.001J$, $\kappa_{\rm in} = 2.6J$, $\kappa_{\rm out} = 3J$, $\kappa_{\rm sink} = 4.2J$. In the disordered simulations, the offset energies $\delta\omega_{\rm j}$, represented by the greyscale in (a-b), are random numbers in the interval $-0.1J < \delta\omega_{\rm j} < 0.1J$]

amplifier. We choose parametric driving parameters similar as in Fig. 4.2. In the finite geometry, the quasimomentum matching will be approximately realized only on the upper edge. Thus, the amplification occurs mainly in the region between the input and the output port.

The linear response of the amplifier is investigated numerically in Fig. 4.3. A signal injected into the array from the input port propagates chirally until it leaves the array through the output port, see Fig. 4.3a. Depending on its phase, it can be amplified or de-amplified along the way. Treating the amplifier as a phase-sensitive amplifier, we find that the power gain for the amplified signal quadrature is flat over a large bandwidth, corresponding to the frequency range over which the edge state dispersion is purely linear (see panel d). At the same time, any signals incident upon the output port will be almost entirely dumped into the sink port, and not reach the input port, see 4.3b. The residual reverse gain and input reflection are much smaller than unity, see panel e, ensuring the protection of a potentially fragile signal source (e.g. a qubit). Crucially, this strongly non-reciprocal amplifying behavior is of topological origin and is thus robust against disorder. We demonstrate this resilience by including moderate levels of disorder in our simulations (see Fig. 4.3).

Our numerical results are in qualitative agreement with analytical results for a model in which a 1D chiral edge state is coupled to three waveguides, see Appendix 4.D. In this context, we find simple expressions for the impedence matching condition and the maximum power gain

$$\kappa_i = \frac{4v}{|u(j_y = -1)|^2}, \quad G \approx \exp\left[\frac{2\nu L}{v}\right],$$

respectively. Here, $u(j_y)$ is the transverse edge state wavefunction, v is the edge state velocity and L is the number of sites separating the input and the output ports. Thus, we

see that the gain is the exponential of the rate 2ν of creation of down-converted pairs times the time of flight L/v from the input to the output port. While we have focused on operation as a phase-sensitive amplifier, for frequencies different from $\omega_p/2$, one could also use the device as a quantum-limited phase preserving (i.e. non-degenerate) amplifier.

Quantum-limited amplification

The noise floor of our amplifier is determined by the spectral density of the amplified quadrature of the field leaving the output waveguide; see Appendix 4.C for more details. It is plotted in dark (light) red for a clean (disordered) sample in Fig. 4.4a. The quantum limit on a phase-sensitive amplifier is to have zero added noise [38], implying that the noise floor is simply set by the amplification of the vacuum fluctuations entering the input port. The added noise (expressed as an equivalent number of input quanta) is plotted in Fig. 4.4b; despite disorder and noise associated with internal loss, the amplifier is nearly quantum limited over the entire amplification bandwidth.

4.4 Topological stationary state

Next, we investigate the quantum fluctuations in the stationary state that arise from the steady flow of photons from the parametric pump to the amplifier ports in the form of down-converted radiation. Physically, such a flow arises because vacuum fluctuations entering the input port (within the amplification bandwidth) are amplified inside the array before exiting through the output port. The resulting stationary state of each cavity is Gaussian, and can be represented by a Wigner function; these are visualized as a set of noise ellipses in Fig. 4.4c. The non-zero eccentricity of these ellipses indicate that the noise is maximally large in one direction in phase space (corresponding to the

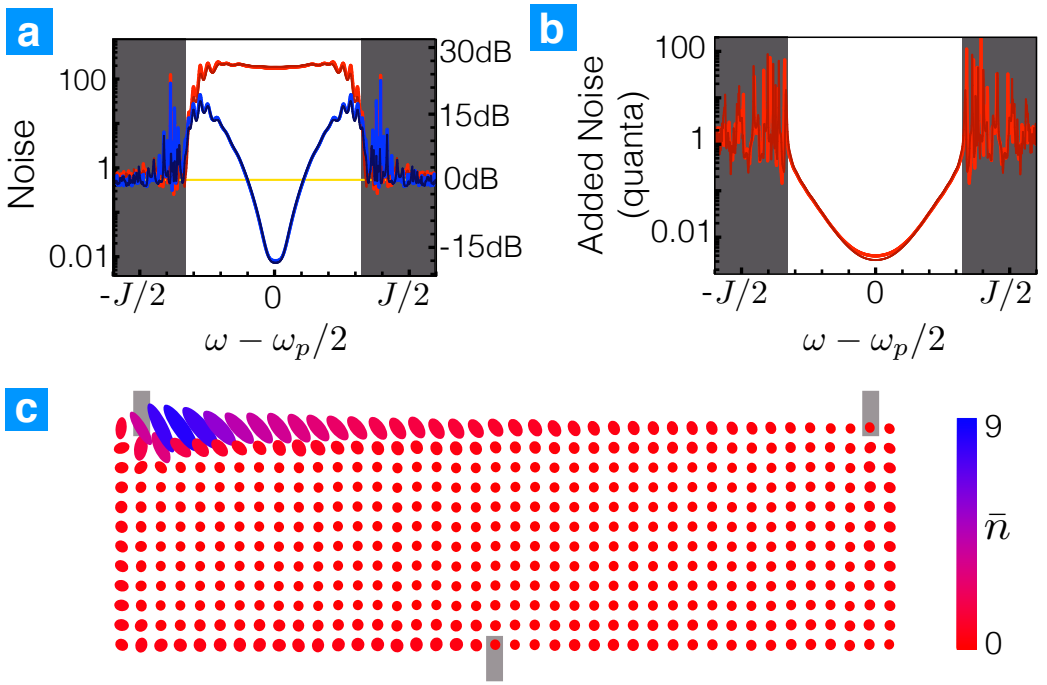

Figure 4.4: Quantum stationary state and noise properties of the topological amplifier. (a) Noise spectral densities for the both the amplified (red) and squeezed (blue) quadratures of the field leaving the output waveguide as a function of frequency, c.f. Eqs.(4.C.9); the noise is plotted in units of quanta (left-hand axis), and also in decibels relative to the vacuum noise level (right-hand axis). The field leaking out of the output waveguide [top left corner in panel (c)] is strongly squeezed. We plot results both for a disordered system (light thick lines) and a clean sample (dark thin lines). The noise in the amplified quadrature is only slightly larger than the quantum-limit value for a phase-preserving amplifier (i.e. the amplified vacuum noise from the input port). The added noise in the amplified quadrature (in units of quanta. c.f. Eq. (4.C.10)) for both a disordered and a clean sample is shown in panel (b). (c) Ellipses representing the Gaussian Wigner function of state of each site *inside* the cavity array (c.f. Eq. (4.C.11)). In the bulk, the ellipses have a circular shape and their area is as small as allowed by the Heisenberg principle, representing a standard vacuum state. In contrast, the ellipses at the edge are anisotropic and have areas larger than the minimum required by the uncertainty principle, implying that one has a thermal squeezed state. This excess noise does not come from a finite temperature of the environment but rather by the amplification of the zero-point fluctuations (quantum heating). Plotted as a color code is also the average number of photons on each site. The grey bars indicate the sites which are attached to coupling waveguides. ([Parameters: 40×12 sites, $\omega_0 = 2.14J$, $\Phi = \pi/2$, $\nu = 0.08J$, $k_p = 2.2$, $\kappa = 0.001J$, $\kappa_{\rm in} = 2.6J$, $\kappa_{\rm out} = 3J$, $\kappa_{\rm sink} = 4.2J$. For the disordered simulations the offset energies $\delta\omega_{\rm j}$ are random numbers in the interval $-0.1J < \delta\omega_{\rm j} < 0.1J$. For all plots, there is only vacuum noise entering from each waveguide.]

amplified quadrature), and a minimum in the orthogonal direction (the de-amplified, or "squeezed" quadrature). Each noise ellipse completely characterizes the steady state of the corresponding site once all remaining sites and the waveguides have been traced out. The areas of the ellipses are constrained from below by the Heisenberg uncertainty principle and assume the minimal possible value for pure states. The bulk sites are all in the trivial quantum groundstate, which is characterized by circular ellipses with the minimal area and zero photons. On the other hand, the eccentricity, the area and the average on-site photon number (color code) grow while moving from the input to the output port along the upper edge (the major axis corresponds to the amplified quadrature). We emphasize that in a thermal equilibrium setting, the area of the ellipses would be equal on all sites and directly reflect the environment temperature. Here, the excess noise of the sites on the upper edge has a quantum origin. This phenomenom has been termed quantum heating [39–41].

Due to quantum heating, the stationary state of each cavity along the edge corresponds to a thermal squeezed state, implying that the de-amplified, or squeezed, quadrature has a larger variance than required by the uncertainty principle. Nonetheless, the frequency-resolved output noise is strongly squeezed below the vacuum level (for frequencies within the amplification bandwidth). Remarkably, the quality of the output squeezing is not deteriorated in the presence of disorder. For the parameters considered here, more than $15\mathrm{dB}$ of output squeezing are predicted both in the case of a clean and a disordered sample, see the blue curves in Fig. 4.4a.

4.5 Implementation

Photonic gauge fields have been already realized in several experimental platforms [7, 9, 10]. The only additional ingredient of our proposal is the parametric pumping with a

finite quasimomentum. In the setup of Ref. [10], one could fabricate the microrings from a nonlinear optical $\chi^{(2)}$ material and drive them with a single laser impinging at a finite angle. The implementation of parametric pumping [32] and synthetic gauge fields [13, 20, 22, 25, 32] is in principle possible in any cavity array platform where a nonlinear resource is available. These include photonic crystals microcavities [42] fabricated from nonlinear optical $\chi^{(2)}$ materials [43–45] or piezoelectric materials, and optomechanical arrays based on optomechanical crystals [46, 47]. An alternate route would be to use lattices of superconducting resonators with embedded Josephson nonlinearities [48]. To that end, we note the recent work by Anderson et al. [49] which outlines a detailed experimental proposal for constructing a square lattice of low-loss 3D cavities with exactly the value of synthetic flux required by our proposal. Crucially, the synthetic flux is obtained without any time-dependent driving. By adding Josephson junctions to this setup (as is also proposed in Ref. [49]), one has an extremely promising venue for realizing the topological amplifier physics discussed here. We also note that very recently, a proposal for realizing topological insulator physics in a classical optical network with nonlinearities was put forward [50]; such a setup could also be adapted to implement our scheme, as it contains all the necessary ingredients.

4.6 Conclusions and outlook

In this work, we have introduced a means to tie the squeezing and amplification of vacuum fluctuations to topological properties of a band structure. Our work represents a new design principle for a non-reciprocal quantum-limited amplifier which has topological protection. Non-reciprocal amplifiers have the potential to revolutionize experiments with superconducting qubits, as they could eliminate the need for ferrite-based circulators and the accompanying insertion losses which limit current experiments. A variety of

(non-topological) designs based on multiple parametric interactions have been proposed recently [51, 52] and even realized experimentally [53, 54], including a travelling wave parametric amplifier (TWPA) built using an array of over 2000 Josephson junctions [55]. In such a conventional TWPA, the reverse transmission is at best unity, and even small amounts of disorder can lead to large amounts of unwanted reflection gain. In contrast, the topological underpinnings of our design ensure reverse transmission and input reflection coefficients that are well below unity even in the presence of disorder. Our design also has advantages over cavity-based approaches, namely the lack of any fundamental constraint on its gain-bandwidth product.

More generally, our topological amplifier differs markedly from other proposed topological devices such as isolators or non-amplifying circulators [6], in that it has some protection against internal losses: in the large gain limit, only the loss (and corresponding noise) in the immediate vicinity of the input port hinder quantum limited operations, as it is only this noise which is amplified to any significant degree (see Appendix 4.D for a quantitative discussion of this point).

In conclusion, our work shows how utilizing the topological properties of an unstable bosonic Hamiltonian provides a new route for both engineering electromagnetic vacuum fluctuations, and correspondingly, constructing a new kind of topologically-protected, non-reciprocal quantum amplifier. It opens the door to future studies, both pursuing other kinds of novel applications, as well as more fundamental issues (e.g. the effects of additional photon-photon interactions in such systems).

Acknowledgements

V.P., C.B., and F.M. acknowledge support by an ERC Starting Grant OPTOMECH, by the DARPA project ORCHID, and by the European Marie-Curie ITN network cQOM.

M.H. and A.A.C. acknowledge support from NSERC. We thank Ignacio Cirac, Sebastian Huber, and André Xuereb for discussion.

4.A Generalized normal mode decomposition

We consider the generic Hamiltonian Eq. (4.1.2). We group all ladder operators with quasimomentum $\mathbf{k}$ in a vector of ladder operators,

$$|\hat{a}_{\mathbf{k}}\rangle = (\hat{a}_{\mathbf{k},1}, \ldots, \hat{a}_{\mathbf{k},N}, \hat{a}^{\dagger}_{\mathbf{k_p}-\mathbf{k},1}, \ldots, \hat{a}^{\dagger}_{\mathbf{k_p}-\mathbf{k},N})^T. \tag{4.A.1}$$

The Heisenberg equation of motion for $|\hat{a}_{\mathbf{k}}\rangle$ reads

$$\frac{d}{dt}|\hat{a}_{\mathbf{k}}\rangle = -i\sigma_{\mathrm{z}} h_{\mathbf{k}} |\hat{a}_{\mathbf{k}}\rangle, \tag{4.A.2}$$

where

$$\sigma_{\mathrm{z}} = \begin{pmatrix} \mathbb{1}_N & 0 \\ 0 & -\mathbb{1}_N \end{pmatrix}$$

and $h_{\mathbf{k}}$ is the Bogoliubov de Gennes Hamiltonian

$$h_{\mathbf{k}} = \begin{pmatrix} \mu_{\mathbf{k}} & i\nu_{\mathbf{k}} \\ -i\nu^{\dagger}_{\mathbf{k}} & \mu_{\mathbf{k_p}-\mathbf{k}} \end{pmatrix}.$$

In the following, we explicitly construct a complete set of Bogoliubov operators $\hat{\beta}_{n,\mathbf{k}}$, leading to the generalized normal mode decomposition Eq. (4.1.3), from the solutions of the eigenvalue problem

$$\sigma_{\mathrm{z}} h_{\mathbf{k}} |\mathbf{k}_{n,l}\rangle = \Lambda_{\mathbf{k},n,l} |\mathbf{k}_{n,l}\rangle. \tag{4.A.3}$$

We note that we need to find only N annihilation operators while the eigenvalue prob-

lem has dimension $2N$. However, the equations for quasimomentum $\mathbf{k_p} - \mathbf{k}$ are not independent from the equations for quasimomentum $\mathbf{k}$. The ones can be obtained from the others by taking the adjoint. This doubling of the degrees of freedom accompanied by an embedded particle-hole symmetry occurs because we are effectively applying a single-particle formalism to a problem where the number of excitations is not conserved.

From Eq. (4.A.3) it is easy to prove that eigenvalues which are not related by complex conjugation $\Lambda_{n,l,\mathbf{k}} \neq \Lambda^*_{n',l',\mathbf{k}}$ have σ_z-orthogonal eigenvectors, $\langle \mathbf{k}_{n,l}|\sigma_\mathrm{z}|\mathbf{k}_{n',l'}\rangle = 0$. Moreover, the eigenvectors with real eigenvalues have a non-zero symplectic norm, $\langle \mathbf{k}_{n,l}|\sigma_\mathrm{z}|\mathbf{k}_{n,l}\rangle \neq 0$ (which can also be negative). We assign the label $l = +$ to the positive norm eigenvectors. We construct a set of orthonormal Bogoliubov creation operators from these positive norm solutions with the definition,

$$\hat{\beta}_{n,\mathbf{k}} \equiv \langle \mathbf{k}_{n,+}|\sigma_z|\hat{a}_\mathbf{k}\rangle. \tag{4.A.4}$$

We note that the scalar product between a standard vector and a vector of operators is an operator. Moreover, we have to normalize the positive vectors $|\mathbf{k}_{n,l}\rangle$ according to $\langle \mathbf{k}_{n,+}|\sigma_\mathrm{z}|\mathbf{k}_{n,+}\rangle = 1$ such that $[\hat{\beta}_{n,\mathbf{k}}, \hat{\beta}^\dagger_{n',\mathbf{k}}] = \delta_{nn'}$. By taking the time derivative of Eq. (4.A.4) and plugging Eq. (4.A.2) and the adjoint of Eq. (4.A.3) we immediately find

$$\dot{\hat{\beta}}_{n,\mathbf{k}} = -i\langle \mathbf{k}_{n,+}|\sigma_z\sigma_z h_\mathbf{k}|\hat{a}_\mathbf{k}\rangle = -i\Lambda_{n,+,\mathbf{k}}\hat{\beta}_n$$

Thus, $\hat{\beta}_{n,\mathbf{k}}$ is the annihilation operator of a harmonic oscillator with energy $E_{n,\mathbf{k}} = \Lambda_{n,+,\mathbf{k}}$. In the same way, one could construct a set of creation operators $\hat{\beta}^\dagger_{n,\mathbf{k_p}-\mathbf{k}}$ from the negative norm eigenvectors $|\mathbf{k}_{n,-}\rangle$. However, it is possible to focus only on the positive norm solutions because of the particle-hole symmetry: the information encoded in the negative norm solutions $|\mathbf{k}_{n,-}\rangle$ is also encoded in the positive norm solutions $|(\mathbf{k_p} - \mathbf{k})_{n,+}\rangle$.

The remaining eigenvectors have zero norm, $\langle \mathbf{k}_{n,\pm}|\sigma_{\rm z}|\mathbf{k}_{n,\pm}\rangle = 0$. They appear whenever the Hamiltonian is unstable. In this case, the matrix $\sigma_z h_{\mathbf{k}}$ has pairs of complex conjugated eigenvalues $\Lambda_{n,+,\mathbf{k}} = \Lambda^*_{n,-,\mathbf{k}}$. For concreteness, we indicate with the label $+$ the eigenvalues with positive imaginary part. The pair of eigenvectors $|\mathbf{k}_{n,\pm}\rangle$ are not ortoghonal to each other, $\langle \mathbf{k}_{n,+}|\sigma_{\rm z}|\mathbf{k}_{n,-}\rangle \neq 0$. In this case, we define a pair of commuting ladder operators as,

$$\hat{\beta}_{n,\mathbf{k}} \equiv \frac{1}{\sqrt{2}}\left(\langle \mathbf{k}_{n,-}| + i\langle \mathbf{k}_{n,+}|\right)\sigma_z|\hat{a}_{\mathbf{k}}\rangle, \tag{4.A.5}$$

$$\hat{\beta}^\dagger_{n,\mathbf{k_p-k}} \equiv \frac{1}{\sqrt{2}}\left(\langle \mathbf{k}_{n,-}| - i\langle \mathbf{k}_{n,+}|\right)\sigma_z|\hat{a}_{\mathbf{k}}\rangle. \tag{4.A.6}$$

The bosonic commutation relations are recovered by requiring the normalization $\langle \mathbf{k}_{n,-}|\sigma_{\rm z}|\mathbf{k}_{n,+}\rangle = i$. By taking the time derivative of Eq. (4.A.5) and using Eq. (4.A.2), the transpose of Eq. (4.A.3), and Eq. (4.A.6) we find

$$\dot{\hat{\beta}}_{n,\mathbf{k}} = -i\mathrm{Re}[\Lambda_{n,+,\mathbf{k}}]\hat{\beta}_{n,\mathbf{k}} + \mathrm{Im}[\Lambda_{n,+,\mathbf{k}}]\hat{\beta}^\dagger_{n,\mathbf{k_p-k}}.$$

Likewise, we find

$$\dot{\hat{\beta}}^\dagger_{n,\mathbf{k_p-k}} = -i\mathrm{Re}[\Lambda_{n,+,\mathbf{k}}]\hat{\beta}^\dagger_{n,\mathbf{k_p-k}} + \mathrm{Im}[\Lambda_{n,+,\mathbf{k}}]\hat{\beta}_{n,\mathbf{k_p-k}}.$$

The corresponding Hamiltonian is the two-mode squeezing Hamiltonian (Eq.(4.1.4)) with energies $E_{n,\mathbf{k}} = -E_{n,\mathbf{k_p-k}} = \mathrm{Re}[\Lambda_{n,+,\mathbf{k}}]$ and amplification amplitude $\lambda_{n,\mathbf{k}} = \mathrm{Im}[\Lambda_{n,+,\mathbf{k}}]$.

When the matrix $\sigma_z h$ is diagonalizable, the set of Bogoliubov annihilation operators defined in Eqs. (4.A.4) and (4.A.5) is complete. The pathological case where the matrix $\sigma_z h$ is not diagonalizable occurs only exactly at the threshold of an instability.

4.B Details of the calculation of the band structure

Stability of the bulk Hamiltonian

In the main text, we have explained that a bosonic Hamiltonian with anomalous pairing terms is unstable when it allows the creation of a pair of Bogoliubov excitations without any net energy change. In other words, the sum of two quasiparticle energies should be zero. We have also claimed that for the parameters of Figure 2 the bulk Hamiltonian is stable because no combination of bulk states whose energies add up to zero exists. This is not immediately obvious from the plot of the standard band structure. In order to visually illustrated the absence of such combination of bulk states one has rather to plot the corresponding Bogolibov de Gennes band structure, see Fig. 4.5. For each value of k_x, the latter is formed by both the quasiparticle energies E_{n,k_x} (blue bands) as well as the energies $-E_{n,k_p-k_x}$ (grey bands). In analogy to the descriptions of quasiparticles in fermionic superconductors, one refers to the former (latter) as the particle (the hole) bands of the system. The absence of crossings between particle and hole bands for the chosen pump laser frequency implies that there is no combination of a pair of bulk quasiparticles whose energies add up to zero while at the same time the corresponding quasimomenta add up to k_p. In the limit of vanishing parametric driving ($\nu = 0$), the minimal distance between particle and hole bands is the minimal detuning of a parametric transition involving two bulk states.

In the presence of weak disorder, there is no selection rule for the quasimomenta of the pair of quasiparticles created in a parametric transition. Nevertheless, all possible parametric transitions are still detuned because the band gap separating particle and hole bands is not merely locally defined (for a fixed k_x) but rather extends to the whole Brillouin zone. Thus, the stability of the bulk Hamiltonian is a robust feature.

As explained in Appendix 4.A, the Bogoliubov de Gennes band structure can be

calculated by diagonalizing the matrix $\sigma_z h(k_x)$ where $h(k_x)$ is the first-quantized Bogoliubov de Gennes Hamiltonian equivalent to the second quantized Hamiltonian Eq. (5) of the main text in the presence of periodic boundary conditions both in the x- and y-directions.

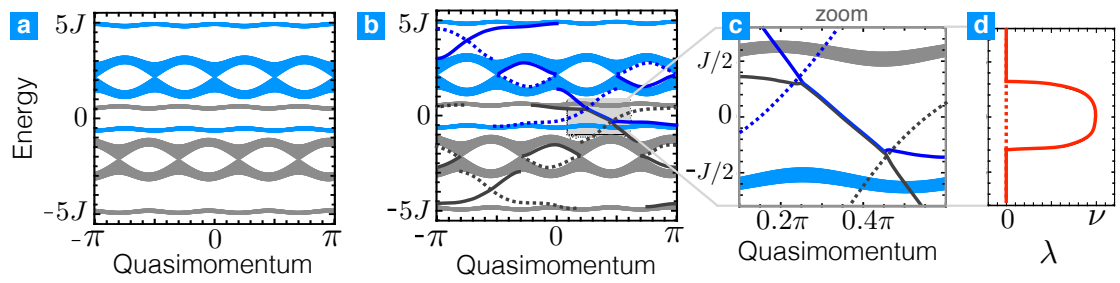

Figure 4.5: Bogoliubov de Gennes band structures. (a) BdG band structure for a system without boundaries. Here and in (b-c), the particle (hole) bands are plotted in blue (grey). The stability of the bulk is protected by the complete band gaps separating neighboring particle and hole bands. (b-c) BdG band structure of a finite strip of width $M = 40$ magnetic unit cells. The upper (lower) edge states are represented as thick solid (dashed) lines. (d) Corresponding amplification amplitudes λ_n. The parameters are the same as for Figure 2 of the main text [$\omega_0 = 2.15J$, $\Phi = \pi/2$, $k_p = 2.2$, $\nu = 0.08J$].

Band structure of a strip

Figure 2 of the main text represents the band structure and the amplification amplitudes of a semi-infinite strip. Those have been derived from the the Bogoliubov de Gennes band structure and the amplification rates of a strip with two physical edges as explained below.

We have simulated a finite strip of width $M = 40$ magnetic unit cells. For each value of the quasimomentum k_x, the set of energies E_{n,k_x} and $-E_{n,k_p-k_x}$ forming the BdG band structure and the corresponding amplification rates $\lambda_n(k_x)$ are calculated by diagonalizing the relevant $4M \times 4M$ matrix $\sigma_z h(k_x)$. While strictly speaking the energy spectrum is discrete, the spacing between subsequent bulk states is not visible

on the figure scale. The resulting band structure [panels (b-c)] and the corresponding amplification rates [panel (d)] are shown in Fig. 4.5. By inspecting the corresponding wavefunctions one can easily distiguish between particle and hole bands (plotted in blue and grey, respectively), edge and bulk states (plotted by the thick dark and thin light lines, respectively) and upper- and lower-edge states (solid and dashed lines, respectively).

Since the hole bands are not independent from the particle bands and refer to the same set of normal modes, we have not displayed the hole energies in the plots in the main text. Moreover, we have shown only the edge states localized on the upper edge. Removing the edge states localized on the lower edge effectively corresponds to plotting the band structure of a semi-infinite strip extending to the lower half plane.

We note that the particle (hole) edge states cross the hole (particle) band. Thus, a pair formed by an edge and a bulk excitation can in principle also be resonantly excited. However, the corresponding matrix element is very small and the resulting amplification rate is not visible on the scale of the figure.

Analytical derivation of Edge state dispersion and amplification rate

Here, we outline a direct derivation of the edge state dispersion for a semi-infinite strip.

We first, consider the case where the parametric driving is switched off ($\nu = 0$). This first part of the derivation follows the approach of Ref. [56]. The Hamiltonian in terms of the annihilation operators $\hat{a}_{j_y,k_x}$ of a plane wave with quasimomentum k_x on the $|j_y|$-th row reads

$$\begin{aligned}\hat{H} &= \sum_{j_y,k_x} \left(\omega_0 - 2J\cos(k_x + \pi j_y/2)\right) \hat{a}^\dagger_{j_y,k_x}\hat{a}_{j_y,k_x} \\ &\quad -J\left(\hat{a}^\dagger_{j_y-1,k_x}\hat{a}_{j_y,k_x} + \hat{a}^\dagger_{j_y,k}\hat{a}_{j_y-1,k_x}\right). \end{aligned} \tag{4.B.1}$$

Since, the strip extends to the lower-half plane the j_y-th sum runs over the negative integers. By definition of the normal modes $\hat{\alpha}_{n,k_x}$ and eigenenergies $E_n[k_x]$ we have $\hat{H} = \sum_{n,k_x} E_n[k_x]\hat{\alpha}^\dagger_{n,k_x}\hat{\alpha}_{n,k_x}$, or equivalently $[\hat{\alpha}_{n,k_x}, \hat{H}] = E_n[k_x]\hat{\alpha}_{n,k_x}$. By plugging the ansatz $\hat{\alpha}^\dagger_{n,k_x} = \sum_{j_y} u_{n,k_x}[j_y]\hat{a}^\dagger_{j_y,k_x}$, we arrive to the first-quantized time-independent Schrödinger equation which we set in the matrix form,

$$\begin{aligned}\begin{pmatrix} u_{n,k_x}[j_y-1] \\ u_{n,k_x}[j_y] \end{pmatrix} &= \tilde{M}_{j_y}(\epsilon_n[k_x]) \begin{pmatrix} u_{n,k_x}[j_y] \\ u_{n,k_x}[j_y+1] \end{pmatrix} \\ = \begin{pmatrix} -\epsilon_n[k_x] - 2\cos(k_x + \pi j_y/2) & -1 \\ 1 & 0 \end{pmatrix} &\begin{pmatrix} u_{n,k_x}[j_y] \\ u_{n,k_x}[j_y+1] \end{pmatrix}. \end{aligned} \tag{4.B.2}$$

Here, we have defined $\epsilon_n[k_x] = (E_n[k_x] - \omega_0)/J$. In principle, the above equation holds only for $j_y \leq -2$ but not for $j_y = -1$ because there is no row corresponding to $j_y = 0$. One can circumvent this problem by formally adding the row $j_y = 0$ together with the boundary condition $u_{n,k_x}[0] = 0$. Thus, one immediately finds

$$\begin{pmatrix} u_{n,k_x}[j_y] \\ u_{n,k_x}[j_y-1] \end{pmatrix} = \prod_{|j'_y|<|j_y|} \tilde{M}_{j'_y}(\epsilon_n[k_x]) \begin{pmatrix} u_{n,k_x}[-1] \\ 0 \end{pmatrix}. \tag{4.B.3}$$

Next, we focus on the edge state solutions. In the following, we drop the subscript n because there is only one edge state in each band gap, see below. For the edge states we have to enforce the boundary condition

$$\lim_{j_y \to -\infty} u_{k_x}[j_y] = 0 \tag{4.B.4}$$

Equivalently, one can require

$$\lim_{m\to\infty} \begin{pmatrix} u_{k_x}[-4m-1] \\ u_{k_x}[-4m] \end{pmatrix} = \lim_{m\to\infty} (M(\epsilon[k_x]))^m \begin{pmatrix} u_{k_x}[-1] \\ 0 \end{pmatrix} = 0. \tag{4.B.5}$$

where $M(\epsilon[k_x])$ is the transfer matrix by a full magnetic unit cell (four sites),

$$M(\epsilon[k_x]) = \tilde{M}_{-4}(\epsilon[k_x])\tilde{M}_{-3}(\epsilon[k_x])\tilde{M}_{-2}(\epsilon[k_x])\tilde{M}_{-1}(\epsilon[k_x]). \tag{4.B.6}$$

Equation (4.B.5) is fullfilled if and only if the vector $(1, 0)$ is an eigenvector of the 4-site transfer matrix $M(\epsilon[k_x])$ whose eigenvalue has modolous smaller than unity. In other words, the edge state dispersion is determined by the conditions,

$$\begin{aligned} M_{2,1}(\epsilon[k_x]) &= -\epsilon(-4+\epsilon^2+2\cos[2k_x]) \\ &\quad +2\cos[k_x](\epsilon^2-4\sin[k_x]^2) = 0, \end{aligned} \tag{4.B.7}$$

$$\begin{aligned} |M_{1,1}(\epsilon[k_x])| &= |\epsilon^4-7\epsilon^2-2\epsilon(\cos[k_x]+\sin[k_x]) \\ &\quad +3+2\sin[2k_x]-4\cos[4k_x]| < 1. \end{aligned} \tag{4.B.8}$$

Equation (4.B.7) is a third order polynomial in the dimensionless energy ϵ. Thus, it has three roots for each value of k_x. Each root corresponds to a solution inside one of the three band gaps (lower, middle, or upper). By plugging the analytical expression of each root of Equation (4.B.7) into Equation (4.B.8) we find the range of k_x where the corresponding edge state is defined: the interval $-\pi < k_x < 0$ for the upper edge state, $0 < k_x < \pi$ for the lower edge state, and the two intervals $-\pi/2 < k_x < 0$

and $\pi/2 < k_x < \pi$ for the edge state in the local band gap between the two central bands. In order to enforce the bosonic commutation relations $[\hat{\alpha}_{k_x}, \hat{\alpha}^\dagger_{k_x}] = 1$, we have to appropriately normalize the single-particle wavefunctions $\sum_{j_y} |u_{k_x}[j_y]|^2 = 1$. This condition fixes the modulus of the wavefunction on the initial site $u_{k_x}[-1]$. The complex phase of $u_{k_x}[-1]$ is arbitrary. For concreteness, we choose $u_{k_x}[-1]$ to be real.

Next, we show how the edge state is modified by the parametric pump. The pump drive written in terms of the annihilation operators $\hat{a}_{j_y,k_x}$ reads,

$$\hat{H}_{\text{pump}} = i\frac{\nu}{2}\sum_{j_y,k_x}\left(\hat{a}^\dagger_{j_y,k_x}\hat{a}^\dagger_{j_y,k_p-k_x} - \hat{a}_{j_y,k_x}\hat{a}_{j_y,k_p-k_x}\right). \tag{4.B.9}$$

Before pursuing an exact numerical solution we adopt a semi-analytical treatment. We focus on the lower band gap edge state which is resonantly driven for the parameters of Fig. 2 of the main text. As in the main text, we consider the case where the frequency and quasimomentum of the pump laser are chosen to resonantly excite pair of edge photons with quasimomentum $k_p/2$,

$$\omega_0 = -J\varepsilon[k_p/2]. \tag{4.B.10}$$

In this case, it is convenient to introduce the quasimomentum $\delta k = k_x - k_p/2$ counted off from $k_p/2$. We rewrite the full Hamiltonian (including the pump) in terms of the ladder opperators of the eigenstates of the Hofstadter Hamiltonian (without the pump). We focus on the edge state's ladder operators $\hat{\alpha}_{\delta k}$ and neglect pump interactions which include bulk modes and the other edge modes (the dominating interacting is that which resonantly

excites pair of edge state photons). Doing so, we find $H^{(\mathrm{edge})} = \sum_{\delta k} H^{(\mathrm{edge})}_{\delta k}/2$

$$\begin{aligned} H^{(\mathrm{edge})}_{\delta k} &= \tilde{E}_n(\delta k)(\hat{\alpha}^\dagger_{\delta k}\hat{\alpha}_{\delta k} - \hat{\alpha}^\dagger_{-\delta k}\hat{\alpha}_{-\delta k}) \\ &\quad +\Delta[\delta k](\hat{\alpha}^\dagger_{\delta k}\hat{\alpha}_{\delta k} + \hat{\alpha}^\dagger_{-\delta k}\hat{\alpha}_{-\delta k}) \\ &\quad +iV[\delta k]\left(\hat{\alpha}^\dagger_{\delta k}\hat{\alpha}^\dagger_{-\delta k} - \hat{\alpha}_{\delta k}\hat{\alpha}_{-\delta k}\right). \end{aligned} \tag{4.B.11}$$

Here, we have expanded the edge state energy (B10) around $k_p/2$ and grouped all excitation conserving terms into two contributions whose amplitudes $\tilde{E}_n(\delta k)$ and $\Delta_n(\delta k)$ are an odd and even function of δk, repectively,

$$\tilde{E}_n(\delta k) = J\sum_{n\geq 1} \frac{\mathrm{d}^{2n-1}\varepsilon}{\mathrm{d}k_x^{2n-1}}\Big|_{k_p/2} \frac{\delta k^{2n-1}}{(2n-1)!} \tag{4.B.12}$$

$$\Delta(\delta k) = J\sum_{n\geq 1} \frac{\mathrm{d}^{2n}\varepsilon}{\mathrm{d}k_x^{2n}}\Big|_{k_p/2} \frac{\delta k^{2n}}{(2n)!}. \tag{4.B.13}$$

Note that $\Delta(\delta k)$ is the quasimomentum dependent detuning of the parametric transition creating pairs of photons with quasimomentum $k_p/2 \pm \delta k$. The corresponding parametric coupling, expressed in terms of the edge state wavefunction, is given by

$$V(\delta k) = \nu \sum_{j_y} u_{\delta k}[j_y]u_{-\delta k}[j_y]. \tag{4.B.14}$$

Next, we expand the above formula in powers of δk. The leading term is ν because the wavefunctions $u_{\delta k}$ are normalized. Moreover, V is obviously an even function of δk (it is invariant if δk is replaced by $-\delta k$). Thus, the expansion has the form

$$V(\delta k) = \nu - \sum_{n\geq 1} \nu_n \delta k^{2n}. \tag{4.B.15}$$

The edge state is unstable over the finite quasimomentum interval where $V(\delta k) > |\Delta(\delta)|$.

Following the general procedure presented in Appendix 4.A, we find the eigenenergies and amplification amplitude of the Bogoliubov edge state normal modes

$$E(\delta k) = \tilde{E}(\delta k), \quad \lambda(\delta k) = \sqrt{V(\delta k)^2 - \Delta(\delta k)^2}. \tag{4.B.16}$$

and

$$E(\delta k) = \tilde{E}(\delta k) + \sqrt{\Delta(\delta k)^2 - V(\delta k)^2}. \tag{4.B.17}$$

in the unstable and stable quasimomentum ranges, respectively.

We can recover the edge state dispersion and lineshape of the amplification amplitude obtained numerically and shown in Fig 2 of the main text by keeping the leading order contributions in Eqs. (4.B.12,4.B.13,4.B.15),

$$V(\delta k) \approx \nu - \nu_1 \delta k^2 \quad \nu_1 = 0.014, \tag{4.B.18}$$

$$\tilde{E}(\delta k) \approx v\delta k, \quad \frac{v}{J} = \frac{\mathrm{d}\varepsilon}{\mathrm{d}k_x}\Big|_{k_p/2} = -1, \tag{4.B.19}$$

$$\Delta(\delta k) \approx J\frac{\mathrm{d}^2\varepsilon}{\mathrm{d}k_x^2}\Big|_{k_p/2}\frac{\delta k^2}{2}, \quad \frac{\mathrm{d}^2\varepsilon}{\mathrm{d}k_x^2}\Big|_{k_p/2} = 1.4. \tag{4.B.20}$$

4.C Input-output formalism

We include the effects of dissipation using the standard input-output formalism [1]. Each site is described by the Langevin equation

$$\dot{\hat{a}}_{\mathbf{j}} = i[\hat{H}, \hat{a}_{\mathbf{j}}] - \kappa_{\mathbf{j}}\hat{a}_{\mathbf{j}}/2 + \sqrt{\kappa_{\mathbf{j}}}\hat{a}_{\mathbf{j}}^{(\mathrm{in})}. \tag{4.C.1}$$

Here, $\kappa_{\mathbf{j}}$ is the decay rate on site $\mathbf{j}$. On the sites coupled to waveguides, the decay rates κ_{in}, κ_{out}, and κ_{sink} are induced by the coupling to the waveguides and are chosen to achieve impedance matching. In this case, the input fields $\hat{a}_{\mathbf{j}}^{(\mathrm{in})}$ describe the field impinging on

site $\mathbf{j}$ from the corresponding waveguide including the field vacuum fluctuations. The field $\hat{a}_{\mathbf{j}}^{(\mathrm{out})}$ leaking out of the waveguide is given by the input-output relations

$$\hat{a}_{\mathbf{j}}^{(out)} = \hat{a}_{\mathbf{j}}^{(in)} - \sqrt{\kappa_{\mathbf{j}}}\hat{a}_{\mathbf{j}}. \tag{4.C.2}$$

On the remaining sites (i.e. those not coupled to waveguides), we assume a small uniform decay rate κ ($\kappa_{\mathbf{j}} = \kappa$) corresponding to internal loss; $\hat{a}_{\mathbf{j}}^{(\mathrm{in})}$ describes the corresponding incident vacuum fluctuations associated with this loss port.

The linear response and the noise properties of the array are simple functions of the retarded Green's functions

$$\tilde{G}_E(\omega, \mathbf{j}, \mathbf{j}') = -i\int_{-\infty}^{\infty} dt\Theta(t)e^{i\omega t}\langle[\hat{a}_{\mathbf{j}}(t), \hat{a}_{\mathbf{j}'}^{\dagger}(0)]\rangle, \tag{4.C.3}$$

$$\tilde{G}_I(\omega, \mathbf{j}, \mathbf{j}') = -i\int_{-\infty}^{\infty} dt\Theta(t)e^{i\omega t}\langle[\hat{a}_{\mathbf{j}}^{\dagger}(t), \hat{a}_{\mathbf{j}'}^{\dagger}(0)]\rangle. \tag{4.C.4}$$

We calculate the above Green's functions numerically for a finite array.

Response Ellipses

In Fig. 4.3a (Fig. 4.3b) we show the linear response of the pair of quadratures

$$\begin{aligned}\hat{X}_{\mathbf{j}} &= \frac{1}{\sqrt{2}}\left(e^{i\theta_{\mathbf{j}}/2}\hat{a}_{\mathbf{j}}^{\dagger}(t) + e^{-i\theta_{\mathbf{j}}/2}\hat{a}_{\mathbf{j}}(t)\right), \\ \hat{Y}_{\mathbf{j}} &= \frac{i}{\sqrt{2}}\left(e^{i\theta_{\mathbf{j}}/2}\hat{a}_{\mathbf{j}}^{\dagger}(t) - e^{-i\theta_{\mathbf{j}}/2}\hat{a}_{\mathbf{j}}(t)\right).\end{aligned} \tag{4.C.5}$$

to a classical field of frequency $\omega_p/2$ injected at the input (output) port as a function of the field phase ϑ,

$$\langle\hat{a}_{\mathbf{j}'}^{(in)}\rangle = \sqrt{\kappa_{\mathbf{j}'}}e^{i\vartheta},$$

$\mathbf{j}'$ indicates the site attached to the relevant injection waveguide ($\mathbf{j}' = \mathbf{j}_{\rm in}$ for Fig. 4.3a, $\mathbf{j}' = \mathbf{j}_{\rm out}$ for Fig. 4.3b). The response on each site is represented by the ellipse

$$\begin{pmatrix} \langle \hat{X}_{\mathbf{j}} \rangle \\ \langle \hat{Y}_{\mathbf{j}} \rangle \end{pmatrix} = \begin{pmatrix} \cos\gamma_{\mathbf{jj}'} & -\sin\gamma_{\mathbf{jj}'} \\ \sin\gamma_{\mathbf{jj}'} & \cos\gamma_{\mathbf{jj}'} \end{pmatrix} \begin{pmatrix} r^{+}_{\mathbf{jj}'}\cos(\vartheta - \eta_{\mathbf{jj}'}) \\ r^{-}_{\mathbf{jj}'}\sin(\vartheta - \eta_{\mathbf{jj}'}) \end{pmatrix},$$

where

$$r^{\pm}_{\mathbf{jj}'} = \kappa_{\mathbf{j}'}\left(|\tilde{G}_E(0,\mathbf{j},\mathbf{j}')| \pm |\tilde{G}_I(0,\mathbf{j},\mathbf{j}')|\right)$$

are the major and minor semiaxes of the ellipse, and

$$\gamma_{\mathbf{jj}'} = \arg\left(\frac{G_E(0,\mathbf{j},\mathbf{j}')}{G_I(0,\mathbf{j},\mathbf{j}')}\right)\Big/2 - \theta_{\mathbf{j}}/2 \tag{4.C.6}$$

is the angle parametrizing the orientation of the major semiaxis. In the figure, the reference angle $\gamma_{\mathbf{jj}'} = 0$ is rotated by $\pi/2$ compared to the page vertical. The maximum (minimum) response $r^{+}_{\mathbf{jj}'}$ ($r^{-}_{\mathbf{jj}'}$) at site $\mathbf{j}$ to an input field at the port $\mathbf{j}'$ is obtained for the driving phase $\vartheta = \eta_{\mathbf{jj}'}$ ($\vartheta = \eta_{\mathbf{jj}'} + \pi/2$),

$$\eta_{\mathbf{jj}'} = \pi/2 - \arg\left(G_E(0,\mathbf{j},\mathbf{j}')G_I(0,\mathbf{j},\mathbf{j}')\right)/2. \tag{4.C.7}$$

Gain, Reverse Gain, and Input Reflection

As we analyze our amplifier in the phase-sensitive mode of operation, it is useful to consider its scattering properties in a quadrature representation, using an optimal quadrature basis fields in the input and output waveguides. The relevant scattering

between these waveguides is described by

$$\begin{aligned}\hat{\mathcal{X}}_{\rm out}[\omega] &= s_{\mathcal{X},\mathcal{U}}[\omega]\hat{\mathcal{U}}_{\rm in}[\omega] + s_{\mathcal{X},\mathcal{V}}[\omega]\hat{\mathcal{V}}_{\rm in}[\omega] + ... \\ \hat{\mathcal{Y}}_{\rm out}[\omega] &= s_{\mathcal{Y},\mathcal{U}}[\omega]\hat{\mathcal{U}}_{\rm in}[\omega] + s_{\mathcal{Y},\mathcal{V}}[\omega]\hat{\mathcal{V}}_{\rm in}[\omega] + ...\end{aligned}$$

where we have omitted writing terms describing contributions from vacuum noise incident from the internal loss ports, as well as terms describing the reflection of noise incident from the output waveguide (due to slightly imperfect impedance matching). We define the quadratures of the output waveguide as

$$\begin{aligned}\hat{\mathcal{X}}_{\rm out}(t) &= \frac{1}{\sqrt{2}}\left(e^{i\theta_{\rm out}}\hat{a}^{({\rm out})\dagger}_{\mathbf{j}_{\rm out}}(t) + e^{-i\theta_{\rm out}}\hat{a}^{({\rm out})}_{\mathbf{j}_{\rm out}}(t)\right), \\ \hat{\mathcal{Y}}_{\rm out}(t) &= \frac{i}{\sqrt{2}}\left(e^{i\theta_{\rm out}}\hat{a}^{({\rm out})\dagger}_{\mathbf{j}_{\rm out}}(t) - e^{-i\theta_{\rm out}}\hat{a}^{({\rm out})}_{\mathbf{j}_{\rm out}}(t)\right).\end{aligned}$$

while the quadratures of the input-waveguide are defined as

$$\begin{aligned}\hat{\mathcal{U}}_{\rm in}(t) &= \frac{1}{\sqrt{2}}\left(e^{i\theta_{\rm in}}\hat{a}^{({\rm in})\dagger}_{\mathbf{j}_{\rm in}}(t) + e^{-i\theta_{\rm in}}\hat{a}^{({\rm in})}_{\mathbf{j}_{\rm in}}(t)\right), \\ \hat{\mathcal{V}}_{\rm in}(t) &= \frac{i}{\sqrt{2}}\left(e^{i\theta_{\rm in}}\hat{a}^{({\rm in})\dagger}_{\mathbf{j}_{\rm in}}(t) - e^{-i\theta_{\rm in}}\hat{a}^{({\rm in})}_{\mathbf{j}_{\rm in}}(t)\right).\end{aligned}$$

We will define both the quadrature basis in each coupling waveguide so that $|s_{\mathcal{X},\mathcal{U}}[\omega = 0]|$ is maximal. This implies that the largest amplification of a narrow-band signal centered at zero frequency ($\omega_p/2$ in the lab frame) occurs when the incident signal is in the $\hat{\mathcal{U}}_{\rm in}$ quadrature of the input waveguide, with the amplified output being contained in the output field $\hat{\mathcal{X}}_{\rm out}$ quadrature of the output waveguide. It also follows naturally that for vacuum noise inputs, $\hat{\mathcal{Y}}_{\rm out}$ will be the optimally squeezed quadrature. An explicit calculation of the scattering matrix in terms of the Green's functions introduced above shows that the angles defining these preferred input and output quadratures are given by

$$\theta_{\rm in} = \eta_{\mathbf{j}_{\rm out}\mathbf{j}_{\rm in}}, \quad \theta_{\rm out} = \gamma_{\mathbf{j}_{\rm out}\mathbf{j}_{\rm in}} + \theta_{\mathbf{j}_{\rm out}}/2, \tag{4.C.8}$$

see Eqs. (4.C.6,4.C.7). The fact that in general $\theta_{\rm in} \neq \theta_{\rm out}$ is a simple reflection of the fact that our system can both perform phase-sensitive amplification of incident signals, as well as simply rotate incident signals in phase space.

The frequency dependent power gain is then by definition given by the transmission probability:

$$\begin{aligned} G(\omega) &= |s_{\mathcal{X},\mathcal{U}}(\omega)|^2 \\ &= \kappa_{\rm in}\kappa_{\rm out}\Big| e^{i(\theta_{\rm in}-\theta_{\rm out})} G_E(\omega, \mathbf{j}^{(\rm out)}, \mathbf{j}^{(\rm in)}) \\ &\quad + e^{i(\theta_{\rm in}+\theta_{\rm out})} G_I(\omega, \mathbf{j}^{(\rm out)}, \mathbf{j}^{(\rm in)}) \\ &\quad + e^{i(\theta_{\rm out}-\theta_{\rm in})} G_E^*(-\omega, \mathbf{j}^{(\rm out)}, \mathbf{j}^{(\rm in)}) \\ &\quad + e^{-i(\theta_{\rm in}+\theta_{\rm out})} G_I^*(-\omega, \mathbf{j}^{(\rm out)}, \mathbf{j}^{(\rm in)}) \Big|^2 \Big/ 4 \end{aligned}$$

The reverse gain is obtained similarily by exchanging the two indices of the Green's functions in the above formula and in Eq. (4.C.8). Finally, the input reflection probability describes the reflection of signals incident in the (amplified) $\mathcal{U}$ quadrature of the input port

$$\begin{aligned} R[\omega] &= |s_{\mathcal{U},\mathcal{U}}(\omega)|^2 \\ &\quad \Big(\Big| e^{i\theta_{\rm in}} \left(1 - i\kappa_{\rm in} G_E(\omega, \mathbf{j}^{(\rm out)}, \mathbf{j}^{(\rm in)})\right) \\ &\quad + e^{-i\theta_{\rm in}} \left(1 + i\kappa_{\rm in} G_I^*(-\omega, \mathbf{j}^{(\rm out)}, \mathbf{j}^{(\rm in)})\right) \Big| \\ &\quad + \Big| e^{i\theta_{\rm in}} \left(1 - i\kappa_{\rm in} G_I(\omega, \mathbf{j}^{(\rm out)}, \mathbf{j}^{(\rm in)})\right) \\ &\quad + e^{-i\theta_{\rm in}} \left(1 + i\kappa_{\rm in} G_E^*(-\omega, \mathbf{j}^{(\rm out)}, \mathbf{j}^{(\rm in)})\right) \Big| \Big)^2 \Big/ 4. \end{aligned}$$

Noise spectral densities and amplifier added noise

In general, the output of an amplifier will consist of the amplified input signal (including its intrinsic fluctuations) plus extra fluctuations generated by the amplifier [38]. It is standard to express these extra output fluctuations as an effective number of noise quanta inserted at the amplifier input: this is the “added noise quanta of the amplifier". For a phase-sensitive amplifier like ours (which only amplifies one quadrature of an input signal), quantum mechanics allows the added noise to be arbitrarily small. Approaching this limit of zero added noise thus represents the “amplifier quantum limit" for this kind of amplifier. See, e.g., Ref. [57] for a extended pedagogical discussion of these topics.

The symmetrized noise spectral densities for the the amplified and de-amplified output-waveguide output field quadratures (as shown in Figure 4.4(a)) are defined as

$$S_{\mathcal{X},\mathcal{X}}(\omega) = \int_{-\infty}^{\infty} \frac{dt}{2} e^{i\omega t} \langle \left\{ \hat{\mathcal{X}}_{\rm out}(t), \hat{\mathcal{X}}_{\rm out}(0) \right\} \rangle, \tag{4.C.9a}$$

$$S_{\mathcal{Y},\mathcal{Y}}(\omega) = \int_{-\infty}^{\infty} \frac{dt}{2} e^{i\omega t} \langle \left\{ \hat{\mathcal{Y}}_{\rm out}(t), \hat{\mathcal{Y}}_{\rm out}(0) \right\} \rangle. \tag{4.C.9b}$$

To obtain the amplifier added noise at a given frequency (as shown in Figure 4.4(b)), we take the output noise in the amplified quadrature at this frequency, divide through by gain at this frequency (so as to have an effective amount of noise at the input of the amplifier), and then subtract off the contribution due to vacuum noise entering through the input port (as this is part of the input signal, as opposed to noise added by the amplifier). We thus obtain:

$$S_{\rm add}(\omega) \equiv \frac{S_{\mathcal{X},\mathcal{X}}(\omega)}{G(\omega)} - \frac{1}{2}. \tag{4.C.10}$$

This quantity approaches zero for a quantum-limited phase preserving amplifier.

Noise Ellipses

In Figure 4.4(c), the stationary state of each site $\mathbf{j}$ is represented as a noise ellipse. The noise ellipse on a particular site $\mathbf{j}$ is obtained by diagonalizing the corresponding covariance matrix

$$\begin{aligned} V_{\mathbf{j}} &= \begin{pmatrix} \langle \hat{X}_{\mathbf{j}}^2 \rangle & \langle \hat{X}_{\mathbf{j}} \hat{Y}_{\mathbf{j}} + \hat{Y}_{\mathbf{j}} \hat{X}_{\mathbf{j}} \rangle \\ \langle \hat{X}_{\mathbf{j}} \hat{Y}_{\mathbf{j}} + \hat{Y}_{\mathbf{j}} \hat{X}_{\mathbf{j}} \rangle & \langle \hat{Y}_{\mathbf{j}}^2 \rangle \end{pmatrix} \\ &= \begin{pmatrix} \cos\tilde{\gamma}_{\mathbf{j}} & \sin\tilde{\gamma}_{\mathbf{j}} \\ -\sin\tilde{\gamma}_{\mathbf{j}} & \cos\tilde{\gamma}_{\mathbf{j}} \end{pmatrix} \begin{pmatrix} \left(\tilde{r}_{\mathbf{j}}^{+}\right)^2 & 0 \\ 0 & \left(\tilde{r}_{\mathbf{j}}^{-}\right)^2 \end{pmatrix} \begin{pmatrix} \cos\tilde{\gamma}_{\mathbf{j}} & -\sin\tilde{\gamma}_{\mathbf{j}} \\ \sin\tilde{\gamma}_{\mathbf{j}} & \cos\tilde{\gamma}_{\mathbf{j}} \end{pmatrix}, \end{aligned} \tag{4.C.11}$$

and identifying the square root of its eigenvalues $\tilde{r}_{\mathbf{j}}^{+}$ and $\tilde{r}_{\mathbf{j}}^{-}$ as the ellipse semi-axes and the angle $\tilde{\gamma}_{\mathbf{j}}$ as the ellipse rotation angle (the reference angle $\tilde{\gamma}_{\mathbf{j}} = 0$ is rotated by $\pi/2$ compared to the page vertical).

4.D Effective model for the edge state coupled to waveguides

In this supplementary note we want to derive an effective quantum field theory for the edge state coupled to a waveguide. We want to model a finite system which will then support a single edge state with a ring geometry (i.e. periodic boundary conditions). We adopt the simplest possible approach valid when the input signal has a bandwidth well within the amplifier bandwidth. In this case, we can approximate the edge state velocity and amplification rates to be constant, $\tilde{E} \approx v\delta k$, $\Delta \approx 0$, and $V(\delta k) \approx \nu$, respectively. Moreover, we can neglect the quasimomentum dependence of the edge state transverse

wavefunction. We thus arrive at the edge state ladder operator

$$\hat{c}(j_\parallel) = \sqrt{\frac{1}{N}} \sum_{n=1}^{N} e^{i\delta k_n j_\parallel} \hat{\alpha}_{\delta k} \approx e^{-i\kappa_p j_\parallel/2} \sum_{j_\perp} u[j_\perp] \hat{a}_{j_\parallel, j_\perp}, \tag{4.D.1}$$

where N is the number of sites along the edge, and the indexes $j_\parallel$ and $j_\perp$ ($j_\perp \geq 1$) label the position in the directions parallel and longitudinal to the edges (for the edge state along the upper edge described above $j_\parallel = j_x$ and $j_\perp = -j_y$). Moreover, $u(j_\perp)$ is the transverse edge state wavefunction, $u(j_\perp) \equiv u_{k_p/2}(-j_\perp)$ see Eqs. (4.B.3,4.B.7). The periodic boundary conditions $\hat{c}(j_\parallel) = \hat{c}(N + j_\parallel)$ are enforced by the quasimomentum quantization $\delta k_n = 2\pi n/N$.

We consider a waveguide attached to a single site along the edge in the logitudinal position $j_\parallel \equiv j_{\rm ex}$. The coupling to the waveguide as described by standard input-output theory is entirely characterized by the decay rate κ. Since, the edge state is the only state within the amplifier bandwidth the coupling of the waveguide to a single site is equivalent to a direct coupling to the edge state at the same longitudinal position $j_{\rm ex}$ with the renormalized decay rate $\kappa' = \kappa |u[j_\perp = 1]|^2$. The resulting Langevin equation reads

$$\dot{\hat{c}}(j_\parallel) = i[\hat{H}^{(\rm edge)}, \hat{c}(j_\parallel)] - \frac{\kappa'}{2} \delta_{j_\parallel, j_{\rm ex}} \hat{c}(j_\parallel) + \sqrt{\kappa'} \delta_{j_\parallel, j_{\rm ex}} \hat{a}^{(\rm in)}, \tag{4.D.2}$$

with the input-output relations

$$\hat{a}^{(\rm out)} = \hat{a}^{(\rm in)} - \sqrt{\kappa'} \hat{c}(j_{\rm ex}) \tag{4.D.3}$$

Next we take the continoum limit by defining the chiral edge field

$$\hat{c}(z) = \sqrt{\frac{1}{L}} \sum_{n=-\infty}^{\infty} e^{i\delta k_n j_\parallel} \hat{\alpha}_{\delta k}, \tag{4.D.4}$$

where L is the edge length and the periodic boundary conditions $\hat{c}(z) = \hat{c}(z+L)$ follow from the quasimomentum quantization $\delta k_n = 2\pi n/L$. From Eq. (4.B.11) with $\tilde{E} = v\delta k$, $\Delta = 0$, and $V(\delta k) = \nu$, and Eq. (4.D.2) we find the field equations

$$(\partial_t + v\partial_z)\hat{c}(z) = \nu\hat{c}^\dagger(z) - \frac{\kappa'}{2}\delta(z - z_{\rm ex})\hat{c}(z) + \sqrt{\kappa'}\delta(z - z_{\rm ex})\hat{a}^{(\rm in)}. \tag{4.D.5}$$

We note that due to the point-interaction with the waveguide the field $\hat{c}(z)$ is not continous at the position $z = z_{\rm ex}$ where the waveguide is attached, $\hat{c}(z_{\rm ex} + 0_+) \neq \hat{c}(z_{\rm ex} + 0_-)$ (0_+ and 0_- are infinitesimal positive and negative numbers, respectively). Keeping this in mind, the input output relation in the continous limit reads

$$\hat{a}^{(\rm out)} = \hat{a}^{(\rm in)} - \sqrt{\kappa'}\left(\hat{c}(0_+) + \hat{c}(0_-)\right)/2. \tag{4.D.6}$$

Impedance matching and gain

Before investigating the interaction with the waveguide, we first discuss the propagation inside the ring. For concreteness we consider $v > 0$ such that $\hat{c}(z_{\rm ex}+0_+)$ ($\hat{c}(z_{\rm ex}+0_-)$) is the field immediately after (before) the interaction with the waveguide. A signal travels an almost complete round trip from $z = z_{\rm ex} + 0_+$ to $z = L + z_{\rm ex} + 0_+ = z_{\rm ex} + 0_-$ in the time $t = L/v$. During this time no interaction with the waveguide takes place. From Eq. (4.D.5), one readily finds

$$\begin{aligned}
\hat{X}(z_{\rm ex} + 0_-, L/v + t_0) &= e^{\nu L/v}\hat{X}(z_{\rm ex} + 0_+, t_0), \\
\hat{Y}(z_{\rm ex} + 0_-, L/v + t_0) &= e^{-\nu L/|v|}\hat{Y}(z_{\rm ex} + 0_+, t_0).
\end{aligned}$$

Here, we have introduced the amplified and de-amplified quadratures, $\hat{X} = (\hat{c}^\dagger + \hat{c})/\sqrt{2}$ and $\hat{Y} = i(\hat{c}^\dagger - \hat{c})/\sqrt{2}$, respectively. We can conclude that a signal with the right phase

during a complete round trip inside the ring experience a power gain

$$G = e^{2\nu L/v}. \tag{4.D.7}$$

Next, we discuss the interaction with the waveguide. An input signal from the waveguide will be partly reflected and partly transmitted into the ring at $z = 0_+$. Then, it will propagate inside the ring until it has completed a round trip. A signal with the right phase will be amplified along the way. Before starting a new round trip, part of the amplified signal returns into the waveguide. If the signal remaining in the ring at the beginning of the second round trip is smaller compared to the signal in the ring at the beginning of the first round trip, the signal will decay after few round trips. In this regime, the waveguide stabilizes the edge state. By integrating the Heisenberg equations (4.D.5) close to $z = 0$ we find

$$\begin{pmatrix} \sqrt{|v|}\hat{c}(0_+) \\ \hat{a}^{(\mathrm{out})} \end{pmatrix} = \begin{pmatrix} r & t \\ -t & r \end{pmatrix} \begin{pmatrix} \sqrt{|v|}\hat{c}(0_-) \\ \hat{a}^{(\mathrm{in})} \end{pmatrix} \tag{4.D.8}$$

where r and t are the reflection and transmission probability amplitudes,

$$r = \frac{4 - g^2}{4 + g^2}, \qquad t = \frac{4g}{4 + g^2}, \quad g = \sqrt{\frac{\kappa'}{v}}. \tag{4.D.9}$$

To prevent instability, we require that the transmission t be large enough that the field in the edge-mode ring does not grow with each round trip. The simplest case is where we tune the decay rate κ so that all of the incident wave in the edge mode ends up in the coupling waveguide, i.e. $r = 0$, $t = 1$. This requires $g = 2$, or in terms of the decay rate κ, the edge state velocity v, and the edge state transversal wavefunction at the edge

$u(j_\perp = 1)$, we find

$$\kappa = \frac{4v}{|u(j_\perp = 1)|^2} \equiv \kappa_{\mathrm{id}}. \tag{4.D.10}$$

If this impedance matching condition is met, signals incident from the waveguide in the $\hat{X}$ quadrature will be reflected back with a power gain $G = G_{\mathrm{Max}}$ independent of frequency. The impedance matching ensures that multiple traversals of the ring are impossible, which both precludes instability, but also prevents the formation of standing wave resonances and a strongly frequency-dependent gain.

We note that the effective model described above can be straightforwardly extended to describe a chiral edge state coupled to several waveguides. In particular, we consider a set up with two impedance matched waveguides at position $z = z_{\mathrm{in}}$ and $z = z_{\mathrm{out}}$ ($z_{\mathrm{out}} - z_{\mathrm{in}} = L$), respectively. A signal from the first waveguide entering the edge state at position $z = z_{\mathrm{in}}$ is entirely transmitted into the second waveguide at position $z = z_{\mathrm{out}}$. For the appropriate phase of the input signal, we have

$$\hat{\mathcal{U}}^{\mathrm{in}}(t) = \sqrt{v}\hat{X}(z_{\mathrm{in}} + 0_+, t), \tag{4.D.11}$$

where $\hat{\mathcal{U}}^{(\mathrm{in})}$ is the input quadrature. We denote $\hat{\mathcal{X}}^{\mathrm{out}}$, the corresponding amplified quadrature at $z = z_{\mathrm{out}}$,

$$\hat{\mathcal{X}}^{\mathrm{out}}(t) = -\sqrt{v}\hat{X}(z_{\mathrm{out}} + 0_-, t). \tag{4.D.12}$$

From Eq. (4.D.5) one finds

$$|\hat{\mathcal{X}}^{\mathrm{out}}(t + L/v)|^2 = G|\hat{\mathcal{U}}^{\mathrm{out}}(t)|^2 \tag{4.D.13}$$

where the gain G is given by Eq. (4.D.7).

Impedance mismatch

If the coupling waveguides are not perfectly impedance matched as per Eq. (4.D.10), signals incident on the waveguides from the edge state can be transmitted past the waveguide, and multiple traversals of the edge become possible. If such transmission becomes too strong, one can have instabilities. Using the effective 1D model with coupling to the three waveguides (as introduced above), we find that in the presence of impedance mismatch, the stability condition is

$$e^{2\nu L/v}\left(\frac{1-\frac{\kappa_{\rm in}}{\kappa_{\rm id}}}{1+\frac{\kappa_{\rm in}}{\kappa_{\rm id}}}\right)^2\left(\frac{1-\frac{\kappa_{\rm out}}{\kappa_{\rm id}}}{1+\frac{\kappa_{\rm out}}{\kappa_{\rm id}}}\right)^2\left(\frac{1-\frac{\kappa_{\rm sink}}{\kappa_{\rm id}}}{1+\frac{\kappa_{\rm sink}}{\kappa_{\rm id}}}\right)^2<1, \tag{4.D.14}$$

where the ideal impedance-match value of the couplings is $\kappa_{\rm id}$ (c.f. Eq. (4.D.10)). This condition simply corresponds to requiring that there is no net gain for waves that successfully complete a round-trip along the edge. Considering the worst case scenario where all impedances mismatches are the same, and writing $\kappa_{\rm coupling}/\kappa_{\rm id}=1+\epsilon$, the stability condition becomes

$$\left(\frac{\epsilon}{2}+\epsilon\right)^3<\frac{1}{\sqrt{G}} \tag{4.D.15}$$

where G is the forward photon number gain of the amplifier defined in Eq. (4.D.7). For a gain of roughly 20 dB, we see that mismatches of $\approx\pm15\%$ do not lead to instabilities. Furthermore, for mismatches of -10%, impedance mismatch induces small ripples (on the order of ±1) in the frequency-dependent gain (see Figure 6). For even larger gains one could stabilize the system engineering more sophisticated sinks. For example, one could have two or more impedance matched sink waveguides. The gain after a round-trip will then decrease exponentially with the number of waveguides and will be reduced below unity, thus, stabilizing the system in the presence of a sufficient number of waveguides. Thus, the lack of perfect impedance matching does not set any fundamental limit to the

achievable gain.

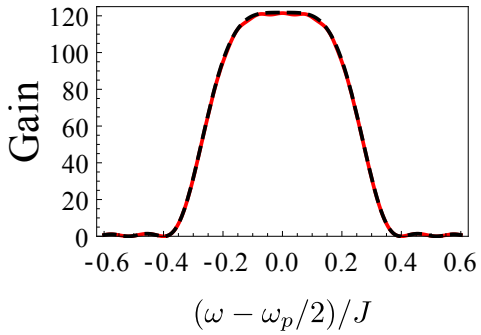

Figure 4.6: Gain profile obtained in the effective 1D model with impedance matched (black dashed line) and mismatched (red solid line) waveguides. Small (almost invisible) ripples appear in the gain for the impedance mismatched case. [Parameters: total length 80 sites, length of the amplification region 30 sites, $\omega_0 = 2.14J$, $\Phi = \pi/2$, $\nu = 0.08J$, $\kappa = 0.001J$, impedance mistmatch $\epsilon = -0.1$]

Added noise

In order to show that our quantum amplifier design offers some degree of resilience to intrinsic losses and the corresponding noise we calculate the added noise in the effective model. We consider a loss channel on each site and denote the corresponding decay rate as $\kappa_{\mathbf{j}}^{(\mathrm{loss})}(z)$. In the continous limit, and with the same approximations as above, we find the quantum field equations valid in the region between the input and output port

$$\begin{aligned}(\partial_t + v\partial_z)\hat{X}(z,t) &= (\nu - \kappa^{(\mathrm{loss})}(z)/2)\hat{X}(z,t) \\ &\quad \sqrt{\kappa^{(\mathrm{loss})}(z)}\hat{X}^{(\mathrm{loss})}(z,t). \end{aligned} \tag{4.D.16}$$

where $\hat{X}^{(\mathrm{loss})}(z,t)$ is the vacuum noise: $\langle \hat{X}^{(\mathrm{loss})}(z,t)\rangle = 0$ and

$$\langle \hat{X}^{(\mathrm{loss})}(z,t)\hat{X}^{(\mathrm{loss})}(z',t')\rangle = \frac{1}{2}\delta(z-z')\delta(t-t'). \tag{4.D.17}$$

We fourier transform into frequency space and find the solution

$$\begin{aligned}\hat{X}[z,\omega] &= e^{[(i\omega+\nu)(z-z_{\rm in})-\int_{z_{\rm in}}^{z}\kappa^{(\rm loss)}(z')dz'/2]/v}\hat{X}(z_{\rm in}+0_+,\omega)\\ &+\frac{1}{v}\int_{z_{\rm in}}^{z}dz' e^{[(i\omega+\nu)(z-z')-\int_{z'}^{z}\kappa^{(\rm loss)}(z'')dz''/2]/v}\\ &\times\sqrt{\kappa^{(\rm loss)}(z')}\hat{X}^{(\rm loss)}(z',\omega).\end{aligned} \tag{4.D.18}$$

Putting together Eq. (4.D.18) for $z = z_{\rm out} - 0_-$ with Eqs. (4.D.11,4.D.12) we can relate the output signal $\hat{\mathcal{X}}^{\rm out}$ to the input signal $\hat{\mathcal{U}}^{\rm in}$ of the amplifier

$$\begin{aligned}&\hat{\mathcal{X}}^{\rm out}[\omega] = -e^{[(i\omega+\nu)L-\int_{z_{\rm in}}^{z_{\rm out}}\kappa^{(\rm loss)}(z')dz'/2]/v}\hat{\mathcal{U}}^{(\rm in)}[\omega]\\ &+\frac{1}{\sqrt{v}}\int_{z_{\rm in}}^{z_{\rm out}}dz' e^{[(i\omega+\nu)(z_{\rm out}-z')-\int_{z'}^{z_{\rm out}}\kappa^{(\rm loss)}(z'')dz''/2]/v}\\ &\times\sqrt{\kappa^{(\rm loss)}(z')}\hat{X}^{(\rm loss)}(z',\omega).\end{aligned} \tag{4.D.19}$$

The added noise $S_{\rm add}(\omega)$ in noise quanta is by definition,

$$S_{\rm add}(\omega) = \frac{S_{\mathcal{X},\mathcal{X}}(\omega)}{G(\omega)} - \frac{1}{2}. \tag{4.D.20}$$

where $S_{\mathcal{X},\mathcal{X}}(\omega)$ is the symmetrized noise at the output port,

$$S_{\mathcal{X},\mathcal{X}}[\omega]\delta(\omega+\omega') = \frac{1}{2}\langle\{\hat{\mathcal{X}}[\omega],\hat{\mathcal{X}}[\omega']\}\rangle. \tag{4.D.21}$$

and $G(\omega)$ is the gain. We note that in our simple approach $S_{\mathcal{X},\mathcal{X}}$, G and $S_{\rm add}$ are frequency independent. From Eqs. (4.D.19,4.D.17) we find

$$G = e^{[2\nu L-\int_{z_{\rm in}}^{z_{\rm out}}\kappa^{(\rm loss)}(z')dz']/v} \tag{4.D.22}$$

and

$$S_{\rm add} = \frac{1}{v}\int_0^L dr e^{-[2\nu r - \int_0^L \kappa^{(\rm loss)}(r+z_{\rm in})dr']/v}\kappa^{(\rm loss)}(r+z_{\rm in}). \tag{4.D.23}$$

From this expression we see that for $2\nu > \kappa^{(\rm loss)}(z)$ the noise added at position $r + z_{\rm in}$ is cut off exponentially as a function of the distance r from the input. In particular, in the large gain limit and assuming that $\kappa^{(\rm loss)}(z)$ is smooth close to $z = z_{\rm in}$, we can approximate

$$S_{\rm add} \approx \frac{\kappa^{(\rm loss)}(z_{\rm in})}{2\nu}. \tag{4.D.24}$$

Note crucially that as one increases the length L of the amplifying channel, the gain increases exponentially, while the added noise remains constant. We thus see explicitly that the amplifying channel is immune to the majority the internal loss noise in the system.

Comparison between finite size simulations and effective model

In the regime where our effective theory applies (for signals well within the amplifier bandwidth), it can reproduce well the simulations of finite arrays. There are some quantitative differences due to well understood finite size effects. For instance, the edge state velocity is not constant in the finite size array but rather decreases close to the edges where the edge state propagation changes direction. For this reason the gain does not depend only on the number of sites separating the input and the output port but also on the precise position of the ports. We have placed the input and output port close to the edges to enhance the gain. Indeed, the gain in the finite size simulations is slightly larger than predicted by Eq. (4.D.7). Due to the position dependent edge state velocity also the value of the decay rate required to obtain impedance matching depends on the position where the waveguide is attached (and is lower at the edges).

We note that the analytic continuum model can be extended to capture the frequency dependence of the gain and noise of our travelling wave amplifier; one needs however to incorporate into the model the leading-order quasimomentum dependence of the edge state velocity (which creates an effective pump detuning for the relevant parametric process). This is will be presented in a future work.

References

[1]C. C. Gerry, and P. L. Knight, in *Introductory quantum optics* (Cambridge University Press, 2005).

[2]C. M. Caves, Phys. Rev. D **23**, 1693–1708 (1981).

[3]B. Yurke, S. McCall, and J. Klauder, Phys. Rev. A **33**, 4033–4054 (1986).

[4]V. Giovannetti, S. Lloyd, and L. Maccone, Science **306**, 1330–1336 (2004).

[5]D. J. Thouless, M. Kohmoto, M. P. Nightingale, and M. den Nijs, Phys. Rev. Lett. **49**, 405–408 (1982).

[6]L. Lu, J. D. Joannopoulos, and M. Soljacic, Nat Photon **8**, 821–829 (2014).

[7]Z. Wang, Y. Chong, J. D. Joannopoulos, and M. Soljacic, Nature **461**, 772–775 (2009).

[8]T. Kitagawa, M. A. Broome, A. Fedrizzi, M. S. Rudner, E. Berg, I. Kassal, A. Aspuru-Guzik, E. Demler, and A. G. White, Nat Commun **3**, 882– (2012).

[9]M. C. Rechtsman, J. M. Zeuner, Y. Plotnik, Y. Lumer, D. Podolsky, F. Dreisow, S. Nolte, M. Segev, and A. Szameit, Nature **496**, 196–200 (2013).

[10]M. Hafezi, S. Mittal, J. Fan, A. Migdall, and J. M. Taylor, Nature Photonics **7**, 1001–1005 (2013).

[11]E. Prodan, and C. Prodan, Phys. Rev. Lett. **103**, 248101 (2009).

[12]C. L. Kane, and T. C. Lubensky, Nature Phys. **10**, 39–45 (2013).

[13]V. Peano, C. Brendel, M. Schmidt, and F. Marquardt, Phys. Rev. X **5**, 031011 (2015).

[14]Z. Yang, F. Gao, X. Shi, X. Lin, Z. Gao, Y. Chong, and B. Zhang, Phys. Rev. Lett. **114**, 114301 (2015).

[15]J. Paulose, B. G.-g. Chen, and V. Vitelli, Nature Phys. **11**, 153–156 (2015).

[16]R. Süsstrunk, and S. D. Huber, Science **349**, 47–50 (2015).

[17]L. M. Nash, D. Kleckner, A. Read, V. Vitelli, A. M. Turner, and W. T. M. Irvine, Proceedings of the National Academy of Sciences **112**, 14495–14500 (2015).

[18]F. D. M. Haldane, and S. Raghu, Phys. Rev. Lett. **100**, 013904 (2008).

[19]S. Raghu, and F. D. M. Haldane, Phys. Rev. A **78**, 033834 (2008).

[20]J. Koch, A. A. Houck, K. L. Hur, and S. M. Girvin, Phys. Rev. A **82**, 043811 (2010).

[21]R. O. Umucalılar, and I. Carusotto, Phys. Rev. A **84**, 043804 (2011).

[22]K. Fang, Z. Yu, and S. Fan, Nature Photon. **6**, 782–787 (2012).

[23]A. Petrescu, A. A. Houck, and K. Le Hur, Phys. Rev. A **86**, 053804 (2012).

[24]L. D. Tzuang, K. Fang, P. Nussenzveig, S. Fan, and M. Lipson, Nature Photonics **8**, 701–705 (2014).

[25]M. Schmidt, S. Kessler, V. Peano, O. Painter, and F. Marquardt, Optica **2**, 635–641 (2015).

[26]M. Hafezi, E. A. Demler, M. D. Lukin, and J. M. Taylor, Nature Phys. **7**, 907–912 (2011).

[27]A. B. Khanikaev, S. H. Mousavi, W.-K. Tse, M. Kargarian, A. H. MacDonald, and G. Shvets, Nature Mat. **12**, 233–239 (2012).

[28]S. Mittal, J. Fan, S. Faez, A. Migdall, J. M. Taylor, and M. Hafezi, Phys. Rev. Lett. **113**, 087403 (2014).

[29]R. Shindou, R. Matsumoto, S. Murakami, and J.-i. Ohe, Phys. Rev. B **87**, 174427 (2013).

[30]G. Engelhardt, and T. Brandes, Phys. Rev. A **91**, 053621 (2015).

[31]C.-E. Bardyn, T. Karzig, G. Refael, and T. C. H. Liew, Phys. Rev. B **93**, 020502 (2016).

[32]V. Peano, M. Houde, C. Brendel, F. Marquardt, and A. A. Clerk, Nat Commun **7**, (2016).

[33]R. Barnett, Phys. Rev. A **88**, 063631 (2013).

[34]B. Galilo, D. K. K. Lee, and R. Barnett, Phys. Rev. Lett. **115**, 245302 (2015).

[35]G. Engelhardt, M. Benito, G. Platero, and T. Brandes, Phys. Rev. Lett. **117**, 045302 (2016).

[36]D. R. Hofstadter, Phys. Rev. B **14**, 2239–2249 (1976).

[37]M. Z. Hasan, and C. L. Kane, Rev. Mod. Phys. **82**, 3045–3067 (2010).

[38]C. M. Caves, Phys. Rev. D **26**, 1817–1839 (1982).

[39]M. I. Dykman, M. Marthaler, and V. Peano, Phys. Rev. A **83**, 052115 (2011).

[40]V. Peano, and M. Thorwart, Phys. Rev. B **82**, 155129 (2010).

[41]M.-A. Lemonde, and A. A. Clerk, Phys. Rev. A **91**, 033836 (2015).

[42]M. Notomi, E. Kuramochi, and T. Tanabe, Nature Photon. **2**, 741–747 (2008).

[43]S. Mookherjea, and A. Yariv, Ieee J Quantum Elect **8**, 448 (2002).

[44]B. J. Eggleton, B. Luther-Davies, and K. Richardson, Nat Photonics **5**, 141 (2011).

[45]J. Dahdah, M. Pilar-Bernal, N. Courjal, G. Ulliac, and F. Baida, J. Appl. Phys. **110**, 074318 (2011).

[46]A. H. Safavi-Naeini, S. Gröblacher, J. T. Hill, J. Chan, M. Aspelmeyer, and O. Painter, Nature **500**, 185–189 (2013).

[47]T. P. Purdy, P. L. Yu, R. W. Peterson, N. S. Kampel, and C. A. Regal, Phys. Rev. X **3**, 031012 (2013).

[48]D. L. Underwood, W. E. Shanks, J. Koch, and A. A. Houck, Phys. Rev. A **86**, 023837 (2012).

[49]B. M. Anderson, R. Ma, C. Owens, D. I. Schuster, and J. Simon, Phys. Rev. X **6**, 041043 (2016).

[50]T. Shi, H. J. Kimble, and J. I. Cirac, arXiv:1603.03266v1 (2016).

[51]A. Metelmann, and A. A. Clerk, Phys. Rev. X **5**, 021025 (2015).

[52]L. Ranzani, and J. Aumentado, New J. Phys. **17**, 1–14 (2015).

[53]B. Abdo, K. Sliwa, S. Shankar, M. Hatridge, L. Frunzio, R. Schoelkopf, and M. Devoret, Phys. Rev. Lett. **112**, 167701 (2014).

[54]K. M. Sliwa, M. Hatridge, A. Narla, S. Shankar, L. Frunzio, R. J. Schoelkopf, and M. Devoret, Phys. Rev. X **5**, 041020 (2015).

[55]C. Macklin, K. O'Brien, D. Hover, M. E. Schwartz, V. Bolkhovsky, X. Zhang, W. D. Oliver, and I. Siddiqi, Science **350**, 307–310 (2015).

[56]B. A. Bernevig, and T. L. Hughes, in *Topological insulators and topological superconductors* (Princeton University Press, 2013).

[57]A. A. Clerk, M. H. Devoret, S. M. Girvin, F. Marquardt, and R. J. Schoelkopf, Reviews of Modern Physics **82**, 1155–1208 (2010).

Preface to Chapter 5

Chapter 5 builds directly on the contents of chapter 4. In the latter, we obtained a topologically protected travelling wave parametric amplifier by properly tuning the phases of the on-site parametric drives. This requires us to drive every site on the lattice which is experimentally demanding. In this chapter, we numerically study the transport properties of quantum fluctuations, using input-output theory, for finite systems in which fewer sites on the lattice are parametrically driven. We consider the same physical system as in chapter 4, however, we allow for the drive to be turned off for sites of our choosing. We find that by properly placing the parametric drives, and tuning the drive strength, we obtain similar results to those of chapter 4 with just three parametrically driven sites on the edge. We also show that by allowing the output angle to vary we can obtain squeezing over a broader range of frequencies.

5

Resource efficient topological travelling wave amplifier

Martin Houde[1], **Aashish. A. Clerk**[2]

[1]Department of Physics and the Centre for Physics of Materials, McGill University, Montreal, Quebec, Canada H3A 2T8

[2]Institute for Molecular Engineering, University of Chicago, 5640 S. Ellis Ave., Chicago, IL 60637

This chapter will be submitted for publication.

Abstract

Building on the work of Ref[1], we show how to obtain a resource efficient topologically-protected travelling wave amplifier. Implementing parametric driving uniformly over a lattice is resource heavy. We study how the properties of the travelling-wave amplifier are affected when only a subset of lattice sites are driven. The lack of phase-matching in this case would lead us to believe that unwanted processes could be excited by the drives, leading to instabilities. However, we find that it is possible to get almost ideal behaviour with only three parametric drives.

5.1 Introduction

In recent years, there has been much work and interest in the study of topological photonic systems which are subject to particle nonconserving interactions that coherently created pairs of photons such as parametric driving [1–7]. In such systems, it was shown that it is possible to selectively induce dynamical instabilities of the edge modes while leaving the bulk modes stable [1, 6, 7].

Recently, in [1], we proposed a method of obtaining a topologically-protected, quantum-limited, travelling-wave amplifier from a system where the edge modes become dynamically unstable. While interesting, it is experimentally hard to realize as proposed. Although it is possible to engineer on-site parametric drives in experimental setups such as those proposed in Ref.[8], it is still however an experimental challenge to construct a lattice where every site is parametrically driven. We therefore wish to understand if it is possible to obtain similar amplifying and noise properties for a system where the parametric driving occurs on a smaller number of sites.

When all sites are parametrically driven, the parametric pump injects pairs of photons in the lattice with net quasimomentum k_p. When fewer sites are driven, the pump quasimomentum is not clearly defined and thus pairs can be injected with different quasimomenta. The lack of phase-matching breaks quasimomentum conservation. Certain processes which were initially suppressed by quasimomentum conservation could now be excited, leading to spurious instabilities. We might thus expect that one always needs a number of parametric drives that is comparable to the number of lattice sites to realize a topologically-protected, quantum-limited, travelling wave amplifier. Surprisingly, we find that this is not the case. In fact, we find that it is possible to get almost ideal behaviour with only *three* parametric drives with increased drive strength.

5.2 Model

We consider the same Hamiltonian as in Ref.[1]. That is to say, we consider photons hopping on a two-dimensional array of coupled cavities, forming a square lattice, subject to on-site two-photon parametric driving. An engineered synthetic gauge field also generates a flux per plaquette of Φ, inducing topology. Setting $\hbar = 1$ and moving to a rotating frame, the Hamiltonian is

$$\hat{H} = \sum_{\mathbf{j}} \omega_{\mathbf{j}} \hat{a}_{\mathbf{j}}^{\dagger} \hat{a}_{\mathbf{j}} - \sum_{\langle \mathbf{i},\mathbf{j} \rangle} J_{\mathbf{ij}} \hat{a}_{\mathbf{i}}^{\dagger} \hat{a}_{\mathbf{j}} + \frac{i}{2} \sum_{\mathbf{j}} \left(e^{i\theta_{\mathbf{j}}} \nu_{\mathbf{j}} \hat{a}_{\mathbf{j}}^{\dagger} \hat{a}_{\mathbf{j}}^{\dagger} - h.c. \right), \tag{5.2.1}$$

where $\hat{a}_{\mathbf{j}}$ annihilates a photon on site $\mathbf{j} = (j_x, j_y)$. The on-site energies $\omega_{\mathbf{j}} = \omega_0 + \delta\omega_{\mathbf{j}}$ include ω_0, which represents the detuning of half the pump frequency ($\omega_p/2$) from the cavity frequency (ω_{cav}) (i.e. $\omega_0 = \omega_{\mathrm{cav}} - \omega_p/2$), and a site-dependent offset energy $\delta\omega_{\mathbf{j}}$. The engineered synthetic gauge field is encoded in the pattern of phases $\phi_{\mathbf{ij}}$ of the nearest-neighbour hopping rates, $J_{\mathbf{ij}} = J \exp(i\phi_{\mathbf{ij}})$. We take the synthetic flux per plaquette to be $\Phi = \pi/2$. We work in the Landau gauge such that we have $\phi_{\mathbf{ij}} = 0$ for vertical hopping and $\phi_{\mathbf{ij}} = -\pi j_y/2$ for rightwards hopping. This is known as the Hofstadter model.

Unlike Ref.[1], since we are not parametrically driving every site, we take the parametric driving amplitude on a given site $\mathbf{j}$ to be $\nu_{\mathbf{j}} e^{i\theta_{\mathbf{j}}}$ where $\nu_{\mathbf{j}} = 0$ when a site is not driven. We again take the phase to vary as $\theta_{\mathbf{j}} = k_p j_x$, implying the injection of pairs with a quasimomentum $\mathbf{k}_{\mathrm{p}} = k_{\mathrm{p}} \mathbf{e}_x$ when all sites are driven.

5.3 Numerical Methods

From our choice of parametrization, where the flux per plaquette is $\Phi = \pi/2$ and $k_p > 0$, we only phase-match on the top edge. Hence, a finite-size system will only exhibit amplification properties on the top edge of the sample. That is to say, signals will only be amplified when they propagate along the top edge. We consider a finite-size realization of our system using a 30×12 array of nanocavities, and additionally include three couplings to external waveguides. Each of these waveguides is coupled to a site at the edge of the sample and serves as ports either to inject or collect signals from. This coupling is described using standard input-output theory[9], and is entirely characterized by the three rates κ_{in}, κ_{out}, and κ_{sink}. In addition, we take each cavity to have an internal-loss decay rate κ_{int} arising from a coupling to a zero-temperature, Markovian and Gaussian reservoir. We also take energy offset $\delta\omega_{\mathbf{j}}$ to be a random variable to simulate random on-site disorder.

The linear response and noise properties of the array, are combinations of the retarded Green's functions

$$\tilde{G}_E(\omega, \mathbf{j}, \mathbf{j}') = -i \int_{-\infty}^{\infty} dt \Theta(t) e^{i\omega t} \langle [\hat{a}_{\mathbf{j}}(t), \hat{a}^{\dagger}_{\mathbf{j}'}(0)] \rangle, \tag{5.3.1}$$

$$\tilde{G}_I(\omega, \mathbf{j}, \mathbf{j}') = -i \int_{-\infty}^{\infty} dt \Theta(t) e^{i\omega t} \langle [\hat{a}^{\dagger}_{\mathbf{j}}(t), \hat{a}^{\dagger}_{\mathbf{j}'}(0)] \rangle. \tag{5.3.2}$$

which we calculate numerically for the finite-size array described above. All the relevant quantities are defined in section 4.C.

5.4 Results

We now focus on the case where, when all sites are driven, the edge mode in the lower topological band gap becomes dynamically unstable for arbitrarily small ν. To achieve this, we will tune the pump photon frequency ω_p and quasimomentum k_p such that a single pump photon can be converted into two edge excitations with frequency $\omega_p/2$ and quasimomentum $k_p/2$ in the lab frame. Note that when all site are driven, any two bulk mode energies always add up to a finite value. Thus, processes which create pairs of bulk modes are suppressed by energy conservation.

As we mentioned previously, when we are driving a fewer number of sites, pairs of photons can be injected with arbitrary quasimomentum. It is now possible to excite processes that create pairs of excitations, at little energy cost, which are not injected with quasimomentum k_{p}. Fig. 5.1 shows the possible energy levels for a finite-size Hofstadter model without parametric driving. By zooming in on the energy range for which amplification occurs when all sites are driven, we find two modes which have nearly equal and opposite energies at the edges of the energy range. Parametric processes that create one of each mode would be nearly energy conserving and favoured. In fact, these processes cause the system to become unstable first. In a periodic system, we find that the modes corresponding to these two energies do not conserve quasimomentum. Hence, in the fully-driven case, the parametric process is suppressed by phase-matching. When we lose this phase-matching (e.g. when only a subset of sites are driven), these processes are no longer suppressed leading to peaks in the gain profile. Note that the specific procceses reponsible for these spurious instabilities will depend on the lattice dimensions.

Furthermore, the fewer the number of interacting sites we have, the harder it becomes to achieve similar, or in some cases any, levels of gain while maintaining stability. With

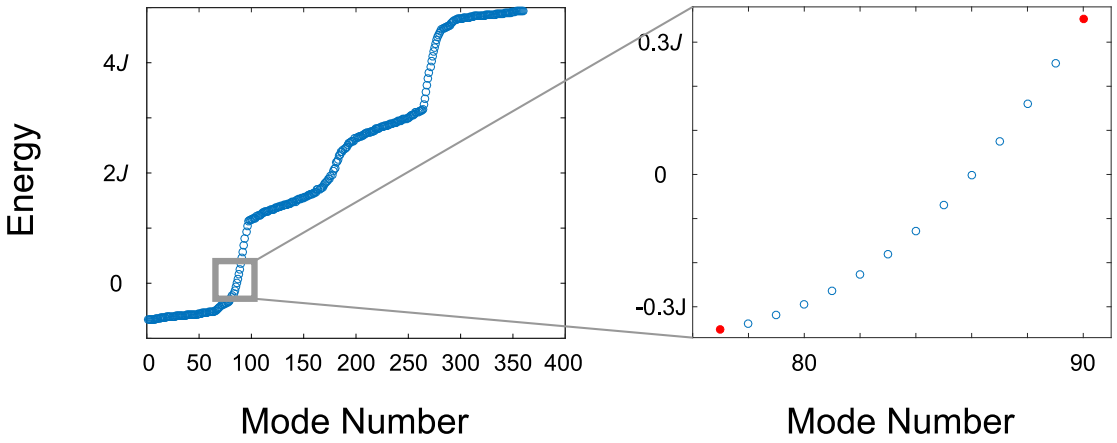

Figure 5.1: Energies of a 30×12 finite size array for the Hofstadter model with a flux of $\pi/2$ (when the parametric driving is switched off). We zoom in for energies around the amplification bandwidth (consequently corresponding to edge modes). Two modes, lying outside the region of amplification (red dots), have nearly equivalent and opposite energies. Parametric processes which coherently create these modes are nearly energy conserving ($E_1 + E_2 \approx 0.001J < \nu$). When all sites are parametrically driven, quasimomentum conservation prevents these processess. However, when only three sites are driven, quasimomentum is no longer conserved and such processes occur, resulting in side-peaks in the gain profile.

fewer sites, we need to increase the parametric drive strength to maintain gain levels. By increasing the interaction strength, we increase the probability that our system becomes unstable. Increasing the interaction strength may result in highly localized instabilities. At high parametric strengths, pairs of photons are created on the site at a rate faster than which they can decay or hop to neighbouring sites leading to instability. To maintain stability, in this case, we must increase the internal decay rate. We must therefore reach a balance between increasing the interaction strength while maintaining stability such that gain is possible.

With lack of phase-matching leading to possible unwanted parametric processes to be excited as well as the interplay between increasing the interaction strength without causing localized instabilities, one might expect that one always needs the number of driven sites to be on the order of the lattice to have a topologically protected travelling

wave amplifier. Interestingly, we find that this is not the case. By systematically reducing the number of driven sites, we are able to obtain near optimal behaviour for such an amplifier with only three driven sites.

5.4.1 Parametrically driven edge

We first begin by considering the case where only the sites on the amplifying edge are parametrically driven. In this setup, none of the bulk sites are interacting and only the thirty sites on the top edge of our finite array are interacting. Fig. 5.3 shows the amplifying and noise properties of such a setup while using the same parameters as in [1]. As we can see, we still obtain high levels of gain, albeit lower than when all sites are driven. The slight decrease can be explained by the fact that the edge modes being amplified have non-zero amplitude along the bulk (although they are highly confined to the edge). As these bulk sites are no longer driven, the edge modes are effectively amplified at a smaller rate. We also still achieve high amounts of squeezing and low levels of added noise. For the same reason as the gain, the squeezing is not as high and the added noise is slightly higher than the case where all sites are driven. The reverse gain and reflection at the input port have similar behaviour to the case where all sites are driven: since amplification only occurs along the top edge, the fact that the bulk sites are non-interacting has little to no effect on these properties. Having shown that it works for the case where only the sites on the amplifying edge are driven, we want to consider the setup which will give us similar results for the fewest number of driven sites along the amplifying edge.

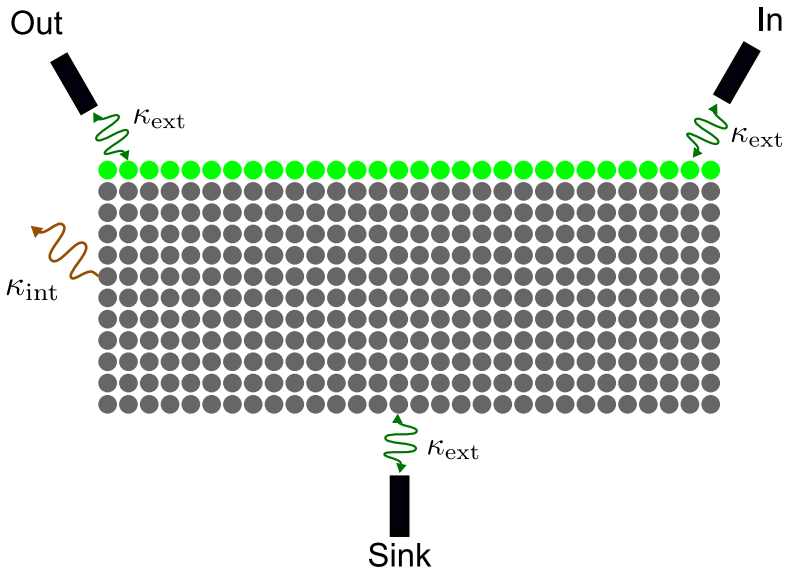

Figure 5.2: Finite size array formed by 30×12 photonic nanocavities, thirty of which are parametrically driven. These interacting cavities are all placed along the edge where amplification took place in the case where all sites were driven. Three cavities along the edge are connected to waveguides; the input and output ports of the amplifier, and an additional sink port to ensure stability. Each nanocavity experiences decay at a rate κ_{int}.

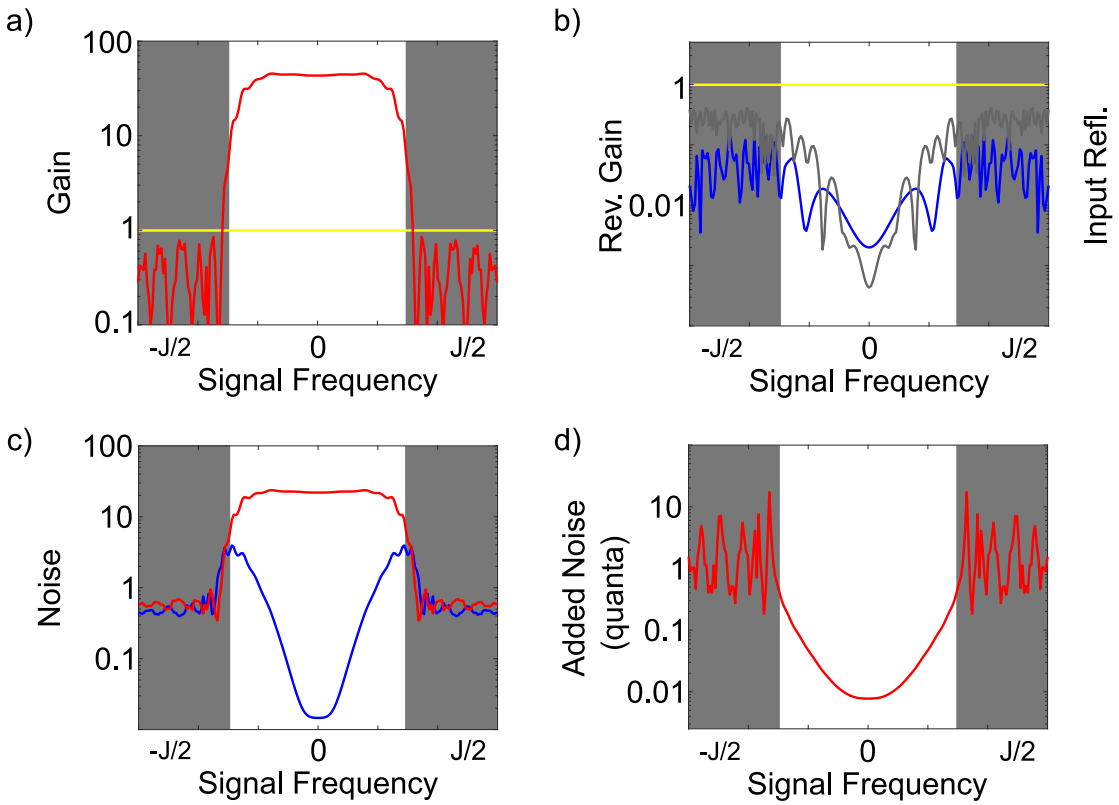

Figure 5.3: Linear response and noise properties of the topological amplifier where only cavities along the amplifying edge are parametrically driven.(a) Transmission power gain, for a signal with the right phase injected at the input port and collected at the output port, as a function of signal frequency (counted off from half the pump frequency). Even though we are only parametrically driving the sites on the edge we still obtain high levels of gain inside the amplification bandwidth. The reflection coefficient at the input port is shown by the grey curve in (e). (b) Transmission power gain for a signal injected at the output port and collected at the input, denoted by the reverse gain and shown by the blue curve. A proper impedance matching ensures that most of the signal leaks through the sink port, resulting in small reverse transmission.(c) Noise spectral densities for both the amplified (red) and squeezed (blue) quadratures of the field leaving the output port, plotted in units of quanta, as a function of signal frequency. The field leaving the output port is still relatively strongly squeezed.(d) Noise added by our topological amplifier to the amplified quadrature in units of quanta. The added noise is still only slightly larger than the quantum-limit for a phase preserving amplifier. Parameters: $\omega_0 = 2.14J$, $\Phi = \pi/2$, $\nu = 0.08J$, $k_p = 2.2$, $\kappa_{int} = 0.001J$, $\kappa_{in} = 2.6J$, $\kappa_{out} = 3J$, $\kappa_{sink} = 4.2J$. Simulations were done with random on-site energy disorder, $\omega_j = \omega_0 + \delta\omega_j$, with random numbers in the interval $-0.1J < \delta\omega_j < 0.1J$

5.4.2 Two parametrically driven sites

For the simplest case where only one site is parametrically driven, we find that there is no way to obtain a topologically-protected, travelling-wave amplifier. The driving strength must be increased so much that a highly localized instability occurs. At this parametric strength, pairs of photons are created on the site at a rate faster than which they can decay or hop to neighboring sites. To stabilize, we must have such a high internal decay rate that we never obtain gain over unity.

We next consider driving two sites on the edge. We now have a high amount of liberty as to how to place these two drives. We find that the best configuration is placing them in a centralized manner and then spreading them apart by five sites, which corresponds to roughly $2\lambda_p$ (see Fig. 5.4 for schematic representation of system). This is the wavelength associated with the quasimomentum k_p. If we place the drives too close together, we get a similar effect to the single driven site: a highly localized instability around the two sites. If we place them too far apart, the little phase-matching that occurs when placing them as specified above breaks down and we see two highly localized instabilities around the two sites. Fig. 5.5 shows the linear response properties of the two driven sites setup. Looking at Fig. 5.5(a), we see that the levels of gain we are able to obtain in the central amplification region are considerably lower than in the case where all sites are driven. This is the highest level of gain we can obtain while maintaining dynamical stability for the choice of internal decay. Higher levels of internal decay lead to much lower levels of gain. Furthermore, there are very sharp peaks which appear outside the amplification region, as discussed previously, which have higher gain levels than the central amplification region. This is a very undesirable effect which we wish to avoid.

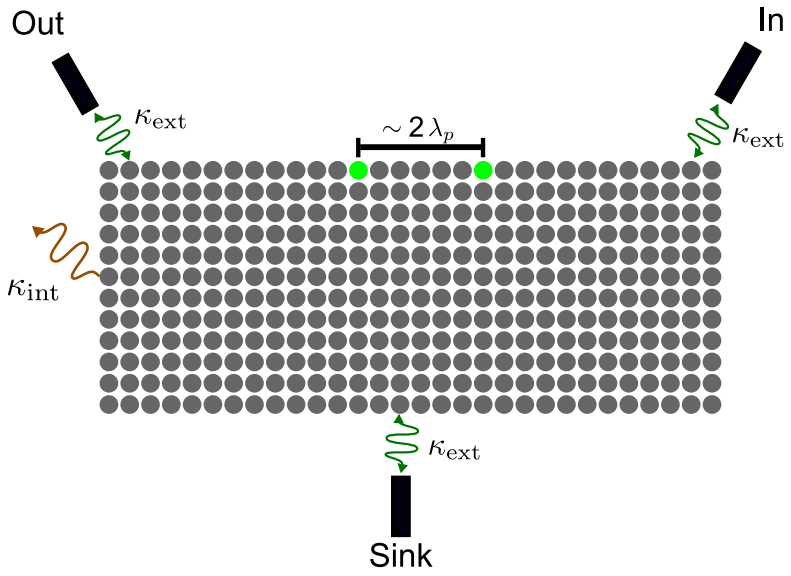

Figure 5.4: Finite size array formed by 30×12 photonic nanocavities, two of which are parametrically driven. These interacting cavities are placed along the edge where amplification took place in the case where all sites were driven. The sites are placed roughly $2\lambda_p$ sites apart, where λ_p is the wavelength corresponding to the quaismomentum, k_p with which the photons are injected, around the center of the edge. Each nanocavity experiences decay at a rate κ_{int}. Three cavities along the edge are connected to waveguides; the input and output ports of the amplifier, and an additional sink port to ensure stability.

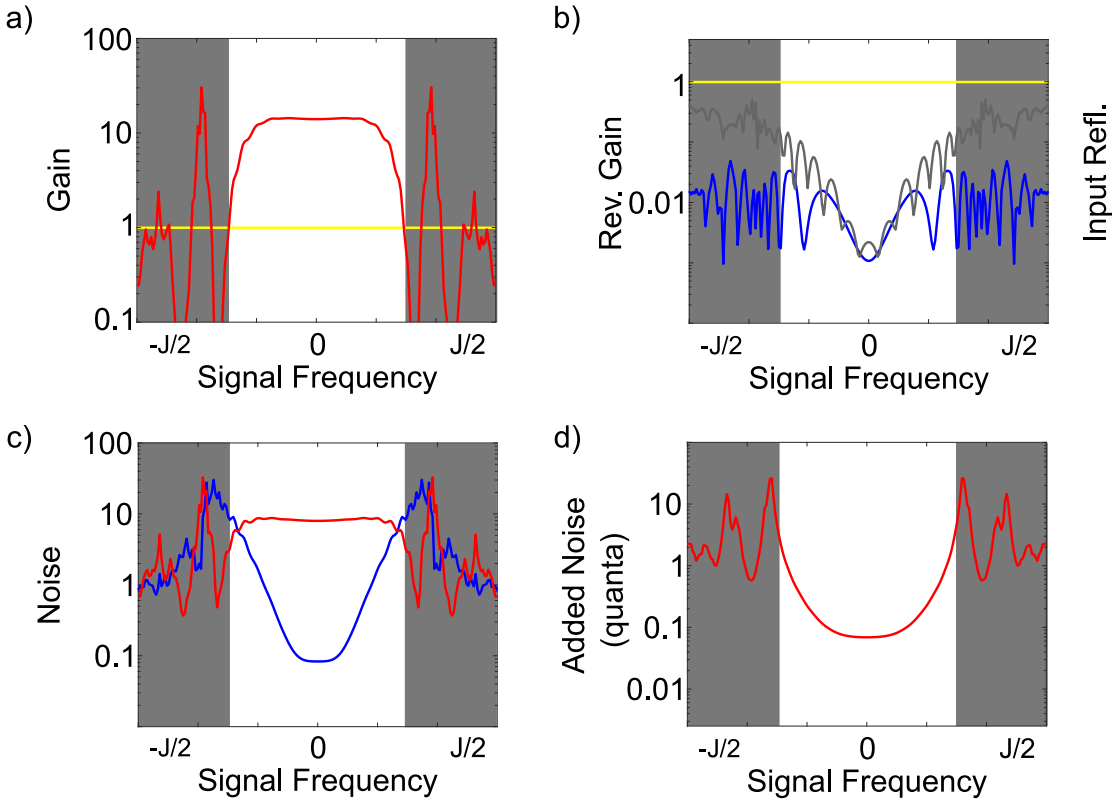

Figure 5.5: Linear response and noise properties of the topological amplifier where only two cavities along the amplifying edge are parametrically driven (see fig. (5.4) for diagram of setup). To obtain these optimal results, we need to increase the parametric interaction strength. We further need to increase the on-site cavity decay rate to stabilize our system.(a) Transmission power gain, for a signal with the right phase injected at the input port and collected at the output port, as a function of signal frequency (counted off from half the pump frequency). Two parametrically driven sites with a higher interaction strength does not lead to high levels of gain in the amplification bandwidth. Unlike the fully driven case, new resonant processes take place leading to side-peaks appearing with higher levels of gain. The reflection coefficient at the input port is shown by the grey curve in (e). (b) Transmission power gain for a signal injected at the output port and collected at the input, denoted by the reverse gain and shown by the blue curve. A proper impedance matching ensures that most of the signal leaks through the sink port, resulting in small reverse transmission.(c) Noise spectral densities for both the amplified (red) and squeezed (blue) quadratures of the field leaving the output port, plotted in units of quanta, as a function of signal frequency. Due to increased on-site cavity decay, more noise enters each cavity and the amount of squeezing achieved is lower than in the fully driven case, however, it is still below vacuum squeezing.(d) Noise added by our topological amplifier to the amplified quadrature in units of quanta. Once again, due to increased on-site cavity decay, our amplifier adds more noise to the amplified quadrature. Parameters: $\omega_0 = 2.14J$, $\Phi = \pi/2$, $\nu = 0.75J$, $k_p = 2.2$, $\kappa_{int} = 0.01J$, $\kappa_{in} = 2.6J$, $\kappa_{out} = 3J$, $\kappa_{sink} = 4.2J$. Simulations were done with random on-site energy disorder, $\omega_j = \omega_0 + \delta\omega_j$, with random numbers in the interval $-0.1J < \delta\omega_j < 0.1J$

5.4.3 Three parametrically driven sites

The fewest number of sites we find where it is possible to find a balance between increasing the parametric drive strength and internal decay rate is three. These three sites must also be placed properly. We find that the best configuration is again placing them in a centralized manner and then spreading them apart by five sites, which corresponds to roughly $2\lambda_p$ (see Fig. 5.6 for schematic representation of system). If we place the three sites too close together, we get a similar effect to the single driven site: a highly localized instability around the three sites. On the other hand, if we place either of the sites closer to the input/output port, due to the increased drive strength, we either get terrible input reflection or instability close to the output port.

Having found a configuration where we can increase the parametric drive strength substantially while keeping internal decay rates low, we study its amplifying and noise properties. Fig. 5.7 shows these results for the mentioned configuration of fig. 5.6. We have increased both the parametric interaction strength and internal decay rates but we are able to obtain levels of gain as high as the case where all sites are driven (see fig. 5.7(a)). However, unlike the case where all sites are driven, we see that we also obtain sharp peaks of high gain outside the original amplification region (which we refer to as side-peaks). In contrast to the two driven site case, the central amplification region has a higher level of gain than the side-peaks. Fig. 5.7(b) shows that we still obtain low levels of input reflection and reverse gain. As we have had to increase the internal decay rates to stay stable, the noise properties are not as good as the case where all sites are driven. Indeed, fig. 5.7(c) shows that the levels of squeezing obtained are lower but still greater than vacuum squeezing(roughly 10 dB rather than 17 dB). These squeezing levels are also greater than those obtained when two sites are driven. The added noise is also higher in this case for the same reasons.

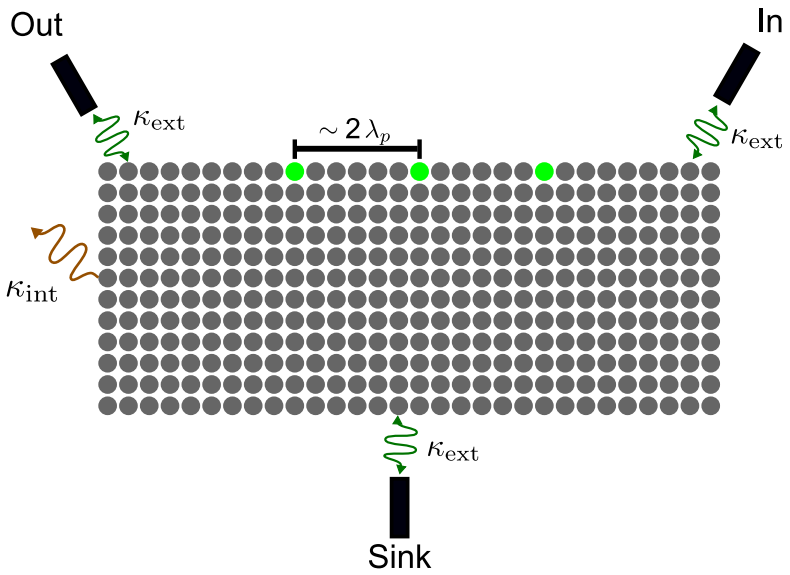

Figure 5.6: Finite size array formed by 30×12 photonic nanocavities, three of which are parametrically driven. These interacting cavities are placed along the edge where amplification took place in the case where all sites were driven. The sites are placed roughly $2\lambda_p$ sites apart, where λ_p is the wavelength corresponding to the quasimomentum, k_p, with which the photons are injected. Each nanocavity experiences decay at a rate κ_{int}. Three cavities along the edge are connected to waveguides; the input and output ports of the amplifier, and an additional sink port to ensure stability.

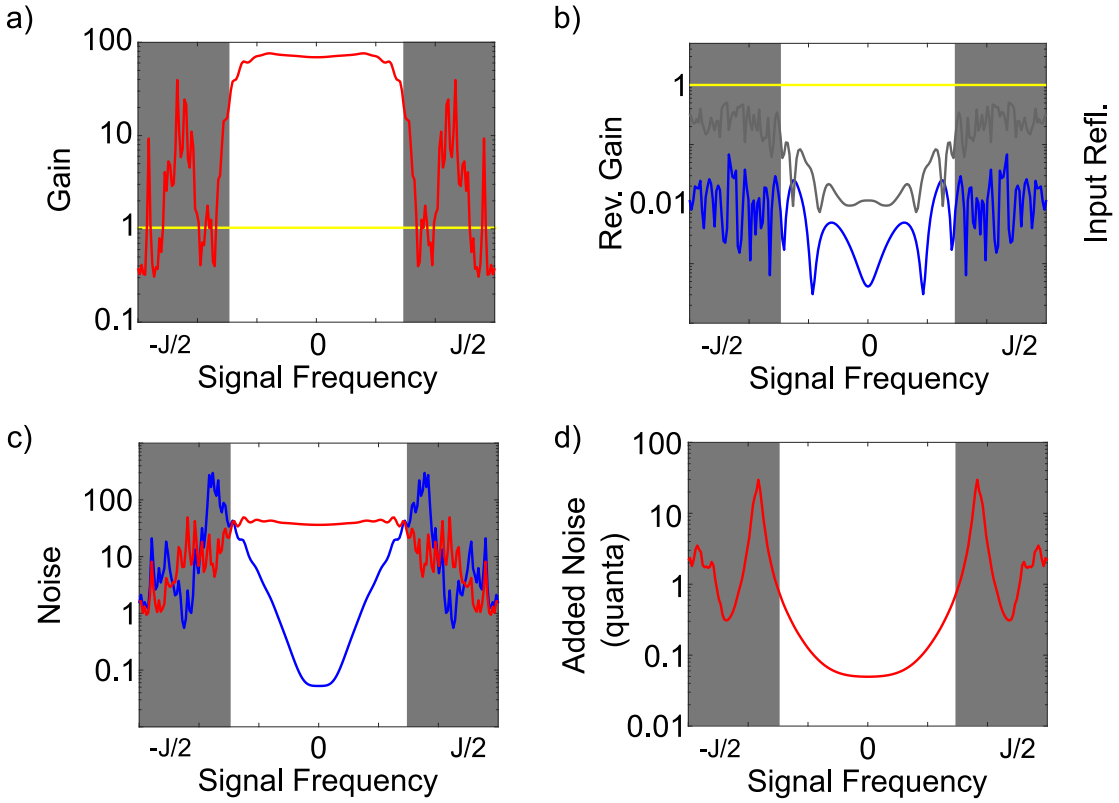

Figure 5.7: Linear response and noise properties of the topological amplifier where only three cavities along the amplifying edge are parametrically driven (see fig. (5.6) for diagram of setup). To obtain similar results to the fully driven case, we need to increase the parametric interaction strength. We further need to increase the on-site cavity decay rate to stabilize our system.(a) Transmission power gain, for a signal with the right phase injected at the input port and collected at the output port, as a function of signal frequency (counted off from half the pump frequency). Three parametrically driven sites with a higher interaction strength still leads to high levels of gain in the amplification bandwidth. Unlike the fully driven case, new resonant processes take place leading to side-peaks appearing in the gain profile. The reflection coefficient at the input port is shown by the grey curve in (e). (b) Transmission power gain for a signal injected at the output port and collected at the input, denoted by the reverse gain and shown by the blue curve. A proper impedance matching ensures that most of the signal leaks through the sink port, resulting in small reverse transmission.(c) Noise spectral densities for both the amplified (red) and squeezed (blue) quadratures of the field leaving the output port, plotted in units of quanta, as a function of signal frequency. Due to increased on-site cavity decay, more noise enters each cavity and the amount of squeezing achieved is lower than in the fully driven case, however, it is still below vacuum squeezing.(d) Noise added by our topological amplifier to the amplified quadrature in units of quanta. Once again, due to increased on-site cavity decay, our amplifier adds more noise to the amplified quadrature. Parameters: $\omega_0 = 2.14J$, $\Phi = \pi/2$, $\nu = 0.8J$, $k_p = 2.2$, $\kappa_{int} = 0.01J$, $\kappa_{in} = 2.6J$, $\kappa_{out} = 3J$, $\kappa_{sink} = 4.2J$. Simulations were done with random on-site energy disorder, $\omega_j = \omega_0 + \delta\omega_j$, with random numbers in the interval $-0.1J < \delta\omega_j < 0.1J$

5.5 Varying Output angle

Having shown that we can obtain almost ideal behaviour with only three parametric drives with increased drive strength, we change focus and study another way of optimizing the topologically-protected, travelling-wave amplifier. Although we are able to obtain high levels of squeezing with our amplifier, all the figures show a very small bandwidth over which we attain these levels. We now study how the squeezing properties are affected when we allow for the angle of the output quadrature to vary as a function of frequency. We shall show that this further lets us optimize the performance of our amplifier, even with only just three driven sites.

As specified in Ref.[1], we have defined the output angle, $\theta[\omega]$, used to define the output quadratures,

$$\hat{\mathcal{Y}}_{\text{out}}[\omega] = \frac{i}{\sqrt{2}}\left[e^{i\theta[\omega]}\hat{a}^{\dagger}_{\text{out}}[\omega] - e^{-i\theta[\omega]}\hat{a}_{\text{out}}[\omega]\right] \tag{5.5.1}$$

$$\hat{\mathcal{X}}_{\text{out}}[\omega] = \frac{1}{\sqrt{2}}\left[e^{i\theta[\omega]}\hat{a}^{\dagger}_{\text{out}}[\omega] + e^{-i\theta[\omega]}\hat{a}_{\text{out}}[\omega]\right], \tag{5.5.2}$$

such that the gain is maximized at zero frequency. Hence, we kept the angle constant for all signal frequencies. There is nothing that limits us from defining the output quadrature at every signal frequency and studying the noise properties of the output state when we allow the angle to vary.

We now choose the output angle such that the squeezing is maximized at every frequency. Recall that the squeezed output quadrature is given by $\hat{\mathcal{Y}}_{out}[\omega]$ and its noise spectral density is defined by

$$S_{\mathcal{Y},\mathcal{Y}}(\omega) = \int_{-\infty}^{\infty} \frac{dt}{2} e^{i\omega t} \langle \left\{ \hat{\mathcal{Y}}_{\text{out}}(t), \hat{\mathcal{Y}}_{\text{out}}(0) \right\} \rangle. \tag{5.5.3}$$

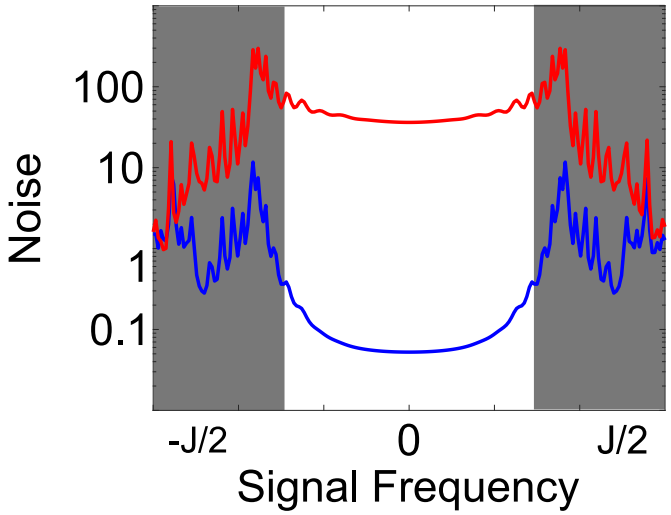

Figure 5.8: Noise spectral density of the topological amplifer where only three cavities along the amplifying edge are parametrically driven (see fig. 5.6 for diagram of setup) as a function of signal frequency (counted off from half the pump frequency). By properly choosing the output angle at every signal frequency (see fig. 5.9 for output angle profile), we are able to obtain high levels of squeezing over a larger bandwidth. This increases the usefulness of our amplifier as a source of squeezing. Parameters: $\omega_0 = 2.14J$, $\Phi = \pi/2$, $\nu = 0.8J$, $k_p = 2.2$, $\kappa_{int} = 0.01J$, $\kappa_{in} = 2.6J$, $\kappa_{out} = 3J$, $\kappa_{sink} = 4.2J$. Simulations were done with random on-site energy disorder, $\omega_j = \omega_0 + \delta\omega_j$, with random numbers in the interval $-0.1J < \delta\omega_j < 0.1J$

To maximize the squeezing, we must minimize the noise spectral density. Optimizing, we find

$$e^{4i\theta[\omega]} = \frac{\langle\{a_{out}[-\omega], a_{out}[\omega]\}\rangle}{\langle\{a^\dagger_{out}[-\omega], a^\dagger_{out}[\omega]\}\rangle}. \tag{5.5.4}$$

The numerator and denominator are just complex conjugates of each other and so expressing these in polar form we find

$$\theta[\omega] = \arg[\langle\{a^\dagger_{out}[-\omega], a^\dagger_{out}[\omega]\}\rangle]/2. \tag{5.5.5}$$

Using Eq. (5.5.5) we find the output angle and study the noise spectral density for the setup where we have three interacting sites on the edge (see fig. 5.6). Fig. 5.8 shows

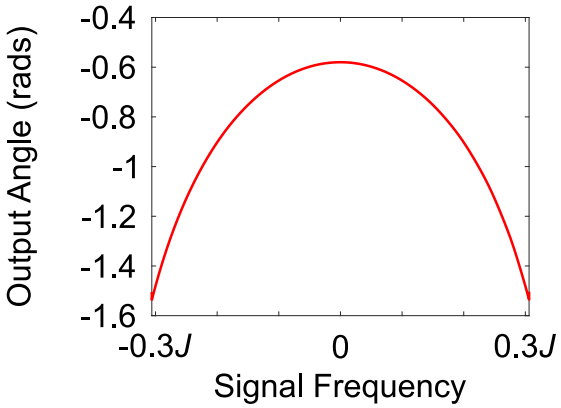

Figure 5.9: Output angle as a function of signal frequency (counted off from half the pump frequency) which maximizes the amount of squeezing over the whole amplifying bandwidth. Since the modes responsible for amplification have a non-constant dispersion, the optimal angles is frequency dependent. We are now able to obtain squeezing below vacuum over the entire bandwidth. Parameters: $\omega_0 = 2.14J$, $\Phi = \pi/2$, $\nu = 0.8J$, $k_p = 2.2$, $\kappa_{int} = 0.01J$, $\kappa_{in} = 2.6J$, $\kappa_{out} = 3J$, $\kappa_{sink} = 4.2J$. Simulations were done with random on-site energy disorder, $\omega_j = \omega_0 + \delta\omega_j$, with random numbers in the interval $-0.1J < \delta\omega_j < 0.1J$

the noise spectral density with the varying output angle. We see that we now obtain high levels of squeezing over the entire bandwidth of the amplification region. This increases the usefulness of our topological amplifier as a source of squeezing.

Fig. 5.9 shows the variation of the output angle as a function of signal frequency. The fact that the optimal angle depends on frequency is not a surprise. The modes responsible for amplification do not have a constant dispersion. The fact that these modes have a frequency dependent dispersion relation leads to a frequency dependent output angle.

We can see these effects in a simpler single cavity model connected to a waveguide. We consider a single mode degenerate parametric amplifier which allows for additional dispersion of the mode. We take the onsite energy to be $\omega_{\text{cav}} = \omega_0 + \Delta$. Working in the rotating frame where $\omega_0 = \omega_p/2$, setting $\hbar = 1$, the Hamiltonian is

$$\hat{H} = \Delta \hat{a}^\dagger \hat{a} + \frac{i\nu}{2}\left((\hat{a}^\dagger) - \hat{a}^2\right) \tag{5.5.6}$$

where Δ is a detuning parameter and accounts for additional dispersion, ν is the parametric drive strength, and $\hat{a}$ annihilates a bosonic mode ($[\hat{a}, \hat{a}^\dagger] = 1$). The Heisenberg-Langevin equation are

$$\partial_t \hat{a} = (-i\Delta - \frac{\kappa}{2})\hat{a} - \sqrt{\kappa} a_{in} \tag{5.5.7}$$

where $\hat{a}_{in}$ are the modes injected by the waveguide. By Fourier transforming into frequency space and using input-output theory, we are able to obtain the solutions for $\hat{a}_{in}[\omega]$ and obtain the output angle given by Eq.(5.5.5). For this model, we find

$$\theta[\omega] = \tan\left(\frac{4\Delta\kappa}{4(\omega^2 + \nu) - 4\Delta^2 - 3\kappa^2}\right) \tag{5.5.8}$$

which is frequency dependent. Hence, choosing a different output angle for each frequency leads to a broader bandwidth of squeezing.

5.6 Conclusion

In this work, we have studied an extension of the work presented in Ref. [1] by allowing for the parametric driving to be non-zero on a small subset of the lattice. By studying the linear response and noise properties of the system, we have shown that it is still possible to realize a topologically-protected, travelling-wave amplifier when as few as three sites are parametrically driven. This is very resource-efficient and more experimentally feasible that the original proposal.

By allowing for the definition of the output quadrature to vary as a function of frequency, we have also shown that it is possible to obtain a broader bandwidth squeezing spectrum. This further adds to the utility of the topologically-protected, travelling-wave amplifier.

References

[1]V. Peano, M. Houde, F. Marquardt, and A. A. Clerk, Phys. Rev. X **6**, 041026 (2016).

[2]R. Shindou, R. Matsumoto, S. Murakami, and J.-i. Ohe, Phys. Rev. B **87**, 174427 (2013).

[3]G. Engelhardt, and T. Brandes, Phys. Rev. A **91**, 053621 (2015).

[4]C.-E. Bardyn, T. Karzig, G. Refael, and T. C. H. Liew, Phys. Rev. B **93**, 020502 (2016).

[5]V. Peano, M. Houde, C. Brendel, F. Marquardt, and A. A. Clerk, Nat Commun **7**, 10779 (2016).

[6]R. Barnett, Phys. Rev. A **88**, 063631 (2013).

[7]B. Galilo, D. K. K. Lee, and R. Barnett, Phys. Rev. Lett. **115**, 245302 (2015).

[8]B. M. Anderson, R. Ma, C. Owens, D. I. Schuster, and J. Simon, Phys. Rev. X **6**, 041043 (2016).

[9]A. A. Clerk, M. H. Devoret, S. M. Girvin, F. Marquardt, and R. J. Schoelkopf, Reviews of Modern Physics **82**, 1155–1208 (2010).

Preface to Chapter 6

In this final chapter, we study more generic travelling wave parametric amplifiers which are not necessarily topologically protected. Being motivated by recent experiments on such amplifiers using arrays of Josephson junctions, we study how having different amounts of loss at signal and idler frequencies affects the properties of the output state. We consider two different loss models. The first is a beamsplitter model where the loss is added at the end of the travelling wave parametric amplifier. We consider the output state of the amplifier to be a pure two-mode squeezed state and model the loss by passing it through a beamsplitter. The second is an extension of the effective model developed in chapter 4 which allows for loss to be distributed along the amplifier. As the signal and idler modes propagate through the amplifier, loss occurs continuously and at independent rates for both modes. We find that loss asymmetry leads to interesting results. For the quantum squeezing of collective output quadratures, asymmetric loss is quite detrimental: even small levels of asymmetry can eliminate any amount of squeezing. On the other hand, asymmetric loss has little effect on the entanglement of the output state. It is therefore possible to have non-zero entanglement while having no squeezing of collective

output quadratures. Furthermore, we find that asymmetric loss increases the added noise of the amplifier when compared to the symmetric loss case.

6

Loss asymmetries in quantum travelling wave parametric amplifiers

Martin Houde[1], **L. C. G. Govia**[2], **Aashish. A. Clerk**[2]

[1]Department of Physics and the Centre for Physics of Materials, McGill University, Montreal, Quebec, Canada H3A 2T8

[2]Institute for Molecular Engineering, University of Chicago, 5640 S. Ellis Ave., Chicago, IL 60637

This chapter will be submitted for publication.

Abstract

We study theoretically how loss impacts the amplification and squeezing performance of a generic quantum travelling wave parametric amplifier. Unlike previous studies, we analyze how having different levels of loss at signal and idler frequencies can dramatically alter properties compared to the case of frequency-independent loss. We find that loss asymmetries increase the amplifier's added noise in comparison to the symmetric loss case. More surprisingly, even small levels of loss asymmetry can completely destroy any quantum squeezing of collective output quadratures, while nonetheless leaving the output state strongly entangled.

6.1 Introduction

High fidelity qubit readout is a crucial ingredient to any viable quantum computing technology. Superconducting qubits operated in circuit QED architectures are among the most promising platforms for quantum computing. Here, readout is typically performed through homodyne detection of the output signal from a cavity dispersively coupled to a qubit [1]. High readout fidelity requires the use of quantum limited amplifiers [2, 3] at the cavity output. The recently developed Josephson traveling-wave parametric amplifier (TWPA), a non-degenerate parametric amplifier built from a chain of Josephson junctions, offers this capability across a broad bandwidth of several GHz [4–6], and will likely be a centerpiece of future circuit QED experiments of increasing size [7, 8].

While TWPAs have proven to be excellent signal amplifiers, their utility is not limited to amplification. Even with only vacuum input, the output of an ideal TWPA exhibits broadband two-mode squeezing and entanglement, and can be viewed as a source of two-mode squeezed vacuum states (TMSS). Such states have a myriad of possible applications. The collective symmetric quadratures of a TMSS are squeezed below vacuum, which directly enables enhanced readout protocols [9, 10]. Further, the signal-idler entanglement generated at the output could be used to entangle remote qubits [11–13], and opens up the possibility for many continuous variable protocols [14], such as quantum teleportation [15].

All of the above applications require high quality output states, implying that it is necessary to carefully model and understand how loss mechanisms in a TWPA degrade its output; experiments suggest such losses are non-negligible [5]. Previous theoretical studies of loss in TWPAs have either treated the loss as occurring only at the end of the device by introducing a fictitious beamsplitter [13], or have considered distributed loss throughout the device, but only for a degenerate parametric amplifier (signal and idler

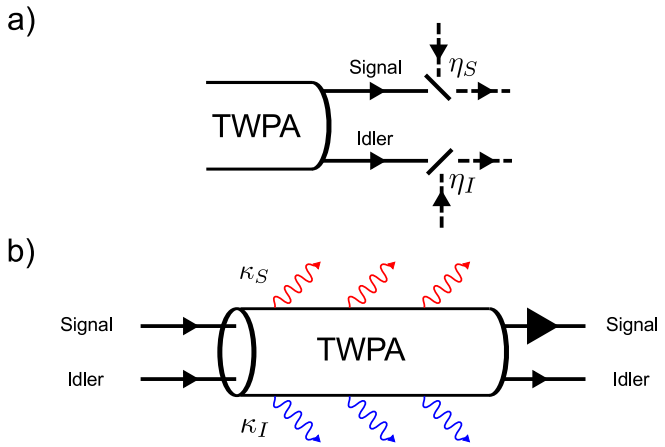

Figure 6.1: Schematic figure of two loss models. a) Beamsplitter loss model: signal and idler modes are passed through beamsplitters with transmission coefficients η_S and η_I respectively.b) Distributed loss model: signal and idler modes experience different decay rates κ_S and κ_I, respectively, as they propagate through the TWPA.

at the same frequency) [16]. Furthermore, these previous treatments consider the case where signal and idler modes of the TWPA have equal (or symmetric) loss rates.

In this work, we extend the methodology of Refs. [13, 16] to the more general situation of unequal (or asymmetric) signal and idler loss, in both the beamsplitter and distributed models of loss. Although we are motivated by recent work on the Josephson travelling-wave amplifier, we note that our models and results are general and independent of the source of the nonlinearities present in the device. Our results apply to more general TWPAs such as those of Refs. [17–20]. By analyzing the TWPA as a source of squeezing, we find that asymmetric loss is detrimental to collective quadrature squeezing: asymmetry feeds amplified noise into the squeezed quadrature, thus quickly suppressing squeezing.

We further show how the output states of such models can be understood as thermal two-mode squeezed states. This allows us to quantify the states' entanglement and purity in simple terms. With this description, we find that these quantities are hardly degraded by asymmetric loss. It is thus possible to have non-zero entanglement while having no

squeezing of symmetric collective quadratures below the vacuum level (see Fig. 6.3). For applications where one desires the joint quadratures to be squeezed, we propose a correction protocol to the lossy output state which allows one to regain squeezing below zero point.

We also analyze the impact of asymmetric loss on the amplification properties of a TWPA. By analyzing the TWPA as a non-degenerate parametric amplifier with distributed loss, we find that asymmetry increases the level of gain (compared to the case of symmetric loss). The amount of noise added by the amplifier is also increased by loss asymmetries; nonetheless, the TWPA still remains nearly quantum limited.

This paper is organized as follows. In section 6.3 we introduce an ideal way to describe the output an imperfect TMSS in terms of thermal two-mode squeezed states. In section 6.2 we outline the general setup of the different models we consider. In section 6.4 we consider the effective beamsplitter model for a lossy TWPA, what we term "lumped element" loss. We show how symmetric and asymmetric loss affects the output state and quantities of interest. We conclude section 6.4 with a proposal to correct the output state from an asymmetric lossy TWPA.

In section 6.5 we extend the distributed loss model of Ref. [16] to non-degenerate parametric amplifiers, and apply this model to the lossy TWPA. We quantify the effect of symmetric and asymmetric distributed loss on the output squeezing and gain of the TWPA, thereby characterizing its use as both a squeezing source and an amplifier. Further, we explore the interplay between phase mismatch [4] and asymmetric distributed loss. Finally, in section 6.6 we present our conclusions.

6.2 Model of an ideal TWPA

As is standard [16], we model a generic TWPA as a nonlinear one-dimensional transmission line or waveguide. The basic amplification process involves driving the system with a large coherent pump tone (frequency $\bar{\omega}_P$, wavevector $k_P > 0$), which is then scattered by the nonlinearity into photons at signal and idler frequencies. For a four-wave mixing nonlinearity (as relevant to setups employing Josephson junctions), two pump photons are converted to a pair of signal and idler photons. We will consider signal photons with frequency $\omega_S \in (\bar{\omega}_S - D, \bar{\omega}_S + D)$, where D is the maximum bandwidth of interest. Energy conservation then determines the relevant range of idler photons via $\omega_I = 2\omega_P - \omega_S$. We will focus exclusively on non-degenerate modes of operation, where signal and idler frequencies do not overlap; we thus require $\bar{\omega}_S - D > \bar{\omega}_P$. Given this condition, we can treat signal and idler photons by effectively independent one-dimensional bosonic channels (with the provision that we restrict attention to the frequencies in the bandwidths described above). We take these fields to have infinite extent, with a non-zero interaction only between $x = 0$ and $x = L$. Further, only right-moving signal and idler fields will be phase-matched to the pump, hence we do not consider left-moving fields (which are decoupled from the dynamics).

To write the system Hamiltonian, we will work in a rotating frame at frequency $\bar{\omega}_S$ ($\bar{\omega}_I = 2\bar{\omega}_P - \bar{\omega}_S$) for the signal (idler) channel. Treating the nonlinear interaction at a mean-field level and setting $\hbar = 1$, the basic TWPA Hamiltonian is:

$$\hat{H} = \int dx \left[\hat{a}_S^\dagger(x) \left(-iv_S \partial_x\right) \hat{a}_S(x) + \hat{a}_I^\dagger(x) \left(-iv_I \partial_x\right) \hat{a}_I(x) + \frac{i}{2} \left(\nu(x) \hat{a}_S^\dagger(x) \hat{a}_I^\dagger(x) - h.c. \right) \right], \tag{6.2.1}$$

Here, v_n denotes the group velocity of channel $n = S, P, I$, and the lowering operator

for channel n is $\hat{b}_n(x) = e^{ik_n x}\hat{a}_n(x)$, where $k_n = \bar{\omega}_n/v_n$. The operators $\hat{a}_n(x)$ describe the spatial envelope of the signal and idler fields, and are canonical bosonic fields: $\left[\hat{a}_n(x), \hat{a}_m^\dagger(x')\right] = \delta(x-x')\delta_{nm}$. Finally, the parametric interaction, with units of a rate, is

$$\nu(x) = \lambda|\psi_P|^2 e^{i(2k_P - k_S - k_I)x}\left[\theta(x) - \theta(x-L)\right] \tag{6.2.2}$$

where ψ_P is the classical pump amplitude, λ is the bare four-wave mixing interaction strength, $\theta(x)$ is the Heaviside function, and the exponential factor accounts for a lack of phase matching. We start by assuming all group velocities are the same, implying perfect phase matching; $\nu(x)$ can then be taken to be real and positive without any loss of generality.

Working in the Heisenberg picture, the output of our amplifier is described by the operators $\hat{a}_{S/I}(L,t)$, and the input by $\hat{a}_{S/I}(0,t)$. For the ideal TWPA described by Eq. (6.2.1), one can easily solve the Heisenberg equations of motion for the system. By relating output fields to input fields in the frequency domain, one finds the basic scattering relations that characterize the system as a non-degenerate (phase-preserving) amplifier:

$$\hat{a}_S[L,\omega] = e^{i\omega L/v}\sqrt{G_{\text{ideal}}}\hat{a}_S[0,\omega] + e^{i\omega L/v}\sqrt{G_{\text{ideal}} - 1}\hat{a}_I^\dagger[0,\omega] \tag{6.2.3}$$

where we have taken the Fourier transform of our fields, and defined the power gain as

$$G_{\text{ideal}} = \cosh^2(L\nu/v) \equiv \cosh^2(r) \tag{6.2.4}$$

with r denoting the frequency-independent squeezing parameter for our model. Note that in a more realistic model, r will be frequency dependent due to e.g. dispersion effects

that cause a lack of phase matching.

In the case where the input fields are just vacuum noise, the output of the ideal TWPA is characterized by the correlation functions

$$\left\langle \hat{a}^{\dagger}_{S/I}[L,\omega]\hat{a}_{S/I}[L,\omega']\right\rangle = 2\pi \sinh^2(r)\delta(\omega+\omega'), \tag{6.2.5}$$

$$\langle \hat{a}_S[L,\omega]\hat{a}_I[L,\omega']\rangle = \pi \sinh(2r)\delta(\omega+\omega'), \tag{6.2.6}$$

where we have made use of the δ-function to get rid of the phase factors.This describes a product of two-mode squeezed states. Introducing Hermitian quadrature operators via $\hat{a}_{S/I}(L,t) = (\hat{X}_{S/I}(L,t) + i\hat{P}_{S/I}(L,t))/\sqrt{2}$, we define the symmetric collective quadratures

$$\hat{X}_{\pm}(L,t) = \frac{\hat{X}_S(L,t) \pm \hat{X}_I(L,t)}{\sqrt{2}}. \tag{6.2.7}$$

with a similar definition for $\hat{P}_{\pm}(L,t)$. The noise spectral density of a generic quadrature is defined as:

$$S_{\hat{X}}[\omega] = \int_{-\infty}^{\infty} \frac{dt}{2}\, e^{i\omega t} \left\langle \left\{ \hat{X}(t), \hat{X}(0) \right\} \right\rangle. \tag{6.2.8}$$

One finds that with the choice of interaction phase in Eq. (6.2.1), the ideal TWPA squeezes fluctuations in both the $\hat{X}_-$ and $\hat{P}_+$ quadratures. The noise spectral density of these squeezed quadratures are

$$S^{\text{ideal}}_{\hat{X}_-}[\omega] = S^{\text{ideal}}_{\hat{P}_+}[\omega] = \frac{1}{2}e^{-2r}. \tag{6.2.9}$$

For any $r > 0$ we obtain squeezing below zero point ($S_{X_-}[\omega] = 1/2$).

6.3 Thermal two-mode squeezed state parameterization of a lossy TWPA

The main goal of this paper is to characterize the output state of an imperfect TWPA. Losses will degrade the perfect two-mode squeezing of signal and idler generated at each frequency by an ideal TWPA. Generically, the state at each frequency will now be a thermal two-mode squeezed state (th-TMSS). Such a state has the form

$$\hat{\rho}_{\mathrm{th-TMSS}} = \hat{S}_2(R)\left[\hat{\rho}_S^{\mathrm{th}}(\bar{n}_S)\otimes\hat{\rho}_I^{\mathrm{th}}(\bar{n}_I)\right]\hat{S}_2^{\dagger}(R) \tag{6.3.1}$$

where $\hat{S}_2(R) = \exp\left[R\left(\hat{B}_S\hat{B}_I - h.c.\right)\right]$ is the two-mode squeezing operator for bosonic modes $\hat{B}_{S/I}$ with squeezing parameter R, and $\hat{\rho}_i^{\mathrm{th}}(\bar{n}_i)$ describes a single-mode thermal state with average photon number $\bar{n}_i$. An imperfect TMSS can be fully described by these three parameters: $\bar{n}_S, \bar{n}_I$, and R. In general R can be complex, however, we can always work in a gauge where R is real.

A general th-TMSS, for bosonic modes, has correlation functions

$$\left\langle \hat{B}_i^{\dagger}\hat{B}_i \right\rangle = \bar{n}_i + (\bar{n}_S + \bar{n}_I + 1)\sinh^2(R), \tag{6.3.2}$$

$$\left\langle \hat{B}_S\hat{B}_I \right\rangle = \frac{\bar{n}_S + \bar{n}_I + 1}{2}\sinh(2R). \tag{6.3.3}$$

where $i = S, I$. Note that $\bar{n}_S - \bar{n}_I$ determines the asymmetry of the state (e.g. how different is the state if we exchange the S and I modes).

Important properties of the state have a simple expression in terms of the th-TMSS description. The purity μ of the state is

$$\mu \equiv \mathrm{Tr}\left(\hat{\rho}_{\mathrm{th-TMSS}}\right)^2 = \frac{1}{(1+2\bar{n}_S)(1+2\bar{n}_I)}. \tag{6.3.4}$$

The entanglement of the modes S and I in this state can be characterized by the logarithmic negativity [14], and takes the form [21]

$$E_{\mathrm{N}} = -\ln\left[n_R - \sqrt{n_R^2 - (1+2\bar{n}_S)(1+2\bar{n}_I)}\right], \tag{6.3.5}$$

where

$$n_R = (\bar{n}_S + \bar{n}_I + 1)\cosh(2R). \tag{6.3.6}$$

Introducing Hermitian quadrature operators via $\hat{B}_{S/I} = (\hat{X}_{S/I} + i\hat{P}_{S/I})/\sqrt{2}$, we define symmetric collective quadratures $\hat{X}_\pm = (\hat{X}_S \pm \hat{X}_I)/\sqrt{2}$. A crucial quantity is the variance of the squeezed collective quadrature $\hat{X}_+$,

$$S_{\hat{X}_+} \equiv \langle \hat{X}_+^2 \rangle - \langle \hat{X}_+ \rangle^2 = \frac{1}{2}\left[1 + \bar{n}_S + \bar{n}_I\right] e^{-2R}. \tag{6.3.7}$$

Finally, note that the multimode output of the TWPA (even with loss) can be understood as a product of th-TMSS states. For each frequency ω of interest, we can introduce frequency-resolved temporal modes, defined as

$$\hat{B}^{\mathrm{out}}_{S/I}[\omega] = \lim_{\delta\to 0} \frac{1}{\sqrt{\delta}} \int_{\pm\omega-\delta/2}^{\pm\omega+\delta/2} d\omega' \hat{a}^{\mathrm{out}}_{S/I}[\omega'], \tag{6.3.8}$$

where the $+$ $(-)$ sign is for the signal (idler) mode. These modes have center frequency $\pm\omega$, a vanishing bandwidth δ, and satisfy $[\hat{B}_j[\omega], \hat{B}^\dagger_{j'}[\omega]] = \delta_{j,j'}$ For each frequency ω, the pair of modes $\hat{B}^{\mathrm{out}}_{S/I}[\omega]$ will be a th-TMSS state, and thus can be completely parameterized by $\bar{n}_S, \bar{n}_I, R$.

6.4 Lumped element loss

We begin our treatment of loss in a TWPA by considering the simplest possible model of loss, the so-called “lumped element model". Here, we model the final output of a lossy TWPA by applying an independent beamsplitter transformation to each output (S,I) of an ideal TWPA, see Fig. 6.1a). This is described by the transformation

$$\hat{a}_S^{\text{out}}[\omega] = \sqrt{\eta_S[\omega]}\hat{a}_S[L,\omega] + \sqrt{1-\eta_S[\omega]}\hat{\xi}_S[\omega], \tag{6.4.1}$$

$$\hat{a}_I^{\text{out}}[\omega] = \sqrt{\eta_I[\omega]}\hat{a}_I[L,\omega] + \sqrt{1-\eta_I[\omega]}\hat{\xi}_I[\omega], \tag{6.4.2}$$

where $\hat{a}_{S/I}[L,\omega]$ are the modes leaving the amplification region of the ideal TWPA, $\eta_{S/I}[\omega]$ are the transmission rates of the signal/idler through the beamsplitters, and $\hat{\xi}_{S/I}[\omega]$ are the noise modes coming from the other input ports of the beamsplitters. We take this noise to be simple delta-correlated vacuum noise. Using Eqs. Equation 6.4.1 and Equation 6.4.2, we find the output field variances that characterize the output of the lossy TWPA:

$$\left\langle \left[\hat{a}_S^{\text{out}}[\omega']\right]^\dagger \hat{a}_S^{\text{out}}[\omega] \right\rangle = 2\pi\eta_S[\omega]\sinh^2(r)\delta(\omega+\omega'), \tag{6.4.3}$$

$$\left\langle \left[\hat{a}_I^{\text{out}}[-\omega']\right]^\dagger \hat{a}_I^{\text{out}}[-\omega] \right\rangle = 2\pi\eta_I[-\omega]\sinh^2(r)\delta(\omega+\omega'), \tag{6.4.4}$$

$$\left\langle \hat{a}_S^{\text{out}}[\omega]\hat{a}_I^{\text{out}}[\omega'] \right\rangle = \pi\sqrt{\eta_S[\omega]\eta_I[\omega']}\sinh(2r)\delta(\omega+\omega'). \tag{6.4.5}$$

Recall that the signal and idler channels correspond to different frequency intervals of the single nonlinear transmission line that makes up the TWPA. In the original lab frame, $\eta_S[\omega]$ describes loss at frequency $\bar{\omega}_S+\omega$, whereas $\eta_I[\omega]$ describes loss at frequency $\bar{\omega}_I+\omega = 2\bar{\omega}_P - \bar{\omega}_S + \omega$. It is thus entirely possible that these channels will experience different levels of loss. The simplest way to model this is to allow the transmissions $\eta_S[\omega]$

and $\eta_I[\omega]$ to differ from one another. While the effects of symmetric lumped element loss, $\eta_S = \eta_I$, have been studied previously in Ref. [13], asymmetric loss effects have not.

To quantify the effects of loss asymmetry on the two-mode squeezing between $\hat{a}_S[\omega]$ and $\hat{a}_I[-\omega]$, we will use the following parameterization:

$$\eta_S[\omega] = 1 - \bar{\epsilon}(1+\delta), \qquad \eta_I[-\omega] = 1 - \bar{\epsilon}(1-\delta) \tag{6.4.6}$$

where $\bar{\epsilon}$ describes the average loss and δ is the relative asymmetry, and we have suppressed the explicit ω dependence of ϵ, δ. Without loss of generality we take $\delta > 0$, implying that the signal mode has higher loss than the idler mode. As discussed in detail below, we find that asymmetry in the loss (i.e. non-zero δ) starts to play a significant role when the average amount of loss is large enough to disrupt the squeezing of an ideal TWPA. This corresponds to the condition $\bar{\epsilon} \gtrsim e^{-2r}$ (c.f. Eq. 6.2.9).

6.4.1 Thermal two-mode squeezed states (th-TMSS)

As discussed in Sec. 6.3, for each frequency ω, the output of the lossy TWPA can be mapped onto a thermal TMSS using Eqs. (6.3.8) and Eqs. (6.3.2),(6.3.3). We will use this parameterization to discuss the effect of loss.

Weak average loss

Consider first the limit of weak average loss, $\bar{\epsilon} \ll 1$ and a large intrinsic squeeze parameter r. Useful expressions are obtained by taking the large-r and small $\bar{\epsilon}$ limit while keeping $\bar{\epsilon}e^{2r}$ finite and small. This amounts to an expansion in $\bar{\epsilon}e^{2r}$. For purely symmetric loss, $\bar{\epsilon}e^{2r} \ll 1$ implies the amount of vacuum noise added from the loss channels to the output is small enough to not appreciably change the squeezing in the

output.

Following this procedure, the effective thermal occupancies $\bar{n}_{S/I}$ are given to second order in $\bar{\epsilon}$ by

$$\bar{n}_{S/I} \approx \frac{1}{4}\left(\bar{\epsilon}e^{2r}\right)(1 \pm \delta) - \frac{1}{16}\left(\bar{\epsilon}e^{2r}\right)^2(1-\delta^2) + \mathcal{O}(\bar{\epsilon}^3), \tag{6.4.7}$$

where $+/-$ corresponds to S/I. Similarly, the effective squeezing parameter is given by:

$$\frac{\cosh(R)}{\cosh(r)} \approx 1 - \frac{1}{4}\left(\bar{\epsilon}e^{2r}\right) + \frac{1}{32}\left(\bar{\epsilon}e^{2r}\right)^2\left(5-2\delta^2\right) + \mathcal{O}(\bar{\epsilon}^3). \tag{6.4.8}$$

Thus, in this regime the effect of loss asymmetry is minimal: it only changes the coefficients in the expansions for each parameter, and is not exponentially enhanced (compared to the symmetric loss case). As we now show, this is not true for larger levels of loss.

Larger average loss, weak asymmetry

For larger values of average loss, we consider the large-r limit where $\bar{\epsilon}$ is no longer arbitrarily small. In this case, $\bar{\epsilon}e^{2r}$ is no longer a small parameter and we therefore cannot expand with respect to it. Insight is instead obtained by first assuming a weak asymmetry ($\delta \ll 1$) and expanding in δ. We again consider the case of large intrinsic squeezing, and take the asymptotic large-r form of each coefficient in our expansion while keeping $\bar{\epsilon}$ fixed. Doing this, the effective thermal numbers are given by

$$\bar{n}_{S/I} \approx \frac{\sqrt{(1-\bar{\epsilon})\bar{\epsilon}}}{2}e^r \pm \frac{e^{2r}}{4}\bar{\epsilon}\delta + \frac{1}{16\sqrt{(1-\bar{\epsilon})\bar{\epsilon}}}e^{3r}\bar{\epsilon}^2\delta^2 + \mathcal{O}(\delta^3). \tag{6.4.9}$$

We now see that asymmetry has a dramatic effect: for $\delta = 0$ the thermal numbers scale as e^r, whereas with asymmetry (i.e. $\delta \neq 0$), there is a much stronger heating scaling as

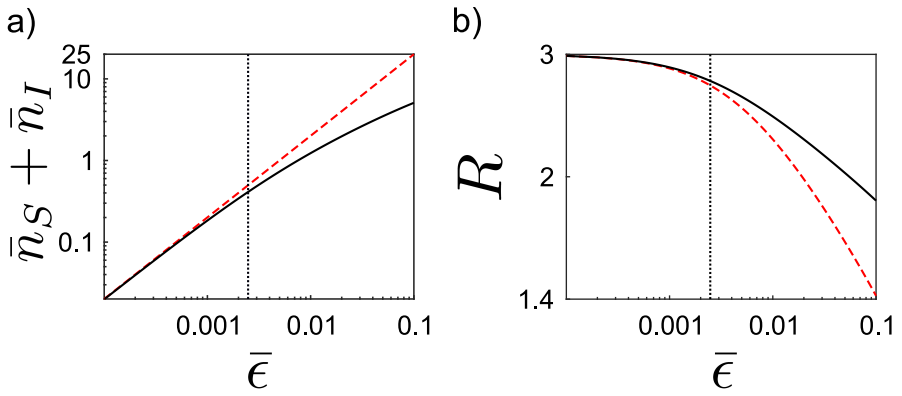

Figure 6.2: Properties of the TWPA output state as a function of average loss for the effective beamsplitter model (c.f. Sec. 6.4). Using the th-TMSS description, we plot a) the sum of the average effective thermal photon populations ($\bar{n}_S + \bar{n}_I$) and b) the effective squeezing parameter R for symmetric (black-solid curve) and fully asymmetric (red-dashed curve, asymmetry parameter $\delta = 1$) loss, as functions of the average loss $\bar{\epsilon}$. The asymmetry parameter is defined in Eq. (6.4.6). The vertical dotted lines are markers for the crossover point, $\bar{\epsilon} = e^{-2r}$; for larger $\bar{\epsilon}$ loss asymmetry has a strong impact. The ideal TWPA output squeezing parameter is $r = 3$ for both figures.

e^{3r}.

For the effective squeezing parameter in the same weak-δ, large-r regime, we find

$$\frac{\cosh(R)}{\cosh(r)} \approx \frac{\sqrt{1-\bar{\epsilon}}}{\left(1+(1-\bar{\epsilon})\bar{\epsilon}e^{2r}\right)^{1/4}} \left[1 - \frac{\bar{\epsilon}^2\delta^2 e^{4r}}{16\left[1+(1-\bar{\epsilon})\bar{\epsilon}e^{2r}\right]} + \mathcal{O}(\delta^3)\right]. \tag{6.4.10}$$

Again, we see that the loss-induced suppression of R is more pronounced in the asymmetric loss case.

The above analysis suggests the existence of a kind of crossover: for weak average loss $\bar{\epsilon} < e^{-2r}$, loss asymmetry has a minor effect on our output state, where as for larger $\bar{\epsilon}$ it has a pronounced effect. This behaviour is highlighted in Fig. 6.2, where we compare the exact behaviour of $\bar{n}_{S/I}$ and R as a function of average loss, with and without asymmetry; the cross over scale $\bar{\epsilon} \sim e^{-2r}$ beyond which asymmetry is important is clearly seen.

6.4.2 Squeezing below vacuum

As we are interested in the TWPA as a squeezing source, we consider here how loss affects the quadrature squeezing generated at the TWPA output.

Symmetric loss

Recall that our choice of pump phases ensures that without loss, the collective $\hat{X}_-$ and $\hat{P}_+$ quadratures will be squeezed, c.f. Eq. (6.2.7). For the symmetric loss case ($\eta_S = \eta_I \equiv \eta$), we find directly from Eqs. Equation 6.4.3 and Equation 6.4.5 that

$$S^{\rm sym}_{\hat{X}_-}[\omega] = \frac{1}{2}\left[1 - \eta + \eta e^{-2r}\right] \tag{6.4.11}$$

with a similar result for $S^{\rm sym}_{\hat{P}_+}[\omega]$. As might be expected, with symmetric loss, we simply interpolate between the perfect squeezed state at $\eta = 1$ and a vacuum state when $\eta = 0$. Note that unless the loss level is 100%, there is always some squeezing in the output in this symmetric loss case.

Asymmetric loss

When the transmission rates for the signal and idler modes are different, the noise spectral density of the minus quadrature of the output field is

$$\begin{aligned} S^{\rm asym}_{\hat{X}_-}[\omega] = \frac{1}{2}\Bigg[\left(1 - \frac{\eta_S + \eta_I}{2}\right) + \frac{e^{-2r}}{4}\left(\sqrt{\eta_S} + \sqrt{\eta_I}\right)^2 \\ + \frac{e^{2r}}{4}\left(\sqrt{\eta_S} - \sqrt{\eta_I}\right)^2\Bigg]. \end{aligned} \tag{6.4.12}$$

In this expression, η_S (η_I) is evaluated at frequency $+\omega$ ($-\omega$). The first bracketed term of Eq. Equation 6.4.12 describes the vacuum noise added to the output field as a result of the lossy transmission lines, and the second term describes the usual squeezed noise (which

is suppressed when $\eta_s, \eta_I < 1$). The third term, unique to asymmetric loss, describes amplified noise $\propto e^{2r}$ that is now mixed into the minus quadrature due to the asymmetry in the beamsplitters' transmission rates. This mixing in of amplified noise is clearly detrimental to achieving squeezing below zero point. In Fig. 6.3 we see that for larger levels of average loss, the squeezing for asymmetric loss is above zero point, whereas for symmetric loss it is still below zero point. Loss asymmetries can thus have a large impact on the production of squeezing, and will greatly affect schemes that use the output of a TWPA as a squeezing source, such as two-mode qubit readout [10].

Squeezing of asymmetric collective quadratures

While the symmetric $\hat{X}_-$ collective quadrature rapidly becomes unsqueezed with loss asymmetry, one might ask whether there are other collective quadratures that remain squeezed. It is easy to verify that any symmetric collective quadrature of the form $\sqrt{2}\hat{X}_{\text{sym}} = \hat{X}_S + e^{i\phi}\hat{X}_I$ will have a contribution from amplified noise ($\propto e^{2r}$) in its noise spectral density when there is loss asymmetry; hence, loss asymmetry prevents any such quadrature from being squeezed.

That being said, one can define *asymmetric* collective quadratures (i.e. S and I modes weighted unequally) that exhibits squeezing even with asymmetric loss. We define

$$\hat{X}_-^{\text{asym}} = \cos\theta \hat{X}_S^{\text{out}} - \sin\theta \hat{X}_I^{\text{out}}, \tag{6.4.13}$$

$$\hat{P}_+^{\text{asym}} = \cos\theta \hat{P}_S^{\text{out}} + \sin\theta \hat{P}_I^{\text{out}}. \tag{6.4.14}$$

By taking the parameter $\tan\theta = \sqrt{\eta_S/\eta_I}$, one finds

$$S_{\hat{X}_-^{\text{asym}}}[\omega] = \frac{1}{2}\left[1 - \frac{2\eta_S\eta_I}{\eta_S + \eta_I}\left(1 - e^{-2r}\right)\right]. \tag{6.4.15}$$

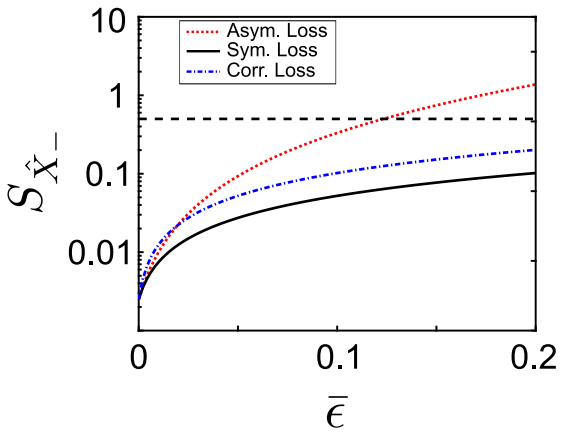

Figure 6.3: Output squeezing of the output state of a TWPA, for the beamsplitter model (c.f. section 6.4), as a function of average loss $\bar{\epsilon}$. For a fully asymmetric situation where only the signal mode is lossy (i.e. $\delta = 1$ in Eq. (6.4.6), red curve), loss can destroy any squeezing below the vacuum level. In contrast, if the loss is symmetric, one always has squeezing below vacuum (black curve). Even with fully asymmetric loss, one can use our proposed correction scheme (c.f. section 6.4.4) to regain squeezing below zero-point (blue curve). Note that while asymmetric loss can kill vacuum squeezing, signal-idler entanglement always remains non-zero (see Fig. 6.4).

with a similar result for $S_{\hat{P}_+^{\rm asym}}$. Where again, in this expression, η_S (η_I) is evaluated at frequency $+\omega$ ($-\omega$). We thus see that these quadratures are squeezed below vacuum whenever $r > 0$, irrespective of loss asymmetries. Note crucially that the definition of this quadrature depends sensitively on the amount of loss asymmetry; further for $\theta \neq \pi/4$, the squeezed collective quadratures $\hat{X}_-^{\rm asym}, \hat{P}_+^{\rm asym}$ do not commute with one another.

The utility of having such non-commuting, asymmetric quadratures squeezed is mixed. They do imply the presence of entanglement, as they allow violation of generalized versions of the well known Duan and Tan inequalities [14, 22]. As we will see in Sec. 6.4.3, this implies that loss asymmetry does not prevent using the TWPA output state to entangle other systems. However, there are other applications that crucially require two commuting joint quadratures to be squeezed, e.g. the enhanced dispersive measurement scheme described in Ref. [10].

6.4.3 Purity and logarithmic negativity

We now study how loss (modelled using the lumped-element approach) impacts the purity and entanglement (as measured by the logarithmic negativity [14]) of the TWPA output state at a given frequency.

Symmetric loss

Without any loss asymmetry (i.e. $\delta = 0$ in Eq. (6.4.6)), the log negativity is given by:

$$E_{\mathrm{N}} = -\ln\left[e^{-2r} + (1 - e^{-2r})\bar{\epsilon}\right]. \tag{6.4.16}$$

This saturates to $E_{\mathrm{N}} = \ln\left[1/\bar{\epsilon}\right] > 0$ in the large r limit. The logarithmic negativity mimics the behaviour of the symmetric squeezed quadrature (see Eq. (6.4.11)): it decreases monotonically from $2r$ to 0 as the loss $\bar{\epsilon}$ increases.

In contrast, the purity of the state for symmetric losses is given by

$$\mu = \frac{1}{1 + 2(1 - \bar{\epsilon})\bar{\epsilon}(\cosh(2r) - 1)}. \tag{6.4.17}$$

For any nonzero loss $\bar{\epsilon}$, the purity decays exponentially as e^{-2r} in the large-r limit. Thus, for large intrinsic squeezing r, even a small amount of loss leads to a highly impure output state that nonetheless possesses a potentially large logarithmic negativity. The utility of such a state in potential applications is thus at first glance somewhat suspect.

To test the utility of such an entangled thermal two-mode squeezed state, we consider the remote entanglement protocol of Ref. [11]. Here, the signal and idler of a TMSS are each sent to a separate qubit, with the goal of stabilizing a two-qubit entangled state (see Appendix 6.A for further details). In the ideal (zero loss) case, when the signal (idler) qubit is resonant with the signal (idler) mode, the steady-state of the two-qubit system is

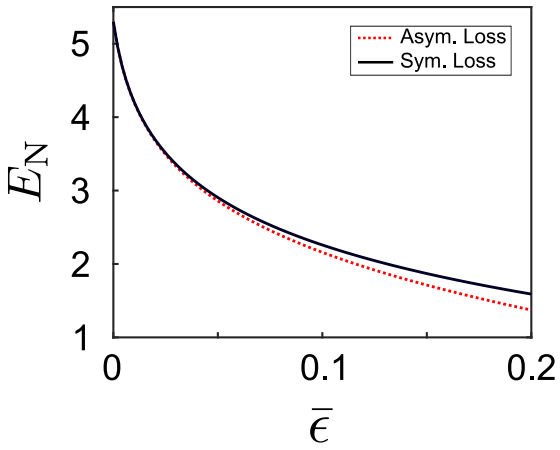

Figure 6.4: Logarithmic negativity of the output state of a TWPA, for the beamsplitter model (c.f. section 6.4), as a function of average loss $\bar{\epsilon}$. For asymmetric loss (red curve), we consider the maximally asymmetric case where all loss in in the signal mode (i.e. $\delta = 1$ in Eq. (6.4.6)). Logarithmic negativity is much less sensitive to asymmetry (c.f. section 6.4.3). Even with asymmetry we retain non-zero logarithmic negativity.

a pure entangled state, and reaches a maximally entangled Bell state in the large gain limit [11].

The situation changes when there is loss, and the output state from the TWPA becomes a th-TMSS. Consider first the case where the loss is identical for signal and idler modes, and completely frequency independent. As was shown in Ref. [13], the qubit entanglement (quantified by the concurrence [23]) has a distinct maximum as a function of ideal squeezing parameter r (see Fig. 6.5), which is at odds with the fact that the logarithmic negativity of a th-TMSS increases monotonically with r. We show here that this can be simply understood as being a result of the decreasing purity of the th-TMSS with increasing r.

An example of this is shown in Fig. 6.5, where we plot the qubit concurrence in the steady-state ($C(\rho_{\rm SS})$), as a function of the intrinsic gain $G_{\rm ideal} = \cosh^2 r$ of the TWPA. We also plot the corresponding th-TMSS purity and logarithmic negativity (normalized so that its maximum is one).The qubit concurrence is calculated by solving for the

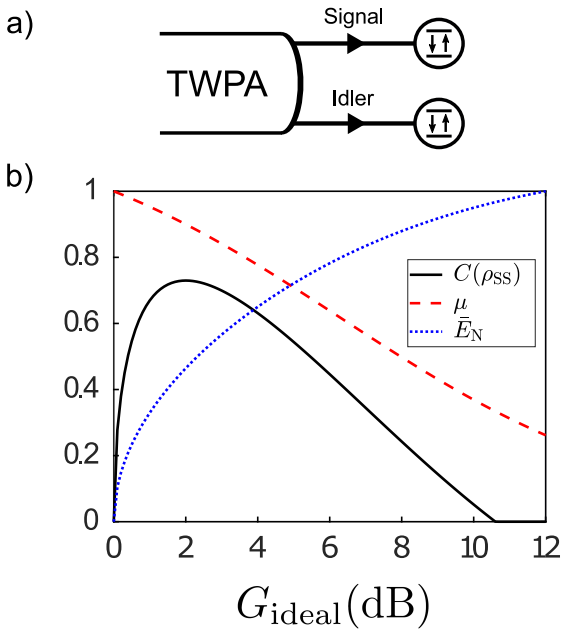

Figure 6.5: Signal and idler modes at the output of a TWPA are each sent to separate qubits, resulting in the entanglement of qubits. a) Schematic figure of protocol. b) Concurrence ($C(\rho_{\rm SS})$) of the two-qubit steady-state of Eq. (6.A.1), along with the purity (μ), and logarithmic negativity ($E_{\rm N}$) of the qubits' thermal TMSS environment, all as functions of r. The logarithmic negativity is normalized such that its maximum value is one, i.e. the plot shows $\bar{E}_{\rm N} = E_{\rm N}/E_{\rm N}^{\rm max}$. While $E_{\rm N}$ saturates at a non-zero value, the qubit concurrence has a distinct maximum, eventually dropping to zero as the purity of the thermal TMSS decays. $\bar{\epsilon} = 0.05$ and $\delta = 0$ for these curves.

steady-state of the master equation given in Appendix 6.A. As can be seen, for increasing r the qubit entanglement initially grows as the th-TMSS entanglement; however, very quickly the th-TMSS becomes too impure, and the qubit entanglement rapidly decays.

This qubit-based example highlights the fact that the logarithmic negativity alone is not enough to quantify the usefulness of the entanglement found in a th-TMSS, and therefore from the output of a lossy TWPA. The purity of the state also plays a crucial role.

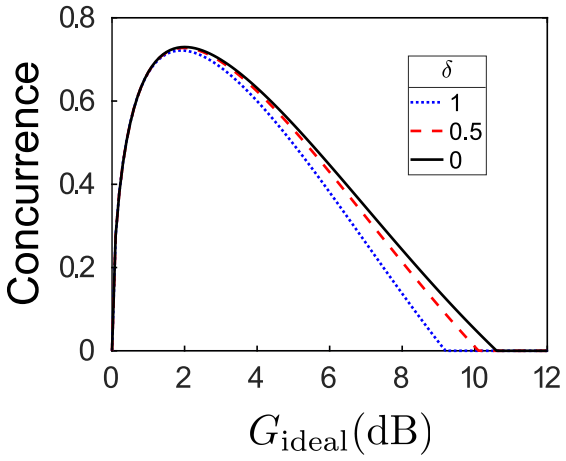

Figure 6.6: Concurrence ($C(\rho_{\text{SS}})$) of the two-qubit steady-state of Eq. , as a function of r, for various values of loss asymmetry δ, with $\bar{\epsilon} = 0.05$ for all three curves. While an asymmetric th-TMSS leads to lower qubit entanglement the difference is minimal, and the asymmetric states perform almost equally as well as the symmetric state in producing qubit entanglement.

Asymmetric loss

Extending to the asymmetric case, $\delta \neq 0$, we use the small $\bar{\epsilon}$ expansion for the three th-TMSS parameters derived in Sec. 6.3 to calculate asymptotic forms of the logarithmic negativity and purity. To second order in $\bar{\epsilon}$ this gives a logarithmic negativity

$$E_{\text{N}} \approx -\ln\left[e^{-2r} + (1 - e^{-2r})\bar{\epsilon} + \tanh(r)\bar{\epsilon}^2\delta^2\right]. \tag{6.4.18}$$

While introducing asymmetry further decreases the logarithmic negativity, in the large r limit asymmetry adds only a constant correction of order $\bar{\epsilon}^2$ to the expression, and hence does not affect the th-TMSS entanglement significantly.

The purity, similarly to the logarithmic negativity, is also only minimally affected by asymmetry. In the large r limit, the expansion takes the form

$$\mu \approx \frac{1}{1 + 2(1-\bar{\epsilon})\bar{\epsilon}(\cosh(2r) - 1)} - \left(\frac{\bar{\epsilon}\delta}{2(1-\bar{\epsilon})\bar{\epsilon}}\right)^2 e^{-2r}. \tag{6.4.19}$$

As before, the asymmetric correction can be thought of as a renormalization of the coefficient of the exponential decay (since the first term also decays as $\exp(-2r)$ in the large-r limit when $\bar{\epsilon} > 0$).

As neither the logarithmic negativity or purity are affected drastically by loss asymmetry it is likely that an asymmetric version of the two-qubit entanglement protocol considered previously will also be only minimally affected. The concurrence of the two-qubit steady-state is shown in Fig. 6.6 for various amounts of loss asymmetry, and as can be seen, the fully asymmetric case is only marginally worse than the symmetric case, and the asymmetric state is almost as useful as the symmetric state for generating two-qubit entanglement.

6.4.4 Correcting for asymmetric loss

We now consider how to correct for asymmetric loss such that we are able to achieve squeezing below vacuum of *symmetric* and commuting joint quadratures, while ideally minimally affecting the purity and logarithmic negativity. The idea here is simple: to counteract asymmetric loss, simply add extra loss to the less lossy channel (i.e. the mode with the larger transmission rate in its effective beam-splitter). For our choice of parametrization (see Eq. (6.4.6)), the signal mode has more loss ($\eta_S < \eta_I$), one adds an additional beamsplitter at the output mode with transmission rate $\eta_I' < 1$ (thus attenuating the idler output). Choosing $\eta_I' = \eta_S/\eta_I$ results in a noise spectral density of the final output X_- quadrature given by

$$S_{\hat{X}_-}^{\text{cor}} = \frac{1}{2}\left[1 - \eta_S + \eta_S e^{-2r}\right], \tag{6.4.20}$$

which for $r > 0$ is below zero point for any $\eta_S > 0$. Remarkably, by deliberately attenuating the output of the lossy TWPA by a specific amount, we have regained the

possibility of squeezing below zero point in a symmetric joint quadrature, as is shown in Fig. 6.3. Thus, the Tan and Duan inequalities can now be violated while using symmetric, commuting joint quadratures. Further, the purity and logarithmic negativity of the final output state are minimally affected, taking the value of that for symmetric loss with transmission rate η_S. Overall, this deliberate introduction of loss can increase the usefulness of the lumped element model lossy TWPA output state in certain applications that require two-mode squeezing of commuting joint quadratures.

6.5 Distributed Loss

We now consider a more realistic model of an imperfect TWPA, where loss occurs continuously as photons propagate through the device, and where there is imperfect phase matching between pump, signal and idler. We start again with the set-up shown in Fig. 6.1b), as described by Eq. Equation 6.2.1. We now allow both signal idler modes to decay, at independent rates, as they interact parametrically in the region between $x = 0$ to $x = L$.

To implement this distributed loss, we follow the approach used in Ref. [16] to model loss in a degenerate TWPA. We imagine connecting independent loss ports at a set of regularly spaced points x_j along the TWPA; at each point, there is an independent loss channel for signal and for idler photons. These loss ports both provide a means for photons to leave the TWPA, and also inject additional vacuum noise into signal and idler modes; their effects are described by standard input-output theory. We label the injected vacuum noise from these ports as $\hat{a}^{(\text{loss})}_{S/I}(x)$ (where x labels the noise injected at position x). The coupling rate to the loss port at each point is taken to be the same: κ_S for signal photons, κ_I for idler photons. Finally we consider the limit where the spacing between the coupling points x_j tends to zero, resulting in a continuous loss per unit length [16].

In addition to this distributed loss, we also now include the effects of imperfect phase matching between pump, signal and idler modes. Such phase matching is known to be important in realistic TWPAs constructed using Josephson junctions (c.f. Ref [4, 5]). In such system the group velocity is the same for all modes (as they correspond to the same transmission line), but a phase mismatch can arise from nonlinearity-induced frequency shifts. Imperfect phase matching is characterized by a non-zero wavevector mismatch $\Delta k = 2k_P - k_S - k_I$. For non-zero mismatch, we can no longer ignore the phase factor in Eq.(6.2.2).

With both of these imperfections included, the Heisenberg-Langevin equations for our system become:

$$\left(\partial_t + v\partial_x + \frac{i\Delta k}{2}\right)\hat{a}_S(x) = \nu\hat{a}_I^\dagger(x) - \frac{\kappa_S}{2}\hat{a}_S(x) + \sqrt{\kappa_S}\hat{a}_S^{(\text{loss})}(x), \tag{6.5.1}$$

$$\left(\partial_t + v\partial_x - \frac{i\Delta k}{2}\right)\hat{a}_I^\dagger(x) = \nu\hat{a}_S(x) - \frac{\kappa_I}{2}\hat{a}_I^\dagger(x) + \sqrt{\kappa_I}\hat{a}_I^{\dagger(\text{loss})}(x). \tag{6.5.2}$$

Here v is the group velocity (taken to be the same for signal and idler), ν is the parametric interaction strength, and $\kappa_{S/I}$ are the respective decay rates for the signal/idler modes.These equations are valid from $x = 0$ to $x = L$.

Solving the equations of motion in frequency space (see Appendix 6.B), we are able to relate the modes at the end of the amplification regions to those at the beginning, allowing us to calculate the system's scattering matrix and performance as a non-degenerate parametric amplifier. Note that in our model, the frequency dependence drops out in the quantities of interest. From the solutions for the output modes (see Appendix 6.B), the frequency dependence comes as a phase factor and this cancels out when calculating the gain and squeezing generated by our TWPA.

6.5.1 Gain

Effects of asymmetric loss

For the case of symmetric, distributed loss (i.e. $\kappa_S = \kappa_I$), we find the gain is given by

$$\begin{aligned} G_{\text{sym}} &= e^{-\bar{\kappa}L/v} \cosh^2(L\nu/v) \\ &\approx \frac{e^{(2\nu-\bar{\kappa})L/v}}{4} \end{aligned} \tag{6.5.3}$$

which is equivalent to the result of Ref. [16] obtained for a degenerate parametric amplifier. This result can be mapped to the effective beam-splitter model of loss in Sec. 6.4, if we take the beamsplitter transmission to be $\eta = e^{-\bar{\kappa}L/v}$.

For the case of asymmetric loss, a simple mapping to the effective beam-splitter model is no longer possible. Letting $\kappa_S = \bar{\kappa} + \epsilon$, $\kappa_I = \bar{\kappa} - \epsilon$, and considering the large length limit, we find the gain with asymmetric loss to be

$$G_{\text{asym}} \approx \frac{e^{(2\tilde{\nu}-\bar{\kappa})L/v}}{4} \left[1 - \frac{\epsilon}{2\tilde{\nu}}\right]^2, \tag{6.5.4}$$

where

$$\tilde{\nu} = \sqrt{\nu^2 + \left(\frac{\epsilon}{2}\right)^2} \tag{6.5.5}$$

plays the role of renormalized interaction amplitude.

Comparing symmetric and asymmetric loss results, we see that the for fixed average loss $\bar{\kappa}$, introducing loss asymmetry can increase the gain through its exponential dependence on length (outweighing any reduction due to the non-exponential prefactor). While this might seem surprising, a similar effect occurs in a simple cavity-based non-degenerate parametric amplifier. Following the results of Ref. [3], the zero-frequency

gain for such a system is given by

$$\sqrt{G} = \frac{Q^2+1}{Q^2-1} \;;\; Q = \frac{2\nu}{\sqrt{\kappa_S \kappa_I}} = \frac{2\nu}{\bar{\kappa}\sqrt{1-\epsilon^2}}. \tag{6.5.6}$$

where $\kappa_{S/I} = \bar{\kappa} \pm \epsilon$ are the damping rates of signal and idler cavities, and ν is again the parametric interaction amplitude. Again, keeping $\bar{\kappa}$ fixed and increasing ϵ increases the gain.

Phase mismatch

We now consider the effects of having imperfect phase matching ($\Delta k \neq 0$) in addition to asymmetric, distributed loss. For small asymmetry and in the large length limit, the gain becomes

$$G \approx e^{-\bar{\kappa}L/v} e^{2L\Re(\tilde{\nu})/v} \left| 1 - \frac{\epsilon + i\Delta k}{2\tilde{\nu}} \right|^2. \tag{6.5.7}$$

where the effective complex parametric interaction amplitude is defined as

$$\tilde{\nu} = \sqrt{\nu^2 + \left(\frac{\epsilon + i\Delta k}{2}\right)^2} \tag{6.5.8}$$

Without asymmetry, and for large enough Δk, the effective interaction amplitude $\tilde{\nu}$ becomes purely complex and there is no amplification (i.e. G remains smaller than one) [4, 13]. The above result suggests that the effective increase in the parametric interaction amplitude brought on by loss asymmetry can be used to partially offset the decrease in gain due to phase-mismatch.

6.5.2 Added noise

We also consider the added noise of our amplifier with distributed loss and imperfect phase matching. Recall that even in the ideal case, a non-degenerate parametric amplifier must add half a quantum of noise to the input signal. To calculate the added noise, denoted by S_{added}, we look at the spectral density of the output signal mode, normalize by the gain and subtract off the input singal contribution to obtain

$$2\pi S_{\text{added}}\delta(\omega+\omega') \equiv \frac{\langle\{a_{S,out}[\omega'], a^\dagger_{S,out}[\omega]\}\rangle}{2G_{\text{asym}}} - \frac{\langle\{a_{S,in}[\omega'], a^\dagger_{S,in}[\omega]\}\rangle}{2}. \tag{6.5.9}$$

Including both asymmetric loss and phase mismatch, in the large gain, small asymmetry , and small phase mismatch limit, we find

$$S_{\text{added}} \approx \frac{1}{2} + \frac{1}{2\nu-\bar{\kappa}}\left(\bar{\kappa}+\epsilon+\frac{(\Delta k^2-\epsilon^2)}{4\nu(2\nu-\kappa)}\right), \tag{6.5.10}$$

where the frequency dependent phase factors have cancelled out due to the δ-functions. We see that loss increases the added noise above the quantum-limited value of $1/2$ a quantum, and that this extra noise is sensitive to the amount of asymmetry. The first order in asymmetry term ($\propto \epsilon$) reflects the fact that $\bar{\kappa}+\epsilon$ is the loss of the signal mode. The additional terms (which involve both the amount of phase mismatch and asymmetry ϵ) reflect the effective modification of the parametric interaction amplitude due to imperfections, c.f. Eq. (6.5.8)

6.5.3 Phase-matched symmetric squeezing

Having analyzed how the gain and added noise are affected by asymmetric loss, we now focus on the squeezing. We begin by considering the symmetric case where the signal and idler modes decay at the same rate (i.e. $\kappa_S = \kappa_I \equiv \bar{\kappa}$) and the modes are

phase-matched ($\Delta k = 0$). In this case, we find that the noise in the squeezed output quadrature is given by

$$S_{\hat{X}_-}^{\mathrm{sym}}[\omega] = \frac{1}{2(\bar{\kappa} + 2\nu)} \left(\bar{\kappa} + 2\nu e^{-2L\nu/v} e^{-\bar{\kappa}L/v}\right). \tag{6.5.11}$$

Note there is no mixing-in of amplified noise, and that taking the large-length limit is always beneficial, as the squeezing decreases monotonically with L, saturating at a value $\bar{\kappa}/(2(2\nu + \bar{\kappa}))$ (c.f. Fig. 6.7).

We find that for symmetric amounts of loss in signal and idler modes, the distributed loss model predicts a less severe degradation of squeezing than the lumped element model of Sec. 6.4. To see this, we first re-express Eq. (6.5.11) as

$$S_{\hat{X}_-}^{\mathrm{sym}}[\omega] = \frac{1}{2}\left[(1-\eta)\, e^{-2r'} + \eta e^{-2r}\right] \tag{6.5.12}$$

where

$$\eta = \frac{2\nu}{\bar{\kappa} + 2\nu} e^{-\bar{\kappa}L/v}, \tag{6.5.13}$$

$$e^{-2r'} = \frac{\bar{\kappa}}{\bar{\kappa} + 2\nu\left(1 - e^{-\bar{\kappa}L/v}\right)}, \tag{6.5.14}$$

and $r = L\nu/v$. This expression is reminiscent of Eq. (6.4.11) for the squeezing in the lumped element model of loss. It is in fact equivalent to a lumped element loss model where squeezed light (characterized by squeezing parameter $r' > 0$) is injected into the dark port of the effective beam-splitter (rather than just vacuum noise). By varying the transmission coefficient (via $\bar{\kappa}$), we are interpolating between two different levels of squeezing rather than one level of squeezing and vacuum (no squeezing). Thus, unlike the symmetric lumped element model, the symmetric distributed model always has

squeezing below zero point.

A heuristic understanding of this effect comes from our model of symmetric distributed loss, where we consider vacuum noise entering throughout the TWPA, (i.e. from $x = 0$ to $x = L$). One might naively expect this to be detrimental; however, these fluctuations are themselves squeezed by the TWPA interaction. In fact, by considering a spatially varying decay rate ($\bar{\kappa} = \bar{\kappa}(x)$), we can show that only the fluctuations entering near the end of the TWPA section matter. For such a decay rate, the noise in the squeezed output quadrature takes the form

$$2S^{\text{sym}}_{\hat{X}_-}[\omega] = e^{-\frac{1}{v}\int_0^L dx\bar{\kappa}(x)}e^{-2L\nu/v} + \frac{1}{v}\int_0^L dx\ \bar{\kappa}(x)e^{-\frac{1}{v}\int_x^L dx'\bar{\kappa}(x')}e^{-2\nu(L-x)/v} \quad (6.5.15)$$

where the second term corresponds to the contribution from vacuum fluctuations injected from the loss ports . Note that all frequency dependence has cancelled out in the expression above. In the large-length limit and assuming $\nu \gg \bar{\kappa}(x)\ \forall x$, the contribution to the squeezing from the added noise integral is exponentially insensitive to noise close to the input port. In other words, it is only the added noise coming from a small region near the end of the amplification region which affects the squeezing. Hence, by minimizing the decay rate near the end of the TWPA section, one could obtain higher amounts of squeezing.

6.5.4 Phase-matched asymmetric squeezing

Next, we consider the asymmetric loss case where $\kappa_S \neq \kappa_I$, while keeping the phase-matching condition ($\Delta k = 0$). Without loss of generality, we assume $\kappa_S > \kappa_I$ and define $\kappa_S = \bar{\kappa} + \epsilon$, $\kappa_I = \bar{\kappa} - \epsilon$, where $\bar{\kappa}$ is the average loss and ϵ is the asymmetry. The full expression for $S^{\text{asym}}_{\hat{X}_-}[\omega]$ is cumbersome, and so we consider the low-asymmetry limit. Expanding in the small parameter ϵ/ν and keeping only the lowest order term for each

possible component of the noise (constant, squeezed, and amplified), we find

$$S_{\hat{X}_-}^{\text{asym}}[\omega] \approx \frac{1}{2(\bar{\kappa}+2\nu)}\left[\bar{\kappa}+2\nu e^{-2L\tilde{\nu}/v}e^{-\bar{\kappa}L/v}\right]+G_{\text{eff}}\frac{\epsilon^2 e^{-\bar{\kappa}L/v}}{4\nu(2\nu-\bar{\kappa})}, \tag{6.5.16}$$

where

$$G_{\text{eff}} = \frac{e^{2L\tilde{\nu}/v}}{4}, \tag{6.5.17}$$

is an effective gain parameter and $\tilde{\nu}$ is the renormalized interaction strength given by Eq. (6.5.5). As can be seen in Eq. Equation 6.5.16, asymmetric distributed loss introduces a component to the noise spectral density which scales like the gain of the TWPA. Similarly to the result of Eq. Equation 6.4.12 for the lumped element model of asymmetric loss, we find that asymmetric distributed loss introduces amplified noise to the X_- quadrature.

If the gain is large enough this amplified component dominates the noise, even for small asymmetries. This can be seen in Fig. 6.7. The squeezing for asymmetric distributed loss (red curve) initially goes below zero point, however, as the gain for the ideal TWPA increases, our X_-^{out} quadrature itself experiences gain. Unlike the symmetric distributed loss case, there is now an optimal length for maximal squeezing below zero point. Working in the low-asymmetry regime, we find that the optimal length is

$$L_{\text{opt}} \approx \frac{v}{2\nu}\log\frac{\nu}{|\kappa_S-\kappa_I|}. \tag{6.5.18}$$

Fortunately, we can do better than just using the optimal length to achieve squeezing below zero point in the asymmetric distributed loss case. By correcting for the asymmetry, we can remove this length limitation.

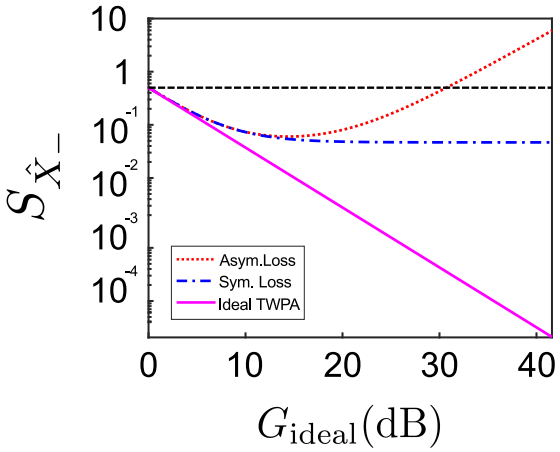

Figure 6.7: Output squeezing of a TWPA for the distributed loss model (c.f. section 6.5). Curves are plotted as a function of the gain of the ideal distributed model (see Eq. 6.2.4), where the ideal gain is increased by increasing the length L. We set $\nu/v = 1$, $\bar{\kappa}/v = 1/5$, and $\epsilon = \bar{\kappa}/2$. As we increase gain, asymmetric loss (red curve) goes above zero-point squeezing whereas symmetric loss (blue curve) saturates to a value below zero point squeezing. The dashed black line represents zero-point squeezing and the pink curve represents the output squeezing of an ideal TWPA.

6.5.5 Correcting for asymmetric distributed loss

To correct for the asymmetry, we wish to remove the amplified component of the noise in Eq. Equation 6.5.16. Similarly to the lumped element model, we do so by introducing a beamsplitter on the mode with the smaller decay rate (idler mode), therefore adding additional loss to this mode. Using the full expression for $S^{\text{asym}}_{\hat{X}_-}[\omega]$, we find that setting the transmission of this beamsplitter to

$$\sqrt{\eta_I} = \frac{\nu}{\sqrt{\nu^2 + \left(\frac{\epsilon}{2}\right)^2} + \frac{\epsilon}{2}}, \tag{6.5.19}$$

completely cancels the coefficient of the amplified component of the noise to all orders. The noise is now given, to lowest order, by the expression

$$S_{\hat{X}_-}[\omega] \approx \frac{1}{2(\bar{\kappa} + 2\nu)} \left(\bar{\kappa} + 2\nu e^{-2L\tilde{\nu}/v} e^{-\bar{\kappa}L/v}\right) + \frac{1}{4}(1 - \eta_I). \tag{6.5.20}$$

We see that the corrected low-asymmetry distributed loss squeezing is what would be obtained with symmetric distributed loss (at decay rate $\bar{\kappa}$) plus a constant term coming from the additional beamsplitter loss. Once again, the large-length limit is always beneficial after this correction. Importantly, for sufficiently large gain, adding loss (through the additional beam splitter) allows for squeezing below zero point of the commuting, symmetrically-defined collective quadratures X_- and P_+.

6.6 Conclusion

In this work, we have studied the effects of frequency-dependent loss on the output state of a TWPA, where photons at signal and idler frequencies see different amounts of dissipation. Within a simple lumped-element model of loss , we have shown that asymmetric loss can be very detrimental to output squeezing, yet has only minimal effect on the entanglement. It is thus possible to have no joint quadrature squeezing while still having entanglement, and this entanglement may even be useful. By further adding loss to the least lossy mode, we have shown that we are able to regain squeezing below zero point; this could be useful in applications that require the squeezing of symmetric and commuting collective quadratures.

Using a more realistic distributed loss model, we have shown that asymmetric loss increases the gain of the TWPA. By effectively modifying the interaction strength, the exponential dependence of the gain increases. Asymmetric loss can also offset the effects of phase mismatch, to a certain extent, and allow for gain in a situation where it would not occur otherwise. We have shown that when asymmetric loss in included, there is an optimal length for the TWPA after which output squeezing starts to deteriorate. By mapping the distributed loss to a lumped-element model, we show that distributed loss can be thought of as lumped-element loss where we inject squeezed noise rather than

vacuum, and that the output squeezing can be corrected in a similar manner as for the true lumped element model.

We note that while we are motivated by the Josephson traveling-wave parametric amplifiers used in circuit QED [5], our results apply universally to traveling-wave non-degenerate parametric amplifiers of any design at any frequency [17–20, 24–26]. Furthermore, the lumped element model applies to any two-mode squeezing source that is injected into lossy waveguides [27–30], and our work represents the first exploration of the effects of asymmetric loss in such systems.

6.A Master equation for two qubits driven by an imperfect TWPA

The evolution of a pair of qubits sharing a correlated environment, as described in Refs. [11, 13], can be described by the master equation (for a detailed derivation consult Ref. [13])

$$\begin{aligned}\dot{\rho}_q = &\sum_{k=1,2} \gamma_k \left[(1+N_k)\,\mathcal{D}[\hat{\sigma}_-^k] + N_k \mathcal{D}[\hat{\sigma}_+^k]\right] \rho_q \\ &- \sqrt{\gamma_1\gamma_2} M \left(\hat{\sigma}_+^1 \rho_q \hat{\sigma}_+^2 + \hat{\sigma}_+^2 \rho_q \hat{\sigma}_+^1 - \left\{\hat{\sigma}_+^1 \hat{\sigma}_+^2, \rho_q\right\} + h.c.\right)\end{aligned} \tag{6.A.1}$$

where $\mathcal{D}[x]\rho = x\rho x^\dagger - \left\{x^\dagger x, \rho_q\right\}/2$ is the usual dissipator, $\hat{\sigma}_\pm^k$ are the raising and lowering operators for qubit k, and γ_k is the coupling rate between qubit k and the environment. The thermal photon population of the environment for each qubit (N_k), defined by $\left\langle \hat{a}_k^\dagger(\omega_k)\hat{a}_k(\omega_k')\right\rangle = 2\pi\, N_k\, \delta(\omega_k + \omega_k')$, as well as the two-qubit anomalous bath correlator (M), defined by $\langle \hat{a}_1(\omega_1)\hat{a}_2(\omega_2)\rangle = 2\pi\, M\, \delta(\omega_1 + \omega_2)$, depend on the nature of the environment at the qubit frequencies $\omega_{1/2}$. For the output from a

lossy TWPA with signal/idler mode resonant with qubit 1/2 at frequency $\omega/-\omega$, these quantities are given by

$$N_{1/2} = \bar{n}_{S/I} + (\bar{n}_S + \bar{n}_I + 1)\sinh^2(R) = \eta_{S/I}\sinh^2(r), \tag{6.A.2}$$

$$M = \frac{\bar{n}_S + \bar{n}_I + 1}{2}\sinh(2R) = \frac{\sqrt{\eta_S\eta_I}}{2}\sinh(2r), \tag{6.A.3}$$

where we have given the form of N_k and M in terms of both the th-TMSS parameterization and the lumped element lossy beamsplitter model. Recall that $\eta_S(\eta_I)$ is evaluated at frequency $\omega(-\omega)$.

For the results of section 6.4.3 shown in Figs. 6.5 and 6.6, we solve for the steady-state of Eq. Equation 6.A.1 numerically, and calculate the concurrence of this state. We set $\gamma_1 = \gamma_2 = \gamma$ for convenience, and in this case the numerical value of γ has no effect on the form of the steady-state.

6.B Distributted loss solutions

In this appendix, we provide details on how to obtain the solutions to the distributed-loss model. From the Hamiltonian of Eq. (6.2.1) we obtain the followiing Heisenberg-Langevin equations of motion:

$$\left(\partial_t + v\partial_x + \frac{i\Delta k}{2}\right)\hat{a}_S(x) = \nu\hat{a}_I^\dagger(x) - \frac{\kappa_S}{2}\hat{a}_S(x) + \sqrt{\kappa_S}\hat{a}_S^{(\text{loss})}(x), \tag{6.B.1}$$

$$\left(\partial_t + v\partial_x - \frac{i\Delta k}{2}\right)\hat{a}_I^\dagger(x) = \nu\hat{a}_S(x) - \frac{\kappa_I}{2}\hat{a}_I^\dagger(x) + \sqrt{\kappa_I}\hat{a}_I^{\dagger(\text{loss})}(x), \tag{6.B.2}$$

where $\hat{a}_{S/I}^{(\text{loss})}(x)$ is vacuum noise injected at position x. To obtain the expressions in this form, we have gauged away the phase of the parametric interaction (recall Eq. (6.2.2)).

Before tackling the full solution, we begin by solving the differential equations without source terms ($\hat{a}_{S/I}^{(\text{loss})}(x)$). We Fourier transform to frequency space and express everything in matrix form

$$\partial_x \begin{pmatrix} \hat{a}_S[x,\omega] \\ \hat{a}_I^\dagger[x,\omega] \end{pmatrix} = \tag{6.B.3}$$
$$\frac{1}{v} \begin{pmatrix} i\omega - (\kappa_S + i\Delta k)/2 & \nu \\ \nu & i\omega - (\kappa_I - i\Delta k)/2 \end{pmatrix} \begin{pmatrix} \hat{a}_S[x,\omega] \\ \hat{a}_I^\dagger[x,\omega] \end{pmatrix}.$$

The eigenvalues of the matrix on the right-hand side are

$$\lambda_\pm = \frac{1}{v}\left(i\omega - \left(\tfrac{\kappa_S+\kappa_I}{4}\right) \pm \sqrt{\nu^2 + \left(\tfrac{\kappa_S-\kappa_I+2i\Delta k}{4}\right)^2}\right) \tag{6.B.4}$$

and the (un-normalized) eigenvectors are

$$\vec{v}_\pm = \left(\tfrac{\kappa_I-\kappa_S-2i\Delta k}{4\nu} \pm \sqrt{1 + \left(\tfrac{\kappa_S-\kappa_I+2i\Delta k}{4\nu}\right)^2}, 1\right)^T. \tag{6.B.5}$$

The solutions are given by

$$\begin{pmatrix} \hat{a}_S[x,\omega] \\ \hat{a}_I^\dagger[x,\omega] \end{pmatrix} = C_1 e^{\lambda_+ x}\vec{v}_+ + C_2 e^{\lambda_- x}\vec{v}_-. \tag{6.B.6}$$

We use the boundary conditions $\hat{a}_S[x=0,\omega] = \hat{a}_S[0,\omega]$ and $\hat{a}_I^\dagger[x=0,\omega] = \hat{a}_I^\dagger[0,\omega]$. We know the signal/idler that enters the chain and we wish to study how they evolve along the TWPA. From these boundary conditions, we can obtain expressions for the

coefficients C_1 and C_2:

$$C_1 = \frac{\hat{a}_S[0,\omega] - \left(\frac{\kappa_I-\kappa_S-2i\Delta k}{4\nu} - \sqrt{1+\left(\frac{\kappa_S-\kappa_I+2i\Delta k}{4\nu}\right)^2}\right)\hat{a}_I^\dagger[0,\omega]}{2\sqrt{1+\left(\frac{\kappa_S-\kappa_I+2i\Delta k}{4\nu}\right)^2}} \tag{6.B.7}$$

$$C_2 = -\frac{\hat{a}_S[0,\omega] - \left(\frac{\kappa_I-\kappa_S-2i\Delta k}{4\nu} + \sqrt{1+\left(\frac{\kappa_S-\kappa_I+2i\Delta k}{4\nu}\right)^2}\right)\hat{a}_I^\dagger[0,\omega]}{2\sqrt{1+\left(\frac{\kappa_S-\kappa_I+2i\Delta k}{4\nu}\right)^2}}. \tag{6.B.8}$$

We now wish to express the solutions in the form of a scattering matrix equation

$$\begin{pmatrix} \hat{a}_S[x,\omega] \\ \hat{a}_I^\dagger[x,\omega] \end{pmatrix} = \begin{pmatrix} s_{\hat{a}_S,\hat{a}_S}[x,\omega] & s_{\hat{a}_S,\hat{a}_I^\dagger}[x,\omega] \\ s_{\hat{a}_I^\dagger,\hat{a}_S}[x,\omega] & s_{\hat{a}_I^\dagger,\hat{a}_I^\dagger}[x,\omega] \end{pmatrix} \begin{pmatrix} \hat{a}_S[0,\omega] \\ \hat{a}_I^\dagger[0,\omega] \end{pmatrix}. \tag{6.B.9}$$

Using the form of C_1 and C_2 above, we isolate in terms of $\hat{a}_S[0,\omega]$ and $\hat{a}_I^\dagger[0,\omega]$. The elements of the scattering matrix are

$$\begin{aligned}
s_{\hat{a}_S,\hat{a}_S}[x,\omega] &= e^{(i\omega-(\kappa_S+\kappa_I)/4)x/v}\left[\cosh(x\tilde{\nu}/v)\right. \\
&\quad \left. + \tfrac{\kappa_I-\kappa_S-2i\Delta k}{4\tilde{\nu}}\sinh(x\tilde{\nu}/v)\right], \\
s_{\hat{a}_S,\hat{a}_I^\dagger}[x,\omega] &= s_{\hat{a}_I^\dagger,\hat{a}_S}[x,\omega] = e^{(i\omega-(\kappa_S+\kappa_I)/4)x/v}\tfrac{\nu\sinh(x\tilde{\nu}/v)}{\tilde{\nu}} \\
s_{\hat{a}_I^\dagger,\hat{a}_I^\dagger}[x,\omega] &= e^{(i\omega-(\kappa_S+\kappa_I)/4)x/v}\left[\cosh(x\tilde{\nu}/v)\right. \\
&\quad \left. - \tfrac{\kappa_I-\kappa_S-2i\Delta k}{4\tilde{\nu}}\sinh(x\tilde{\nu}/v)\right]
\end{aligned} \tag{6.B.10}$$

where

$$\tilde{\nu} = \sqrt{\nu^2 + \left(\frac{\kappa_S-\kappa_I+2i\Delta k}{4}\right)^2}. \tag{6.B.11}$$

We can construct the full solution to the differential equation, including the source terms,

using these scattering matrix elements. The full solution is given by

$$\begin{aligned}\begin{pmatrix}\hat{a}_S[x,\omega]\\ \hat{a}_I^\dagger[x,\omega]\end{pmatrix} =&\mathbf{s}[\mathbf{x},\omega]\begin{pmatrix}\hat{a}_S(0)\\ \hat{a}_I^\dagger(0)\end{pmatrix}\\ &+\frac{1}{v}\int_0^x dx'\mathbf{s}[\mathbf{x}-\mathbf{x}',\omega]\begin{pmatrix}\sqrt{\kappa_S}\hat{a}_S^{(loss)}[x',\omega]\\ \sqrt{\kappa_I}\hat{a}_I^{\dagger(loss)}[x',\omega]\end{pmatrix}\end{aligned} \tag{6.B.12}$$

where $\mathbf{s}(\mathbf{x})$ is the transfer matrix defined with the above elements in Eq. Equation 6.B.10.

6.C Logarithmic negativity and purity

In this section, we derive the form of Eq. Equation 6.3.5 from its definition based on the covariance matrix of a two mode squeezed state (taking our two modes to be the signal and idler modes). We define a four-dimensial basis vector $\hat{\mathbf{X}} = (\hat{X}_S, \hat{P}_S, \hat{X}_I, \hat{P}_I)^T$. In this basis, the covariance matrix takes the form

$$\sigma = \begin{pmatrix} 2\langle\hat{a}_S^\dagger\hat{a}_S\rangle+1 & 0 & \langle\hat{a}_I\hat{a}_S\rangle+\langle\hat{a}_I^\dagger\hat{a}_S^\dagger\rangle & 0\\ 0 & 2\langle\hat{a}_S^\dagger\hat{a}_S\rangle+1 & 0 & -\langle\hat{a}_I\hat{a}_S\rangle-\langle\hat{a}_I^\dagger\hat{a}_S^\dagger\rangle\\ \langle\hat{a}_I\hat{a}_S\rangle+\langle\hat{a}_I^\dagger\hat{a}_S^\dagger\rangle & 0 & 2\langle\hat{a}_I^\dagger\hat{a}_I\rangle+1 & 0\\ 0 & -\langle\hat{a}_I\hat{a}_S\rangle-\langle\hat{a}_I^\dagger\hat{a}_S^\dagger\rangle & 0 & 2\langle\hat{a}_I^\dagger\hat{a}_I\rangle+1 \end{pmatrix}. \tag{6.C.1}$$

To find the logarithmic negativity, we need to take the partial transpose of the covariance matrix and then find its eigenvalues. The logarithmic negativty will be given by

$$E_{\mathrm{N}} = -\sum_i \ln\lambda_i, \tag{6.C.2}$$

where λ_i are distinct eigenvalues with value less than 1. Due to its symplectic form, the partially transposed covariance matrix will only have 2 distinct eigenvalues. Of those two, only one will ever be less than one. We find the eigenvalues to be

$$\begin{aligned}\lambda_\pm =&\langle \hat{a}_S^\dagger \hat{a}_S\rangle + \langle \hat{a}_I^\dagger \hat{a}_I\rangle + 1 \\ &\pm \sqrt{\left(\langle \hat{a}_S^\dagger \hat{a}_S\rangle - \langle \hat{a}_I^\dagger \hat{a}_I\rangle\right)^2 + \left(\langle \hat{a}_I \hat{a}_S\rangle + \langle \hat{a}_I^\dagger \hat{a}_S^\dagger\rangle\right)^2}\end{aligned} \tag{6.C.3}$$

where only λ_- can ever be less than one.

We can now express the needed averages using the thermal TMSS parameters as introduced in Eqs. (6.3.2) and (6.3.3). A straightforward calculation then yields:

$$E_N = -\ln\left[n_R - \sqrt{n_R^2 - (1+2\bar{n}_S)(1+2\bar{n}_I)}\right]. \tag{6.C.4}$$

The purity, as a function of the covariance matrix is given by

$$\mu = \frac{1}{\sqrt{\det(\sigma)}}. \tag{6.C.5}$$

For the case of a TMSS, the eigenvalues of the covariance matrix are the same as the partially transposed one. Since the eigenvalues are repeated, the determinant can be expressed as

$$\begin{aligned}\det &= (\lambda_+)^2 (\lambda_-)^2 \\ &= \left(n_R^2 - \left(\sqrt{n_R^2 - (1+2\bar{n}_S)(1+2\bar{n}_I)}\right)^2\right)^2 \\ &= \left((1+2\bar{n}_S)(1+2\bar{n}_I)\right)^2.\end{aligned} \tag{6.C.6}$$

Hence, the purity takes the form

$$\mu = \frac{1}{(1+2\bar{n}_S)(1+2\bar{n}_I)}. \tag{6.C.7}$$

References

[1]A. Blais, R.-S. Huang, A. Wallraff, S. Girvin, and R. Schoelkopf, Physical Review A **69**, 062320 (2004).

[2]C. M. Caves, Phys. Rev. D **26**, 1817–1839 (1982).

[3]A. A. Clerk, M. H. Devoret, S. M. Girvin, F. Marquardt, and R. J. Schoelkopf, Rev. Mod. Phys. **82**, 1155–1208 (2010).

[4]K. O'Brien, C. Macklin, I. Siddiqi, and X. Zhang, Phys. Rev. Lett. **113**, 157001 (2014), published.

[5]C. Macklin, K. O'Brien, D. Hover, M. E. Schwartz, V. Bolkhovsky, X. Zhang, W. D. Oliver, and I. Siddiqi, Science **350**, 307–310 (2015), published.

[6]T. C. White, J. Y. Mutus, I.-C. Hoi, R. Barends, B. Campbell, Y. Chen, Z. Chen, B. Chiaro, A. Dunsworth, E. Jeffrey, J. Kelly, A. Megrant, C. Neill, P. J. J. O'Malley, P. Roushan, D. Sank, A. Vainsencher, J. Wenner, S. Chaudhuri, J. Gao, and J. M. Martinis, Appl. Phys. Lett. **106**, 242601 (2015).

[7]A. G. Fowler, M. Mariantoni, J. M. Martinis, and A. N. Cleland, Phys. Rev. A **86**, 032324 (2012).

[8]R. Versluis, S. Poletto, N. Khammassi, B. Tarasinski, N. Haider, D. J. Michalak, A. Bruno, K. Bertels, and L. DiCarlo, Phys. Rev. Applied **8**, 034021 (2017).

[9]S. Barzanjeh, D. P. DiVincenzo, and B. M. Terhal, Physical Review B **90**, 134515 (2014).

[10]N. Didier, A. Kamal, W. D. Oliver, A. Blais, and A. A. Clerk, Phys. Rev. Lett. **115**, 093604 (2015).

[11]B. Kraus, and J. I. Cirac, Phys. Rev. Lett. **92**, 013602 (2004).

[12]N. Didier, S. Shankar, and M. Mirrahimi, arXiv:1703.03379, 2017.

[13]A. L. Grimsmo, and A. Blais, npj Quant. Inf. **3**, 20 (2017).

[14]S. L. Braunstein, and P. van Loock, Rev. Mod. Phys. **77**, 513–577 (2005).

[15]A. Furusawa, J. L. Sørensen, S. L. Braunstein, C. A. Fuchs, H. J. Kimble, and E. S. Polzik, Science **282**, 706–709 (1998).

[16]C. M. Caves, and D. D. Crouch, J. Opt. Soc. Am. B **4**, 1535–1545 (1987).

[17]B. Ho Eom, P. K. Day, H. G. LeDuc, and J. Zmuidzinas, Nature Physics **8**, 623–627 (2012).

[18]A. A. Adamyan, S. E. de Graaf, S. E. Kubatkin, and A. V. Danilov, Journal of Applied Physics **119**, 083901 (2016).

[19]M. R. Vissers, R. P. Erickson, H.-S. Ku, L. Vale, X. Wu, G. C. Hilton, and D. P. Pappas, Appl. Phys. Lett. **108**, 012601 (2016).

[20]R. P. Erickson, and D. P. Pappas, Phys. Rev. B **95**, 104506 (2017).

[21]Y.-D. Wang, S. Chesi, and A. A. Clerk, Phys. Rev. A **91**, 013807 (2015).

[22]S. M. Tan, Phys. Rev. A **60**, 2752–2758 (1999).

[23]W. K. Wootters, Quant. Inf. Comput. **1**, 27–44 (2001).

[24]C. Kim, and P. Kumar, Phys. Rev. Lett. **73**, 1605–1608 (1994).

[25]V. Boyer, A. M. Marino, R. C. Pooser, and P. D. Lett, Science **321**, 544–547 (2008).

[26]C. S. Embrey, M. T. Turnbull, P. G. Petrov, and V. Boyer, Phys. Rev. X **5**, 031004 (2015).

[27]C. Eichler, D. Bozyigit, C. Lang, M. Baur, L. Steffen, J. M. Fink, S. Filipp, and A. Wallraff, Phys. Rev. Lett. **107**, 113601 (2011).

[28]J. U. Fürst, D. V. Strekalov, D. Elser, A. Aiello, U. L. Andersen, C. Marquardt, and G. Leuchs, Phys. Rev. Lett. **106**, 113901 (2011).

[29]M. Förtsch, J. U. Fürst, C. Wittmann, D. Strekalov, A. Aiello, M. V. Chekhova, C. Silberhorn, G. Leuchs, and C. Marquardt, Nat. Comm. **4**, 1818 (2013).

[30]C. Reimer, M. Kues, P. Roztocki, B. Wetzel, F. Grazioso, B. E. Little, S. T. Chu, T. Johnston, Y. Bromberg, L. Caspani, D. J. Moss, and R. Morandotti, Science **351**, 1176–1180 (2016).

7

Conclusions

7.1 Summary of results

In this thesis, we have first presented how parametric driving induces topological phase transitions in otherwise topologically-trivial systems. We considered a two-dimensional array of coupled cavities which form a Kagome lattice. The coupling between the cavities was taken to be real so that without parametric driving, the system was topologically-trivial. We then added on-site and nearest-neighbour parametric driving. By properly choosing the phases of the parametric drives and varying the parametric drive strengths, we have shown that it is possible to open band gaps. This allowed us to calculate the band Chern numbers, a topological invariant, as a function of parametric drive strength and study the topological phase diagram of our system. From the Chern number calculations, we have shown that parametric driving leads to a very rich phase diagram which is unlike any fermionic analogue previously studied. Interestingly, since this system cannot be mapped by a local transformation to a system without parametric drive, we have found a new type of topological system. Moreover, by studying the transport properties of classical signals due to the edge states present in our system, we have shown that these

states mediate a new chiral inelastic transport as well as the usual chiral elastic transport.

Moving away from the band structures induced by parametric driving, we studied how the steady-states of parametrically driven systems become occupied when weakly coupled to a zero-temperature environment, by focusing our attention to a one-dimensional array of coupled cavities subject to parametric drive. More specifically, we have studied under what circumstances such systems become thermally occupied. For the simple case of nearest-neighbour hopping and on-site parametric drive, we have shown that it is not possible to have a steady-state which is thermally occupied. However, when the energy dispersion of the band is very narrow (i.e. when the hopping is small compared to the on-site energy), the behaviour is thermal-like with high fidelity. By allowing for long-range parametric drives, where photons are created on different sites, we have shown that it is possible to obtain steady-states which are thermally occupied. Interestingly, even though we are coupled to a zero-temperature environment, the parametric driving induces thermal occupancies. Furthermore, we have shown that these long-range drives are experimentally feasible, never creating photons more than a few sites apart. There have been several proposals to generate thermally occupied states of non-conserved bosons, such as photons. Here we have shown an alternative proposal using only parametric driving.

Having studied how classical signals propagate in topological systems with parametric driving, we in turn investigated how vacuum fluctuations propagated in similar systems. However, rather than inducing the topological phase via parametric driving we began with a topologically non-trivial system. We studied an array of coupled cavities, forming a square lattice where an engineered synthetic gauge field generated a flux per plaquette of $\Phi = \pi/2$, with additional on-site parametric driving. By properly tuning the phases and frequency of the parametric drive, we have shown that it is possible to obtain parametrically-unstable chiral edge states, all the while keeping all bulk modes

stable. This behaviour is very peculiar and we have shown that it can be exploited to realize a topologically protected, quantum-limited travelling-wave parametric amplifier. Consequently, due to topology, this device is robust to losses and disorder.

Directly extending our work on the topologically-protected, travelling-wave amplifier, we studied how having fewer parametrically-driven sites affected its properties. By numerically investigating systems with fewer parametric drives, we have shown that it is possible to obtain very similar results to case where every site is driven with only three driven sites and an increased drive strength. Although it is experimentally feasible to construct the original system, it is experimentally resource-heavy to parametrically-drive every site on a lattice. Our results show that we can obtain similar results, as in the original proposal, in a resource-efficient way with considerably fewer driven sites. Furthermore, we have shown how to obtain a broader squeezing spectrum by allowing for the angle of the output quadrature to vary as a function of frequency.

Finally, we turned our attention away from topologically-protected, travelling-wave amplifiers and focused on more generic travelling-wave parametric amplifiers which are not robust to disorders in the system. Using two separate models, we studied how having different decay rates at signal and idler frequencies affected the output state of the amplifier. This is experimentally relevant as there is no reason to believe that the two frequencies should experience equal loss rates. Our analysis shows that having asymmetric loss leads to several interesting outcomes. By studying the logarithmic negativity, we have shown that asymmetric loss has minimal effect on the entanglement of the output state. On the other hand, when studying the squeezing of collective quadratures generated by our system, we have shown that it is greatly deteriorated by any level of asymmetry. This can be explained by the fact that asymmetric loss causes amplified noise to enter the squeezed collective quadrature. Interestingly, it is thus possible to have a strongly entangled output state while having no squeezing of collective

quadratures. Furthermore, we have proposed a correction protocol which allows one to regain squeezing below zero point for collective quadratures. This is of importance to protocols which specifically need collective quadratures to be squeezed. By studying the amplification properties of our device, we have shown that asymmetric loss increases the amount of noise added by the amplifier when compared to the symmetric case. This is an adverse effect as we want the added noise to be as low as possible. This work shows that asymmetries in the decay rates at signal and idler frequencies lead to important changes to the output state of the amplifier.

7.2 Future directions

This thesis presented five studies which show new fundamental uses and physical applications of parametric driving. Here we discuss some possible extensions of each study.

In chapter 2, we studied how parametric driving induces topology in an array of coupled cavities. As in Chapter 4, this requires that all cavities be parametrically driven. This is experimentally demanding. Similarly to the work of Chapter 5, it would be interesting to see if having fewer driven cavities also leads to similar results, i.e. rich topological phases and inelastic transport properties, alleviating the experimental difficulty.

In the context of topological classification [1], Chapter 2 and Chapter 4 both deal with new topological classes that cannot be characterized by the usual classification scheme because our systems do not conserve particle number and can potentially be unstable. It is of fundamental importance to further study how to extend the classification scheme to properly characterize the topological systems of Chapter 2 and 4.

One of the main results of Chapter 3 is that it is possible to obtain a thermally

occupied steady-state for bosonic particles by making use of long-range parametric drives. An interesting direction would be to use this model to initialize a thermal steady-state of bosons and then quickly turn on interactions and study quench dynamics. It would also be very interesting to see if it is possible to find long-range parametric drives which both induce a topological state and cause the edge states to be thermally occupied.

As Chapter 5 is a direct extension of the work presented in Chapter 4, we could further extend both works by studying the entanglement of the output state. These properties were not studied in Chapter 4 and 5. It would thus be interesting to see how the entanglement of the output state behaves. More specifically, it would be interesting to see how having fewer driven sites, such as in Chapter 5, modifies the entanglement properties.

The results of Chapter 6 showed that having different decay rates for the bosonic modes of a generic travelling-wave parametric amplifiers was very detrimental to the squeezing of collective quadratures. Although we propose a correction protocol, it would be interesting to study how such result would differ in a topologically-protected travelling-wave parametric amplifier (similar to the system proposed in Chapter 4, however, with non-degenerate parametric driving rather than degenerate). One could study whether or not topology would protect us from loss asymmetry, and if so, study to what extent.

References

[1]S. Ryu, A. P. Schnyder, A. Furusaki, and A. W. W. Ludwig, New J. Phys **12**, 065010 (2010).